Mathematical and computational analysis of Kelvin ship wave patterns

Ravindra Pethiyagoda
BAppSc (Hons) (Maths), BMaths, BInfoTech

Under the supervision of
Prof. Scott McCue and Dr Timothy Moroney

School of Mathematical Sciences
Science and Engineering Faculty
Queensland University of Technology

2016

Submitted in fulfilment of the requirements of the degree of
Doctor of Philosophy

Abstract

When a ship moves through the water it generates a wake. If the water is relatively calm and the ship is moving with a constant speed, the wake will appear stationary in the reference frame of the moving ship. This thesis is concerned with developing new mathematical and computational techniques for analysing steady ship wakes.

The accurate simulation of ship wakes has many applications, such as: calculating wave drag on a ship, calculating the impact a ship wake has on coastal erosion and as a tool to infer properties of a ship based solely on its wake. The two primary aims of this thesis are to develop and implement a numerical scheme for the simulation of ship wakes on a fluid of infinite depth and to use the scheme to determine the effect that wave properties (ship speed, wave nonlinearity, etc.) have on the observable features of the wake. The problem of free-surface flow due to a driving force (ship) is highly nonlinear and challenging to analyse. In this thesis we concentrate on the simplified problems of flow past a submerged singularity or a pressure distribution. The simplified geometries (submerged singularity, pressure distribution) can be thought of as building blocks for more realistic ship geometries and, regardless, provide useful tools for studying the key issues involved.

The mathematical problem that governs gravity waves on the surface of an ideal fluid is highly nonlinear due to the unknown location of the surface itself (which forms the boundary of the domain) and the application of Bernoulli's equation on the surface, which includes a quadratic dependence on velocity. If the effect of a given disturbance (a ship, say) is small enough, then the problem can be linearised by projecting the unknown surface onto a known plane and linearising Bernoulli's equation. Thus there are two formulations of interest, linear and nonlinear. While methods for analysing linear problems are well-known and effective, progress for nonlinear ship wave problems has been held back by the lack of appropriate computational techniques required to produce accurate solutions. With this in mind, the first task in this thesis is to develop a new approach to calculate numerical solutions to the problem of steady nonlinear ship waves. This work is contained in Chapter 3.

In Chapter 3 we consider the problem of uniform free-surface flow past a submerged point source in a fluid of infinite depth. We reformulate the governing equations, using a boundary integral method, into an integro-differential equation. The equation is discretised onto a collocation mesh, resulting in a system of nonlinear equations. In order to develop our new computational approach we use a preconditioned Jacobian-free Newton-Krylov (JFNK) method to solve the system of equations. We develop a linear

block-banded preconditioner to ensure efficiency of the JFNK method. Additionally, we make use of a graphics processing unit (GPU) to greatly decrease the time taken to evaluate the system of equations. By using the JFNK method, we are able to compute solutions to our ship wave problem on meshes with a much larger number of collocation points than is present in the literature. The significance of this work is that the increased number of collocation points leads to more accurate solutions with finer detail around the crests of the wave. The fine detail around the wave crests allows for analysis of highly nonlinear results for the first time. Additionally, the numerical method is easily adapted to other problems such as uniform flow past any number of submerged singularities or a pressure distribution.

While problems involving ship wakes are inherently three-dimensional, much attention has been dedicated to two-dimensional steady free-surface flow problems. In two dimensions the boundary-integral formulation is based on complex analysis and conformal mapping, and the computational challenges are more easily overcome. However, there are certain highly nonlinear solutions that require significant resolution that is not available with standard numerical approaches. With this in mind, we show in Appendix A how our computational approach developed in Chapter 3 can be adapted and applied to problems in two dimensions. We illustrate our ideas by presenting results for a range of previously studied geometries.

In Chapters 4 and 5 we examine the wake angle, the half angle of the characteristic v-pattern caused by a ship moving at a constant speed which has been of much recent interest in the literature. We define the *apparent wake angle* as the angle between the centreline of the ship wake and a line of best fit, through the highest peaks of the wake. It is well-known that for linear infinite depth flows the wake pattern is enclosed in a half-angle of 19.47°, known as Kelvin's angle. In Chapter 4 we show that, for the problem considered in Chapter 3 (with either a submerged point source or doublet), the apparent wake angle decreases like $1/F_L$ for sufficiently large F_L, where F_L is the length-based Froude number. Additionally, we observe the effect of nonlinearity on the wake angle. We find that increasing the nonlinearity of the problem increases the apparent wake angle, in some cases to a value greater than Kelvin's angle. The effect of nonlinearity on the apparent wake angle has not been studied previously, thus this work represents a significant contribution to the general wake angle knowledge base.

In Chapter 5 we observe the apparent wake angle for linear free-surface flow past a pressure distribution in finite depth. For finite depth flows the analogue of Kelvin's angle, the wedge angle, varies with the depth-based Froude number, F_H. For moderately deep fluid, we show that the apparent wake angle is different from the wedge angle and varies smoothly through the critical value $F_H = 1$. Conversely, for shallow water, the apparent wake angle closely follows the wedge angle. These results are interesting because we shed light on the seemingly contradictory results for the wedge angle and recently reported apparent wake angle.

In Chapter 6 we consider a practical application of our work. In order to analyse water waves in the real world, measurements of the surface height can be taken either over a patch or at a series of points over a period of time. These measurements can then be used to determine properties of waves such as the directional wave spectrum. One method of analysis that has gained recent popularity in the study of ship wakes is the

spectrogram. The spectrogram is constructed through time-frequency analysis of the surface height taken at a single point over time, and visually separates the different frequency components of a ship wake. Certain features of experimental spectrograms can be explained by linear theory, but until now, other features were not at all well understood. To make progress on this issue we simulate a steadily moving ship and use linear, weakly nonlinear and fully nonlinear theory to explain additional components not explained by linear theory. For the nonlinear results we extend our computational approach of Chapter 3 to allow for solutions over a larger domain. This work is significant because it allows for more information to be derived from an experimental spectrogram. This work also serves as a step toward greatly expanding the usefulness of spectrograms when analysing ship wakes.

Declaration

I hereby declare that this submission is my own work and to the best of my knowledge it contains no material previously published or written by another person, nor material which to a substantial extent has been accepted for the award of any other degree or diploma at QUT or any other educational institution, except where due acknowledgement is made in the thesis. Any contribution made to the research by colleagues, with whom I have worked at QUT or elsewhere, during my candidature, is fully acknowledged.

I also declare that the intellectual content of this thesis is the product of my own work, except to the extent that assistance from others in the project's design and conception or in style, presentation and linguistic expression is acknowledged.

QUT Verified Signature

Signature Date 14/10/2016

Acknowledgements

Firstly, I would like to thank my principal supervisor, Professor Scott McCue, for introducing me to this ship wake problem and the area of fluid dynamics during my honours year. I thank Dr Timothy Moroney for introducing me to various computational tools and techniques and for his constant help with debugging and troubleshooting any problems with the numerical schemes. I would also like to thank both Scott and Timothy for their constant guidance throughout my candidature.

My PhD was supported by an Australian Postgraduate Award (APA) and a QUT Excellence Top-Up Scholarship. I acknowledge financial support for conference travel by the School of Mathematical Sciences and the CSIRO-ANZIAM Student Support Scheme. The computational component of this work was undertaken using QUT's High Performance Computing facilities.

I wish to thank Tomas Torsvik for providing a copy of the experimental data in Figure 6.1 and Tarmo Soomere for some fruitful discussions with regard to the work in Chapter 6.

I greatly thank the staff at the School of Mathematical Sciences for their help with all the forms required to attend the many great conferences that I have. Additionally, I would like to thank the QUT High Performance Computing support team for their help with any technical computing problems.

Finally, I thank my fellow PhD students, friends and family for the general support and encouragement.

Contents

1 Introduction

As a ship moves through relatively calm water it generates a wake (Figure 1.1). The study of these ship wake patterns has continued for over a century (Darrigol 2003). The interest in three-dimensional ship waves was initiated with the work of Rayleigh (1883) and Thomson (1887). The size and shape of the wake generated by a ship is of great interest for many practical reasons, such as wave drag, coastal erosion and ship detection.

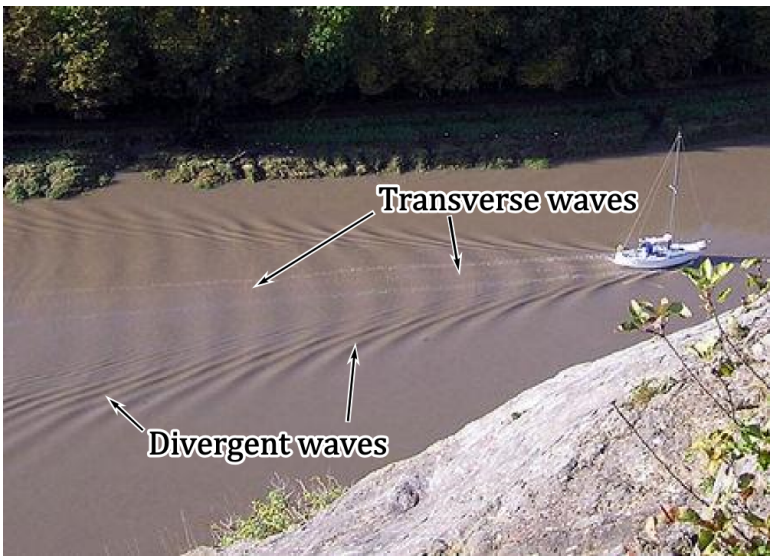

Figure 1.1: A photograph of a ship travelling down a river. The wake is clearly visible on the water's surface. Note the transverse and divergent waves.

Wave drag is one of the two main sources of drag on a ship (the other is viscous drag); the larger the wake generated by a ship the larger the drag force on the ship. Therefore, simulating the wake for various different hull shapes can help inform ship design with respect to minimising wave drag. Because drag is an important factor in ship construction, the study of wave drag began during the earliest period of ship wake research (Michell 1898) and has continued into the present (Barratt 1965; Havelock

1932b; Noblesse 1981).

In a similar vein to calculating wave drag on a ship from the ship's wake, the energy contained in a ship's wake can be calculated. This is important when considering erosion of a coastline or a riverbank due to the ship wake impaction (Sheremet, Gravois, and Tian 2013; Torsvik et al. 2015b). Knowing how the energy distribution of a ship wake changes with respect to certain properties (e.g. ship speed) can help inform environmentally friendly shipping policies (e.g. speed limits).

Finally, inferring characteristics of a ship from its wake is of great interest academically as a pseudo-inverse problem to help identify ships that have been detected by monitoring instruments. A full ship wake can be recorded by satellite photography (Rabaud and Moisy 2013) and radar (Hennings et al. 1999; Reed and Milgram 2002; Munk, Scully-Power, and Zachariasen 1987). Alternatively, a cross section can be recorded by a wave slope meter (Hughes, Grant, and Chappell 1977), a wave wire gauge (Markle and Greer 1992) or an echosounder (Parnell et al. 2008). These recordings can be analysed either visually (Rabaud and Moisy 2013) or spectrally (Didenkulova et al. 2013; Gomit et al. 2014) and compared with expected outcomes from analytic and simulated ship wakes to infer properties of the original ship.

The above discussion provides a broad background on the practical motivation for studying ship wakes. The present thesis is more theoretical in content, but touches on some of these themes.

From a mathematical perspective, the problem of calculating the wave pattern left behind by a moving ship is highly nonlinear. Even if we assume ideal fluid flow, the formulation leads to a highly nonlinear moving boundary problem with complicated boundary conditions on the ship's hull, especially at the contact line where the surface intersects the solid boundary. However, it turns out that we can effectively study the key features of ship waves by ignoring the ship's hull completely and replacing it with an idealised disturbance, such as a number of point singularities. With this in mind, the theme of this thesis is to use mathematical analysis and numerical computation to study ship wake patterns generated by idealised disturbances. At all times, we shall attempt to extract as much meaningful information as possible without resorting to modelling actual ship hulls (or actual submarines).

Even without dealing with actual ship hulls, the free-surface flow problems we consider in this thesis are highly nonlinear. They involve solving for Laplace's equation within the fluid domain subject to nonlinear boundary conditions on the free surface. These problems are challenging from a computational perspective, and indeed one of the broad aims is to develop an efficient numerical scheme for solving nonlinear free-surface flow problems in three dimensions. By employing this scheme together with analysis of

linearised versions of our problems, the other broad aim is to determine the effect that various properties (ship speed, wave nonlinearity, etc.) have on the observable features of the wake.

This is a thesis by publication. The thesis contains an introduction (Chapter 1), literature review (Chapter 2), core chapters (Chapters 3–6) containing the results produced during candidature and a conclusion (Chapter 7). The core chapters of this thesis consist of journal articles that have been primarily written by the author and have either been published in or submitted to peer-reviewed journals. The articles (three published, one submitted) are as follows:

1. **R. Pethiyagoda**, S. W. McCue, T. J. Moroney, and J. M. Back (2014). Jacobian-free Newton-Krylov methods with GPU acceleration for computing nonlinear ship wave patterns. *Journal of Computational Physics* **269**, 297–313 (Chapter 3).

2. **R. Pethiyagoda**, S. W. McCue, and T. J. Moroney (2014). What is the apparent angle of a Kelvin ship wave pattern? *Journal of Fluid Mechanics* **758**, 468–485 (Chapter 4).

3. **R. Pethiyagoda**, S. W. McCue, and T. J. Moroney (2015). Wake angle for surface gravity waves on a finite depth fluid. *Physics of Fluids* **27**, 061701 (Chapter 5).

4. **R. Pethiyagoda**, S. W. McCue, and T. J. Moroney (2016). Spectrograms of ship wakes: identifying linear and nonlinear wave signals. Submitted to the *Journal of Fluid Mechanics* (arXiv:1604.05812) (Chapter 6).

The chapters' contents are presented as they were published or submitted. The style and layout of the chapters has been standardised, typographical errors have been fixed and cross references have been added. The author contribution statements for each published and submitted paper are provided in Appendix B

1.1 Objectives and structure of the thesis

In this section we list the specific objectives of the thesis and the structure of the thesis.

The three main objectives of the thesis are:

1. To apply Jacobian-free Newton-Krylov methods to develop a new framework for solving steady nonlinear free-surface flow problems in three dimensions with significantly less computational expense than existing methods; furthermore, to utilise graphics processing unit (GPU) technology to accelerate the computations.

The focus here is on problems that involve classical Kelvin ship wave patterns but, more generally, the objective is to develop an approach that is versatile enough to apply to a wide range of nonlinear free-surface flow problems.

2. To use linear water wave theory and nonlinear simulations (from Objective 1) to explain recent observations presented by Rabaud and Moisy (2012, 2013) that suggest the wake half-angle θ_{app} that is observed for real vessels moving in the open sea is not the Kelvin angle $\arcsin(1/3)$, but in fact decreases with speed U like $O(U^{-1})$ for sufficiently large U. In order to determine the various effects on the apparent wake angle θ_{app}, the objective is to consider model problems with a number of different disturbances (that generate the waves) in both infinite and finite depth.

3. To use linear water wave theory, weakly nonlinear theory and nonlinear simulations (from Objective 1) to identify features of ship wave patterns through the use of spectrograms and to isolate linear and nonlinear effects. The objective is to provide new theory and explanations for the patterns in spectrograms of ship waves that enable the end-user to infer characteristics of a ship, based on an experimental spectrogram.

The structure of the thesis is as follows. In Chapter 2 we provide a review of the literature for the study of ship waves with a focus on the three main objectives. The following chapters, 3 to 6, represent published and submitted papers. Apart from style, layout, adding cross references and fixing typographical errors, the chapters appear as they were published. Chapter 3 addresses Objective 1, Chapters 4 and 5 address Objective 2 and Chapter 6 focuses on Objective 3 with an additional contribution to Objective 1.

In Chapter 3 we consider the problem of uniform flow past a submerged point source in a fluid of infinite depth. We reformulate the problem into a system of nonlinear equations by using a boundary integral method (Forbes 1989; Părău and Vanden-Broeck 2002) and a collocation mesh over a truncated domain. We use a Jacobian-free Newton-Krylov (JFNK) method (Brown and Saad 1990) to solve the resulting nonlinear system of equations. We develop a block-banded linear preconditioner to the JFNK method that is time- and memory-efficient to form and apply. The chosen preconditioner allows for the solution to be computed on a much larger mesh than has previously been possible. Additionally, we make use of a GPU to greatly increase the speed of evaluating the nonlinear function (up to 25 times faster).

In Chapter 4 we observe the apparent wake angle for the problem considered in Chapter 3 along with an additional problem of uniform flow past a submerged doublet. The

apparent wake angle is defined as the angle between the centreline of the wake and a line of best fit going through the highest peaks in the wake. We note that for the linear analogue of both problems the apparent wake angle decreases like $O(1/F_L)$ for $F_L \gg 1$ (fast dimensionless flow speed) where $F_L = U/\sqrt{gL}$ is the Froude number, U is the flow speed, g is acceleration due to gravity and L is the submerged depth of the source/doublet. This result is consistent with the previous work by Darmon, Benzaquen, and Raphaël (2014) and Ellingsen (2014). We compute solutions to the two problems for a range of Froude numbers and nonlinearities and ascertain a relationship between the apparent wake angle and nonlinearity. We find that increasing the nonlinearity of either problem generally has the effect of increasing the apparent wake angle with an exception shown to exist for a doublet with $F_L = 2.5$.

Chapter 5 considers the apparent wake angle property defined in Chapter 4 for the problem of constant linear flow past a pressure distribution in a fluid of finite depth. A range of solutions are calculated to determine the effect of flow speed and fluid depth on the apparent wake angle. We find that, as with the infinite depth problem, the apparent wake angle decreases with increased flow speed. Additionally, as the depth approaches zero the apparent wake angle approaches the theoretical maximum defined by the wedge angle (Havelock 1908).

In Chapter 6 we analyse nonlinear ship wave patterns using spectrograms. Spectrograms are an underutilised tool in the area of ship waves and are generated by performing time-frequency analysis on a cross-section of a ship wake. Using geometric arguments, weakly nonlinear analysis and computer simulations, we determine linear and nonlinear features in a ship wave spectrogram. We further relate these features as well as features caused by an accelerating ship to an experimental spectrogram produced by Didenkulova et al. (2013) and Torsvik et al. (2015b).

We conclude this thesis in Chapter 7 with a summary of our findings and their impact. A discussion of potential future work that builds on the results in this thesis is also provided. A draft paper on the application of the numerical scheme from Chapter 3 to the two-dimensional ship wave problem is given in Appendix A.

2 Literature review

In this chapter we provide a review of the current literature behind the core chapters (Chapters 3–6). We begin with a brief review of small amplitude (linear) ship waves before covering the recent work in computational techniques for the nonlinear ship wave problem. We then cover the recent explosion of work on the apparent wake angle (half angle of the ship wake's characteristic v-pattern). Finally, we cover the different ways the surface height of water can be measured and the spectral analysis that can be performed on the measurements.

Note that here and throughout we shall follow the convention in applied mathematics of referring to surface gravity waves left behind a moving vessel as ship waves, regardless of whether the vessel is a ship, submarine, some other marine vessel, duck, or any idealised mathematical disturbance (Tuck 2004).

2.1 Linear ship waves

The mathematical analysis of ship wave patterns has a very long history (Darrigol 2003), the overwhelming majority of which concerns linear theories. For example, for flow past a pressure distribution applied to the surface of the fluid $z = \zeta(x, y)$, if the pressure is small enough, then the kinematic and Bernoulli boundary conditions on $z = \zeta(x, y)$ can be linearised onto the undisturbed plane $z = 0$ (Noblesse, Delhommeau, and Yang 2009; Scullen and Tuck 2011; Wehausen and Laitone 1960). This framework is used to model the wave pattern caused by an air-cushioned vehicle such as a hovercraft. If instead, the ship has a small draft compared to its length and beam, the hull shape can be linearised to the undisturbed plane (Maruo 1967; Tuck 1975). These "flat ships" are applicable for ships of very shallow draft, or high-speed ships (speedboats). Another approach is to consider the ship wave pattern due to a thin ship. In this case the no-flux conditions on the ship hull are linearised onto the centreplane $y = 0$, while the thinness of the ship is assumed to produce small-amplitude waves, so the free surface conditions are again linearised onto the plane $z = 0$ (Michell 1898; Noblesse

et al. 2009; Tuck, Scullen, and Lazauskas 2001). This set-up has obvious applications to ship hull design, especially for vessels with narrow hulls. Another geometry of interest involves flow past a submerged object, such as a spheroid, or, in a fluid of finite-depth, a bottom topography. If the magnitude of the disturbance is again small, then the usual linearisation of the surface conditions applies (Havelock 1931). Furthermore, one can apply the thin ship approximation to submerged bodies as well (Tuck and Scullen 2002). Flows past submerged bodies have applications to submarine design and detection (Reed and Milgram 2002), for example.

In all of the linear formulations cited above, the linear problem of Laplace's equation in a known domain can be solved in principle with Fourier transforms. The velocity potential $\phi(x, y, z)$ and free surface $z = \zeta(x, y)$ are then given in terms of quadruple integrals that involve the Havelock potential (the Green's function or fundamental solution). In practice, the challenge of evaluating the resulting singular integrals with rapidly oscillating integrands has led to analytical approximations such as the method of stationary phase (Crapper 1964; Tuck, Collins, and Wells 1971; Ursell 1960), although accurate numerical computations have been conducted more recently (Noblesse et al. 2009; Noblesse, Delhommeau, and Yang 2009; Scullen and Tuck 2011). Of particular interest here, we note that the Havelock potential is the velocity potential for the linearised flow past a single submerged point source singularity (Havelock 1932b; Noblesse 1978; Noblesse 1981; Peters 1949). Thus, we see that the problem of computing the wave pattern caused by a submerged source in a uniform stream acts as a building block for all the other flows mentioned (as an example, the thin-ship theory effectively states that the flow past a thin ship hull is equivalent to the flow past a distribution of point sources on the centreplane $y = 0$ whose strength is proportional to the hull slope $\partial y/\partial x$ (Tuck, Scullen, and Lazauskas 2001)).

2.2 Nonlinear ship waves

While the linear solution for steady ship waves in infinite or finite depth is well known (Wehausen and Laitone 1960) it was only with the advent of computers that full nonlinear flow problems could be solved. Nonlinear versions of the ship wave problem have been considered by a number of authors (see Higgins, Read, and Belward 2012; Părău and Vanden-Broeck 2002; Tuck and Scullen 2002, for example). These idealised problems have at least two dimensionless parameters; ϵ (a measure of nonlinearity) and the Froude number (representative of the speed of the flow). There are several different approaches to the nonlinear problem, the simplest of which is a finite difference approach (Von Kerczek and Salvesen 1977). This method involves discretising the flow field over a regular grid and marching the system forward in time from some initial condition

to reach a long time solution that approximates the steady state solution (Ohring and Telste 1977). A significant problem with this method is that the free surface position is unlikely to line up with any regular grid, and thus interpolation is required to resolve the surface position, which restricts the accuracy of the solution.

Another method for determining the free surface profile is the finite element method (Bettess and Bettess 1983). Similar to the finite difference method, the finite element method involves discretising the flow field over an arbitrary mesh that can be updated and changed at each time step to follow the free surface (Chang and Wang 2011). The main advantage of this method is its generality, being applicable to the full Navier-Stokes equations and any simplification thereof. The main disadvantage is the high computational requirements needed to solve a problem in three dimensions.

The approach we are most interested in is to apply a boundary-integral method that relies on Green's second identity. Following the framework of Forbes (1989), the result is a singular integro-differential equation which holds on the unknown free surface $z = \zeta(x, y)$. That is, the free-surface problem in three dimensions is reduced to a two-dimensional problem for the free surface $z = \zeta(x, y)$ and the velocity potential $\phi(x, y, \zeta(x, y))$. To proceed numerically, the rough approach is to place a mesh of $N \times M$ grid points over the truncated (x, y)-plane, so that the integro-differential equation together with Bernoulli's equation can be imposed at each grid point. Newton's method is then used to solve the resulting nonlinear system of $(N-1)M$ equations for the $(N-1)M$ unknowns (which can be the slopes $\partial\zeta/\partial x$ at each point). As discussed by Forbes (1989), efficiencies can be gained by exploiting the symmetry of the problem and using an inexact Newton's method, which re-uses the Jacobian a number of times if possible.

For clarity, using Newton's method (with damping, to provide globalisation) to solve the nonlinear system of equations

$$\mathbf{F}(\mathbf{u}) = \mathbf{0}, \tag{2.1}$$

where $\mathbf{u}$ is the vector of unknowns, involves the iteration

$$\mathbf{J}(\mathbf{u}_k)\delta\mathbf{u}_k = -\mathbf{F}(\mathbf{u}_k), \tag{2.2}$$

$$\mathbf{u}_{k+1} = \mathbf{u}_k + \lambda_k \delta\mathbf{u}_k, \tag{2.3}$$

where $\mathbf{J} = \partial\mathbf{F}/\partial\mathbf{u}$ is the Jacobian matrix, $\mathbf{u}_k$ is the kth iterate in the sequence $\{\mathbf{u}_k\}_{k=0}^{\infty} \to \mathbf{u}$ and the damping parameter $\lambda_k \in (0, 1]$ is chosen such that $||\mathbf{F}(\mathbf{u}_{k+1})|| < ||\mathbf{F}(\mathbf{u}_k)||$ at every iterate. The inexact Newton's method used by Forbes (1989) replaces $\mathbf{J}(\mathbf{u}_k)$ with the initial Jacobian, $\mathbf{J}(\mathbf{u}_0)$, to prevent excess time being spent on forming the updated Jacobians.

In recent times, over a series of papers, Părău, Vanden-Broeck and Cooker (Părău and Vanden-Broeck 2002, 2011; Părău, Vanden-Broeck, and Cooker 2005ab, 2007abc, 2010) have applied Forbes' formulation to solve fully three-dimensional nonlinear ship wave problems. The problem that is closest to the one considered in Chapter 3 is presented by Părău and Vanden-Broeck (2002), and involves a pressure distribution instead of a point source. Părău and Vanden-Broeck (2002) stated that, for the analogous two-dimensional problem, there was no visual difference between solutions computed on meshes with more than 200 collocation points and mesh spacing less than 0.1. However, the mesh used by Părău and Vanden-Broeck for the three-dimensional problem was only 89×13 with $\Delta x = \Delta y = 0.2$, where Δx and Δy are the mesh spacing in the x and y directions, respectively. This mesh was shown to fall short of the desired accuracy for grid independence (Părău and Vanden-Broeck 2002).

Similar meshes are used by Părău, Vanden-Broeck and Cooker (2005a, 2007b). Both papers solve similar gravity-capillary wave problems, where the finest mesh used was 60×60 with $\Delta x = \Delta y = 0.6$ and symmetry in both the x and y directions. However, in both cases there was a visual difference when increasing the number of mesh points, indicating that grid-independence was not achieved. Coarse meshes of 60×20 were also used in Părău, Vanden-Broeck and Cooker (2007c, 2010). The 2007 paper (Părău, Vanden-Broeck, and Cooker 2007c) required a solution for two meshes forcing the use of a coarse mesh due to lack of computer memory. The 2010 paper (Părău, Vanden-Broeck, and Cooker 2010), involving a time dependent problem, required a solution to the system at each time step forcing a coarse mesh due to time constraints. More recently, Părău and Vanden-Broeck (2011) have been using finer meshes of 120×60 with $\Delta x = \Delta y = 0.2$, but only to test the accuracy of the coarse mesh that is used for the majority of the results.

Forbes and Hocking (2005) used the same boundary-integral method to find solutions to a three-dimensional fluid withdrawal problem. Forbes and Hocking (2005) used a mesh of 101×101 points which, were it solved on a modern day desktop computer, would be approaching the upper bound of what is possible in terms of computer memory. To put Forbes' method into context, other approaches for three-dimensional ship wave problems use a similar grid size; for example, Tuck and Scullen (2002) apply a mesh of 91×25 grid points with their Rankine source method, while similar resolution is provided for a Rankine source method in Janson, Leer-Andersen, and Larsson (2003).

The low level of accuracy demonstrated for the three-dimensional problems just mentioned is to be contrasted with the vast literature on two-dimensional flows. For example, by applying a boundary-integral method in two dimensions combined with a straight-forward Newton approach, authors can easily use in excess of 1000 grid points over the two-dimensional surface (McCue and Forbes 2002; Ogilat et al. 2011) or, in

more recent times, 2000 points (Lustri, McCue, and Binder 2012; Trinh, Chapman, and Vanden-Broeck 2011). Although most authors use fewer than 1000 points for their two-dimensional calculations, generally an accepted procedure is to continue to refine the mesh until the results are grid-independent, at least visually. With less than 100 points used along the x-direction for three-dimensional flows, the resolution over each wavelength is simply not of a sufficient standard for any claims about grid-independence to be made. Indeed, for this very reason, there has been little to no detailed study of the effect of high nonlinearity for three-dimensional ship wave problems.

The primary reason for the low number of collocation points used in these meshes is because an inexact Newton's method is used to solve the system of nonlinear equations. The type of inexact Newton's method used requires forming a Jacobian (Forbes 1989), using finite differences, requiring a large number of nonlinear function evaluations, which is very time consuming. Storing the full Jacobian can also occupy a large portion of system memory (Chapter 3). The prevalence of Newton's method is because it is easy to implement and requires minimal analysis of the problem. There are however other methods for solving a system of nonlinear equations such as the Jacobian-free Newton-Krylov (JFNK) method (Brown and Saad 1990), which uses a preconditioned GMRES algorithm (Saad and Schultz 1986) to avoid forming the Jacobian. Instead, a subspace of dimension much less than the Jacobian is formed and an approximate solution to (2.2) is found in the subspace. For the GMRES method to be effective, a preconditioner matrix that approximates the Jacobian while remaining simple and efficient to form and store must be chosen. The use of the JFNK method and the selection of the preconditioner matrix is the subject of Chapter 3.

In Chapter 3, we consider the nonlinear ship wave problem of uniform flow past a submerged point source presented by Forbes (1989) and reformulate the problem into a system of nonlinear equations using the numerical scheme of Părău and Vanden-Broeck (2002). We then solve the system of nonlinear equations with a JFNK method with a linear block-banded preconditioner, which is both quick to form and requires less system memory to store compared to the Jacobian, to efficiently compute solutions. We are able to produce solutions on 721×361 meshes, a significant improvement over other contemporary meshes. Additionally, we parallelise the evaluation of the system of equations and perform the operations on a graphics processing unit (GPU) to greatly speed up the method (approximately 25 times faster). An extension to this method, involving constructing a larger domain with smaller computed domains is presented in Chapter 6.

A similar method to the boundary-integral method mentioned above, which also involves the use of a boundary integral, is the boundary element method. The boundary element method, rather than considering just the collocation points on a discretised

mesh for the integral equation like the boundary integral method, considers the line between two collocation points in two dimensions (Grilli, Skourup, and Svendsen 1989) or the quadrilateral between 4 collocation points in three dimensions (Grilli, Guyenne, and Dias 2001). The integrand in the boundary integral is approximated on this element (line, quadrilateral) through the use of shape functions or splines allowing for the integral to be evaluated over the entire element. As the solution is being solved on the interpolated surface, this can give the appearance of a smooth solution despite having a lower number of collocation points (Fochesato and Dias 2006).

The boundary element method has been used on a variety of water wave problems such as point sources (Bal and Kinnas 2002; Bal, Kinnas, and Lee 2001), hydrofoils (Bal 2008; Bal 2011; Bal and Kinnas 2002), wave tanks (Fochesato and Dias 2006; Grilli, Guyenne, and Dias 2001; Grilli, Skourup, and Svendsen 1989; Grilli and Subramanya 1996; Grilli, Guyenne, and Dias 2000) and ship waves (Sung and Grilli 2006, 2008). The papers on hydrofoils offer a glimpse into the required number of elements with Bal and Kinnas (2002) stating that approximately 30 elements per wavelength should provide sufficient accuracy. However, their solution only uses 100×20 elements, which limits their solution to contain three wavelengths of the wake. The 2011 paper from Bal allows for a slightly larger domain with a 120×60 mesh, but this still does not offer a greater view of the wave created by the hydrofoil.

Using the boundary element method allows for the collocation points to move in all directions, unlike the boundary integral method whose collocation points have a fixed x and y coordinate. This allows for the solution and visualisation of overturning waves, shown in wave tanks for two dimensions (Grilli, Skourup, and Svendsen 1989; Grilli and Subramanya 1996) and three dimensions (Fochesato and Dias 2006; Grilli, Guyenne, and Dias 2001; Grilli, Guyenne, and Dias 2000). The ability to visualise overturning waves allows for insight into the nature of near-breaking and breaking waves, such as where on the wave crest the wave starts to overturn.

A relatively recent development in the computation of the waves in a wave tank by Fochesato and Dias (2006) was the utilisation of the fast multipole algorithm by Greengard and Rokhlin (1987) to improve the efficiency of their boundary element method to near linear scaling with collocation nodes. The fast multipole algorithm (see Beatson and Greengard 1997) works when nodes far away from a given element have little influence on function value compared to nodes closer to the element, as is the case with the boundary element method.

Sung and Grilli (2006, 2008) applied the boundary element method of Grilli et al. (Grilli, Guyenne, and Dias 2000; Grilli, Guyenne, and Dias 2001) with the fast multipole method of Fochesato and Dias (2006) to compute time-dependent solution to

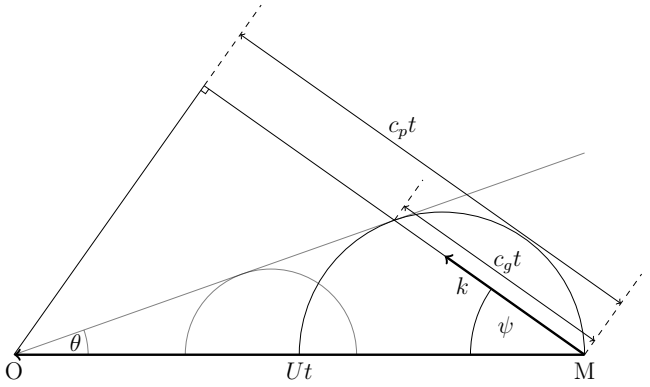

Figure 2.1: This schematic of ship wave dispersion illustrates a ship moving from the point M to the point O with a nondimensional speed 1 over the time period t_0. The waves generated by the ship at the point M propagate at all angles ψ from the sailing line and wavenumbers k with phase velocity, c_p, and group velocity, $c_g = c_p/2$. The large black semicircle is traced out using the group velocity for all ψ. The small grey semicircle follows the same rules but is generated at a different point. The grey line, tangent to the two semi circles, represents the geometric edge of the wake system with angle $\theta = \arcsin(1/3) \approx 19.47°$.

the ship wave problem of uniform flow past a pressure distribution in a fluid of infinite depth. Sung and Grilli (2008), utilising a third order accurate spatial and temporal discretisation, incurred less than 1% numerical error when using at least 8 elements per wavelength. The near linear scaling achieved by Fochesato and Dias (2006) for a wave tank was replicated by Sung and Grilli (2008) for the ship wave problem. As we are not presently interested in time-dependent solutions, we do not attempt to implement the boundary element method in this thesis.

2.3 Wake angle

In his seminal paper, Thomson (1887) showed, using the method of stationary phase, that a linear ship wake was contained within a wedge of half angle $\arcsin(1/3) \approx 19.47°$, measured from the disturbance, now known as the Kelvin angle. In addition to defining Kelvin's angle, Thomson (1887) used the method of stationary phase to perform the far-field approximation to the surface height of the wake. The far-field approximation was shown to decrease algebraically inside the wedge and exponentially outside and blow up at Kelvin's angle. A simple geometric method to derive Kelvin's wake angle requiring only ratio of phase velocity, c_p, and group velocity, c_g, is presented in Figure 2.1 (Crawford 1984). Given $c_p = U\cos\psi$ and $c_p = 2c_g$, the large semicircle in Figure 2.1 has a radius of $Ut/4$ and is centred $3Ut/4$ from the origin. Kelvin's angle can now be recovered as $\theta = \arcsin(1/3)$.

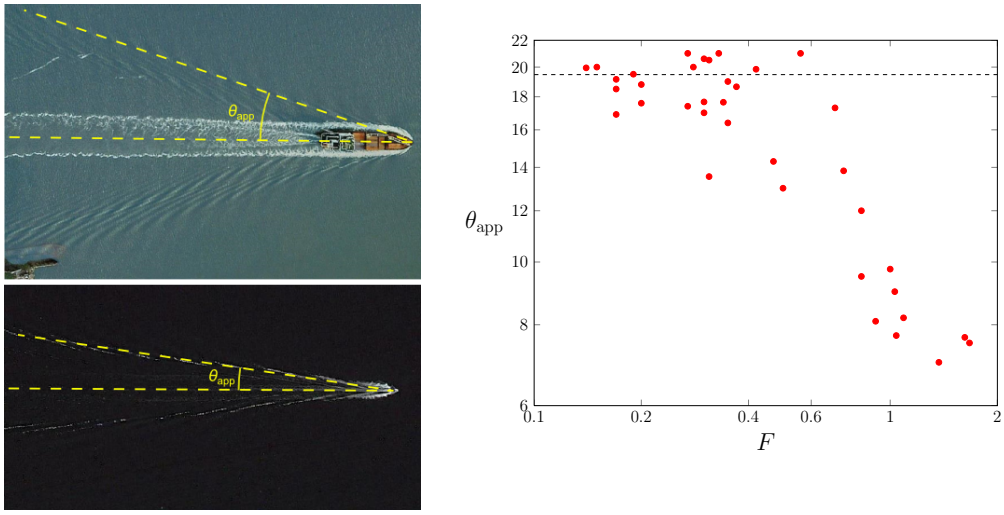

(a) Ship wakes

(b) Wake angle against the Froude number

Figure 2.2: (a) Two ship wakes taken using satellite photography (from the Google Earth database), a yellow dashed line is drawn through the brightest parts of the wake and the wake angle is marked as θ_{app}. (b) A plot of measured wake angles, θ_{app}, against the Froude number, F_L, a nondimensional measure of speed and the dashed line is Kelvin's angle.

Rabaud and Moisy (2013) recently reignited interest in the Kelvin angle by observing multiple ship wakes using satellite photography, measuring their apparent wake angle by fitting a line through the brightest parts of the wake and measuring the angle between the fitted line and the sailing line of the ship (Figure 2.2(a)). Rabaud and Moisy showed that a large number of the measured wakes exhibit apparent wake angles much less than Kelvin's angle and that the apparent wake angle appeared inversely proportional to the speed of the ship (Figure 2.2(b)). To attempt to explain this apparent inverse proportionality, Rabaud and Moisy posited that a ship cannot generate wave lengths much larger than the length of the ship. This assumption led to the result that the apparent wake angle, θ_{app}, goes like $1/(2\sqrt{2\pi}F_L)$ for fast ships, $F_L \gg 1$ where F_L is the length-based Froude number, a nondimensional measure of speed. This result was consistent with the data gathered from the satellite photographs.

The results of Rabaud and Moisy (2013) sparked much controversy with the strong opinion that the assumption used by Rabaud and Moisy cannot be simply stated without evidence (Cho 2013; Darmon, Benzaquen, and Raphaël 2014; Verberck 2013). In order to explain the decrease in wake angle with increase in ship speed and without the use of the assumption made by Rabaud and Moisy (2013), Darmon, Benzaquen, and Raphaël (2014) considered linear ship waves generated by an axisymmetric (Gaussian) pressure distribution and suggested that what was being measured by Rabaud and Moisy was the locations of the highest points in the ship wake. Thus, Darmon, Ben-

zaquen, and Raphaël (2014), looking at the far-field approximation to their linear ship waves, found that the apparent wake angle given by the maximum wave height, θ_{app}, goes like $1/(40^{1/4}\sqrt{\pi}F_L)$, which retains the order $O(1/F_L)$ decrease of Rabaud and Moisy (2013) while not relying on their controversial assumption. Continuing the idea of the apparent wake angle determined by observing the maximum wave height of the ship wake, Ellingsen (2014) looked at an axisymmetric pressure distribution travelling in a fluid with a shear current (current speed linearly varying with depth). Ellingsen (2014) found to leading order the same decrease in wake angle as Darmon, Benzaquen, and Raphaël (2014) with a correction term for the shear current.

Non-axisymmetric pressure distributions have also been considered by Benzaquen, Darmon, and Raphaël (2014) and Moisy and Rabaud (2014b). Benzaquen, Darmon, and Raphaël (2014), using the same method as Darmon, Benzaquen, and Raphaël (2014) found that for fast ships, $F_L \gg 1$, the apparent wake angle decreases like $O(1/(\sqrt{A}F_L))$ where A is the ratio of length of the ship to the beam (A is larger the thinner the ship). Benzaquen, Darmon, and Raphaël (2014) suggested that this relation is why thinner ships, such as rowing boats, exhibit smaller wake angles. The approach Moisy and Rabaud (2014b) used to calculate the wake angle of a non-axisymmetric Gaussian pressure distribution was extended from their earlier paper (Rabaud and Moisy 2013), where instead of assuming that the ship generates waves with wavelengths of the same order as the ship's length or less, they claimed that certain wave lengths are excited more than others and that the excited wavelengths are governed by the pressure distribution. Using this new method Moisy and Rabaud (2014b) discovered an intermediate range of Froude number $1 \ll F_L \ll \sqrt{A}$ for which the wake angle decreased like $O(1/F_L^2)$ on top of the $O(1/(\sqrt{A}F_L))$ decrease from Benzaquen, Darmon, and Raphaël (2014), now applicable for $F_L \gg \sqrt{A}$. While not mentioned by Benzaquen, Darmon, and Raphaël (2014), this intermediate behaviour does exist when determining the wake angle from the maximum surface height.

Another approach used to calculate the apparent wake angle is to consider the interference effects from the bow and stern waves (Noblesse et al. 2014). Noblesse et al. (2014) considered two point disturbances representing the bow and stern waves with the intersection between their respective divergent wave crests corresponding to a point of maximum constructive interference. This method leads to an apparent wake angle that decreases like $O(1/F_L^2)$ for $F_L \gg 1$, which contrasts with the results presented in the previous studies (Benzaquen, Darmon, and Raphaël 2014; Ellingsen 2014; Rabaud and Moisy 2013). Noblesse et al. (2014) also applied the interference theory to catamarans, represented by a point disturbance at the bow of each hull, finding that the wake angle for a catamaran decreased like $O(\sqrt{S}/F_L)$, where S is the separation between hulls of the catamaran.

A comparison between the three methods provided by Rabaud and Moisy (2013), Darmon, Benzaquen, and Raphaël (2014) and Noblesse et al. (2014) was given by He et al. (2014). In the comparison, He et al. (2014) claimed that the limiting wavelength (Rabaud and Moisy 2013) and the Gaussian pressure distribution (Darmon, Benzaquen, and Raphaël 2014) methods utilise unreasonable simplifications to the problem while the wave interference method (Noblesse et al. 2014) offers a better approximation to the mechanics of the problem and better matches the data collected by Rabaud and Moisy (2013). However, He et al. (2014) did note that representing a ship with just the bow and stern waves will overlook the effects contributed by the size and shape of a ship's hull.

The concern of an accurate simplification of ship geometry was addressed by Zhang et al. (2015) and He et al. (2016), who used a distribution of sources to more accurately represent the hull shape of a ship and a catamaran, respectively. Zhang et al. (2015), uses the Fourier-Kochin representation (Noblesse and Yang 1995) with a distribution of sources as given by Noblesse, Huang, and Yang (2013) to describe the ship waves. Zhang et al. (2015) splits the behaviour of the apparent wake angle in to three distinct sections: slow ships (low Froude number), where there is no interference and that apparent wake angle is given by Kelvin's angle; moderate Froude number, where the ship wake is dominated by longitudinal interference (interference between for and aft sources on the ship hull) resulting in an $O(1/F_L^2)$ decrease in apparent wake angle akin to Noblesse et al. (2014); and fast ships (large Froude number), where the ship wake is dominated by lateral interference (interference between the starboard and port sources) resulting in an $O(1/F_L)$ decrease in apparent wake angle. The three wake angle regimes are in agreement with the results of Moisy and Rabaud (2014b), and suggest that, with respect to the apparent wake angle, there are some similarities between representing a ship as a distribution of sources (Neumann-Michell theory) and a non-axisymmetric Gaussian pressure distribution. The potential similarities between the Neumann-Michell theory and the non-axisymmetric Gaussian pressure distribution could dispute the claim by He et al. (2014) that the Gaussian pressure distribution is not an accurate representation of a ship, lending credibility to the analysis of the Gaussian pressure distribution that has been widely used (Darmon, Benzaquen, and Raphaël 2014; Ellingsen 2014; Moisy and Rabaud 2014b).

The exploration of the ship wake of a catamaran by He et al. (2016) yielded more complicated interactions due to the extra ship hull. He et al. (2016) identified inner (caused by lateral interference) and outer (caused by longitudinal interference) wake angles that both exhibit the three regimes as presented by Moisy and Rabaud (2014b) and Zhang et al. (2015). However, the intermediate region proved more complicated and was fitted with an approximate form derived from extensive numerical simulations

of different hull shapes. He et al. (2016) also examined the ratio between the heights of the inner and outer peaks to decide which peaks would be considered to define the apparent wake angle. It was found that for slow ships (low Froude number) with a small spacing between the two hulls the outer peak was greater than the inner peak. If either the Froude number increased or the hulls were separated then the inner peaks would dominate the wake and thus define the wake angle for either fast ships (large Froude numbers) or well separated hulls. Noblesse et al. (2016) observed this result with multiple full surface realisations of the problem presented by He et al. (2016).

Additionally, cases where Kelvin's angle no longer strictly applies as the maximum wake angle have been considered (Moisy and Rabaud 2014a; Zhu et al. 2015). Moisy and Rabaud (2014a) considered the effect of surface tension (gravity-capillary waves) on the apparent wake angle. Surface tension has the effect that waves exist for all wake angles, however, a cusp angle can be defined such that $\mathrm{d}\theta/\mathrm{d}k = 0$ where θ is the angle measured from the ship and k is the wave number (see Figure 2.1). This definition leads to two cusp angles that appear through a saddle-node bifurcation at approximately 22.06° where the gravity wave cusp branch tends towards Kelvin's angle and the capillary wave cusp tends to zero as the speed of the disturbance increases. Moisy and Rabaud (2014a) showed both experimentally and with simulations that the apparent wake angle still decreased like $1/F_L$ due to the fast ship behaviour of the cusp angles, and that wake angles greater than Kelvin's angle were readily observed for a slow moving disturbance due to the effects of surface tension.

Similar to gravity-capillary waves, ship waves in finite depth fluid do not necessarily have a cusp at Kelvin's angle. In fact the finite depth cusp angle increases monotonically from Kelvin's angle to 90° as the depth-based Froude number F_H (related to the length-based Froude number via $F_L = \sqrt{d}F_H$, where d is the ratio between the depth of the fluid and the length of the ship) increases from 0 to 1 and then decreases monotonically for $F_H > 1$ with the asymptotic behaviour of $\theta_{\text{cusp}} \sim 1/F_H$ as $F_H \gg 1$ (Havelock 1908). Finite depth flows have been examined concurrently in Chapter 5 with respect to a Gaussian pressure distribution and by Zhu et al. (2015) with respect to two point pressure disturbances. Zhu et al. (2015) applied the wave interference method of Noblesse et al. (2014) to finite depth flow past a monohull ship modelled by point pressures at the bow and stern. They showed that the apparent wake angle follows that cusp angle up until some depth-based Froude number $F_H < 1$. This Froude number is closer to 1 the shallower the fluid, after which the apparent wake angle separates from the cusp angle and potentially continues to increase if the fluid is shallow enough before decreasing rapidly, eventually exhibiting the same $O(1/F_L^2)$ decrease for $F_L \gg 1$ derived by Noblesse et al. (2014). The interference method has also been applied to finite depth flow past a catamaran (Zhu et al. 2016).

All the recent work in apparent wake angles has been for linear fluid flow. We examine the effect of nonlinearity on the apparent wake angle in Chapter 4 by using the computational techniques developed in Chapter 3 to compute nonlinear solutions to the problem of uniform fluid flow past a submerged point source and doublet. Using the method of Darmon, Benzaquen, and Raphaël (2014) the apparent wake angle for the linear problem is shown to exhibit an $O(1/F_L)$ decrease for $F_L \gg 1$ for both a submerged point source and a doublet. Introducing and increasing the nonlinearity of the problem has the effect of increasing the apparent wake angle. For flow past a submerged source, the apparent wake angle increased with nonlinearity to a value greater than Kelvin's angle for all tested Froude numbers. Similarly, the apparent wake angle for flow past a doublet increases with nonlinearity, however the wake angle only exceeded Kelvin's angle for low Froude numbers.

2.4 Measured surface displacement

The analysis of real world examples of ship waves is limited due to the difficulty of accurately capturing the surface height outside of a towing tank. Two methods of observing ship wakes from a distance are with satellite photography (Munk, Scully-Power, and Zachariasen 1987; Rabaud and Moisy 2013) and radar (Reed and Milgram 2002). Unfortunately, satellite photography requires adequate lighting conditions to highlight the desired wake components (Munk, Scully-Power, and Zachariasen 1987). Even with sufficient clarity a photograph will not provide quantitative data on the surface elevation, leaving only a few viable properties to be measured such as the apparent wake angle (Rabaud and Moisy 2013). With respect to radar, backscattering can cause a bright v-pattern to be observed within the wake, that is highly dependent on the sailing line relative to the radar (Milgram 1988).

There are other optical methods for accurately measuring the surface height of ocean waves (Chatellier et al. 2013; Gomit et al. 2013; Gomit et al. 2015; Wanek and Wu 2006). The method detailed by Wanek and Wu (2006) measures the surface height by utilising three cameras mounted on an array. The three images captured simultaneously are then matched to resolve the height of the water's surface over a roughly two square metre patch. Wanek and Wu's method has the advantage of being non-intrusive allowing for wave measurements in real bodies of water.

For wave tank experiments, suspended particles can be used to assist in measuring the surface height as well as provide information on the velocity field of the fluid (Chatellier et al. 2013; Gomit et al. 2013). Volume seeded particles (Gomit et al. 2013) are used in conjunction with a laser sheet projected into the tank, from the side of the tank below the water line, to measure the surface height when the illuminated particles are

observed by three external cameras. The volume seeded particles also provide a two-dimensional velocity field on the projected laser sheet. Chatellier et al. (2013) used surface seeded particles that contrast with the inner lining of the wave tank to enhance the matching techniques like those presented by Wanek and Wu (2006) to determine surface height as well as provide the three-dimensional velocity field along the water's surface. Unfortunately, the particles along the surface can be pushed aside by an object moving through the water such as a ship, and this creates dead zones on the water's surfaces that cannot be measured. Thus a combination of both volume seeded and surface seeded particles must be used to measure the height of the water's surface everywhere (Gomit et al. 2014). Alternatively, Gomit et al. (2015) projected a grid of laser beams onto the water's surface sequentially and measured the point of impact using two fixed cameras. Due to the sequential nature of this method it is restricted to measuring steady ship waves, but it can do so over an area of several square metres.

Another method of observing ship wakes is to record the water height at a single point over time as a ship passes nearby. The resulting output signal will be a cross-section of the ship wake taken in the direction of travel (Markle and Greer 1992; Parnell et al. 2008; Wyatt and Hall 1988). There are multiple ways to measure the surface height at a single point, such as a wave slope meter (Wyatt and Hall 1988), a capacitance wave gauge (Brown et al. 1989; Markle and Greer 1992) or an echosounder (Parnell et al. 2008). The wave slope meter utilises an upward pointing submerged laser, a focusing lens above the surface and a translucent screen, one focal length away from the lens, to read the slope of the surface from the refraction of the laser beam (Hughes, Grant, and Chappell 1977). The slope can then be integrated to get the surface height. The wave slope meter has the advantage of having a fast sample rate of 400Hz (Wyatt and Hall 1988). The capacitance wave gauge (wave wire gauge) uses a single insulated wire held taut and partially submerged in the water. The capacitance of the gauge is measured and is related linearly to the length of wire submerged in water. The linear relationship between surface height and capacitance exists over a large range, which allows the capacitance wave gauge to measure waves of large amplitude (Hughes 1993; Markle and Greer 1992).

The final device used to measure the height of the water's surface discussed here is the echosounder (Kurennoy, Parnell, and Soomere 2011; Parnell et al. 2008). The echosounder is mounted on a tripod, above the water's surface where it uses ultrasound to measure the distance between the device and the surface. While the echosounder is restricted to gathering data at 5Hz it can be set up to record data autonomously for over a week (Parnell et al. 2008).

After measuring the surface height either over a patch or at a single point over time the collected data must be analysed. A good procedure is to perform a Fourier analysis on

the data to view the spectrum of the wave and separate the different wave components of the ship wake. Tuck, Collins, and Wells (1971) derived the spectra for the linear ship wave problem and showed that the two-dimensional spectrum is infinite along a single curve given in polar coordinates ($\kappa_x = \kappa\cos\alpha$, $\kappa_y = \kappa\sin\alpha$) by $\kappa = k\sec^2\alpha$ and zero everywhere else. Tuck, Collins, and Wells (1971) also showed that for a cross-section of the ship wake taken at some angle to the centreline, the finite Fourier transform will have two peaks corresponding to the transverse and divergent waves. The location of the peaks is given in terms of the angle of the cross-section for positive angles less than Kelvin's angle, $\arcsin(1/3)$.

Gomit et al. (2014) conducted multiple experiments of a model ship hull moving down a towing tank at different constant speeds. The water surface was measured for every wake using a combination of the volume seeded (Gomit et al. 2013) and surface seeded (Chatellier et al. 2013) particle methods. Using a two-dimensional finite Fourier transform, Gomit et al. (2014) showed that the spectrum of the ship wake is clearly localised along a curve and that this curve very closely aligns with the two-dimensional spectra curve mentioned by Tuck, Collins, and Wells (1971) for their chosen speeds. Additionally, Gomit et al. (2014) decomposed the ship wake in spectral space into the disturbance near the ship and the Kelvin wake pattern. This type of decomposition is helpful for choosing an approximate form (pressure distribution) of the real ship for analysis.

When analysing a cross-section of a ship wake, rather than take a single finite Fourier transform as proposed by Tuck, Collins, and Wells (1971) multiple, short-time, discrete Fourier transforms, represented visually as a spectrogram, are used to provide more information (Wyatt and Hall 1988). Spectrograms are well studied and have been used in the field of signal processing for decades (Cohen 1989). A spectrogram of a given signal is characterised by the window size, the length of the signal used for a single short-time Fourier transform, and the window function, a weighting function applied to the window. As the window size increases the spectrogram will produce a refined colour intensity at the frequencies given by Tuck, Collins, and Wells (1971).

Even with the prevalence of spectrograms in signal analysis, spectrograms are a relatively new tool in the field of fluid dynamics, having been used originally by Wyatt and Hall (1988) and Brown et al. (1989) to analyse ship wakes, with more recent work by Benassai, Piscopo, and Scamardella (2015), Didenkulova et al. (2013), Sheremet, Gravois, and Tian (2013), Torsvik et al. (2015a) and Torsvik et al. (2015b). Wyatt and Hall (1988) measured their ship wake with a wave slope meter moving perpendicular to the direction of the ship. Using linear theory, Wyatt and Hall (1988) described a curve that approximated the location of colour intensity presented in their experimental results. Finally, Wyatt and Hall (1988) theorised that some additional colour intensity

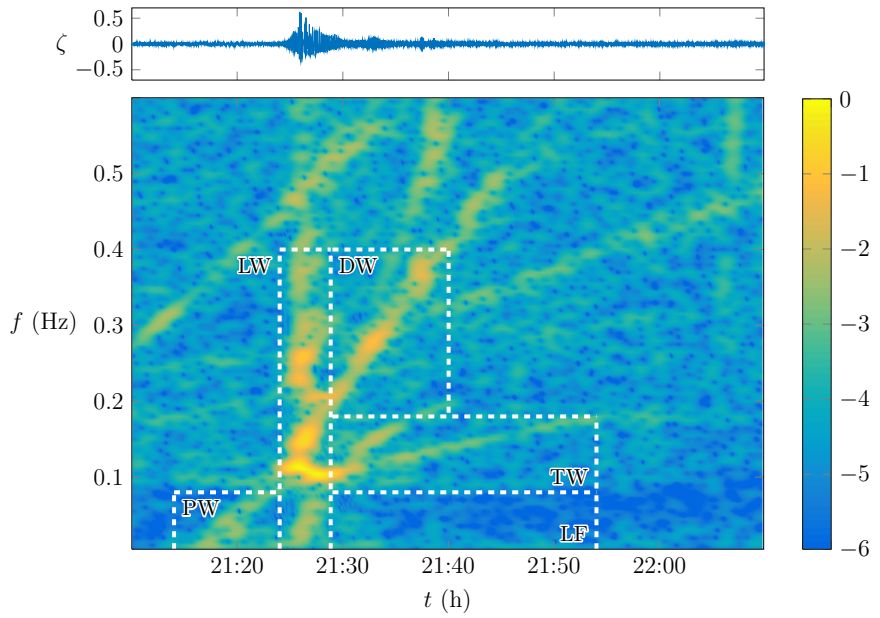

Figure 2.3: A spectrogram of the signal generated by a high speed ferry in the Gulf of Finland. This figure is identical to Figure 9(a) of Torsvik et al. (2015b), except a) we have re-computed the spectrogram using a different colour scheme, and b) we have used the colour intensity interval $(-6, 0)$ whereas they use $(-6, -1)$. The five wake components as identified by Torsvik et al. (2015b) are the precursor solitary (PW), leading (LW), divergent (DW), transverse (TW) and low frequency (LF) waves. The wave signal is presented above the spectrogram. This figure appears again in Chapter 6 as Figure 6.1.

present in their spectrograms, that did not lie on their theoretical curve, was due to nonlinear waves.

The recent work in ship wave spectrograms (Benassai, Piscopo, and Scamardella 2015; Didenkulova et al. 2013; Torsvik et al. 2015b) has primarily been focused on calculating the energy contained in a given wave and the effect that wave will have on the environment (erosion, etc.). Torsvik et al. (2015b) showed that for small amplitude ship waves the spectrogram has two components; a sliding-frequency mode (chirp) and a constant frequency mode, corresponding to the divergent and transverse wave components, respectively. These features can be confirmed by the theoretical work of Wyatt and Hall (1988) if their sensor is taken as stationary. A similar chirp was also detected by Sheremet, Gravois, and Tian (2013). The transverse and divergent components of the spectrogram were used in conjunction with infinite depth linear theory to predict the ship's speed and the minimum distance from the echosounder. However, experimentally Torsvik et al. (2015b) found and classified five wake components present in the spectrogram: precursor solitary, leading, divergent, transverse and low frequency waves (Figure 2.3). Torsvik et al. (2015a) were able to offer some evidence to the notion

that two of the additional wake components (precursor, leading) were a result of wave shoaling and nonlinear effects caused by the ship waves approaching the shore. However, wave shoaling is a complicated process that depends heavily on the underwater topography of the coast, which makes discerning the exact cause of wave components difficult.

The true nature of the precursor, leading and low frequency wave components has not been fully explored in the literature. In Chapter 6 we use a modified version of the numerical scheme presented in Chapter 3 to compute solutions to the problem of uniform fluid flow past a pressure distribution for time-frequency analysis. By taking spectrograms of the cross-sections of the computed solutions, we show that the leading wave component as identified by Torsvik et al. (2015b) is potentially caused by nonlinear ship waves. Additionally, we give an equation for the location of colour intensity in the transverse, divergent and leading wave components. The transverse and divergent equations are similar to the theoretical curve in Wyatt and Hall (1988). Finally, we consider an accelerating ship when explaining a discrepancy between the equation for the transverse wave component and the transverse wave component of the spectrogram of experimental data presented by Torsvik et al. (2015b).

3 Jacobian-free Newton-Krylov methods with GPU acceleration for computing nonlinear ship wave patterns

This chapter was first published as

R. Pethiyagoda, S. W. McCue, T. J. Moroney, and J. M. Back (2014). Jacobian-free Newton-Krylov methods with GPU acceleration for computing nonlinear ship wave patterns. *Journal of Computational Physics* **269**, 297–313.

http://dx.doi.org/10.1016/j.jcp.2014.03.024

Abstract

The nonlinear problem of steady free-surface flow past a submerged source is considered as a case study for three-dimensional ship wave problems. Of particular interest is the distinctive wedge-shaped wave pattern that forms on the surface of the fluid. By reformulating the governing equations with a standard boundary integral method, we derive a system of nonlinear algebraic equations that enforce a singular integro-differential equation at each midpoint on a two-dimensional mesh. Our contribution is to solve the system of equations with a Jacobian-free Newton-Krylov method together with a banded preconditioner that is carefully constructed with entries taken from the Jacobian of the linearised problem. Further, we are able to utilise graphics processing unit acceleration to significantly increase the grid refinement and decrease the run-time of our solutions in comparison to schemes that are presently employed in the literature. Our approach provides opportunities to explore the nonlinear features of three-dimensional ship wave patterns, such as the shape of steep waves close to their limiting configuration, in a manner that has been possible in the two-dimensional analogue for some time.

3.1 Introduction

This study is concerned with steady three-dimensional free-surface profiles that are caused by a disturbance to a free stream. These profiles are characterised by the distinctive Kelvin ship wave patterns that are observed at the stern of a vessel or even behind a duck swimming in an otherwise still body of water. While free-surface flows of this type have ongoing practical applications to ship hull design, as we mention below, the structure of these patterns has sparked renewed interest in the physics literature, with observations that ships moving sufficiently fast may give rise to wake angles that decrease with ship speed (Darmon, Benzaquen, and Raphaël 2014; Ellingsen 2014; Rabaud and Moisy 2013), in apparent contradiction to the well-known Kelvin angle of $\arcsin(1/3) \approx 19.47^\circ$ (Lighthill 1978), which is derived from linear theory. In contrast to these approaches, our purpose here is to treat the fully *nonlinear* equations, and present algorithms for the accurate computation of nonlinear ship wave profiles.

The mathematical analysis of ship wave patterns has a very long history, the overwhelming majority of which concerns linear theories. For example, for the classic problem of flow past a pressure distribution applied to the surface of the fluid $z = \zeta(x, y)$, if the pressure is small enough then the kinematic and Bernoulli boundary conditions on $z = \zeta(x, y)$ can be linearised onto the undisturbed plane $z = 0$ (Havelock 1919; Noblesse, Delhommeau, and Yang 2009; Scullen and Tuck 2011). This framework is used to model the wave pattern caused by an air-cushioned vehicle such as a hovercraft or a high-speed "flat ship" with a small draft. Another approach is to consider the ship wave pattern due to a thin ship. In this case the no-flux conditions on the ship hull are linearised onto the centreplane $y = 0$, while the thinness of the ship is assumed to produce small-amplitude waves, so the free surface conditions are again linearised onto the plane $z = 0$ (Michell 1898; Noblesse et al. 2009; Tuck, Scullen, and Lazauskas 2001). This set-up has obvious applications to ship hull design, especially for vessels with narrow hulls. Another geometry of interest involves flow past a submerged object, such as a spheroid, or, in a fluid of finite-depth, a bottom topography. If the magnitude of the disturbance is again small, then the usual linearisation of the surface conditions applies (Havelock 1931). Furthermore, one can apply the thin ship approximation to submerged bodies as well (Tuck and Scullen 2002). Flows past submerged bodies have applications to submarine design and detection (Reed and Milgram 2002), for example.

In all of the linear formulations cited above, the linear problem of Laplace's equation in a known domain can be solved in principle with Fourier transforms (Lighthill 1978). The velocity potential $\phi(x, y, z)$ and free surface $z = \zeta(x, y)$ are then given as quadruple integrals that involve the Havelock potential (the Green's function or fundamental solution). In practice, the challenge of evaluating the resulting singular

integrals with rapidly oscillating integrands has lead to analytical approximations such as the method of stationary phase (Crapper 1964; Tuck, Collins, and Wells 1971; Ursell 1960), although accurate numerical computations have been conducted more recently (Noblesse et al. 2009; Noblesse, Delhommeau, and Yang 2009; Scullen and Tuck 2011). Of particular interest here, we note that the Havelock potential is the velocity potential for the linearised flow past a single submerged point source singularity (Havelock 1932b; Lustri and Chapman 2013; Noblesse 1978; Noblesse 1981; Peters 1949). Thus we see that the problem of computing the wave pattern caused by turning on a submerged source in a uniform stream acts as a building block for all the other flows mentioned (as an example, the thin-ship theory effectively states that the flow past a thin ship hull is equivalent to the flow past a distribution of point sources on the centreplane $y = 0$ whose strength is proportional to the hull slope $\partial y/\partial x$ (Tuck, Scullen, and Lazauskas 2001)).

Our focus in this study is to compute nonlinear flows, for which the full nonlinear boundary conditions on the actual displaced free surface $z = \zeta(x, y)$ apply. Nonlinear versions of the above problems have been considered by a number of authors (see Higgins, Read, and Belward 2012; Părău and Vanden-Broeck 2002; Tuck and Scullen 2002, for example). In particular, following the framework of Forbes (1989), the approach we are most interested in is to apply a boundary integral technique that relies on Green's second formula. The result is a singular integro-differential equation which holds on the unknown free surface $z = \zeta(x, y)$. That is, the free-surface problem in three dimensions is reduced to a two-dimensional problem for the free surface $z = \zeta(x, y)$ and the velocity potential $\phi(x, y, \zeta(x, y))$. To proceed numerically, the rough approach is to place a mesh of $N \times M$ grid points over the truncated (x, y)-plane, so that the integro-differential equation and Bernoulli's equation can both be applied at each of the $(N-1)M$ half-mesh points. A radiation-type condition for the four unknown functions is applied at each of the M grid points upstream. Newton's method is then used to solve the resulting nonlinear system of $2(N + 1)M$ equations for the $2(N + 1)M$ unknowns (which are slopes $\partial\zeta/\partial x$, $\partial\phi/\partial x$ and the values of ζ, ϕ on the upstream grid points). As discussed by Forbes (1989), moderate efficiencies can be gained by exploiting the symmetry of the problem and using an inexact Newton's method which re-uses the Jacobian a number of times if possible.

In more recent times, over a series of papers, Părău, Vanden-Broeck and Cooker have applied Forbes' formulation to solve fully three-dimensional nonlinear ship wave problems and have typically used meshes of between 60×20 and 80×40 grid points (Părău and Vanden-Broeck 2002, 2011; Părău, Vanden-Broeck, and Cooker 2007abc, 2010). The same authors applied the same formulation to study three-dimensional solitary waves with typical meshes of 50×40 grid points (Părău, Vanden-Broeck, and Cooker

2005ab; Părău and Vanden-Broeck 2011), while Forbes and Hocking (2005) used a mesh of 101×101 points when applying the method to a three-dimensional withdrawal problem. To put the method into context, other approaches for three-dimensional ship wave problems use a similar grid size; for example, Tuck and Scullen (2002) apply a mesh of 91×25 grid points with their Rankine source method, while similar resolution is provided for a Rankine source method in (Janson, Leer-Andersen, and Larsson 2003).

The level of grid refinement demonstrated for the three-dimensional problems just mentioned is to be contrasted with the vast literature on two-dimensional flows. For example, by applying a boundary integral method in two dimensions combined with a straight-forward Newton approach, authors can easily use in excess of 1000 grid points over the two-dimensional surface (McCue and Forbes 2002; Ogilat et al. 2011; Wade et al. 2014) or, in more recent times, even 2000 points (Lustri, McCue, and Binder 2012; Trinh and Chapman 2014; Trinh, Chapman, and Vanden-Broeck 2011). Although most authors end up using fewer than 1000 points for their two-dimensional calculations, generally an accepted procedure is to continue to refine the mesh until the results are grid-independent, at least visually. Turning our attention back to three-dimensional flows, with less than 100 points used along the x-direction, the resolution over each wavelength is simply not of a sufficient standard for any claims about grid-independence to be made. Indeed, this is one of the key reasons why there has been little to no detailed study of the effect of high nonlinearity for three-dimensional ship wave problems.

In the present paper, we use a variation of the numerical scheme developed by Forbes (1989) for the problem of flow past a submerged source singularity, and apply Jacobian-free Newton-Krylov methods and exploit graphics processing unit (GPU) acceleration to drastically increase the grid refinement and decrease the run-time when compared with schemes published in the literature. We choose this particular geometric configuration since, as mentioned above, it can be thought of as the most fundamental flow type within the class that produces three-dimensional ship wave patterns. Further, this is precisely the geometry that Forbes (1989) used when presenting the boundary integral technique described above. Thus we have a direct correspondence and a bigger picture view of how far the community has progressed since that time. Finally, all of our ideas should generalise for other configurations (such as flows past pressure distributions), provided there is a linear problem that arises in the small disturbance regime.

In the following section we formulate the problem of interest and provide a summary of the boundary integral technique developed by Forbes (1989) and Părău and Vanden-Broeck (2002). The numerical scheme is described in Section 3.3, which leads to a

nonlinear system of equations

$$\mathbf{F}(\mathbf{u}) = \mathbf{0}, \tag{3.1}$$

where $\mathbf{u}$ is the vector of unknowns of length $2(N+1)M$. The damped Newton's method approach leads to the iteration

$$\mathbf{u}_{k+1} = \mathbf{u}_k + \lambda_k \delta \mathbf{u}_k, \tag{3.2}$$

where $\mathbf{u}_k$ is the kth iterate in the sequence $\{\mathbf{u}_k\}_{k=0}^{\infty} \to \mathbf{u}$ and the damping parameter $\lambda_k \in (0, 1]$ is chosen such that $||\mathbf{F}(\mathbf{u}_{k+1})|| < ||\mathbf{F}(\mathbf{u}_k)||$ at every iterate. The Newton step $\delta \mathbf{u}_k$ satisfies

$$\mathbf{J}(\mathbf{u}_k)\delta \mathbf{u}_k = -\mathbf{F}(\mathbf{u}_k), \tag{3.3}$$

where $\mathbf{J} = \partial \mathbf{F}/\partial \mathbf{u}$ is the Jacobian matrix. The integral nature of our governing equations results in all of the entries in $\mathbf{u}$ contributing to the evaluation of each component of $\mathbf{F}$ that corresponds to enforcing the integral equation, which means that the lower-half of the Jacobian $\mathbf{J}$ is fully dense. This density has been a significant factor in limiting the number of grid points used in previously published numerical simulations.

A key aspect of our approach is the use of a Jacobian-free Newton-Krylov method to solve the system (3.1). A Jacobian-free Newton-Krylov method requires the action of the Jacobian only in the form of Jacobian-vector products, which can be approximated using difference quotients without ever forming the Jacobian itself (Knoll and Keyes 2004). In practice, the underlying Krylov subspace iterative solver requires preconditioning in order to achieve a satisfactory rate of convergence, meaning the overall method is not typically fully matrix-free; however, for preconditioning purposes, an approximation of the Jacobian is all that is required, and this is where significant savings can be made.

While Jacobian-free Newton-Krylov methods are most commonly associated with problems for which the Jacobian matrices are sparse, they have been used successfully in a number of applications that give rise to dense Jacobian matrices (Chacón et al. 2000; Khatiwala 2008; Moroney and Yang 2013). In each of these applications, a sparse approximation of the Jacobian was used in constructing the preconditioner. We take the same approach in this work. The type of approximation we find to be the most effective involves a banded structure, with its nonzero entries coming from the linearised problem for a Havelock source mentioned above. We emphasise that this approximation is used only for preconditioning purposes; the action of the dense Jacobian is still felt throughout the Newton solver, which distinguishes our approach from the inexact method of Forbes (1989) and others.

In Section 3.5 we present our results. We choose to present most of our results for a particular set of parameter values, which includes the same Froude number as used

by Forbes (1989), and a moderately large value of the dimensionless strength of the submerged source. While Forbes showed results computed with a mesh of 45×13 grid points in 1989, we are able to easily use a 361×121 mesh on a modern desktop PC, computed in under 75 minutes. By utilising graphics processing unit (GPU) acceleration on a more powerful workstation, the same solution was computed in roughly 3.5 minutes. Furthermore, with this technology we are able to significantly improve upon the resolution, and generate results for a 721×241 mesh (in under 2 hours). This sort of resolution is important for three-dimensional ship wave problems, as it provides opportunities to explore the effect that nonlinearity has on the flow field in the same way as has been done in numerous instances for two-dimensional flows. Finally, we close the paper in Section 3.6 with our discussion, including directions as to where our work can be applied.

3.2 Mathematical formulation

3.2.1 Governing equations

We consider the irrotational flow of an inviscid, incompressible fluid of infinite depth, bounded above by a free surface, upon which gravity is acting. The effects of surface tension are ignored. Suppose that initially there is a free stream of fluid travelling with uniform speed U in the positive x-direction, and that a source singularity of strength m is introduced at a distance L below the surface. The disturbance caused by the source will lead to transient waves being generated on the free-surface. We are interested in the steady-state problem that arises in the long-time limit of this flow.

The problem is nondimensionalised by scaling all lengths with respect to L and all speeds with respect to U. By labelling the free-surface $z = \zeta(x, y)$, the dimensionless problem is to solve Laplace's equation for the velocity potential $\Phi(x, y, z)$:

$$\nabla^2\Phi = \frac{\partial^2\Phi}{\partial x^2} + \frac{\partial^2\Phi}{\partial y^2} + \frac{\partial^2\Phi}{\partial z^2} = 0 \quad \text{for} \quad z < \zeta(x, y), \tag{3.4}$$

except at the source singularity itself, whose dimensionless location is at $(x, y, z) = (0, 0, -1)$. The appropriate limiting behaviour is

$$\Phi \sim -\frac{\epsilon}{4\pi\sqrt{x^2 + y^2 + (z+1)^2}} \quad \text{as} \quad (x, y, z) \to (0, 0, -1), \tag{3.5}$$

where

$$\epsilon = \frac{m}{UL^2} \tag{3.6}$$

is the dimensionless source strength. On the free surface there are the kinematic and dynamic boundary conditions

$$\Phi_x\zeta_x + \Phi_y\zeta_y = \Phi_z \quad \text{on} \quad z = \zeta(x, y), \tag{3.7}$$

$$\frac{1}{2}(\Phi_x^2+\Phi_y^2+\Phi_z^2)+\frac{\zeta}{F_L^2}=\frac{1}{2} \quad \text{on} \quad z=\zeta(x,y), \tag{3.8}$$

being satisfied, where the second of two dimensionless parameters in the problem is the Froude number

$$F_L=\frac{U}{\sqrt{gL}}. \tag{3.9}$$

Finally, the flow will approach the free stream both far upstream (the radiation condition) and infinitely far below the free surface, providing the final two conditions

$$(\Phi_x,\Phi_y,\Phi_z)\to(1,0,0), \quad \zeta\to 0 \quad \text{as} \quad x\to-\infty, \tag{3.10}$$

$$(\Phi_x,\Phi_y,\Phi_z)\to(1,0,0), \quad \text{as} \quad z\to-\infty. \tag{3.11}$$

The governing equation (3.4) subject to (3.5)–(3.11) make up a nonlinear free-surface problem with no known analytical solution.

3.2.2 Boundary integral method

In order to solve (3.4)–(3.11) numerically, we first reformulate the problem in terms of an integral equation using Green's second formula. The full derivation is provided in Forbes (1989), while very similar approaches are outlined in a variety of other papers (Forbes and Hocking 2005; Părău and Vanden-Broeck 2002, 2011; Părău, Vanden-Broeck, and Cooker 2005ab, 2007abc, 2010). By setting $\phi(x,y)=\Phi(x,y,\zeta(x,y))$, the final boundary integral equation is

$$\begin{aligned}2\pi(\phi(x^*,y^*)-x^*)=&-\frac{\epsilon}{\left(x^{*2}+y^{*2}+(\zeta(x^*,y^*)+1)^2\right)^{\frac{1}{2}}}\\&+\int_0^\infty\int_{-\infty}^\infty(\phi(x,y)-\phi(x^*,y^*)-x+x^*)K_1(x,y;x^*,y^*)\,\mathrm{d}x\,\mathrm{d}y\\&+\int_0^\infty\int_{-\infty}^\infty\zeta_x(x,y)K_2(x,y;x^*,y^*)\,\mathrm{d}x\,\mathrm{d}y,\end{aligned} \tag{3.12}$$

which holds for any point (x^*,y^*) in the (x,y)-plane. Here K_1 and K_2 are the kernel functions

$$\begin{aligned}K_1(x,y;x^*,y^*)=&\frac{\zeta(x,y)-\zeta(x^*,y^*)-(x-x^*)\zeta_x-(y-y^*)\zeta_y}{\left((x-x^*)^2+(y-y^*)^2+\left(\zeta(x,y)-\zeta(x^*,y^*)\right)^2\right)^{\frac{3}{2}}}\\&+\frac{\zeta(x,y)-\zeta(x^*,y^*)-(x-x^*)\zeta_x-(y+y^*)\zeta_y}{\left((x-x^*)^2+(y-y^*)^2+\left(\zeta(x,y)-\zeta(x^*,y^*)\right)^2\right)^{\frac{3}{2}}},\\K_2(x,y;x^*,y^*)=&\frac{1}{\sqrt{(x-x^*)^2+(y-y^*)^2+\left(\zeta(x,y)-\zeta(x^*,y^*)\right)^2}}\end{aligned}$$

$$+\frac{1}{\sqrt{(x-x^*)^2+(y+y^*)^2+\big(\zeta(x,y)-\zeta(x^*,y^*)\big)^2}}.$$

The integral equation (3.12) identically satisfies Laplace's equation (3.4) and the kinematic condition (3.7), as well as the limiting condition (3.5) and the far-field conditions (3.10)–(3.11). Thus we are left to solve (3.12) and the dynamic condition (3.8). It proves convenient to rewrite (3.8) with the help of (3.7) to be

$$\frac{1}{2}\frac{(1+\zeta_x^2)\phi_y^2+(1+\zeta_y^2)\phi_x^2-2\zeta_x\zeta_y\phi_x\phi_y}{1+\zeta_x^2+\zeta_y^2}+\frac{\zeta}{F_L^2}=\frac{1}{2},\quad \text{on}\quad z=\zeta(x,y). \tag{3.13}$$

3.2.3 Linearised problem

While our focus is on generating numerical solutions to (3.4)–(3.11), it will prove instructive to note the linearised problem which arises in the weak source strength limit $\epsilon \ll 1$. The problem is formulated by writing $\Phi = x + \epsilon\Phi_1(x,y,z) + \mathcal{O}(\epsilon^2)$, $\zeta = \epsilon\zeta_1(x,y) + \mathcal{O}(\epsilon^2)$, and considering the formal limit $\epsilon \to 0$. As a result, the linear problem becomes

$$\nabla^2\Phi = \frac{\partial^2\Phi}{\partial x^2}+\frac{\partial^2\Phi}{\partial y^2}+\frac{\partial^2\Phi}{\partial z^2}=0\quad \text{for}\quad z<0, \tag{3.14}$$

subject to the linearised kinematic and dynamic conditions

$$\zeta_x = \Phi_z\quad \text{on}\quad z=0, \tag{3.15}$$

$$\Phi_x - 1 + \frac{\zeta}{F_L^2} = 0\quad \text{on}\quad z=0. \tag{3.16}$$

The near-source behaviour (3.5) and the far-field conditions (3.10)–(3.11) remain the same.

As discussed in the Introduction, the solution to this linear problem can be found using Fourier transforms (Noblesse 1981); however, for our purposes we shall pursue the equivalent boundary integral approach as that used for the nonlinear problem. This time if we set $\phi(x,y) = \Phi(x,y,0)$, the application of Green's second formula gives

$$2\pi(\phi(x^*,y^*)-x^*) = -\frac{\epsilon}{\big(x^{*2}+y^{*2}+1\big)^{\frac{1}{2}}}+\int_0^\infty\int_{-\infty}^\infty \zeta_x(x,y)K_3(x,y;x^*,y^*)\,\mathrm{d}x\,\mathrm{d}y, \tag{3.17}$$

where

$$K_3(x,y;x^*,y^*) = \frac{1}{\sqrt{(x-x^*)^2+(y-y^*)^2}}+\frac{1}{\sqrt{(x-x^*)^2+(y+y^*)^2}}.$$

Again, the integral equation (3.17) identically satisfies Laplace's equation (3.14), the kinematic condition (3.15), the far-field conditions (3.10)–(3.11) and the near-source condition (3.5).

3.3 Numerical discretisation

For the discretisation of the nonlinear boundary integral equation (3.12), we use a slight variant of the method outlined in Părău and Vanden-Broeck (2002), which is based on the original approach of Forbes (1989). This involves laying a regular mesh of nodes $(x_1, y_1), \ldots, (x_N, y_M)$ on the free surface with spacings of Δx and Δy in the x and y directions, respectively. For a given N and M, we shall refer to the mesh as being an $N \times M$ mesh. The free-surface position $\zeta(x, y)$ and the velocity potential $\phi(x, y)$ are represented by discrete values $\zeta_{k,\ell}$ and $\phi_{k,\ell}$ at the points (x_k, y_ℓ), $k = 1, \ldots, N$, $\ell = 1, \ldots, M$.

We define the vector of $2(N+1)M$ unknowns $\mathbf{u}$ to be

$$\begin{aligned}\mathbf{u} =&[\phi_{1,1}, (\phi_x)_{1,1}, \ldots, (\phi_x)_{N,1}, \phi_{1,2}, (\phi_x)_{1,2}, \ldots, (\phi_x)_{N,2}, \ldots, \phi_{1,M}, (\phi_x)_{1,M}, \ldots, (\phi_x)_{N,M},\\ &\zeta_{1,1}, (\zeta_x)_{1,1}, \ldots, (\zeta_x)_{N,1}, \zeta_{1,2}, (\zeta_x)_{1,2}, \ldots, (\zeta_x)_{N,2}, \ldots, \zeta_{1,M}, (\zeta_x)_{1,M}, \ldots, (\zeta_x)_{N,M}]^T,\end{aligned} \tag{3.18}$$

comprising the x-derivatives of the functions ϕ and ζ at the free-surface mesh points, together with the values of ϕ and ζ at the upstream boundary of the truncated domain. The values of these unknowns are related via $2(N+1)M$ nonlinear equations, of the form (3.1), which we now derive.

Given the elements of the vector of unknowns (3.18), the remaining values of ζ are obtained by trapezoidal-rule integration using the values of ζ_x:

$$\begin{gathered}\zeta_{k+1,\ell} = \zeta_{k,\ell} + \frac{1}{2}\Delta x\big((\zeta_x)_{k,\ell} + (\zeta_x)_{k+1,\ell}\big),\\ \ell = 1, \ldots, M, \quad k = 1, \ldots, N-1.\end{gathered} \tag{3.19}$$

The values of ζ_y are then computed by fitting a cubic spline through the points $\zeta_{k,1}, \ldots, \zeta_{k,M}$ for $k = 1, \ldots, N$. Values of ϕ and ϕ_y at each grid point are similarly computed using ϕ_x.

We must now enforce the integro-differential equation (3.12), which will be evaluated on the half-mesh points $(x_{k+\frac{1}{2}}, y_\ell)$, $k = 1, \ldots, N-1$, $\ell = 1, \ldots, M$ using two-point interpolation. The domain is truncated to the rectangle $x_1 \le x \le x_N$, $y_1 \le y \le y_M$. The singularity in the second integral of (3.12) is removed by the addition and subtraction of the term

$$\zeta_x(x^*, y^*) \int_{y_1}^{y_M} \int_{x_1}^{x_N} S_2(x, y; x^*, y^*)\, \mathrm{d}x\, \mathrm{d}y, \tag{3.20}$$

where

$$S_2(x, y; x^*, y^*) = \frac{1}{\sqrt{A(x-x^*)^2 + B(x-x^*)(y-y^*) + C(y-y^*)^2}} \tag{3.21}$$

$$+\frac{1}{\sqrt{A(x-x^*)^2-B(x-x^*)(y+y^*)+C(y+y^*)^2}}, \tag{3.22}$$

with

$$A=1+\zeta_x^2(x^*,y^*),\quad B=2\zeta_x(x^*,y^*)\zeta_y(x^*,y^*),\quad C=1+\zeta_y^2(x^*,y^*).$$

The second integral of the equation (3.12) becomes

$$\int_{y_1}^{y_M}\int_{x_1}^{x_N}\zeta_x(x,y)K_2(x,y;x^*,y^*)-\zeta_x(x^*,y^*)S_2(x,y;x^*,y^*)\,\mathrm{d}x\,\mathrm{d}y+\zeta_x(x^*,y^*)I,$$

where

$$I=\int_{y_1}^{y_M}\int_{x_1}^{x_N}S_2\,\mathrm{d}x\,\mathrm{d}y. \tag{3.23}$$

The integral I now contains the singularity; it can be evaluated exactly in terms of logarithms (Forbes 1989; Părău and Vanden-Broeck 2002).

The integrals in the approximation to equation (3.12) are discretised using the trapezoidal rule and then evaluated for all half-mesh points $(x_{k+\frac{1}{2}},y_\ell)$, $k=1,\ldots,N-1$, $\ell=1,\ldots,M$. This results in $(N-1)M$ nonlinear algebraic equations for the unknowns in the vector $\mathbf{u}$. An additional $(N-1)M$ equations are given by evaluating the free surface condition (3.13) at the half mesh points. The final $4M$ equations are provided to enforce the far-field condition (3.10) on the relevant boundary of the truncated domain by applying the upstream radiation condition using the approach outlined by Scullen (1998). The idea here is to enforce an equation of the form $xf_x+nf=0$ along the boundary $x=x_1$ for the four functions ζ, ζ_x, $\phi-x$ and ϕ_x-1. The value of $n>0$ represents how fast the functions decay to zero upstream, and in our calculation was taken to be $n=0.05$ (larger values of n were found to amplify the small spurious upstream waves mentioned below). This method for applying the radiation condition gives us the $4M$ equations

$$\begin{aligned}
x_1((\phi_x)_{1,\ell}-1)+n(\phi_{1,\ell}-x_1)&=0,\\
x_1(\phi_{xx})_{1,\ell}+n((\phi_x)_{1,\ell}-1)&=0,\\
x_1(\zeta_x)_{1,\ell}+n\zeta_{1,\ell}&=0,\\
x_1(\zeta_{xx})_{1,\ell}+n(\zeta_x)_{1,\ell}&=0,
\end{aligned} \tag{3.24}$$

for $\ell=1,\ldots,M$, where second derivatives are computed by a forward difference approximation on the first derivative. We now have $2(N+1)M$ equations for our vector of unknowns (3.18). In order to optimise our scheme we have ordered these equations very carefully. This ordering is explained in 3.7.1.

This numerical scheme has two main sources of error. The first is truncation error introduced when approximating the infinite domain of integration with a finite domain. This truncation has the potential to lead to errors if the chosen upstream truncation point (x_1) is too close to the source, as the upstream radiation condition (3.24) may no longer be accurately enforced. Indeed, truncating the domain upstream appears to generate very small nonphysical waves on the surface, as discussed later. Truncating the domain downstream (at x_N) may also introduce significant errors as the amplitude of the wavetrain decays slowly with space, and contribution to the integrals from the truncated waves is nonzero. The second main source of error is from the discretisation of the integrals. Both the mesh spacing and the chosen integration weighting scheme will have an effect on the accuracy of the final result.

3.4 Jacobian-free Newton-Krylov method

3.4.1 Overview

The system (3.1) is solved with a Jacobian-free Newton-Krylov method. At the outer, nonlinear level, this is simply the damped Newton iteration (3.2), with λ_k chosen via a simple linesearch to ensure a sufficient decrease in the nonlinear residual is obtained with each iteration. At the inner, linear level, the system (3.3) is solved using the iterative Generalised Minimum Residual algorithm (Saad and Schultz 1986) with right preconditioning. After m iterations of this algorithm, the approximate solution for the Newton correction $\delta\mathbf{u}_k$ is found by projecting obliquely onto the preconditioned Krylov subspace

$$\mathcal{K}_m(\mathbf{J}_k\mathbf{P}^{-1}, \mathbf{F}_k) = \text{span}\{\mathbf{F}_k, \mathbf{J}_k\mathbf{P}^{-1}\mathbf{F}_k, \ldots, (\mathbf{J}_k\mathbf{P}^{-1})^{m-1}\mathbf{F}_k\},$$

where we are now using the notation $\mathbf{J}_k = \mathbf{J}(\mathbf{u}_k)$, $\mathbf{F}_k = \mathbf{F}(\mathbf{u}_k)$. The matrix $\mathbf{P} \approx \mathbf{J}_k$ is the preconditioner matrix – a sparse approximation to $\mathbf{J}_k$ which is discussed in more detail in the next subsection. Its function is to reduce the dimension m of the Krylov subspace required to obtain a sufficiently accurate solution for $\delta\mathbf{u}_k$.

Krylov subspace methods are very attractive as linear solvers in the context of nonlinear Newton iteration, because they do not require explicit formation of the Jacobian matrix. Indeed, only the action of the Jacobian matrix in the form of Jacobian-vector products is required to assemble a basis for the preconditioned Krylov subspace $\mathcal{K}_m$. These Jacobian-vector products can be approximated without needing to form $\mathbf{J}_k$ by using first order difference quotients:

$$\mathbf{J}_k\mathbf{P}^{-1}\mathbf{v} \approx \frac{\mathbf{F}(\mathbf{u}_k + h\,\mathbf{P}^{-1}\mathbf{v}) - \mathbf{F}(\mathbf{u}_k)}{h}, \tag{3.25}$$

where $\mathbf{v}$ represents an arbitrary vector used in building the Krylov subspace, and h is a suitably-chosen shift (Brown and Saad 1990).

Since the Newton correction is solved for only approximately, and the action of the Jacobian in computing this solution is itself only approximated, we are left with an inexact Newton method, which exhibits superlinear, rather than quadratic, convergence (Knoll and Keyes 2004). The reduction in the convergence rate is of little practical consequence, given the enormous performance gains realised by removing the burden of forming the (dense) Jacobian matrix. Furthermore, only solving for the Newton correction approximately can actually improve performance in the early stages of the nonlinear iteration, by not wasting operations computing an extremely accurate value of the Newton correction which, even if it were computed exactly, would only reduce the nonlinear residual by so much (Knoll and Keyes 2004).

For most values of the parameters F_L and ϵ, it proves sufficient to use a flat surface as the initial guess $\mathbf{u}_0$ in the Newton iteration, which corresponds to:

$$\phi_{1,\ell} = x_0, \quad (\phi_x)_{k,\ell} = 1, \quad \zeta_{1,\ell} = 0, \quad (\zeta_x)_{k,\ell} = 0,$$

for $k = 1, \ldots, N$ and $\ell = 1, \ldots, M$. Another approach is to use the exact solution to the linear problem outlined in Section 3.2.3 (given in (Noblesse 1981), for example). However, for highly nonlinear solutions with large values of ϵ, a further alternative approach is to apply a bootstrapping process in which a solution is computed using $\mathbf{u}_0$ for a moderate value of ϵ, and then this solution is used as an initial guess for a slightly larger ϵ, and so on.

3.4.2 Preconditioning

In forming the preconditioner matrix $\mathbf{P}$, the goal is to construct an approximation to the Jacobian $\mathbf{J}_k$ that is cheap to form and to factorise, such that the spectrum of the preconditioned Jacobian $\mathbf{J}_k\mathbf{P}^{-1}$ exhibits a clustering of eigenvalues (Knoll and Keyes 2004). A common starting point in building such a preconditioner is to consider a matrix constructed from the same problem under simplified physics (Knoll and Keyes 2004). In the present context, this is achieved by applying our numerical scheme to the linearised governing equations which apply formally in the limit $\epsilon \to 0$. These equations make up the well-studied linear problem of computing the Havelock potential for flow past a submerged point source (Havelock 1932b; Lustri and Chapman 2013; Noblesse 1978; Noblesse 1981; Peters 1949), as discussed in the Introduction and Section 3.2.3. The numerical discretisation of the integrals in (3.17) allows for easy differentiation by hand, so that all elements of the linear Jacobian can be calculated exactly, requiring considerably less computational time. The details are included in 3.7.2.

In Figure 3.1, the Jacobian matrix for the full nonlinear problem ((a) "nonlinear Jacobian") for $\mathbf{u}_k = \mathbf{u}_0$ with parameters $\epsilon = 1$ and $F_L = 0.7$ is compared to its counterpart for the linear problem ((b) "linear Jacobian") by means of the magnitude of their

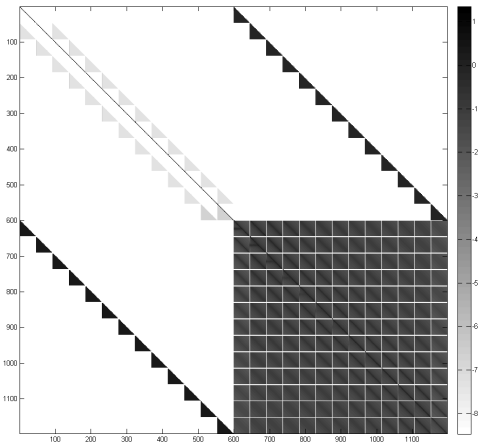

(a) Nonlinear Jacobian

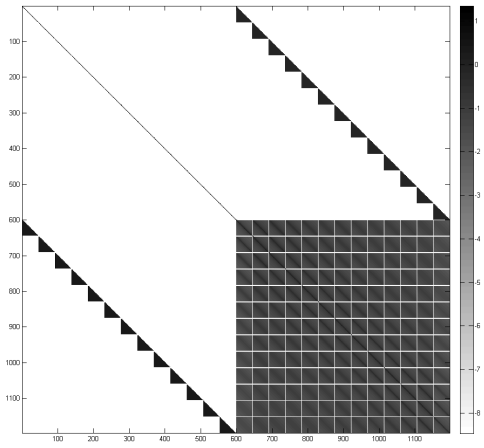

(b) Linear Jacobian

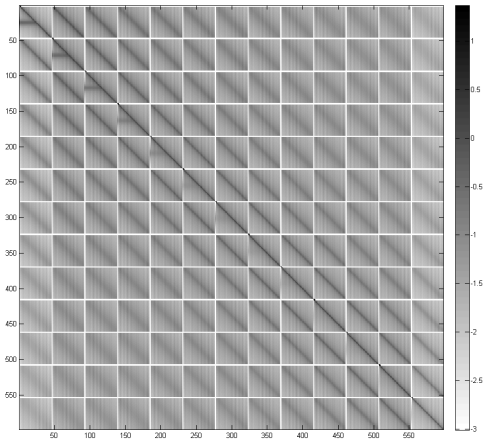

(c) Lower-right submatrix of the nonlinear Jacobian

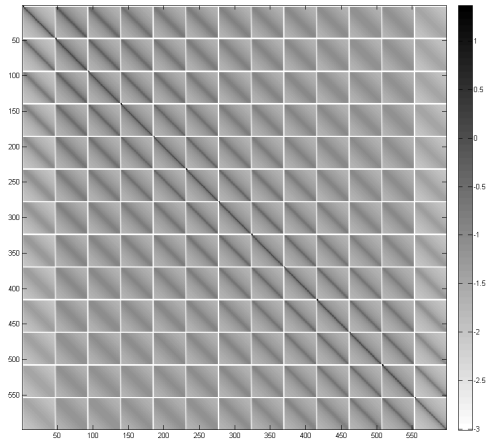

(d) Lower-right submatrix of the linear Jacobian

Figure 3.1: A visualisation of the magnitude of the (a) nonlinear and (b) linear Jacobian entries. A close-up of the lower-right submatrices are shown in (c) and (d) , respectively. Computed for $\mathbf{u}_k = \mathbf{u}_0$ (which corresponds to an initial guess of a flat surface) with parameters $\epsilon = 1$ and $F_L = 0.7$, on a log scale: $\log_{10}|J_{i,j}|$ for all i, j. Each element is assigned a shade based on its value: the larger the value, the darker the shade.

entries. The comparison confirms that, although there are slight differences in the magnitude of these entries (in particular, the grey triangular regions near the diagonal in the upper-left submatrix in Figure 3.1(a) do not appear in Figure 3.1(b)), the general structure of the two matrices is the same. The eigenvalue spectra of the nonlinear Jacobian before and after preconditioning with the linear Jacobian are exhibited in Figure 3.2. The figure reveals that the application of the preconditioner has resulted in a tight clustering of the eigenvalues around unity, confirming its effectiveness.

While the linear Jacobian is significantly cheaper to compute than its nonlinear counter-

part, its lower-right submatrix is nonetheless fully dense, which would ultimately limit the number of mesh nodes that could be used in the discretisation due to storage and factorisation considerations. Therefore, we focus attention on the lower-right submatrix of the two Jacobians (Figure 3.1 (c), (d)), which reveals that the magnitudes of the entries decay with distance from the main block diagonal. This observation suggests using a block-banded approximation to this portion of the matrix for our preconditioner, whereby we keep only the nonzero entries of the lower-right submatrix of the linear Jacobian within a stated block bandwidth b, with block sizes $(N+1)\times(N+1)$. By varying this bandwidth, the sparsity of the preconditioner can be controlled such that the storage and factorisation costs are manageable. The method of storing, factorising and applying the preconditioner is outlined in 3.7.3.

In Figure 3.3 we illustrate that even with block bandwidth $b = 1$ (that is, a block diagonal approximation), the linear Jacobian still functions effectively as a preconditioner, providing the required eigenvalue clustering. The tightness of this clustering can be further improved by increasing the bandwidth, as the results for $b = 3$ and $b = 5$ confirm.

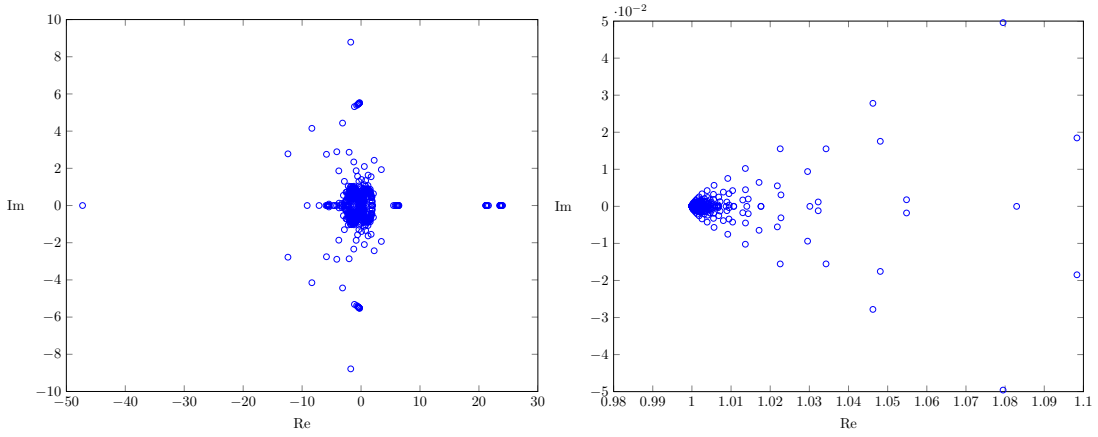

(a) $\sigma(\mathbf{J}_k)$ (b) $\sigma(\mathbf{J}_k\mathbf{P}^{-1})$

Figure 3.2: A plot of the spectrum for $\mathbf{J}_k$ and $\mathbf{J}_k\mathbf{P}^{-1}$ on a 45×13 mesh with $\Delta x = 0.4$, $\Delta y = 0.4$, $x_0 = -9$ with $\mathbf{u}_k = \mathbf{u}_0$ and non-dimensional parameters $\epsilon = 1$ and $F_L = 0.7$. Here, $\mathbf{P}$ is the full linear preconditioner (which is dense in the lower-right submatrix).

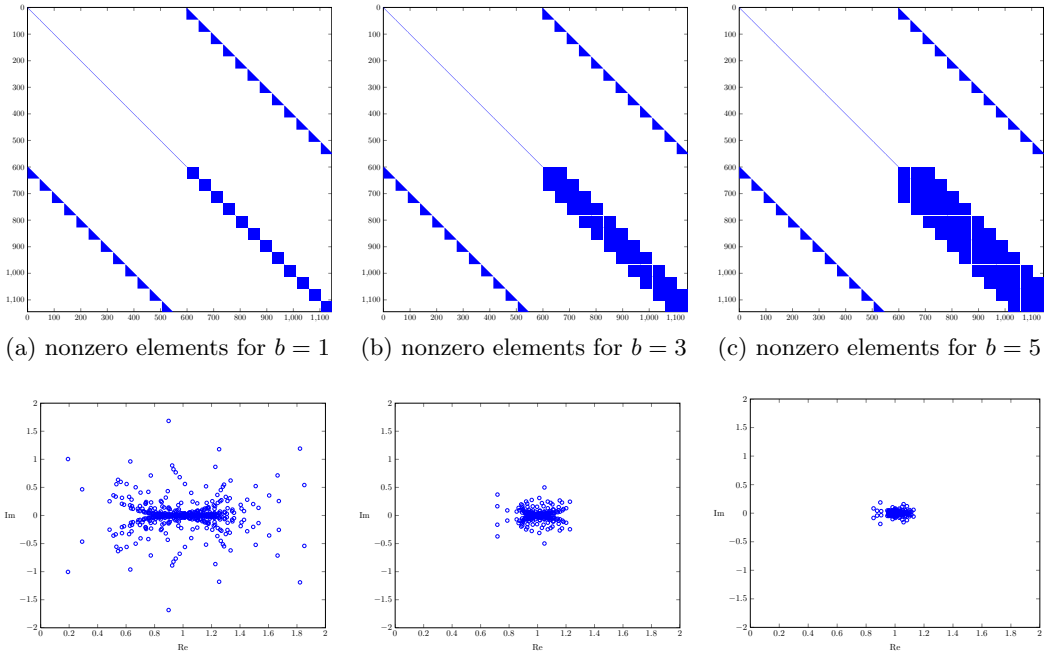

(a) nonzero elements for $b = 1$ (b) nonzero elements for $b = 3$ (c) nonzero elements for $b = 5$

(d) spectrum $\sigma(\mathbf{J}_k\mathbf{P}^{-1})$ for $b = 1$ (e) spectrum $\sigma(\mathbf{J}_k\mathbf{P}^{-1})$ for $b = 3$ (f) spectrum $\sigma(\mathbf{J}_k\mathbf{P}^{-1})$ for $b = 5$

Figure 3.3: Location of nonzero elements in the preconditioner $\mathbf{P}$ for bandwidths (a) $b = 1$, (b) $b = 3$, and (c) $b = 5$, all computed for a 45×13 mesh with $\Delta x = 0.4$, $\Delta y = 0.4$, $x_0 = -9$ and non-dimensional parameters $\epsilon = 1$ and $F_L = 0.7$. Associated plots of the spectrum of $\mathbf{J}_k\mathbf{P}^{-1}$ for $\mathbf{u}_k = \mathbf{u}_0$: (d) $b = 1$, (e) $b = 3$, (f) $b = 5$.

3.5 Results

We have computed solutions using both a standard desktop computer[1] with all code written in MATLAB, and using a more powerful workstation with GPU accelerator[2] using a mixture of MATLAB and CUDA (Compute Unified Device Architecture) code. In all cases the KINSOL (Hindmarsh et al. 2005) implementation of the Jacobian-Free Newton-Krylov method was used. In the following, recall that an $N \times M$ mesh involves N grid points in the x direction and M grid points in the y direction.

3.5.1 Desktop Computer

We present results obtained by solving our system of nonlinear equations on a typical desktop computer for a contemporary mesh (91×31, $\Delta x = \Delta y = 0.3$, $x_0 = -9$) as well as for a significantly finer mesh (361×121, $\Delta x = \Delta y = 0.15$, $x_0 = -14$). The

[1] Intel Core i7-2600 CPU with 3.40 GHz processor and 8 GB of system memory

[2] 2x Intel Xeon E5-2670 CPUs with 2.66 GHz processor, M2090 Nvidia Tesla GPU and 124 GB of system memory

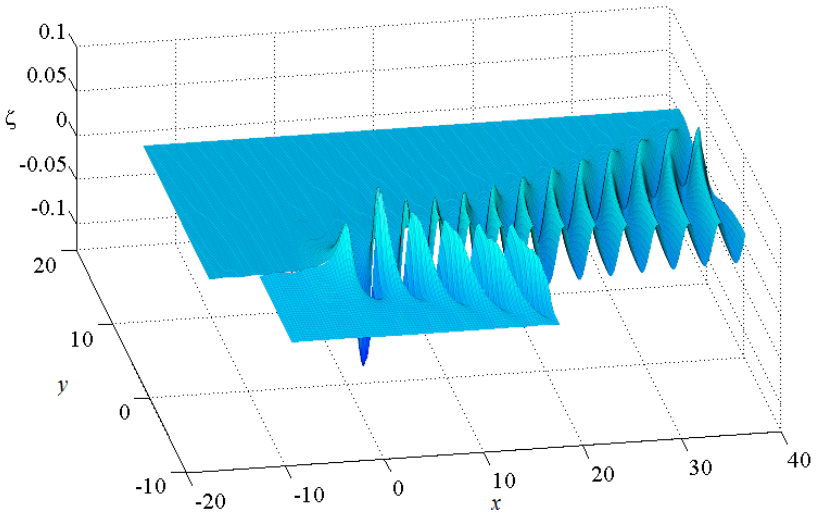

(a) Orthographic view

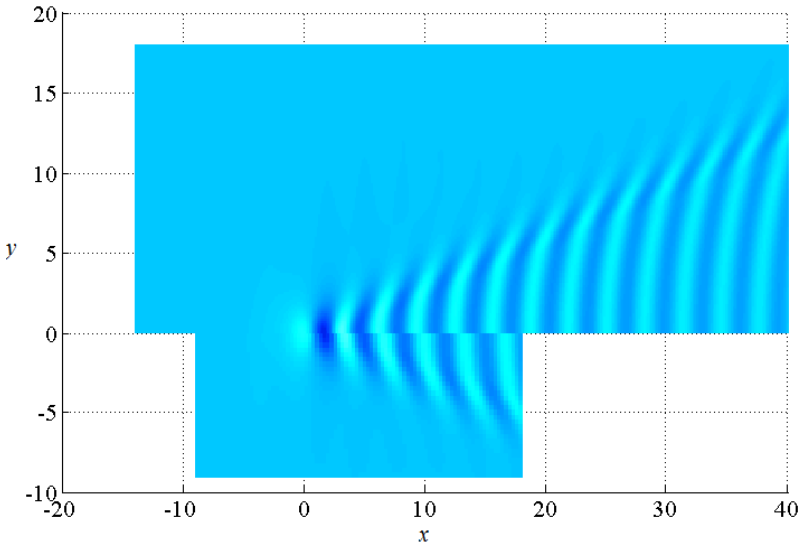

(b) Plan view

Figure 3.4: A comparison of free surface profiles for $F_L = 0.7$ and $\epsilon = 1$ computed on two different grids in (a) orthographic view and (b) plan view. The surface on the near side (bottom) corresponds to a 91×31 mesh with $\Delta x = 0.3$, $\Delta y = 0.3$, $x_0 = -9$, while the surface on the far side (top) is for a 361×121 mesh with $\Delta x = 0.15$, $\Delta y = 0.15$, $x_0 = -14$. Both solutions are computed on a desktop PC.

parameter values we focus on are $F_L = 0.7$ and $\epsilon = 1$, which are representative of a moderately small Froude number and a moderately nonlinear flow regime.

For the contemporary mesh, the resulting problem size is sufficiently small that the full preconditioner (without taking the banded approximation) can be formed and factorised without difficulty on today's desktop machines. Using the Jacobian-free

Newton-Krylov method with this dense preconditioner, the solution was obtained in under 26 seconds. Calculating numerical solutions like this one in such a small time is useful for exploring the effect of different parameter values on the free surface; however, as can be seen in Figure 3.4, the resulting surface is rather coarse, and does not reveal much detail of the wave pattern.

By using the block-banded preconditioner with our Jacobian-free Newton-Krylov method, we are able to compute the solution on the much finer mesh (361×121) in under 75 minutes on the desktop computer. A block bandwidth of $b = 31$ is used for the Jacobian, which means it essentially fills all of the available system memory. This level of mesh refinement represents a comfortable size of problem for the given machine, and produces a free surface profile that is significantly smoother than the one computed with a 91×31 mesh (again, see Figure 3.4). With a modest degree of further refinement, the problem may still be solved on the desktop computer, however the effectiveness of the preconditioner is reduced owing to the limited number of bands that can be accommodated in memory.

3.5.2 Workstation with GPU Accelerator

By coding the nonlinear discretisation in CUDA and executing each evaluation (hereafter a "function evaluation") on the GPU, we were able to significantly accelerate the computations as demonstrated in Table 3.1. Here we are experiencing an approximately 25 times speed up in function evaluation times over the multicore MATLAB code for the larger meshes. This leads to a reduced overall runtime, for example, calculating the solution on the same 361×121 mesh with GPU acceleration took only 3.5 minutes. This dramatic reduction in computational time coupled with the extra system memory available on the workstation allowed us to produce solutions on much finer meshes in a practical amount of time. Our most detailed solution using a 721×241 mesh with $\Delta x = \Delta y = 0.075$ and $x_0 = -14$, was computed in 1.5 hours. The corresponding free surface profile is illustrated in Figure 3.5.

Mesh	Multicore MATLAB on desktop	Multicore MATLAB on workstation	MATLAB with GPU on workstation
91×31	1.43	0.87	0.02
181×61	11.26	4.38	0.18
271×91	54.47	20.40	0.83
361×121	169.46	64.35	2.52
451×151	410.34	153.91	6.04

Table 3.1: A comparison of the function evaluation times using multicore MATLAB on the desktop PC and the workstation with and without GPU acceleration for different meshes with parameters $\epsilon = 1$ and $F_L = 0.7$. Time is in seconds.

3.5.3 Towards grid independence

As mentioned in the Introduction, a common procedure in the free-surface literature is to explore grid independence by computing solutions on a given truncated domain with more grid points (twice as many, say) and visually comparing the free surface profiles to test whether the grid refinement has not significantly altered the solution. Similarly, authors often keep the spatial increment the same and increase the size of the truncated domain (make it twice as long, say), again to test whether the solution changes. For steady two-dimensional flows, this exercise is reasonably straight forward (in principle), as the free surface profile is a curve. Examples of these tests for two-dimensional problems that involve a downstream wavetrain can be found in McCue and Forbes (1999), Mekias and Vanden-Broeck (1991), and Zhang and Zhu (1996), all of which were published at a time when demonstrating grid independence was still a difficult issue.

More recently, equivalent tests of grid independence have been attempted for three-dimensional flows past disturbances (Părău and Vanden-Broeck 2002, 2007ab). In this case, as the wave pattern is a two-dimensional surface, the domain was divided in half, with one part showing a solution computed with a particular grid, and the other part with a solution computed with a more refined or extended grid. Such a comparison is also given in Figure 3.4. What we can see from Figure 3.4 is that the solution computed on the 91×31 mesh is clearly not grid independent, as the more refined surface corresponding to a 361×121 mesh appears to be different, even on this larger scale. We have conducted the same comparison exercise for a variety of parameter sets and meshes for our problem, and conclude that the number of grid points used presently in the literature (for a range of very similar problems) is not nearly enough for authors to claim their solutions are grid independent. Similarly, noting that Părău and coauthors (Părău and Vanden-Broeck 2002; Părău, Vanden-Broeck, and Cooker 2007b) call these visual comparisons 'accuracy checks', we would not say that solutions

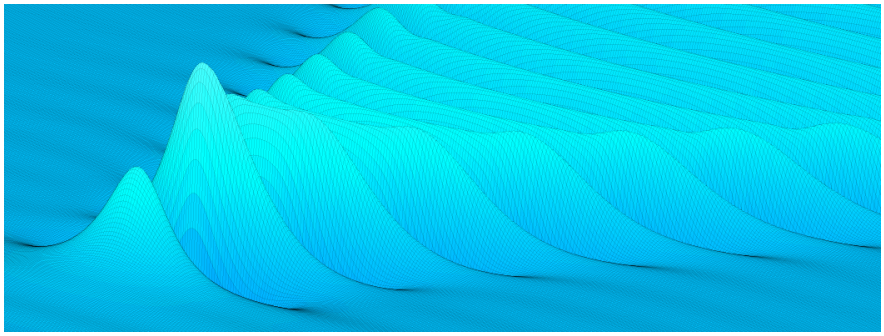

(a) A close up of the wave pattern.

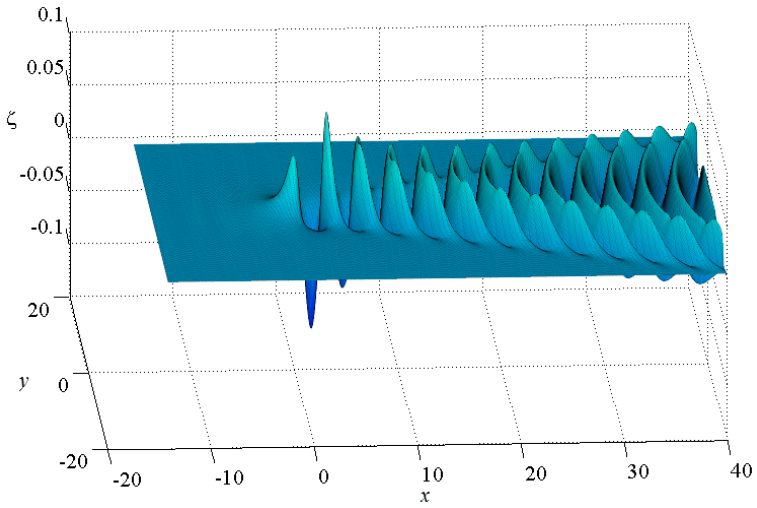

(b) The free surface profile over the full truncated domain.

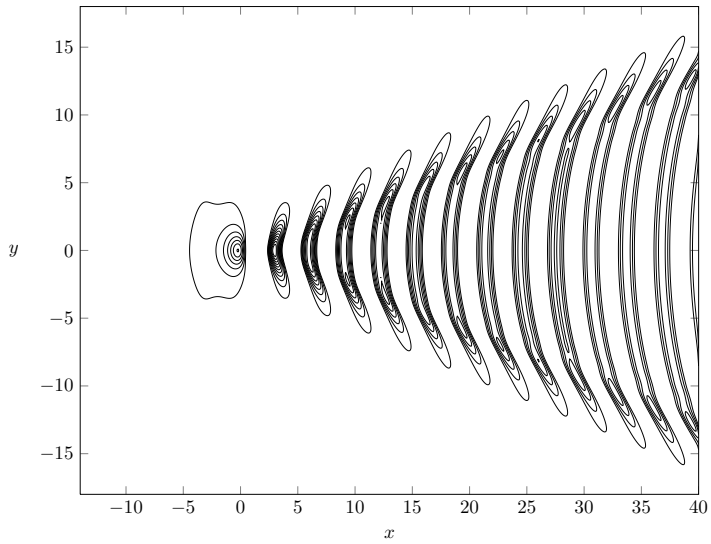

(c) A contour plot, where contours are shown only for positive wave heights to avoid confusion.

Figure 3.5: Perspectives of the free surface for $F_L = 0.7$ and $\epsilon = 1$, computed on a 721×241 mesh with $\Delta x = 0.075$, $\Delta y = 0.075$, $x_0 = -14$. This solution was computed on a workstation with GPU acceleration.

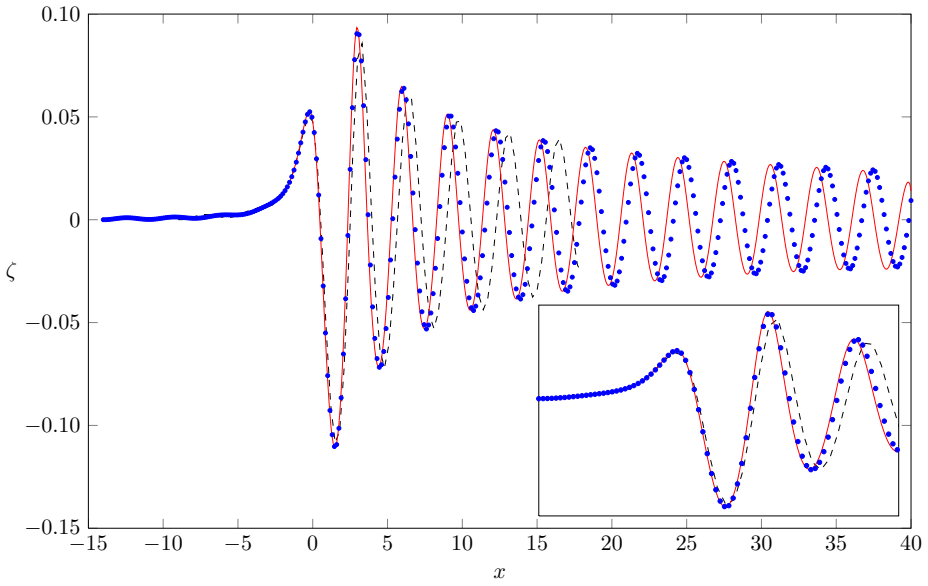

Figure 3.6: A comparison of the centreline profiles for $F_L = 0.7$ and $\epsilon = 1$ computed on three different grids. The dashed curve has 91 nodes in the x-direction with $\Delta x = 0.3$. The surface made up by solid circles has 361 nodes with $\Delta x = 0.15$. Note that each circle here represents an actual grid point (the illusion of uneven grid spacing is due to the vastly different scales in the x and z directions). The solid curve has 721 nodes with $\Delta x = 0.075$. The inset shows a close up of this comparison near $x = 0$.

computed with contemporary meshes are accurate. Of course it is understandable that these coarse meshes have been used in published studies, given the dense nature of the nonlinear Jacobian, the lack of a Jacobian-free approach such as we are using here, and computational power. We hope that the algorithms presented here will allow much more accurate computations in the future.

Another obvious approach for observing the degree of grid independence is to plot the centreline of the free surface ($z = \zeta(x, 0)$) for a number of difference meshes, as shown in Figure 3.6. In addition to the 91×31 and 361×121 meshes used in Figure 3.4, we have also included the centreline plot for the 721×241 mesh used in Figure 3.5. Recall that this latter mesh was implemented on a workstation with GPU acceleration. We see there is quite good agreement between the solutions for the 361×121 and 721×241 meshes, at least over the first four or five wavelengths. Further downstream the amplitudes of the waves appear to agree well, but the actual wavelength is slightly out. This comparison suggests that while we can not yet claim our solutions will not be affected by further grid refinement, we argue that meshes of the order of 361×121 and 721×241 are required for solutions to begin to appear independent of the mesh spacing and truncation.

It is worth making some comments about the truncation errors we discussed at the end of Section 3.3. First, we note that truncating the domain upstream at $x = x_1$ has the effect of introducing very small spurious (almost two-dimensional) waves throughout the domain. These may be seen in Figures 3.4 and 3.5, both ahead of the source and also outside of the Kelvin wedge. This numerical artefact has been an issue for two-dimensional flows for many years, and the associated spurious waves have been eliminated by employing a variety of upstream boundary conditions (Părău and Vanden-Broeck 2002; Zhang and Zhu 1996). A detailed discussion for two-dimensional flows is given by Grandison and Vanden-Broeck (2006). In our scheme, the enforcement of the radiation condition via (3.24) has the effect of dramatically reducing the size of these spurious waves (the coefficient n is chosen based on these observations). This issue deserves further attention.

Further, we note any truncation of the domain at $x = x_N$ will introduce errors in the system, as the contribution from the wavetrain to the integrals for $x > x_N$ will be ignored. Visually, we can see in Figure 3.6 that the final wavelength of the free surface seems affected by this truncation. Again, strategies have been developed to deal with these errors in much simpler two-dimensional problems (Grandison and Vanden-Broeck 2006), and similar work is needed for the types of three-dimensional flows considered here.

3.5.4 Details of wave patterns

The free-surface profiles presented in Figures 3.4-3.5 are computed for the moderately small value of the Froude number, $F_L = 0.7$. In this regime, the transverse waves, which run perpendicular to the flow direction, are prominent. These are the waves we observe in the centreline plot in Figure 3.6. The other type of waves are the divergent waves, whose crests appear to form ridges pointing diagonally away from the source. The amplitude of the transverse waves decays as x increases, leaving the divergent waves to dominate at larger distances away from the source. It is the divergent wave pattern that characterises the well-known V-shaped Kelvin wake.

A free-surface profile computed for $F_L = 1.4$ and $\epsilon = 1$ is presented in Figure 3.7. For this moderately large Froude number, we see that the divergent waves dominate closer to the source, making it more difficult to view the transverse waves. Note that the wavelength of the transverse waves increases with Froude number, which means we need to truncate further downstream for larger Froude numbers in order to capture the same amount of detail. The solution in this figure was computed using a mesh of 721×241 on a workstation with GPU acceleration. With this resolution, we can see fine details of the surface in part (a) of the Figure.

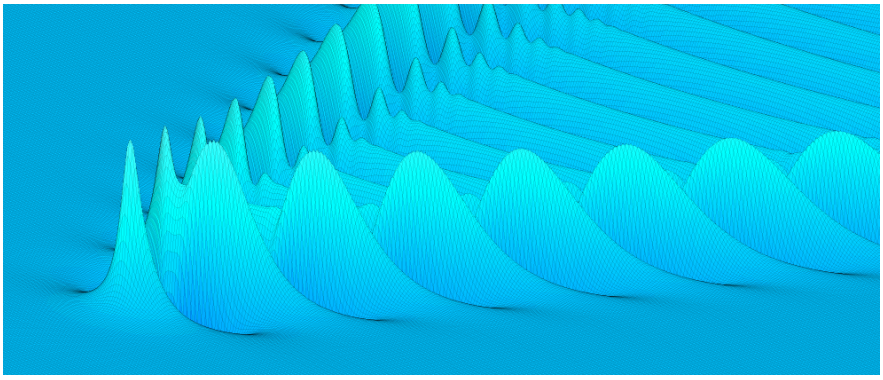

(a) A close up of the wave pattern.

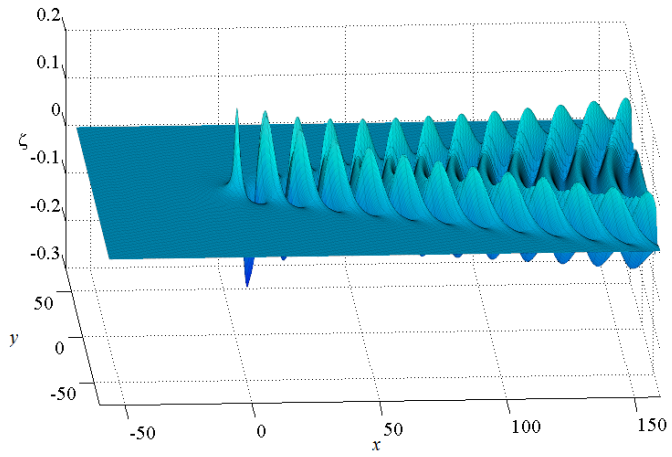

(b) The free surface profile over the full truncated domain.

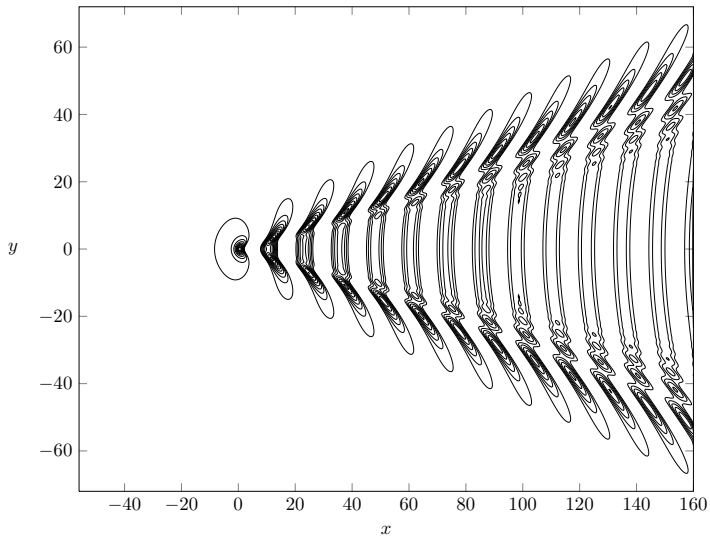

(c) A contour plot, where contours are shown only for positive wave heights to avoid confusion.

Figure 3.7: Perspectives of the free surface for $F_L = 1.4$ and $\epsilon = 1$, computed on a 721×241 mesh with $\Delta x = 0.3$, $\Delta y = 0.3$, $x_0 = -56$. This solution was computed on a workstation with GPU acceleration.

3.6 Discussion

We have considered the fully nonlinear problem of the free-surface flow past a submerged point source. Following Forbes (1989), we apply a boundary integral technique based on Green's second formula to derive a singular integro-differential equation for the velocity potential $\Phi(x, y, z)$ and the shape of the surface $z = \zeta(x, y)$. This equation, together with Bernoulli's equation, is discretised and satisfied at midpoints on a two-dimensional mesh. The resulting system of nonlinear algebraic equations is solved using Newton's method. In the past, numerical approaches of this sort were hindered by the fact that the Jacobian matrix in Newton's method is dense. Our contribution is to apply a Jacobian-free Newton-Krylov method to solve the nonlinear system, thus avoiding the need to ever form or factorise the Jacobian. As such, we are able to use much finer meshes than used in the past by other authors. Further, in order to ensure efficiency, we use a banded matrix preconditioner whose nonzero entries come from the linearised problem. Finally, we code the function to run efficiently on a GPU, to greatly speed up function evaluation times. The resolution of the mesh we use is now essentially up to the standard of many two-dimensional schemes published in the literature.

As discussed in the Introduction, the problem of flow past a source singularity can be thought of as a building block for more complicated configurations such as flow due to a steadily moving applied pressure distribution (like a hovercraft), a thin ship hull, or a submerged body (like a submarine). The next stage in this research is to adapt the present techniques for these more complicated flows. We expect that the key ideas developed in this paper will generalise in a straightforward manner, provided there is a natural linearised version of the problem at hand. With the accuracy and efficiency of our approach, one may be able to devise appropriate optimisation schemes for designing ship hulls with minimal resistance, and so on. Our approach should also translate to time-dependent problems, such as the study by Părău, Vanden-Broeck, and Cooker (2010), who apply a similar boundary integral approach, discretised with 60×40 meshes, to solve for time-dependent flows past a pressure distribution (see (Dias and Bridges 2006; Fochesato and Dias 2006; Grilli, Guyenne, and Dias 2001) for a thorough discussion of further issues that arise in time-dependent problems). We leave all this work for further study.

With the degree of accuracy our numerical schemes allow, we are now in a position to explore the effect of strong nonlinearity on the wave pattern, as has been done extensively in the two-dimensional analogue. For example, as the nonlinearity in a steady ship wave problem increases (for our problem this tendency comes from increasing ϵ), the waves will become more nonlinear in shape, perhaps with sharper crests. Given

the flow is steady, we expect that the waves will ultimately "break" when the most nonlinear wave reaches a limiting configuration (this occurs when the highest wave crest reaches the dimensionless height $F_L^2/2$). While this general behaviour is well understood for two-dimensional waves, with studies of highly nonlinear waves producing highly accurate calculations of near-breaking waves (Cokelet 1977; Dallaston and McCue 2010; Lukomsky, Gandzha, and Lukomsky 2002; Schwartz 1974; Williams 1981) (the breaking point corresponding to the Stokes limiting configuration with a 120° angle at the wave crest), the highly nonlinear regime for fully three-dimensional problems is relatively unexplored. Indeed, the extra dimension makes the pattern structure much more complicated, and so it is not always obvious what part of the domain will break first. As such, the challenge of generalising the two-dimensional results to three dimensions remains.

3.7 Appendix

3.7.1 Ordering the equations

The left-hand side of $\mathbf{F}(\mathbf{u}) = 0$ is a vector valued function made up of six different functions taken from the numerical scheme. The free surface condition (3.13) and boundary integral equation (3.12) evaluated at the half mesh points $(x_{k+\frac{1}{2}}, y_\ell)$ are denoted $\mathbf{F}_{1_{k,\ell}}$ and $\mathbf{F}_{2_{k,\ell}}$, respectively, for $k = 1, \dots, N-1$ and $\ell = 1, \dots, M$. We also have the radiation conditions (3.24) denoted:

$$\begin{aligned}
\mathbf{F}_{3_\ell} &= x_1((\phi_x)_{1,\ell} - 1) + n(\phi_{1,\ell} - x_1),\\
\mathbf{F}_{4_\ell} &= x_1(\phi_{xx})_{1,\ell} + n((\phi_x)_{1,\ell} - 1),\\
\mathbf{F}_{5_\ell} &= x_1(\zeta_x)_{1,\ell} + n\zeta_{1,\ell},\\
\mathbf{F}_{6_\ell} &= x_1(\zeta_{xx})_{1,\ell} + n(\zeta_x)_{1,\ell},
\end{aligned}$$

for $\ell = 1, \dots, M$. We order these equations as

$$\begin{aligned}
\mathbf{F} =[&\mathbf{F}_{3_1}, \mathbf{F}_{4_1}, \mathbf{F}_{1_{1,1}}, \dots, \mathbf{F}_{1_{N-1,1}}, \mathbf{F}_{3_2}, \mathbf{F}_{4_2}, \mathbf{F}_{1_{1,2}}, \dots, \mathbf{F}_{1_{N-1,2}}, \dots, \mathbf{F}_{3_M}, \mathbf{F}_{4_M}, \mathbf{F}_{1_{1,M}}, \dots, \mathbf{F}_{1_{N-1,M}},\\
&\mathbf{F}_{5_1}, \mathbf{F}_{6_1}, \mathbf{F}_{2_{1,1}}, \dots, \mathbf{F}_{2_{N-1,1}}, \mathbf{F}_{5_2}, \mathbf{F}_{6_2}, \mathbf{F}_{2_{1,2}}, \dots, \mathbf{F}_{2_{N-1,2}}, \dots, \mathbf{F}_{5_M}, \mathbf{F}_{6_M}, \mathbf{F}_{2_{1,M}}, \dots, \mathbf{F}_{2_{N-1,M}}]^T,
\end{aligned}$$

which results in the Jacobian structure illustrated in Figure 3.1.

3.7.2 The linear Jacobian

To construct the linear Jacobian, we need to apply the same numerical discretisation outlined in Section 3.3 to the linear problem derived in Section 3.2.3.

The singularity in (3.17) is dealt with in the same way as with the nonlinear problem, by adding and subtracting the term (3.20), except that now $S_2(x_i, y_j; x_k^*, y_\ell^*) =$

$K_3(x_i, y_j; x_k^*, y_\ell^*)$, which simplifies the details. The linear system then becomes

$$\begin{aligned}
\mathbf{F}_{1_{k,\ell}} &= \phi^*_{x_{k,\ell}} + \frac{\zeta^*_{k,\ell}}{F_L^2} - 1, \\
\mathbf{F}_{2_{k,\ell}} &= 2\pi(\phi^*_{k,\ell} - x_k^*) + \frac{\epsilon}{\left(x_k^{*2} + y_\ell^{*2} + 1\right)^{\frac{1}{2}}} - \sum_{i=1}^{N}\sum_{j=1}^{M} w(i,j)\left[\zeta_{x_{i,j}} - \zeta^*_{x_{k,\ell}}\right] K_{3_{i,j,k,\ell}} - \zeta^*_{x_{i,j}} I, \\
\mathbf{F}_{3_\ell} &= x_1\phi_{x_{1,\ell}} + n\phi_{1,\ell} - x_1(n+1), \\
\mathbf{F}_{4_\ell} &= \frac{x_1}{\Delta x}\phi_{x_{2,\ell}} + (n - \frac{x_1}{\Delta x})\phi_{x_{1,\ell}} - n, \\
\mathbf{F}_{5_\ell} &= x_1\zeta_{x_{1,\ell}} + n\zeta_{1,\ell}, \\
\mathbf{F}_{6_\ell} &= \frac{x_1}{\Delta x}\zeta_{x_{2,\ell}} + (n - \frac{x_1}{\Delta x})\zeta_{x_{1,\ell}},
\end{aligned} \tag{3.26}$$

for $k = 1 \ldots (N-1)$, $\ell = 1 \ldots M$ where $\mathbf{F}$ is constructed from these equations and

$$K_{3_{i,j,k,\ell}} = K_3(x_i, y_j; x_k^*, y_\ell^*),$$

I is given by

$$I = \int_{y_1}^{y_M}\int_{x_1}^{x_N} K_3 \,\mathrm{d}x\,\mathrm{d}y,$$

and $w(i,j)$ is the weighting function for numerical integration. As before, I can be evaluated exactly in terms of logarithms.

The next step is to determine how ϕ, ϕ^*, ζ and ζ^* depend on the unknowns in (3.18). We first expand the trapezoidal-rule integration of ζ in (3.19) which gives

$$\zeta_{k,\ell} = \zeta_{1,\ell} + \frac{\Delta x}{2}\zeta_{x_{1,\ell}} + \Delta x\sum_{i=2}^{k-1}\zeta_{x_{i,\ell}} + \frac{\Delta x}{2}\zeta_{x_{k,\ell}}, \quad \text{for } k = 2,\ldots,N,\ \ell = 1,\ldots,M.$$

Similarly, we expand ϕ as

$$\phi_{k,\ell} = \phi_{1,\ell} + \frac{\Delta x}{2}\phi_{x_{1,\ell}} + \Delta x\sum_{i=2}^{k-1}\phi_{x_{i,\ell}} + \frac{\Delta x}{2}\phi_{x_{k,\ell}}, \quad \text{for } k = 2,\ldots,N,\ \ell = 1,\ldots,M.$$

This result immediately provides the values for ϕ^* using two point interpolation

$$\phi^*_{k,\ell} = \frac{1}{2}(\phi_{k,\ell} + \phi_{k+1,\ell}).$$

Substituting this expression and its equivalent in ζ_x^* and ζ^* into (3.26) gives the resulting linear system in terms of the unknowns,

$$\mathbf{F}_{1_{k,\ell}} = \frac{1}{2}(\phi_{x_{k,\ell}} + \phi_{x_{k+1,\ell}}) + \frac{1}{F_L^2}\left(\zeta_{1,\ell} + \frac{\Delta x}{2}\zeta_{x_{1,\ell}} + \Delta x\sum_{i=2}^{k-1}\zeta_{x_{i,\ell}} + \frac{3\Delta x}{4}\zeta_{x_{k,\ell}} + \frac{\Delta x}{4}\zeta_{x_{k+1,\ell}}\right) - 1,$$

$$\mathbf{F}_{2_{k,\ell}} = 2\pi\left[\phi_{1,\ell} + \frac{\Delta x}{2}\phi_{x_{1,\ell}} + \Delta x\sum_{i=2}^{k-1}\phi_{x_{i,\ell}} + \frac{3\Delta x}{4}\phi_{x_{k,\ell}} + \frac{\Delta x}{4}\phi_{x_{k+1,\ell}} - x_k^*\right] + \frac{\epsilon}{\left(x_k^{*2} + y_\ell^{*2} + 1\right)^{\frac{1}{2}}}$$
$$- \sum_{i=1}^{N}\sum_{j=1}^{M} w(i,j)\left[\zeta_{x_{i,j}} - \frac{1}{2}(\zeta_{x_{k,\ell}} + \zeta_{x_{k+1,\ell}})\right] K_{3_{i,j,k,\ell}} - \frac{1}{2}(\zeta_{x_{k,\ell}} + \zeta_{x_{k+1,\ell}})I,$$
$$\mathbf{F}_{3_\ell} = x_1\phi_{x_{1,\ell}} + n\phi_{1,\ell} - x_1(n+1), \tag{3.27}$$
$$\mathbf{F}_{4_\ell} = \frac{x_1}{\Delta x}\phi_{x_{2,\ell}} + (n - \frac{x_1}{\Delta x})\phi_{x_{1,\ell}} - n,$$
$$\mathbf{F}_{5_\ell} = x_1\zeta_{x_{1,\ell}} + n\zeta_{1,\ell},$$
$$\mathbf{F}_{6_\ell} = \frac{x_1}{\Delta x}\zeta_{x_{2,\ell}} + (n - \frac{x_1}{\Delta x})\zeta_{x_{1,\ell}},$$

for $k = 1\ldots(N-1)$, $\ell = 1\ldots M$.

Finally, to calculate the linear Jacobian, the equations in (3.27) can be differentiated with respect to $\phi_{1,m}$, $\phi_{x_{n,m}}$, $\zeta_{1,m}$ and $\zeta_{x_{n,m}}$ to give:

$$\frac{\partial \mathbf{F}_{1_{k,\ell}}}{\partial \phi_{1,m}} = 0,$$
$$\frac{\partial \mathbf{F}_{1_{k,\ell}}}{\partial \phi_{x_{n,m}}} = \begin{cases} \frac{1}{2} & \text{for } n = k, k+1 \text{ and } m = \ell \\ 0 & \text{otherwise} \end{cases}, \tag{3.28}$$
$$\frac{\partial \mathbf{F}_{1_{k,\ell}}}{\partial \zeta_{1,m}} = \begin{cases} \frac{1}{F_L^2} & \text{for } m = \ell \\ 0 & \text{otherwise} \end{cases},$$
$$\frac{\partial \mathbf{F}_{1_{k,\ell}}}{\partial \zeta_{x_{n,m}}} = \begin{cases} \frac{\Delta x}{4F_L^2} & \text{for } n = 1,\ k = 1 \text{ and } m = \ell \\ \frac{\Delta x}{2F_L^2} & \text{for } n = 1,\ k > 1 \text{ and } m = \ell \\ \frac{\Delta x}{F_L^2} & \text{for } n < k \text{ and } m = \ell \\ \frac{3\Delta x}{4F_L^2} & \text{for } n = k \text{ and } m = \ell \\ \frac{\Delta x}{4F_L^2} & \text{for } n = k+1 \text{ and } m = \ell \\ 0 & \text{otherwise} \end{cases}, \tag{3.29}$$
$$\frac{\partial \mathbf{F}_{2_{k,\ell}}}{\partial \phi_{1,m}} = \begin{cases} 2\pi & \text{for } m = \ell \\ 0 & \text{otherwise} \end{cases},$$
$$\frac{\partial \mathbf{F}_{2_{k,\ell}}}{\partial \phi_{x_{n,m}}} = \begin{cases} \frac{\pi\Delta x}{2} & \text{for } n = 1,\ k = 1 \text{ and } m = \ell \\ \pi\Delta x & \text{for } n = 1,\ k > 1 \text{ and } m = \ell \\ 2\pi\Delta x & \text{for } n < k \text{ and } m = \ell \\ \frac{3\pi\Delta x}{2} & \text{for } n = k \text{ and } m = \ell \\ \frac{\pi\Delta x}{2} & \text{for } n = k+1 \text{ and } m = \ell \\ 0 & \text{otherwise} \end{cases}, \tag{3.30}$$

$$\frac{\partial \mathbf{F}_{2_{k,\ell}}}{\partial \zeta_{1,m}} = 0$$

$$\frac{\partial \mathbf{F}_{2_{k,\ell}}}{\partial \zeta_{x_{n,m}}} = \begin{cases} \frac{1}{2}\sum_{i=1}^{N}\sum_{j=1}^{M} w(i,j)K_{3_{i,j,k,\ell}} - \frac{1}{2}I - w(n,m)K_{3_{n,m,k,\ell}} & \text{for } n = k, k+1 \text{ and } m = \ell \\ -w(n,m)K_{3_{n,m,k,\ell}} & \text{otherwise} \end{cases}, \tag{3.31}$$

for $k = 1 \dots (N-1)$, $\ell = 1 \dots M$ and $n = 1 \dots N$, $m = 1 \dots M$. The derivatives for $\mathbf{F}_{3_\ell}, \mathbf{F}_{4_\ell}, \mathbf{F}_{5_\ell}, \mathbf{F}_{6_\ell}$ can be easily calculated and will not be explicitly written here. Our preconditioner is formed by ordering these Jacobian entries in the manner described in 3.7.1.

3.7.3 Preconditioner storage and factorisation

As shown in Figure 3.1, the preconditioner can be divided up into four equal submatrices of size $(N+1)M \times (N+1)M$. This preconditioner can then be factorised using the block decomposition,

$$\mathbf{P} = \begin{bmatrix} A & B \\ C & D \end{bmatrix} = \begin{bmatrix} I & 0 \\ CA^{-1} & I \end{bmatrix} \begin{bmatrix} A & 0 \\ 0 & D - CA^{-1}B \end{bmatrix} \begin{bmatrix} I & A^{-1}B \\ 0 & I \end{bmatrix},$$

where A, B, C, and D are primarily given by equations (3.28), (3.29), (3.30) and (3.31), respectively. Thus we can solve the system $\mathbf{Pr} = \mathbf{b}$ by performing the following operations,

$$\begin{bmatrix} \mathbf{t}_1 \\ \mathbf{t}_2 \end{bmatrix} = \begin{bmatrix} \mathbf{b}_1 \\ \mathbf{b}_2 - CA^{-1}\mathbf{b}_1 \end{bmatrix}, \quad \begin{bmatrix} \mathbf{s}_1 \\ \mathbf{s}_2 \end{bmatrix} = \begin{bmatrix} A^{-1}\mathbf{t}_1 \\ (D - CA^{-1}B)^{-1}\mathbf{t}_2 \end{bmatrix}, \quad \begin{bmatrix} \mathbf{r}_1 \\ \mathbf{r}_2 \end{bmatrix} = \begin{bmatrix} \mathbf{s}_1 - A^{-1}B\mathbf{s}_2 \\ \mathbf{s}_2 \end{bmatrix}.$$

This method provides several advantages. First, A is tridiagonal, allowing for easy storage and fast factorisation and inversion when needed. Second, B and C are only used in matrix vector multiplication operations and thus can be implemented as functions that perform these operations rather than stored as matrices. Furthermore, A, B and C are block diagonal, and each diagonal block is identical within a given matrix, meaning $CA^{-1}B$ need only be computed for one block. Finally, D appears only in the Schur complement $(D - CA^{-1}B)$, which we store and factorise in the preconditioner set-up phase. These advantages mean we only store a $3 \times (N+1)M$ matrix for A and a block-banded matrix for the Schur complement $(D - CA^{-1}B)$ when constructing and factorising the preconditioner.

3.8 Computer code

The code used to generate Figure 3.5(b) is provided at:
`https://github.com/rPethiyagoda/Pethiyagoda-PhD-thesis-code`.

4 What is the apparent angle of a Kelvin ship wave pattern?

This chapter was first published as

R. Pethiyagoda, S. W. McCue, and T. J. Moroney (2014). What is the apparent angle of a Kelvin ship wave pattern? *Journal of Fluid Mechanics* **758**, 468–485.

Abstract

While the half-angle which encloses a Kelvin ship wave pattern is commonly accepted to be 19.47°*, recent observations and calculations for sufficiently fast-moving ships suggest that the apparent wake angle decreases with ship speed. One explanation for this decrease in angle relies on the assumption that a ship cannot generate wavelengths much greater than its hull length. An alternative interpretation is that the wave pattern that is observed in practice is defined by the location of the highest peaks; for wakes created by sufficiently fast-moving objects, these highest peaks no longer lie on the outermost divergent waves, resulting in a smaller apparent angle. In this paper, we focus on the problems of free surface flow past a single submerged point source and past a submerged source doublet. In the linear version of these problems, we measure the apparent wake angle formed by the highest peaks, and observe the following three regimes: a small Froude number pattern, in which the divergent waves are not visible; standard wave patterns for which the maximum peaks occur on the outermost divergent waves; and a third regime in which the highest peaks form a V-shape with an angle much less than the Kelvin angle. For nonlinear flows, we demonstrate that nonlinearity has the effect of increasing the apparent wake angle so that some highly nonlinear solutions have apparent wake angles that are greater than Kelvin's angle. For large Froude numbers, the effect on apparent wake angle can be more dramatic, with the possibility of strong nonlinearity shifting the wave pattern from the third regime to the second. We expect our nonlinear results will translate to other more complicated flow configurations, such*

as flow due to a steadily moving closed body such as a submarine.

4.1 Introduction

Kelvin ship wave patterns are comprised of divergent and transverse waves. For a steadily moving object in an infinitely deep inviscid fluid, the half-angle which encloses the ship wave pattern is widely accepted to be the Kelvin angle 19.47°, at least if the wave amplitude is small (Thomson 1887). This angle can be determined by constructing geometric arguments with the dispersion relation (Lighthill 1978), by locating the caustics using the method of stationary phase (Ursell 1960), or by applying geometric ray theory (Keller 1979). On the other hand, if the object is moving sufficiently fast, the angle that is actually observed in practice is less than the Kelvin angle, and in fact decreases with object speed (Rabaud and Moisy 2013). One explanation for these observations, proposed by Rabaud and Moisy (2013), is that a ship cannot generate wavelengths much greater than its hull length (Carusotto and Rousseaux 2013). However, recently Darmon, Benzaquen, and Raphaël (2014) suggest that Rabaud & Moisy were measuring the angle provided by the peaks of the waves. By treating the linear problem of flow past a pressure distribution, Darmon et al. demonstrate that the apparent wake angle defined by the highest wave peaks is consistent with the experimental observations of Rabaud & Moisy (including a decrease in angle which scales as the inverse object speed), thus describing the trends in the data without making any assumptions about the relationship between wavelengths and the hull length. This research is reviewed by Dias (2014).

A series of very recent papers has followed the work of Rabaud and Moisy (2013) and Darmon, Benzaquen, and Raphaël (2014). Ellingsen (2014) considers the problem of flow past a pressure distribution in a shear flow, Benzaquen, Darmon, and Raphaël (2014) treat elliptic pressure distributions, while Rabaud and Moisy (2014) make connections with wave drag for the same type of flow configuration. In each of these three cases, apparent wake angles are calculated using exact solutions to linear problems. In a slightly different vein, Noblesse et al. (2014) proposes another explanation for the decrease in apparent wake angle by suggesting that smaller angles are due to interference between bow and stern waves, providing an additional regime in which the angle appears to scale like the inverse square of the ship speed. Finally, Moisy and Rabaud (2014b) go some way to connect the work of Noblesse et al. (2014) with the other recent papers by focusing on flows past pressure distributions with large aspect ratios, while He et al. (2014) assess the key assumptions behind each of Rabaud and Moisy (2013), Darmon, Benzaquen, and Raphaël (2014) and Noblesse et al. (2014) in the context of Rabaud & Moisy's original observations of real ships.

All of the above theoretical work is for *linear* flows, while much of the focus of the present paper is on the effect that *nonlinearity* has on the apparent wake angle. We are going to approach this study by considering two flow configurations, the first being the flow due to a point source submerged below the surface in a fluid moving at constant velocity. For this geometry, the problem is closely related to flow past a submerged semi-infinite Rankine-type body. There is no obvious length scale in the direction of travel and thus we completely avoid issues related to wave interference between a ship's bow and stern or the question of disturbances having wavelengths greater than or less than the ship hull length. The second configuration we consider is flow past a submerged source doublet. Here there is a correspondence with flow past a submerged sphere, although for nonlinear flows care must be taken with this analogy, since the nonlinear case is not equivalent to flow past a closed body.

The mathematical problems we consider are formulated in Section 4.2. The method we employ to measure the apparent wake angle, similar to that used in Moisy and Rabaud (2014b), is outlined in Section 4.3. It is instructive to begin with the linear version of our problems in Section 4.4, highlighting the key features for comparison with the nonlinear results. We describe three different regimes. The first is for small Froude numbers, for which the divergent waves are not visible and so our method does not apply. The second regime corresponds to wave patterns that have the maximum peaks on the outermost divergent waves, giving rise to apparent wake angles close the Kelvin angle. For the third regime, the highest peaks form a V-shape with an angle that decreases with the speed of the steadily moving source, scaling as the inverse Froude number in the large Froude number limit. We then generate numerical solutions to the nonlinear problems in Section 4.5 and observe that nonlinear wave patterns can appear qualitatively different to their linear analogues. Our results suggest that, for a fixed Froude number, the apparent wake angle increases as the nonlinearity increases, and in some cases continues to increase *past the Kelvin angle*. Furthermore, for large Froude numbers, strong nonlinearity can have the dramatic effect of shifting the regime to be the second type instead of the third. We conclude that both the speed (the Froude number) and 'size' (the nonlinearity) of a moving ship or submarine influence apparent wake angle. In particular, for sufficiently fast-moving ships, the apparent wake angle tends to decrease with ship speed but increase with ship 'size'.

We mention in passing there are many other physical influences not treated here. For example, the consideration of how surface tension (Carusotto and Rousseaux 2013; Doyle and McKenzie 2013; Moisy and Rabaud 2014a) or a finite-depth channel (Soomere 2007) affects the wake angle raises additional questions that are worth exploring. We leave these issues for further study.

4.2 Mathematical formulation

4.2.1 Governing equations for flow past a point source

We first consider the problem of steady flow caused by submerging a source of strength m at a depth L below the surface of a uniform stream of speed U travelling in the x-direction. The main task is to solve for the velocity potential, $\phi(x, y, z)$, and determine the shape of the free surface, $z = \zeta(x, y)$. There are two dimensionless parameters: the dimensionless source strength, $\epsilon = m/(UL^2)$ and the Froude number, $F_L = U/\sqrt{gL}$, where here g is acceleration due to gravity. For a small source strength ($\epsilon \ll 1$), the problem can be linearised about the undisturbed surface ($z = 0$) (Noblesse 1978; Chung and Lim 1991; Lustri and Chapman 2013), while for moderate to large source strengths, the full nonlinear problem must be solved in the domain $z < \zeta(x, y)$ (Forbes 1989; Pethiyagoda et al. 2014, Ch. 3). We present the dimensionless governing equations for both cases.

Assuming ideal fluid flow conditions, the velocity potential ϕ satisfies Laplace's equation below the free-surface:

$$\nabla^2\phi = \frac{\partial^2\phi}{\partial x^2} + \frac{\partial^2\phi}{\partial y^2} + \frac{\partial^2\phi}{\partial z^2} = 0 \quad \text{for } z < \zeta(x, y) \text{ (nonlinear) or } z < 0 \text{ (linear).} \tag{4.1}$$

We have kinematic and dynamic conditions acting on the free-surface:

$$\phi_x\zeta_x + \phi_y\zeta_y = \phi_z \text{ on } z = \zeta(x, y), \tag{4.2}$$

$$\frac{1}{2}(\phi_x^2 + \phi_y^2 + \phi_z^2) + \frac{\zeta}{F_L^2} = \frac{1}{2} \text{ on } z = \zeta(x, y), \tag{4.3}$$

for the nonlinear problem. The kinematic condition states that no fluid can flow through the surface $z = \zeta(x, y)$, while the dynamic condition combines Bernoulli's equation with a constant atmospheric pressure on $z = \zeta(x, y)$. After linearisation, these two equations become

$$\zeta_x = \phi_z \quad \text{on} \quad z = 0, \tag{4.4}$$

$$\phi_x - 1 + \frac{\zeta}{F_L^2} = 0 \quad \text{on} \quad z = 0, \tag{4.5}$$

respectively. The velocity potential near the source behaves like

$$\phi \sim -\frac{\epsilon}{4\pi\sqrt{x^2 + y^2 + (z+1)^2}} \text{ as } (x, y, z) \to (0, 0, -1). \tag{4.6}$$

Finally, we have far field conditions both infinitely far upstream and below the surface,

$$(\phi_x, \phi_y, \phi_z) \to (1, 0, 0), \quad \zeta \to 0 \quad \text{as} \quad x \to -\infty, \tag{4.7}$$

$$(\phi_x, \phi_y, \phi_z) \to (1, 0, 0), \qquad \text{as} \quad z \to -\infty. \tag{4.8}$$

The governing equations (4.1)–(4.8) define both the nonlinear and linear problems for free-surface flow past a submerged source. Once the solution for ϕ is determined, the velocity field $\mathbf{q}$ is recovered via $\mathbf{q} = \nabla\phi$.

The linear problem (4.1), (4.4)–(4.8) above is equivalent to flow past a submerged semi-infinite Rankine body with a rounded nose (Batchelor 2000, pp. 461). As such, one interpretation is that this problem models the ship wave pattern generated at the bow of a submerged body such as a submarine. Downstream from the nose, the body very quickly approaches a cylinder in shape with cross-sectional radius $\sqrt{\epsilon/\pi}$ and area ϵ. Thus, with our choice of nondimensionalisation, we are able to use the following variation of parameter values to get a sense of the physics involved with this choice of flow configuration. First, we see that increasing (decreasing) the Froude number F_L while keeping the dimensionless source strength ϵ fixed is equivalent to increasing (decreasing) the speed of the flow about the Rankine body while keeping the size and depth of the Rankine body fixed. On the other hand, increasing (decreasing) ϵ while keeping F_L fixed is equivalent to increasing (decreasing) the size of the Rankine body while keeping its depth and the fluid speed fixed. Finally, if we increase (decrease) both F_L and ϵ such that ϵ/F_L^4 is held constant, then this is equivalent to fixing the speed of the flow and the size of the Rankine body, but decreasing (increasing) the depth of the body. For this linear problem we shall make use of the exact solution

$$\begin{aligned}\zeta(x,y) = &-\frac{\epsilon F_L^2 \operatorname{sgn}(x)}{\pi^2}\int_0^{\frac{\pi}{2}} \cos\theta \int_0^{\infty} \frac{k\mathrm{e}^{-k|x|}\cos(ky\sin\theta)g(k,\theta)}{F_L^4k^2+\cos^2\theta}\,\mathrm{d}k\,\mathrm{d}\theta \\ &+\frac{\epsilon H(x)}{\pi}\int_{-\infty}^{\infty}\xi\mathrm{e}^{-F_L^2\xi^2}\cos(x\xi)\cos(y\xi\lambda)\,\mathrm{d}\lambda \end{aligned} \tag{4.9}$$

(Peters 1949), where

$$g(k,\theta) = F_L^2 k\sin(k\cos\theta) + \cos\theta\cos(k\cos\theta), \tag{4.10}$$

$$\xi(\lambda) = \sqrt{\lambda^2+1}/F_L^2, \tag{4.11}$$

$\operatorname{sgn}(x)$ is the sign function, and $H(x)$ is the Heaviside function. The integrals in this exact solution are evaluated numerically to obtain the free-surface profile for a given Froude number, F_L.

The nonlinear problem (4.1)–(4.3), (4.6)–(4.8) is also equivalent to flow past a semi-infinite body, although there is no longer a well-known formula for the body shape. This cigar-like body will have a cross-sectional area in the far-field which is roughly of order ϵ, at least for moderate values of ϵ. For large ϵ, the shape of the submerged body will be highly distorted, and the direct correspondence with the semi-infinite Rankine body is lost.

4.2.2 Governing equations for flow past a source doublet

The second problem we are concerned with is free surface flow past a source doublet of strength κ submerged a depth L below the surface of a uniform stream of speed U (Havelock 1928; Havelock 1932a). This problem has two dimensionless parameters, the source doublet strength, $\mu = \kappa/(UL^3)$, and the Froude number, $F_L = U/\sqrt{gL}$. With this scaling, the governing equations for flow past a doublet are the same as for flow past a source, except that (4.6) is replaced by

$$\phi \sim \frac{\mu x}{4\pi \left(x^2 + y^2 + (z+1)^2\right)^{3/2}} \text{ as } (x, y, z) \to (0, 0, -1)\,. \tag{4.12}$$

The linearised problem of flow past a doublet (4.1), (4.4)–(4.5), (4.7)–(4.8), (4.12) is valid for the weak doublet limit $\mu \ll 1$. In this case the problem is equivalent to flow past a submerged sphere of radius $(\mu/2\pi)^{1/3}$ and volume $2\mu/3$ (Lamb 1916, pp. 116). Thus, increasing the Froude number F_L while keeping μ constant is equivalent to increasing the velocity in the far field while keeping the radius and depth of the submerged sphere fixed. Increasing μ with F_L fixed is like increasing the radius of the sphere while holding its depth and the far-field speed constant. Finally, increasing both F_L and μ with μ/F_L^6 constant is equivalent to fixing the speed of the flow and radius of the sphere while decreasing the sphere's depth. To derive an exact solution to the linear problem of flow past a doublet we can make use of the exact solution for flow past a source (4.9). First, we consider a source and sink of equal strength $\epsilon = \mu/\delta$, where the sink is placed a distance δ downstream of the source. We then take the limit $\delta \to 0$, in effect differentiating (4.9) with respect to x. Thus, an exact solution for this linear problem is given by

$$\begin{aligned}\zeta(x, y) =& \frac{\mu F_L^2}{\pi^2} \int_0^{\frac{\pi}{2}} \cos\theta \int_0^{\infty} \frac{k^2 \mathrm{e}^{-k|x|} \cos(ky \sin\theta) g(k, \theta)}{F_L^4 k^2 + \cos^2\theta} \,\mathrm{d}k \,\mathrm{d}\theta \\ &- \frac{\mu H(x)}{\pi} \int_{-\infty}^{\infty} \xi^2 \mathrm{e}^{-F_L^2 \xi^2} \sin(x\xi) \cos(y\xi\lambda) \,\mathrm{d}\lambda,\end{aligned} \tag{4.13}$$

where $g(k, \theta)$ and $\xi(\lambda)$ are given by (4.10) and (4.11), respectively.

As with flow past a source, nonlinearity has the effect of distorting the shape of the submerged object. In fact, for nonlinear flow past a doublet, the problem is not equivalent to flow past a closed object, as there are no closed streamsurfaces. Regardless, this nonlinear problem is still of considerable interest in the present context, as there is no net increase of fluid in the system, which contrasts the problem of flow past a point source. Further, the nonlinear wave patterns and resulting wake angles are likely to be closely related to those associated with flow past submerged closed bodies (see Tuck and Scullen 2002, for example).

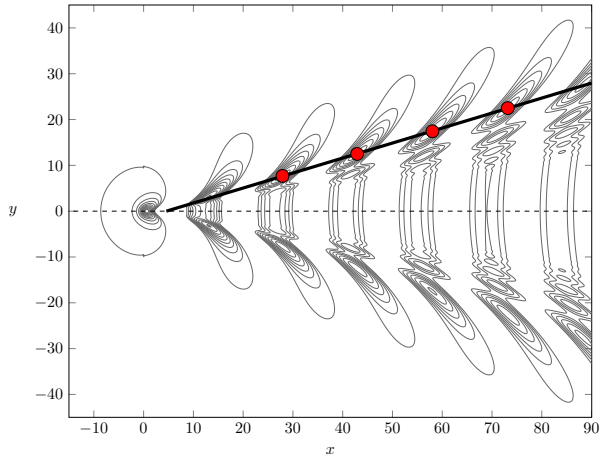

Figure 4.1: Contour plot of the linear free-surface profile for flow past a source with $F_L = 1.5$, with only positive wave heights shown for clarity. The highest wake peaks are marked with solid (red) circles. The thick (black) line represents the line of best fit.

4.3 Method of measuring the apparent wake angle

In order to measure the apparent wake angle, θ_{app}, of a given free-surface profile, we isolate every wavelength of the wave and mark the highest peak. We then fit a line through these points with a least-squares approximation. Finally, we take the angle between the line of best fit and the centreline ($y = 0$) as the apparent wake angle. An illustration of this method is shown in Figure 4.1 for linearised flow past a point source with $F_L = 1.5$. This method was also used very recently by Moisy and Rabaud (2014b); it acts to approximate the manual approach of Rabaud and Moisy (2013), who drew a line through the brightest points in a series of satellite images of ship wakes and measured the resulting angle by hand.

On the other hand, an alternative approach for measuring the apparent wake angle is employed by Darmon, Benzaquen, and Raphaël (2014) and Benzaquen, Darmon, and Raphaël (2014), who define their wake angle in terms of the maximum of a curve which is interpolated from the peaks within a given wavelength far downstream. A line is drawn between this maximum and the origin (which, for their problem, is the centre of an applied pressure distribution), forming an angle with the centreline. A similar method was used by Ellingsen (2014). While this approach works well for measuring wake angles for linear problems with exact solutions, we are unable to compute nonlinear free-surface profiles far downstream without loss of accuracy. Thus we prefer our method, which is more straightforward, and involves fitting a line through data points closer to the disturbance in question.

4.4 Linear ship waves

Using the exact solutions, (4.9) and (4.13) to the linear problems of flow past a source and doublet, respectively, we calculate free-surface profiles for a number of different Froude numbers. By applying our method for measuring the apparent wake angle θ_{app}, we have recorded the dependence of θ_{app} on the Froude number F_L in Figure 4.2, which we now discuss in some detail.

4.4.1 Measured wake angle for flow past a source

Figure 4.2(a) shows results for flow past a source. For the approximate range of Froude numbers $0.8 < F_L < 3$, we see the apparent wake angle remains roughly constant at about 18.5°, which is slightly less than the Kelvin angle. We call this Regime II, and show in Figure 4.3(a) a typical wave pattern from this parameter range. As with other solutions in Regime II, the wave pattern in Figure 4.3(a) is characterised by the highest peaks lying on the outermost divergent waves.

For sufficiently large Froude numbers, we find that the highest peaks on the wave pattern no longer lie on the outermost divergent waves, and so the apparent wake angle is much less than Kelvin's angle. We call this Regime III. Figures 4.3(c),(d), which are drawn for $F_L = 4.5$ and 8.5, respectively, provide examples of wave patterns which lie in this regime. In fact, for $F_L > 4$ we find the apparent wake angle scales as F_L^{-1}, demonstrated by the asymptotic line in Figure 4.2(a) (see Section 4.4.3). This result is consistent with the scalings discussed in Darmon, Benzaquen, and Raphaël (2014), Ellingsen (2014), Benzaquen, Darmon, and Raphaël (2014) and Moisy and Rabaud (2014b). The wave pattern in Figure 4.3(b) falls somewhere between Regimes II and III, since there is small range of Froude numbers for which all peaks downstream of a given value of $\tilde{x}$ lie on the outermost divergent waves, while all peaks upstream do not. By noting the location of the solid circles in this special borderline case, we see that our approach for approximating the apparent angle gives a slightly higher value together with a large root mean squared error (indicated by the dot-dashed curve). The spike in error in Figure 4.2(a) is clearly apparent in this transitional region.

Finally, we note that for sufficiently small Froude numbers, the peaks of the divergent waves are lower than the transverse waves, and in fact for roughly $F_L < 0.6$ the divergent waves are no longer visible for the spatial resolution employed. As such, our method of measuring the apparent wake angle breaks down. We call this Regime I. Roughly speaking, Regime I (and the transition between Regimes I and II) occurs for $F_L < 0.8$ for this problem. We shall not consider this regime in the present study, but note it is analysed recently in some detail for the linearised problem of flow past a submerged source in Lustri and Chapman (2013). The techniques required for this type of

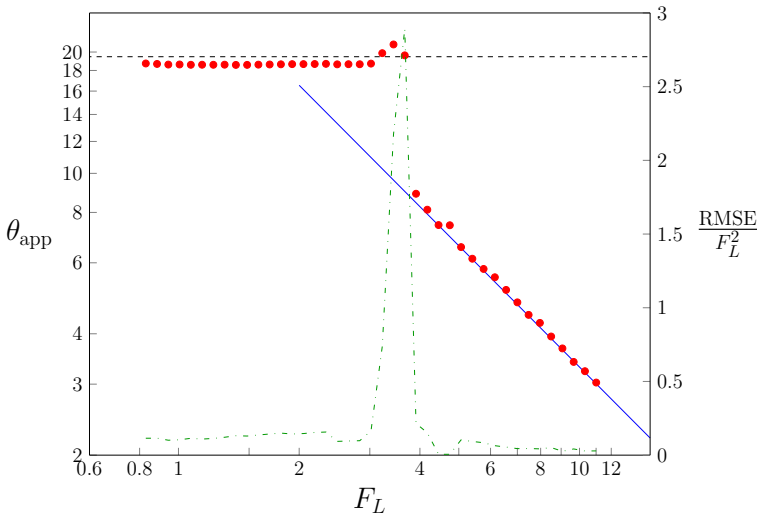

(a) Source

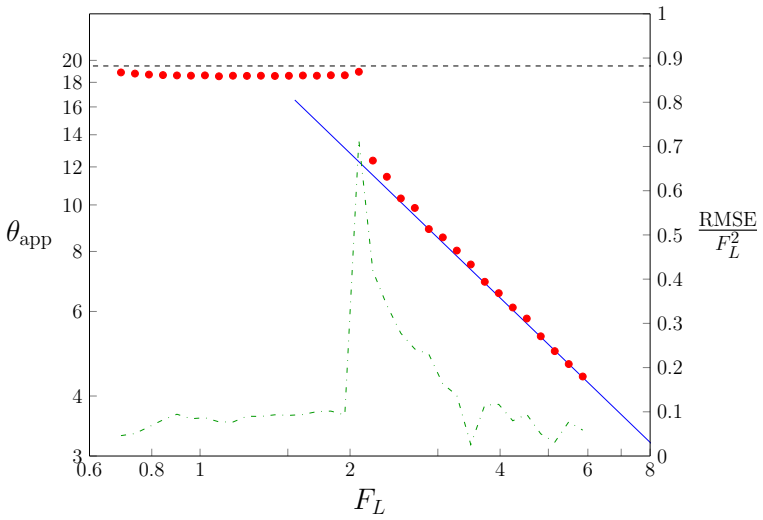

(b) Doublet

Figure 4.2: Measured apparent wake angles θ_{app} in degrees (solid circles) plotted against the Froude number for the linear solution (4.9) and (4.13) for flow past (a) a source and (b) a doublet, respectively, presented on a log-log scale. The dashed line is Kelvin's angle $\arcsin(1/3) \approx 19.47°$. The solid (blue) line is the theoretical asymptote shown in (a) equation (4.17) or (b) equation (4.18), valid for large Froude numbers. The (green) dot-dashed curve represents the root mean squared error of the line of best fit, scaled by F_L^2.

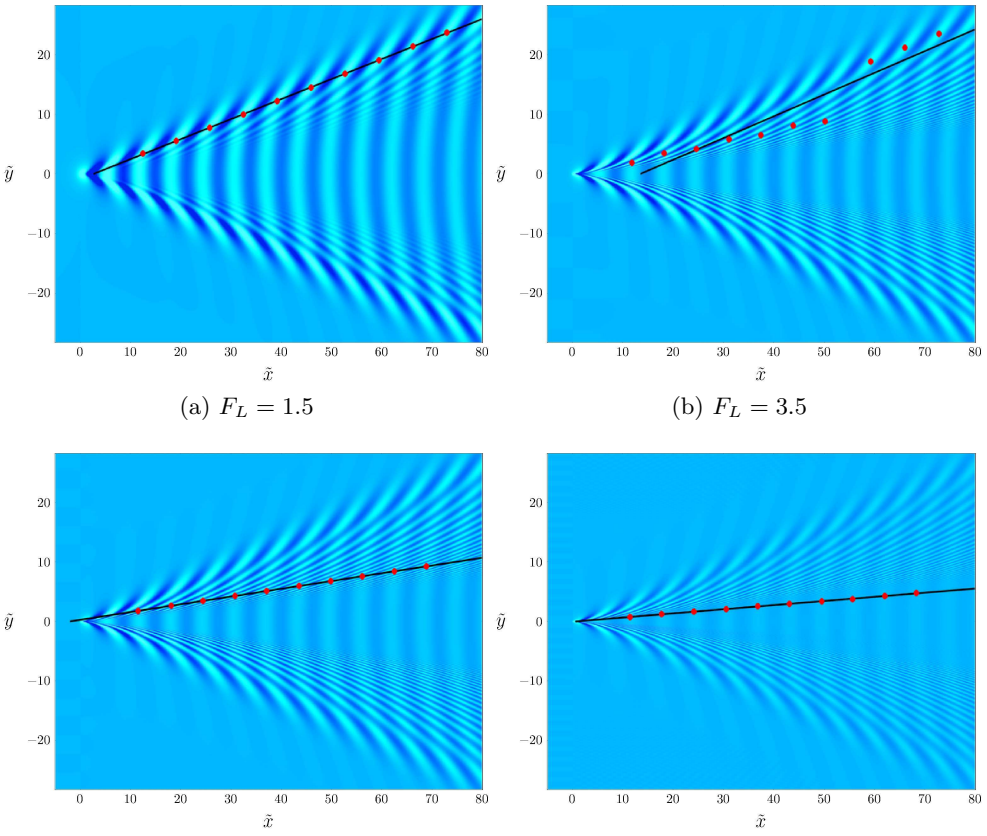

(a) $F_L = 1.5$ (b) $F_L = 3.5$

(c) $F_L = 4.5$ (d) $F_L = 8.5$

Figure 4.3: Plan view of the surface elevation in the linear case, computed for four different Froude numbers. The (red) solid circles are the highest peaks and the solid (black) line is the line of best fit, as described in Section 4.3. The surfaces are plotted on the scaled domain $\tilde{x} = x/F_L^2$ and $\tilde{y} = y/F_L^2$, for ease of comparison.

small Froude number limit are based on the theory of exponential asymptotics outlined in Chapman and Vanden-Broeck (2006) (and developed further by Trinh, Chapman, and Vanden-Broeck 2011; Lustri, McCue, and Binder 2012, for example).

4.4.2 Measured wake angle for flow past a doublet

The relationship between measured apparent wake and the Froude number for flow past a doublet is shown in Figure 4.2(b). The plot exhibits the same trends as for flow past a source; the only differences are the intervals for which the regimes are defined. Regime II now appears to hold for values of the Froude number roughly $0.7 < F_L < 2$ and Regime III for values $F_L > 2.7$. The transition between these two regimes still appears, but it is not as obvious from Figure 4.2(b). While not shown, Regime I occurs for roughly $F_L < 0.5$.

4.4.3 Large Froude number approximation

In the exact solution (4.9) to the linearised problem of flow past a source, the second integral dominates the first far downstream. As such, we can perform a stationary phase approximation on the second integral to provide an analytical approximation to the wave pattern. Thus for large $r = \sqrt{x^2 + y^2}$ we obtain the far field approximation in polar coordinates:

$$\zeta(r,\theta) \sim a_1(r,\theta)\cos\left(rg(\lambda_1(\theta),\theta) + \frac{\pi}{4}\right) + a_2(r,\theta)\cos\left(rg(\lambda_2(\theta),\theta) - \frac{\pi}{4}\right)$$

as $r \to \infty$ for $|\theta| < \arcsin(1/3)$, where

$$\lambda_1(\theta) = \frac{-1+\sqrt{1-8\tan^2\theta}}{4\tan\theta}, \qquad \lambda_2(\theta) = \frac{-1-\sqrt{1-8\tan^2\theta}}{4\tan\theta}, \tag{4.14}$$

$$f(\lambda) = \frac{\sqrt{\lambda^2+1}}{F_L^2}\mathrm{e}^{-\frac{\lambda^2+1}{F_L^2}}, \qquad g(\lambda,\theta) = \frac{\sqrt{\lambda^2+1}}{F_L^2}(\cos\theta + \lambda\sin\theta), \tag{4.15}$$

$$a_1(r,\theta) = \sqrt{\frac{2}{\pi}}\frac{\epsilon f(\lambda_1(\theta))}{\sqrt{r|g_{\lambda\lambda}(\lambda_1(\theta),\theta)|}}, \qquad a_2(r,\theta) = \sqrt{\frac{2}{\pi}}\frac{\epsilon f(\lambda_2(\theta))}{\sqrt{r|g_{\lambda\lambda}(\lambda_2(\theta),\theta)|}}, \tag{4.16}$$

and $g_{\lambda\lambda}(\lambda,\theta)$ is the second partial derivative of $g(\lambda,\theta)$ with respect to λ. Here a_1 and a_2 are the function envelopes of the transverse and divergent waves, respectively.

As the Froude number increases, the divergent waves dominate the wake pattern, thus for large Froude numbers we need only consider the divergent wave (a_2) when calculating the apparent wake angle. Following Darmon, Benzaquen, and Raphaël (2014), we apply a small θ approximation to (4.14)–(4.16) to give

$$a_2(r,\theta) \sim \frac{\epsilon}{2F_L\sqrt{\pi r}}\left(\theta^{-3/2} + \frac{7}{4}\theta^{1/2} + \dots\right)\mathrm{e}^{(\theta^{-2}+2/3+\dots)/4F_L^2}$$

for $\theta \ll 1$. Differentiating with respect to θ and setting the result to zero, we find the maximum of a_2 satisfies $1 + (7/4 - 3F_L^2)\theta^2 + \dots = 0$, which leads to the leading order expression

$$\theta_{\text{app}} \sim \frac{1}{\sqrt{3}F_L} \quad \text{as } F_L \to \infty. \tag{4.17}$$

This result is plotted in Figure 4.2(a). We see that the data for θ_{app} agrees very well with this approximation in Regime III.

Similarly, a far field approximation and subsequent analysis of the divergent wave can be made for flow past a doublet using equation (4.13). This gives the apparent wake angle for the doublet

$$\theta_{\text{app}} \sim \frac{1}{\sqrt{5}F_L} \quad \text{as } F_L \to \infty. \tag{4.18}$$

Again, we have included the asymptotic result in Figure 4.2(b) and the agreement with the data in Regime III is very good. This scaling $\theta_{\text{app}} = O(F_L^{-1})$ as $F_L \to \infty$ for flow

past submerged bodies is the same as that found for flows past pressure distributions on the surface (Benzaquen, Darmon, and Raphaël 2014; Darmon, Benzaquen, and Raphaël 2014; Ellingsen 2014; Moisy and Rabaud 2014b).

4.5 Nonlinear ship waves

The fully nonlinear problems for flow past a source (4.1)–(4.3), (4.6)–(4.8) and flow past a doublet (4.1)–(4.3), (4.7)–(4.8), (4.12) do not have known exact solutions, and must be solved numerically. The approach used here is based on a boundary integral method developed by Forbes (1989) and Părău and Vanden-Broeck (2002) which involves setting $\Phi(x,y) = \phi(x,y,\zeta(x,y))$ and formulating the integral equation

$$\begin{aligned} 2\pi(\Phi(x,y)-x) = S(x,y) &+ \int_0^\infty \int_{-\infty}^\infty (\Phi(x^*,y^*) - \Phi(x,y) - x^* + x) K_1(x^*,y^*;x,y)\, \mathrm{d}x^*\, \mathrm{d}y^* \\ &+ \int_0^\infty \int_{-\infty}^\infty \zeta_x(x^*,y^*) K_2(x^*,y^*;x,y)\, \mathrm{d}x^*\, \mathrm{d}y^*, \end{aligned} \tag{4.19}$$

where K_1 and K_2 are the kernel functions

$$\begin{aligned} K_1(x^*,y^*;x,y) =& \frac{\zeta(x^*,y^*) - \zeta(x,y) - (x^*-x)\zeta_x(x^*,y^*) - (y^*-y)\zeta_y(x^*,y^*)}{\Big((x^*-x)^2 + (y^*-y)^2 + \big(\zeta(x^*,y^*) - \zeta(x,y)\big)^2\Big)^{\frac{3}{2}}} \\ &+ \frac{\zeta(x^*,y^*) - \zeta(x,y) - (x^*-x)\zeta_x(x^*,y^*) - (y^*+y)\zeta_y(x^*,y^*)}{\Big((x^*-x)^2 + (y^*-y)^2 + \big(\zeta(x^*,y^*) - \zeta(x,y)\big)^2\Big)^{\frac{3}{2}}}, \\ K_2(x^*,y^*;x,y) =& \frac{1}{\sqrt{(x^*-x)^2 + (y^*-y)^2 + \big(\zeta(x^*,y^*) - \zeta(x,y)\big)^2}} \\ &+ \frac{1}{\sqrt{(x^*-x)^2 + (y^*+y)^2 + \big(\zeta(x^*,y^*) - \zeta(x,y)\big)^2}}, \end{aligned}$$

and the singular term is given by

$$S(x,y) = \begin{cases} -\dfrac{\epsilon}{(x^2+y^2+(\zeta(x,y)+1)^2)^{\frac{1}{2}}}, & \text{flow past source} \\[2ex] \dfrac{\mu x}{(x^2+y^2+(\zeta(x,y)+1)^2)^{\frac{3}{2}}}, & \text{flow past doublet.} \end{cases}$$

We truncate the domain in the (x,y)-plane and discretise using a rectangular grid. Then, by enforcing Bernoulli's equation (4.3) and the integral equation (4.19) at each of the half-mesh points, we derive a large system of nonlinear algebraic equations (see also Forbes and Hocking 2005; Părău, Vanden-Broeck, and Cooker 2007a, and the

references therein for commentary on this approach). By applying a Jacobian-free Newton-Krylov method to this system, we have been able to significantly refine the mesh used when compared to standard contemporary approaches (see Pethiyagoda et al. 2014, Ch. 3). While full details are included in that paper, we note that a typical mesh employed here was made up of 721 grid points in the x-direction, and 241 in the y-direction. Solutions computed on a workstation with a GPU[1] typically took 1-2 hours to converge.

Recall there are two parameters in each of our problems, one of which is the Froude number F_L. For flow past a source the other parameter is ϵ, while for flow past a doublet it is μ. Linear solutions are valid for $\epsilon \ll 1$ or $\mu \ll 1$, while for moderate and large values of ϵ or μ, the full nonlinear problem must be treated. As discussed in Section 4.2, fully nonlinear solutions to these problem no longer have an exact correspondence with their classical linear interpretations. For example, in Figure 4.4(a) we show some particle paths for a nonlinear solution for flow past a submerged source with source strength $\epsilon = 1.5$. These are computed using the boundary integral formulation, which allows the velocity potential ϕ to be evaluated at each point within the flow domain (using an equation that is very similar to (4.19), but has the 2π on the left-hand side replaced by 4π, and is evaluated within the flow field, not on the surface). Given a starting point and the velocity potential ϕ, it is straight forward to calculate the velocity via finite differences and then determine the particle paths using a modified version of the adaptive pathline-based particle tracking algorithm detailed in Bensabat, Zhou, and Bear (2000). In Figure 4.4(a), a number of starting points is chosen to be very close to the stagnation point within the flow field. The resulting family of particle paths provide an approximate picture of a submerged body over which there is a no-flux condition, meaning that for these parameters, the problem of flow past a point source is equivalent to flow past this submerged semi-infinite body. It is only in the linear limit $\epsilon \ll 1$ that this surface becomes an exact semi-infinite Rankine body with radius $\sqrt{\epsilon/\pi}$.

Similarly, figures 4.4(b) and (c) show particle paths for flow past a submerged doublet of strength $\mu = 0.02$ and 0.88, respectively. Again, in each case a collection of starting points is chosen very close to the upstream stagnation point in the fluid (for this problem there are two stagnation points within the flow domain). Unlike for the linear solution valid for $\mu \ll 1$ (for which the solutions are equivalent to flow past a submerged sphere of radius $(\mu/2\pi)^{1/3}$), these particle paths do not follow the surface of a closed body. A complementary picture is provided by figures 4.4(d) and (e), which show particle paths in the (x, z)-plane. In this case we show only particle paths that intersect the two

[1] 2x Intel Xeon E5-2670 CPUs with 2.66 GHz processor, M2090 Nvidia Tesla GPU and 128GB of system memory.

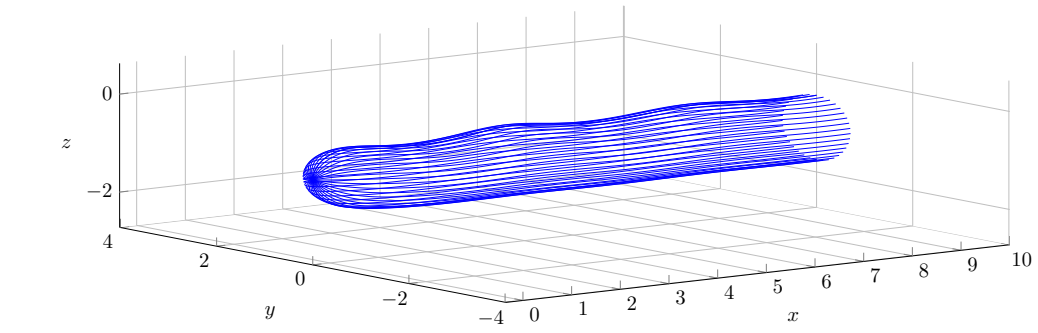

(a) Source, $\epsilon = 1.5$

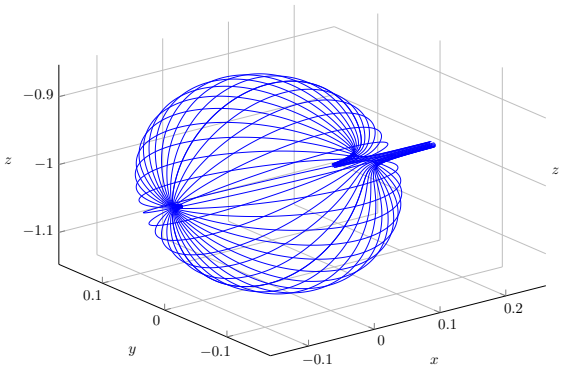

(b) Doublet, $\mu = 0.02$

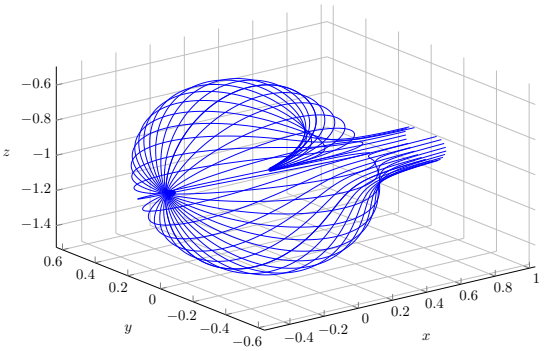

(c) Doublet, $\mu = 0.88$

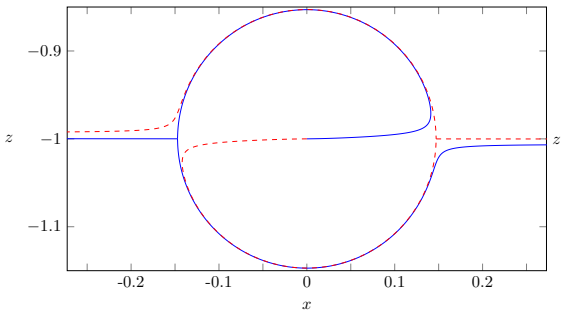

(d) Doublet, $\mu = 0.02$

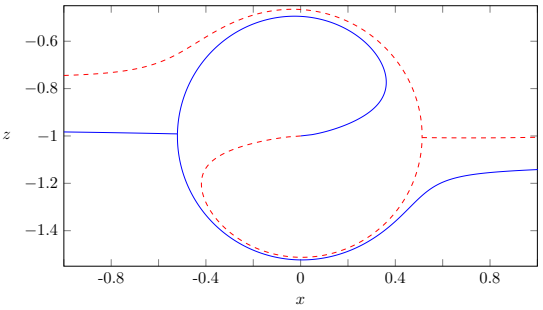

(e) Doublet, $\mu = 0.88$

Figure 4.4: Particle paths for flow past a source with (a) $\epsilon = 1.5$ and flow past a doublet with (b), (d) $\mu = 0.02$ and (c),(e) $\mu = 0.88$. In plots (a)–(c), the particle paths are represented by solid (blue) lines. The particle paths in (d) and (e) lie in the (x, z)-plane, with the (blue) solid lines passing through the upstream stagnation point and the (red) dashed lines passing through the downstream stagnation point. Each nonlinear solution computed for $F_L = 0.8$.

stagnation points. None of these curves in this centre-plane join the two stagnation points, again demonstrating the flow field is not identical to that due to a closed submerged body (see Tuck 1965, for a discussion on the two-dimensional analogue).

It is worth clarifying here that, for a fixed Froude number F_L, there is an upper

limit on the parameters ϵ and μ, which we label ϵ_c and μ_c, respectively. For strongly nonlinear flows, the maximum peak height $\zeta_{\max}$ will increase, until $\zeta_{\max} \to F_L^2/2$ as either $\epsilon \to \epsilon_c$ (flow past a source) or $\mu \to \mu_c$ (flow past a doublet). The solution for either $\epsilon = \epsilon_c$ or $\mu = \mu_c$ will involve some kind of complicated limiting surface configuration, which will include a stagnation point at the highest peak, and possibly even a discontinuous first derivative there (the dynamic condition (4.3) excludes the possibility of solutions that have $\zeta_{\max} > F_L^2/2$, as the square of the velocity can never be negative). The two-dimensional analogue is well-studied, with the Stokes limiting configuration characterised by a 120° angle at the wave crest; in that case, highly accurate calculations of near-limiting waves are made possible because one is able to treat a single wavelength with periodic boundary conditions (Schwartz 1974; Cokelet 1977; Williams 1981; Lukomsky, Gandzha, and Lukomsky 2002; Dallaston and McCue 2010). On the other hand, the limiting configuration for a given fully three-dimensional flow problem is still relatively unexplored. We do not pursue this phenomenon here.

Returning to the issue of wake angle, we have found (in almost all circumstances) that by fixing the Froude number F_L and increasing the nonlinearity ϵ or μ (which is equivalent to increasing the size of the submerged obstacle), the apparent wake angle increases. For example, we show in Figure 4.5 four free-surface patterns for flow past a source, all computed for $F_L = 4.5$, where this trend is evident. Further, this figure suggests the qualitative features of the wave pattern change dramatically as ϵ is varied. These differences appear even more pronounced when viewed from an angle, as in Figure 4.6. We return to these figures shortly.

To demonstrate the effects of nonlinearity on apparent wake angle θ_{app}, we present in Figure 4.7 plots of θ_{app} versus (a) ϵ for flow past a source, and (b) μ for flow past a doublet for the four Froude numbers $F_L = 0.9$, 1.4, 2.5 and 4.5. Focusing for the moment on flow past a source (Figure 4.7(a)), we notice that for $F_L = 0.9$, 1.4 and 2.5, the linear wave patterns ($\epsilon \ll 1$) fall into Regime II, with the maximum peaks lying on the outermost divergent waves and apparent wake angles which are slightly less than the Kelvin angle. In all three cases, by increasing the measure of nonlinearity, ϵ, we see a smooth increase in apparent wake angle, so that eventually it becomes greater than the Kelvin angle. As the nonlinearity continues to increase, the solutions approach a complicated limiting configuration, as discussed above. There are no mathematical solutions beyond this point.

Interestingly, the relationship between apparent wake angle and nonlinearity for the third case, $F_L = 4.5$, is different to that just described for $F_L = 0.9$, 1.4 and 2.5. For $F_L = 4.5$, the linear wave pattern ($\epsilon \ll 1$) falls into Regime III, and the nonlinear solutions for roughly $0 < \epsilon < 26$ also remain in this regime. Here the apparent wake angle is much less than the Kelvin angle, as we can see by referring back to figures 4.5(a),(b),

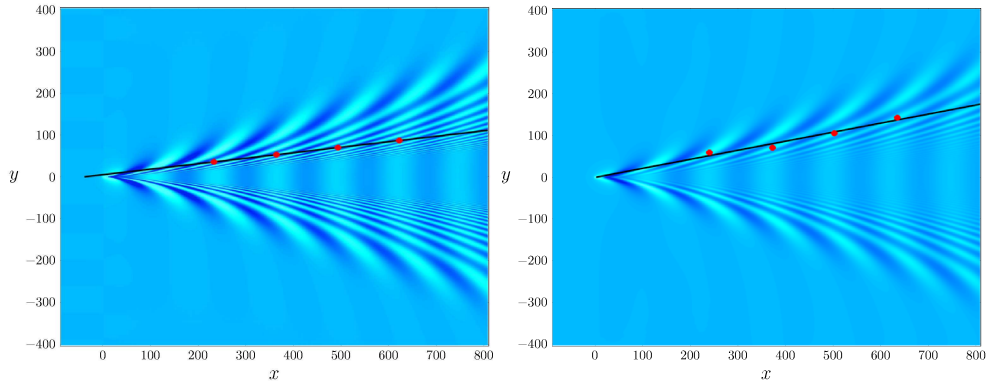

(a) Linear (b) $\epsilon = 12$

(c) $\epsilon = 55$ (d) $\epsilon = 106$

Figure 4.5: Plan view of surface elevation for the problem of flow past a source with $F_L = 4.5$: (a) the linear solution $\epsilon \ll 1$; the nonlinear solution with (b) $\epsilon = 12$, (c) $\epsilon = 55$ and (d) $\epsilon = 106$. The (red) solid circles represent the highest peak. The (black) solid line is the line of best fit, as described in section 4.3.

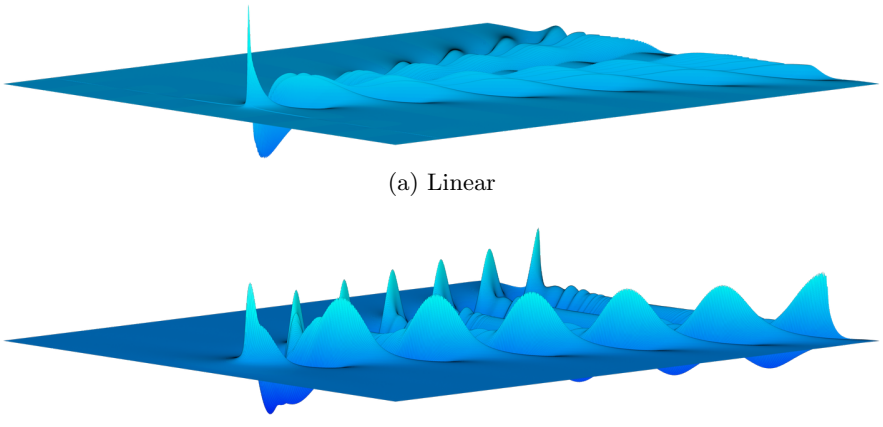

(a) Linear

(b) $\epsilon = 106$

Figure 4.6: Free-surface profiles for flow past a source with $F_L = 4.5$: (a) linear ($\epsilon \ll 1$) and (b) highly nonlinear ($\epsilon = 106$). The z direction has been scaled for comparison. A plan view of these surfaces is given in Figure 4.5(a) and 4.5(d).

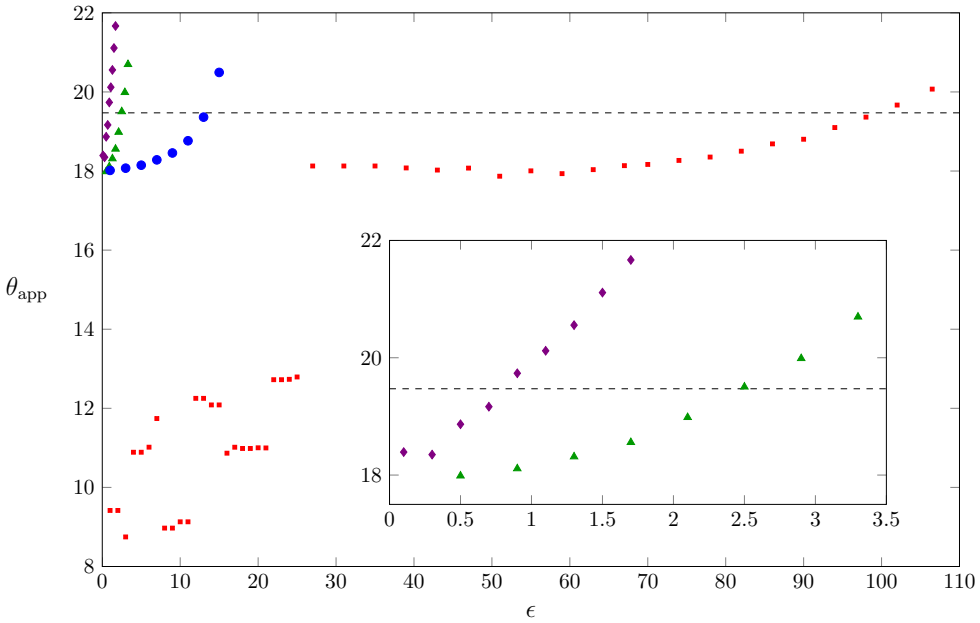

(a) Source

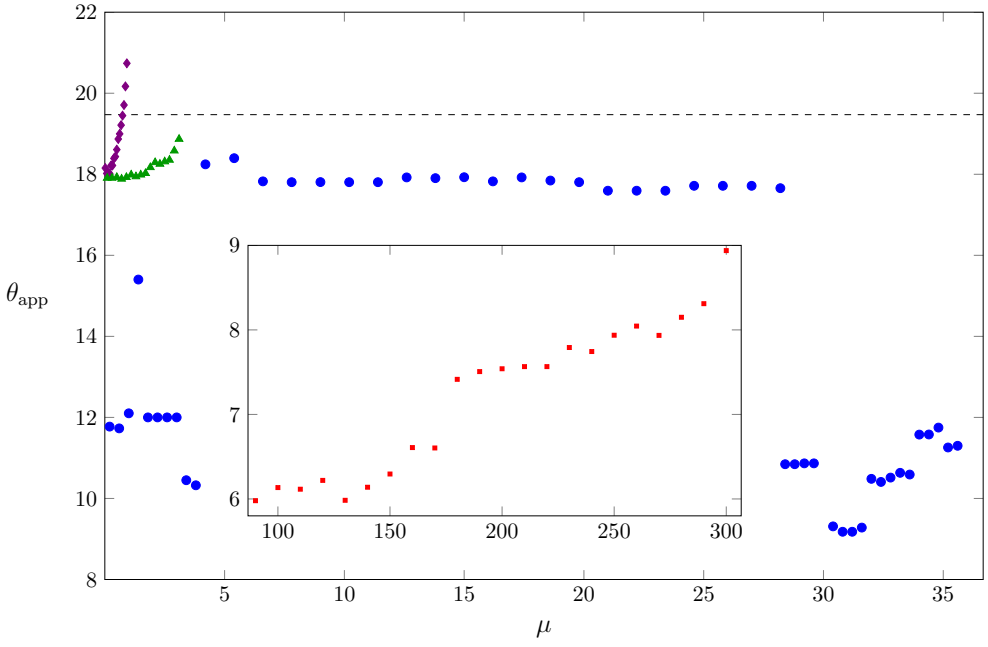

(b) Doublet

Figure 4.7: A plot of apparent wake angle θ_{app} (in degrees) against (a) ϵ for flow past a source, and (b) μ for flow past a doublet with $F_L = 0.9$ (violet diamonds), $F_L = 1.4$ (green triangles), $F_L = 2.5$ (blue circles) and $F_L = 4.5$ (red squares). The dashed line is Kelvin's angle, $\arcsin(1/3) \approx 19.47°$. The insets provide (a) a close-up view of the results for $F_L = 0.9$ and 1.4, and (b) the results for $F_L = 4.5$.

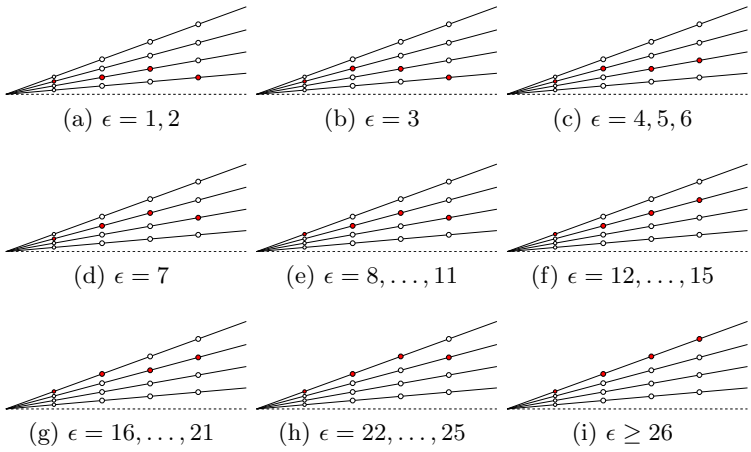

Figure 4.8: A schematic diagram indicating peaks within a given wavelength for flow past a source with $F_L = 4.5$. The solid circles correspond to the highest peak of a given wavelength, while the open circles represent other peaks.

where the peaks are clearly not sitting on the outermost divergent waves. On the other hand, at about $\epsilon = 26$ the pattern changes over to Regime II, and from that point the apparent wake angle increases smoothly with ϵ until the limiting configuration is reached. See figures 4.5(c),(d). The dominant features of the free-surface profiles for linear and highly nonlinear solutions are illustrated in Figure 4.6 for $F_L = 4.5$. In part (a), which is the linear solution, the set of highest diverging waves are found well within the Kelvin wedge. On the other hand, in Figure 4.6(b) we see a highly nonlinear solution for which the outermost diverging waves are shaped like dorsal fins; their amplitude is clearly much larger than the waves closer to the centreline.

Returning to Figure 4.7(a), the trend that the apparent wake angle θ_{app} follows for $F_L = 4.5$ and $\epsilon < 26$ is hard to discern, as the data appears scattered. To explain these results we have included in Figure 4.8 a schematic diagram of which peak in a given wavelength is the highest for a given ϵ and $F_L = 4.5$. We see that all of these solutions fall into Regime III, and as ϵ increases the highest peak within a given wavelength is located further from the centreline. While this new location of the highest peak may increase or decrease the apparent wake angle at each of these increments in ϵ, there is a definite trend of an increasing wake angle, resulting in the wave pattern transitioning from Regime III to Regime II at roughly $\epsilon = 26$.

Moving on to apparent wake angle for flow past a doublet, described by Figure 4.7(b), we see that for moderate Froude numbers the qualitative behaviour is similar to that for flow past a source, while there are some different behaviour for large Froude numbers. For example, the data for $F_L = 0.9$ and 1.4 exhibits the same trends as for flow past a source; that is, the apparent wake angle increases with nonlinearity until the limiting

configuration is reached (when maximum peak height $\zeta_{\max}$ reaches the elevation $F_L^2/2$). For $F_L = 2.5$, the linear solution ($\mu \ll 1$) is in Regime III, and (much like the results for flow past a source with $F_L = 4.5$), the wave patterns transition to Regime II. However, once in Regime II the wake angle no longer increases and instead is roughly constant for $6 < \mu < 28$. For $\mu > 28$ the apparent wake angle transitions back into Regime III and remains there until the limiting solution is met. This example is the only case we show where the apparent wake angle does not appear to increase with nonlinearity. Finally, while the apparent wake angles for $F_L = 4.5$ tend to slightly increase with the measure of nonlinearity, μ, the solutions remain in Regime III and do not transition to Regime II.

To close this section we present in Figure 4.9 two plots that aim to mimic Figure 4.2, except that this time the data is from fully nonlinear calculations with ϵ and μ finite. We have chosen to fix $\epsilon = 1.5$ for Figure 4.9(a) (flow past a source) and $\mu = 0.7$ for Figure 4.9(b) (flow past a doublet). In both cases we observe that the general trends are the same as the linear counterparts. For example, for moderate Froude numbers, the solutions fit in to Regime II, with the apparent wake angle close to the Kelvin angle. For larger Froude numbers, we find the highest peaks no longer lie on the outermost divergent waves, and the wave patterns are therefore in Regime III. As with the linear solutions, the apparent wake angle for Regime III seems to scale as F_L^{-1}, although the data is a little more scattered. The difference is that the constant of proportionality is higher for the nonlinear solutions than the linear counterpart. To demonstrate this effect, we have included the asymptotic results (4.17) and (4.18) in these log-log plots (keeping in mind they are from linear theory), and note that the nonlinear data runs roughly parallel with these lines, but the match is no longer in close quantitative agreement.

4.6 Discussion

Despite the enormous attention the theoretical study of water waves has received since the 19th century (Darrigol 2003), there has been a resurgence of interest in ship wave patterns. In particular, the question of what angle encloses a ship wake, or at least what angle one sees in practice, has been the subject of very recent speculation following the insightful studies of Rabaud and Moisy (2013) and Darmon, Benzaquen, and Raphaël (2014). A noteworthy result of this research is that for fast-moving objects, the angle formed by the highest peaks is not independent of the object's speed, but in fact decreases like the inverse Froude number.

These studies all treat mathematical solutions to linear problems, which are valid in the limit that the disturbance to the flow vanishes. In the present paper we consider the

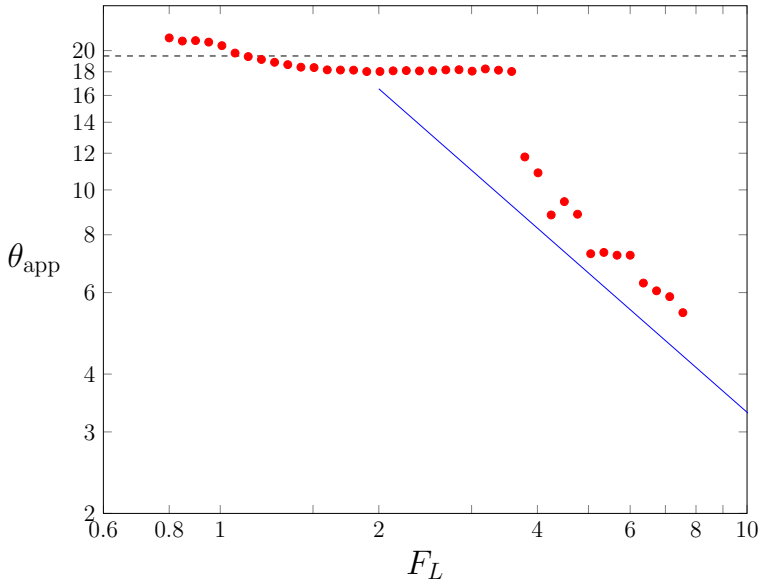

(a) Source

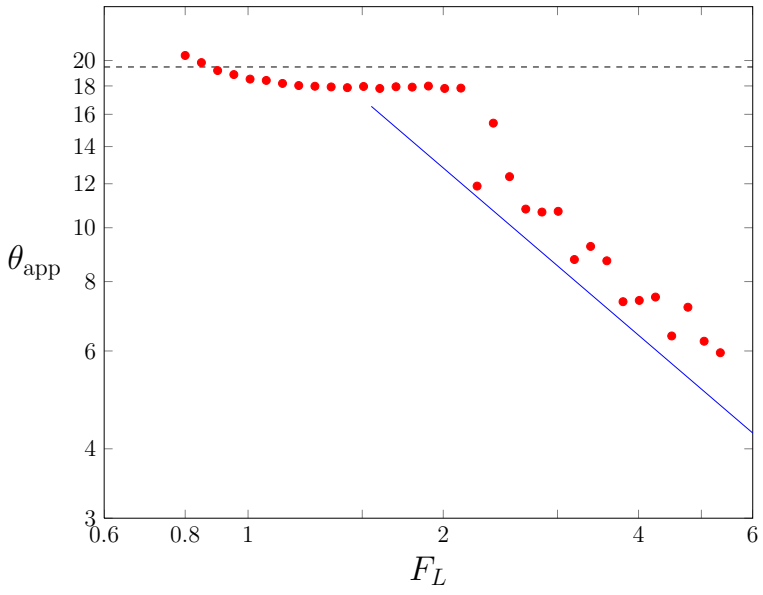

(b) Doublet

Figure 4.9: Measured apparent wake angles θ_{app} in degrees (solid circles) plotted against the Froude number for the for flow past (a) a source with $\epsilon = 1.5$ and (b) a doublet with $\mu = 0.7$, presented on a log-log scale. These data for nonlinear solutions are to be compared with Figure 4.2, which is for linear solutions. The dashed line is Kelvin's angle $\arcsin(1/3) \approx 19.47°$. The solid (blue) line is the theoretical asymptote shown in (a) equation (4.17) or (b) equation (4.18), valid in the linear case for large Froude numbers.

problems of free-surface flow past a submerged source and submerged doublet. For the linearised versions of both of these problems, we also observe the decrease in apparent wake angle for sufficiently high Froude numbers. We are able to explain our results by tracking the location of the highest peaks in a similar fashion to Moisy and Rabaud (2014b), and classifying the wave patterns into three distinct regimes. For the first problem we consider, flow past a submerged source, there is no inherent length scale in the direction of flow. Thus we eliminate the possibility of our results being influenced by interference between the disturbance's 'bow' or 'stern'.

We have found that nonlinear flows, for which the disturbance can no longer be considered small, provide additional interesting results. As the nonlinearity is increased in these problems, the apparent wake angle was found to also increase. For sufficiently fast-moving objects, there is a competition between object speed and nonlinearity, since the angle is tending to decrease with Froude number but increase with the strength of the disturbance. Finally, we have found that for many of our highly nonlinear solutions, the apparent wake angle is greater than the Kelvin angle, so that clearly both the object speed and strength of nonlinearity are required to obtain even a rough guess of the wake angle.

4.7 Computer code

The code used to calculate the apparent wake angles for flow past a doublet with $F_L = 0.9$ as seen in Figure 4.7(b) is provided at:
`https://github.com/rPethiyagoda/Pethiyagoda-PhD-thesis-code`.

5 Wake angle for surface gravity waves on a finite depth fluid

This chapter was first published as

R. Pethiyagoda, S. W. McCue, and T. J. Moroney (2015). Wake angle for surface gravity waves on a finite depth fluid. *Physics of Fluids* **27**, 061701

Abstract

Linear water wave theory suggests that wave patterns caused by a steadily moving disturbance are contained within a wedge whose half-angle depends on the depth-based Froude number F_H. For the problem of flow past an axisymmetric pressure distribution in a finite-depth channel, we report on the apparent angle of the wake, which is the angle of maximum peaks. For moderately deep channels, the dependence of the apparent wake angle on the Froude number is very different to the wedge angle, and varies smoothly as F_H passes through the critical value $F_H = 1$. For shallow water, the two angles tend to follow each other more closely, which leads to very large apparent wake angles for certain regimes.

5.1 Introduction

The linear dispersion relation for small amplitude water waves gives rise to intricate and distinctive surface wave patterns that have been the subject of enduring interest to applied mathematicians and physicists since the 19th century (Craik 2004). When these patterns form at the wake of a steadily moving object, they are often referred to as ship wave patterns or ship wakes, regardless of whether or not the object is an actual ship. Relatively simple geometric arguments (Lighthill 1978) show that ship wave patterns propagate within a travelling wedge; for an infinitely deep fluid, this

wedge has a half-angle of $\theta_{\text{wedge}} = \arcsin(1/3) \approx 19.47^\circ$ (referred to here as the Kelvin angle) regardless of the speed of the disturbance (Thomson 1887).

For a fluid of finite depth, the derivation of the wedge angle is more complicated (Havelock 1908), and turns out to depend on the speed of the disturbance U, which itself is measured by the depth-based Froude number $F_H = U/\sqrt{gH}$. Here H is the depth of the fluid and g is acceleration due to gravity. Of particular interest here, the wedge angle has the following properties: $\theta_{\text{wedge}} \to \arcsin(1/3)^+$ as $F_H \to 0^+$; $\theta_{\text{wedge}} \to \pi/2^-$ as $F_H \to 1^-$; $\theta_{\text{wedge}} \to \pi/2^-$ as $F_H \to 1^+$; $\theta_{\text{wedge}} \sim F_H^{-1}$ as $F_H \to \infty$. We note that for $F_H < 1$, the flow is referred to as being subcritical. Subcritical flows are characterised by two types of waves, transverse and divergent. Transverse waves run roughly perpendicular to the direction the disturbance is travelling. Divergent waves propagate at an acute angle to this direction. For supercritical flows, $F_H > 1$, the wave pattern is entirely made up of divergent waves.

There has been a resurgence of interest in ship wave patterns (Torsvik et al. 2015b), with a particular focus on the wake angle that is actually observed in practice (Dias 2014). Here we pay attention to what we call the apparent wake angle, θ_{app}, which is the angle between the line passing through the highest peaks of the wave and the centreline. For axially symmetric pressure distributions acting on the free surface of an infinitely deep fluid, numerical simulations show that the apparent wake angle is slightly less than the Kelvin angle $\arcsin(1/3)$ for moderately fast disturbances; however, for sufficiently fast-moving disturbances, the apparent wake angle appears to decrease like the inverse of the length-based Froude number, $F_L = U/\sqrt{gL}$, where L is a length-scale associated with the pressure distribution (Rabaud and Moisy 2013; Darmon, Benzaquen, and Raphaël 2014) (see also Barnell and Noblesse 1986; Carusotto and Rousseaux 2013). Further recent studies have been undertaken on the effect of non-axisymmetric pressure distributions (Benzaquen, Darmon, and Raphaël 2014; Moisy and Rabaud 2014b; Noblesse et al. 2014; Rabaud and Moisy 2014), a continuous distribution of sources (Zhang et al. 2015), constant vorticity (Ellingsen 2014), nonlinearity (Pethiyagoda et al. 2014, Ch. 3; Pethiyagoda, McCue, and Moroney 2014, Ch. 4) and surface tension (Moisy and Rabaud 2014a). A comparison of the results in Rabaud and Moisy (2013), Darmon, Benzaquen, and Raphaël (2014), and Noblesse et al. (2014) is given by He et al. (2014). All of these studies are for an infinite-depth fluid.

By considering the problem of flow past an axially symmetric pressure distribution in a fluid of *finite* depth, we shed light on the seemingly contradictory results for the wedge angle and recently reported apparent wake angle. As noted above, the wedge angle θ_{wedge} increases from $\arcsin(1/3)$ to $\pi/2$ as F_H increases to $F_H = 1$, and then monotonically decreases for $F_H > 1$. However, for a moderately deep fluid, we find

the dependence of the apparent angle θ_{app} on F_H is very different, and in fact behaves much like the infinite depth case. This is remarkable because the transition between subcritical ($F_H < 1$) and supercritical ($F_H > 1$) flows is characterised by distinct changes in qualitative behaviour in the wave pattern and the singularity structure of the dispersion relationship, while the apparent wake angle θ_{app} changes smoothly as F_H increases through $F_H = 1$. On the other hand, for shallow water, the apparent angle θ_{app} follows the wedge angle θ_{wedge} closely, giving rise to very large apparent wake angles for moderately small length-based Froude numbers, F_L.

5.2 Mathematical formulation

In the following, we consider an axisymmetric pressure distribution of strength P_0 and intrinsic length L acting on the surface of a fluid flowing in the positive x direction with speed U. We will present solutions for a fluid of infinite depth and a finite depth H. To enable a direct comparison with recent work (Rabaud and Moisy 2013; Darmon, Benzaquen, and Raphaël 2014), our dimensional pressure distribution is $p(x, y) = P_0 \exp(-\pi^2(x^2 + y^2)/L^2)$. For the infinite depth problem we choose to scale speeds by U and lengths by L. This leads to two nondimensional parameters, $\epsilon_L = P_0/(\rho g L)$, a measure of pressure strength (where ρ is the fluid density), and the length-based Froude number, F_L. Using linear theory, an exact solution for the free-surface $\zeta(x, y)$ in the infinite depth case is (Wehausen and Laitone 1960):

$$\begin{aligned}\zeta(x,y) = &-\epsilon_L p(x,y) + \frac{\epsilon_L}{2\pi^2} \int_{-\pi/2}^{\pi/2} \int_0^\infty \frac{k^2 \tilde{p}(k,\psi) \cos(k[|x|\cos\psi + y\sin\psi])}{k - k_0} \, \mathrm{d}k \, \mathrm{d}\psi \\ &- \frac{\epsilon_L H(x)}{\pi} \int_{-\pi/2}^{\pi/2} k_0^2 \tilde{p}(k_0,\psi) \sin(k_0[x\cos\psi + y\sin\psi]) \, \mathrm{d}\psi, \end{aligned} \tag{5.1}$$

where $\tilde{p}(k, \psi) = \delta^2 \exp(-\delta^2 k^2/(4\pi^2))/\pi$ is the Fourier transform of our pressure distribution and $H(x)$ is the Heaviside function. The path of k-integration is diverted below the pole $k = k_0$, where $k_0 = 1/(F_L^2 \cos^2\psi)$.

For the finite depth problem we instead use H as the length scale, which leads to three nondimensional parameters: the pressure strength $\epsilon_H = P_0/(\rho g H)$, the depth-based Froude number F_H, and the ratio of pressure length scale to fluid depth $\delta = L/H$. The nondimensional parameters for the finite and infinite depth problems are related by $F_L = F_H/\sqrt{\delta}$ and $\epsilon_L = \epsilon_H/\delta$. The exact solution for the finite-depth problem

is (Wehausen and Laitone 1960)

$$\zeta(x,y) = -\epsilon_H p(x,y) + \frac{\epsilon_H F_H^2}{2\pi^2} \int_{-\pi/2}^{\pi/2} \int_0^\infty \frac{k^2 \tilde{p}(k,\psi)\cos(k[|x|\cos\psi + y\sin\psi])}{kF_H^2 - \sec^2\psi\tanh k}\,\mathrm{d}k\,\mathrm{d}\psi$$

$$- \frac{2\epsilon_H F_H^2 H(x)}{\pi} \int_{\psi_0}^{\pi/2} \frac{k_1^2 \tilde{p}(k_1,\psi)\sin(k_1 x\cos\psi)\cos(k_1 y\sin\psi)}{F_H^2 - \sec^2\psi\,\mathrm{sech}^2 k_1}\,\mathrm{d}\psi, \tag{5.2}$$

where $\psi_0 = 0$ for $F_H < 1$ and $\psi_0 = \arccos(1/F_H)$ for $F_H > 1$. As with the infinite depth solution (5.1) the path of k-integration is diverted below the pole, which this time is denoted by $k = k_1(\psi)$, where k_1 is the real positive root of

$$kF_H^2 - \sec^2\psi\tanh k = 0, \qquad \psi_0 < \psi < \frac{\pi}{2}. \tag{5.3}$$

In both the infinite-depth (5.1) and finite-depth (5.2) solutions, the double integral rapidly tends to zero far away from the pressure distribution. Therefore, to analyse the wake in the far field, only the single integral term is required.

5.3 The measured apparent wake angle

To measure the apparent wake angle, θ_{app}, we need to locate the line that passes through the highest peaks of the wave, and then calculate the angle between that line and the centreline $y = 0$. The method for locating the highest peaks depends on the flow regime. For subcritical flows (and the infinite depth case), we isolate each transverse wave, mark the highest point, and fit a line through the highest points of all the wavelengths (we call this method 1, used previously in Darmon, Benzaquen, and Raphaël (2014) and Pethiyagoda, McCue, and Moroney (2014) [Ch. 4], for example). For supercritical flows, there are no transverse waves, so we instead use the highest points on each of the divergent waves to fit the line (method 2).

In Figure 5.1 we present data for apparent wake angle against both Froude numbers F_L and F_H for a variety of dimensionless pressure length scales δ. These data are represented by the (red) solid dots. As just mentioned, the data for the infinite depth case and for the subcritical flows $F_H < 1$ are calculated with method 1, while data for supercritical flows $F_H > 1$ are calculated with method 2. We see in Figure 5.1(b)–(d) that for moderately deep channels, the qualitative behaviour is very similar to the infinite depth case in Figure 5.1(a) considered previously (Darmon, Benzaquen, and Raphaël 2014); that is, the apparent wake angle θ_{app} is approximately $\arcsin(1/3)$ for F_L less than some value (roughly $F_L = 1$ or slightly less), then decreases like F_L^{-1} for large values of F_L. Also plotted in each panel of Figure 5.1 is θ_{wedge} (a dashed line).

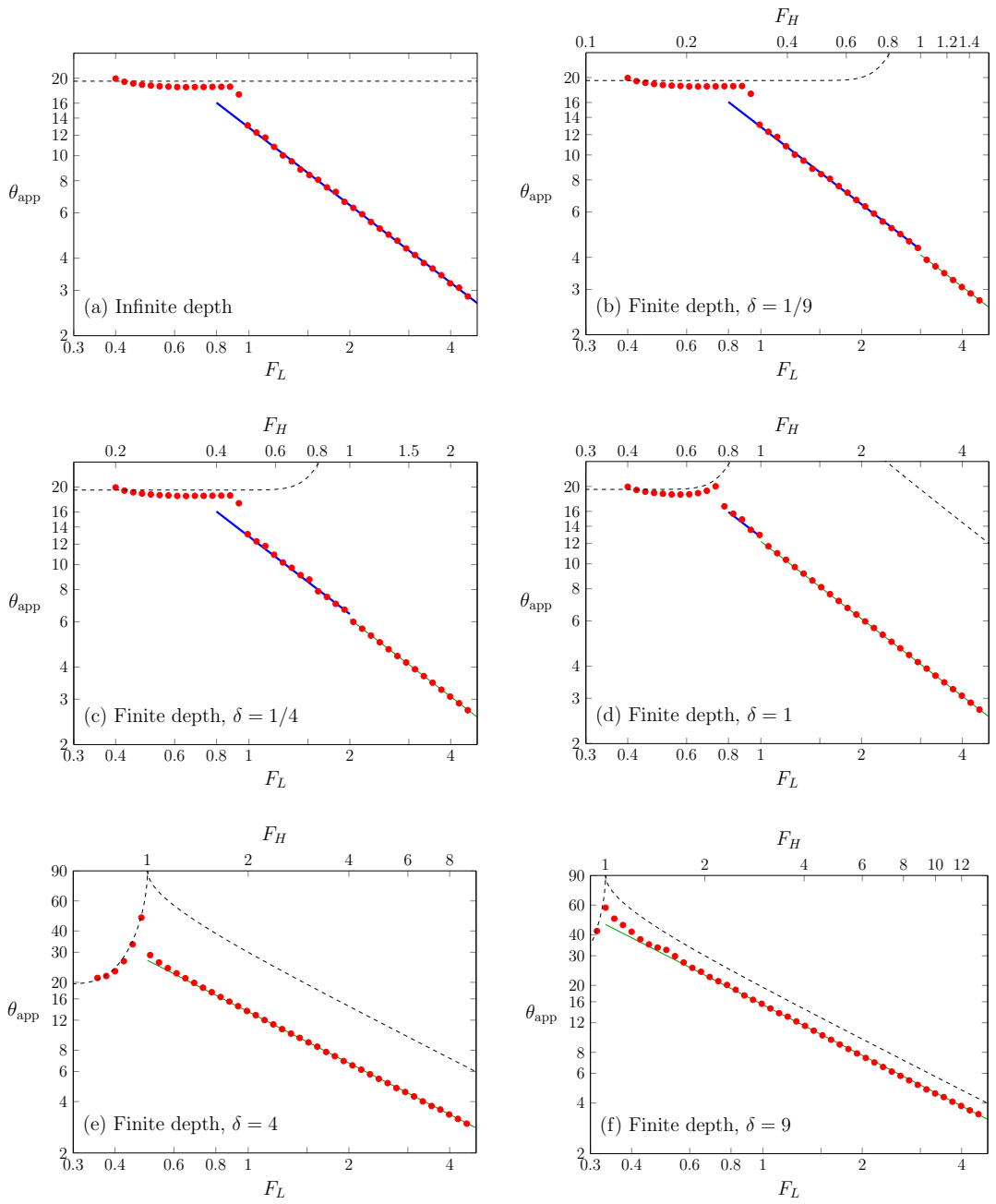

Figure 5.1: Measured apparent wake angles θ_{app} in degrees (solid circles) plotted against the Froude number for the linear solutions (5.1) and (5.2) for a fluid of (a) infinite depth and (b)–(f) finite depth, presented on a log-log scale. The dashed line is (a) the Kelvin angle $\arcsin(1/3) \approx 19.47°$ and (b)–(f) the wedge angle θ_{wedge} in the finite-depth case. The thick (blue) line is the theoretical asymptote (5.6) given by method 1 (valid for subcritical flows) and the thin (green) line is asymptote given by method 2 (required for supercritical flows).

It is interesting to see that for deep to moderately deep channels, the apparent wake angle θ_{app} does not follow θ_{wedge}.

It is insightful to observe the wave patterns themselves in Figure 5.2, especially as the flow transitions from subcritical $F_H < 1$ to supercritical $F_H > 1$. For sufficiently deep channels (δ sufficiently small), the transition has almost no effect on θ_{app} (also refer back to Figure 5.1(b)–(d), where the slight kink in the data for θ_{app} at $F_H = 1$ is due to the change in method of measuring the angle). In Figure 5.2(a)–(b), we present wave patterns for a typical small value (taken to be $\delta = 1/4$), computed for F_H slightly less than and slightly greater than the critical value $F_H = 1$. The corresponding plan view and centreline plots are shown in panels (e)–(f). In the plan view, the highest peaks are represented by open circles, while the angle θ_{wedge} is represented by the dashed lines. These surface profiles help to show how, for sufficiently deep channels, the apparent wake angle θ_{app} varies smoothly through $F_H = 1$ and is not at all close to θ_{wedge}.

Returning to Figure 5.1, for shallow channels, as in Figure 5.1(e)–(f), there are clear differences between supercritical and subcritical flows. In the former regime ($F_H > 1$, $\delta \gg 1$), the trend in the data is dominated by the F_L^{-1} decay. While for the latter regime ($F_H < 1$, $\delta \gg 1$), the apparent wake angle θ_{app} can be very large (much larger than $\arcsin(1/3)$), and here θ_{app} *does* follow θ_{wedge} closely. The transition between subcritical and supercritical flows has a dramatic qualitative effect on the free surface (Figure 5.2(c),(d)(g),(h)) with the absence of the transverse waves for $F_H > 1$, exemplified in the centreline plots of Figure 5.2(g),(h).

5.4 Large Froude number approximation

To calculate the asymptotes for the wake angle θ_{app} in Figure 5.1 (the thick blue line and the thin green line) we perform a far-field stationary phase approximation on the second integral in (5.2) using polar coordinates (r, θ) (defined via $x = r\cos\theta$, $y = r\sin\theta$) to obtain

$$\zeta(r,\theta) \approx a(r,\theta)\sin(rg(\psi_1(\theta),\theta) - \pi/4),$$

where $g(\psi,\theta) = k_1(\psi)\cos(\psi+\theta)$ and

$$a(r,\theta) = \frac{\text{const}}{r^{1/2}} \frac{k_1(\psi_1(\theta))^2 \exp\left(-\delta^2 k_1(\psi_1(\theta))^2/(4\pi^2)\right)}{(F_H^2 - \sec(\psi_1(\theta))^2 \text{sech}(k_1(\psi_1(\theta)))^2)\sqrt{g_{\psi\psi}(\psi_1(\theta),\theta)}}. \tag{5.4}$$

Recall k_1 is the real positive root of (5.3). The function $\psi_1(\theta)$ satisfies

$$k_1'(\psi_1)\cos(\psi_1+\theta) - k_1(\psi_1)\sin(\psi_1+\theta) = 0, \qquad \psi_0 < \psi_1 < \frac{\pi}{2} \text{ and } 0 < \theta < \theta_{\text{wedge}},$$

while $g_{\psi\psi}$ is the second partial derivative of g with respect to ψ.

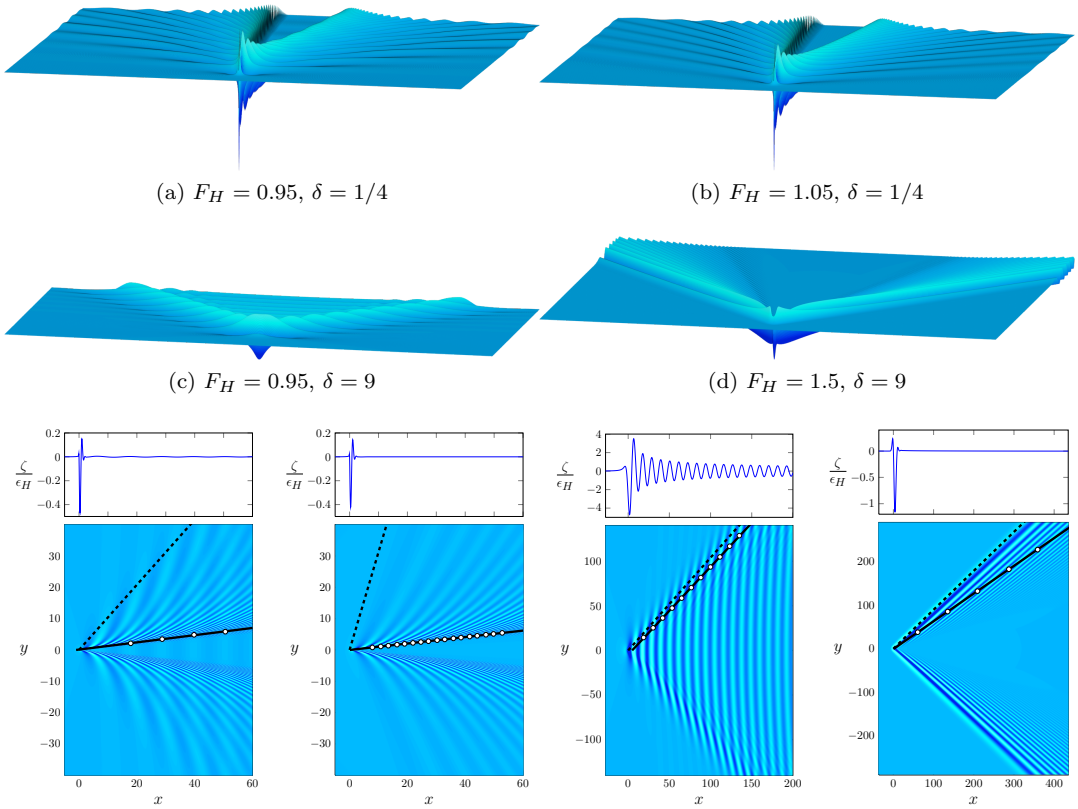

(a) $F_H = 0.95$, $\delta = 1/4$ (b) $F_H = 1.05$, $\delta = 1/4$

(c) $F_H = 0.95$, $\delta = 9$ (d) $F_H = 1.5$, $\delta = 9$

(e) $F_H = 0.95$, $\delta = 1/4$ (f) $F_H = 1.05$, $\delta = 1/4$ (g) $F_H = 0.95$, $\delta = 9$ (h) $F_H = 1.5$, $\delta = 9$

Figure 5.2: (a)–(d) Free surface profiles for various values of F_H and δ. (e)–(h) A plan view of the profiles in (a)–(d) with a centreline plot. The open circles are the highest peaks and the solid line is the line of best fit. The dashed line is the wedge angle θ_{wedge}.

We must now find the maximum of $a(r, \theta)$. The two approaches depend on the method used to measure the wake angle θ_{app}. For method 1, r is held constant (to $r = 1$, say) and we then compute the turning point of $a(1, \theta)$. For method 2 we must choose r such that $\sin(rg(\psi_1(\theta), \theta) - \pi/4) = 1$, which leads to the new amplitude function

$$a(g(\psi_1, \theta)^{-1}, \psi) = \frac{\text{const}\, k_1(\psi_1(\theta))^2 \exp\left(-\delta^2 k_1(\psi_1(\theta))^2/(4\pi^2)\right)}{(F_H^2 - \sec(\psi_1(\theta))^2 \text{sech}(k_1(\psi_1(\theta)))^2} \sqrt{\frac{g(\psi_1(\theta), \theta)}{g_{\psi\psi}(\psi_1(\theta), \theta)}}. \quad (5.5)$$

A simple numerical test shows that, for each value of δ, the maximum of both (5.4) and (5.5) behaves like $F_H \theta_{\text{app}} \to \text{const}$ as $F_H \to \infty$, so that, in both cases,

$$\theta_{\text{app}} \sim \frac{\beta}{F_H} = \frac{\beta}{\sqrt{\delta} F_L} \quad \text{as} \quad F_H \to \infty. \quad (5.6)$$

The numerical values of β for both methods are found to increase from $\beta = 0$ at $\delta = 0$ to $\beta \to 1^-$ as $\delta \to \infty$, thus the asymptotic behaviour of the wake angle is dominated by finite depth effects and approaches the finite depth wedge angle θ_{wedge}. As shown in

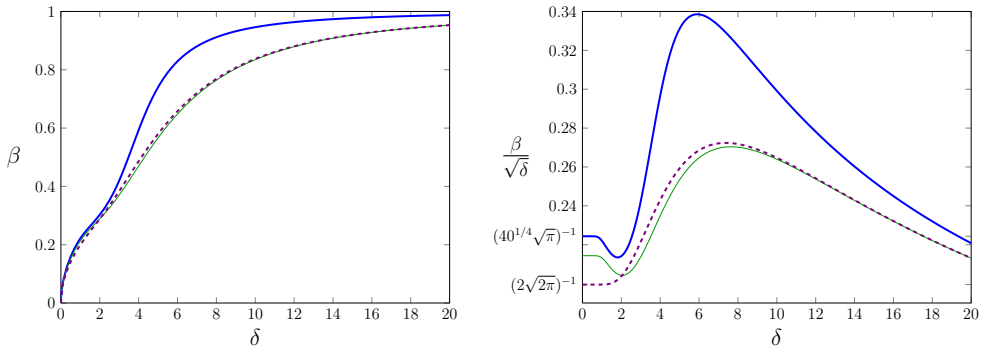

Figure 5.3: Plots of (a) β and (b) $\beta/\sqrt{\delta}$ in (5.6) against δ. The thick (blue) line comes from method 1, the thin (green) line from method 2, the dashed (purple) line by (5.8).

Figure 5.3, we note that method 1 gives $\beta/\sqrt{\delta} \to 1/(40^{1/4}\sqrt{\pi})$ as $\delta \to 0$, which agrees with the infinite depth result computed by Darmon, Benzaquen, and Raphaël (2014).

These results are worth comparing with the phenomenological model of Moisy and Rabaud (2014ab), which for the present finite-depth problem can be extended in a straightforward fashion to predict that

$$\tan\theta_{\text{app}} = c_g(1-c_p^2)^{1/2}/(1-c_g c_p) \quad \text{with} \quad k = 2\pi/\delta, \tag{5.7}$$

where c_g and c_p are the group and phase velocities, respectively, defined by $c_g = \mathrm{d}\omega/\mathrm{d}k$ and $c_p = \omega/k$, and the dispersion relation is $\omega = (k\tanh k)^{1/2}/F_H$. As $c_g = O(F_H^{-1})$ and $c_p = O(F_H^{-1})$ as $F_H \to \infty$, we see that Moisy and Rabaud's method gives $\theta_{\text{app}} \sim c_g$ with $k = 2\pi/\delta$ which, using the notation in (5.6), gives

$$\beta = \frac{\delta\tanh(2\pi/\delta) + 2\pi\operatorname{sech}^2(2\pi/\delta)}{2\sqrt{2\pi\delta\tanh(2\pi/\delta)}}. \tag{5.8}$$

This result is also shown in Figure 5.3 (dashed line). In the deep water limit, (5.8) gives $\beta/\sqrt{\delta} \to (2\sqrt{2\pi})^{-1}$ as $\delta \to 0$, which agrees with Moisy and Rabaud (2014b). For shallow water $\delta \gg 1$, it collapses to our method 2.

We now plot in Figure 5.4 the apparent wake angle θ_{app} against F_H for fixed values of F_L. Note that for each fixed value of F_L, an increase in F_H must be associated with an increase in δ so that $F_L = F_H/\sqrt{\delta}$. If we imagine a given pressure distribution with dimensional length scale L moving at dimensional speed U, then each set of data points in Figure 5.4 corresponds to decreasing the channel depth from infinite ($F_H = 0$) to zero ($F_H = \infty$). With this in mind, Figure 5.4(a) shows that for a faster moving stream (see data for $F_L = 1.5$ and 2.5), the transition from subcritical to supercritical flow via a decreasing fluid depth has little effect on the apparent wake angle θ_{app}. Ultimately, regardless of the speed of the stream (that is, for all fixed values of F_L), the apparent wake angle asymptotes to the wedge angle θ_{wedge} for sufficiently shallow

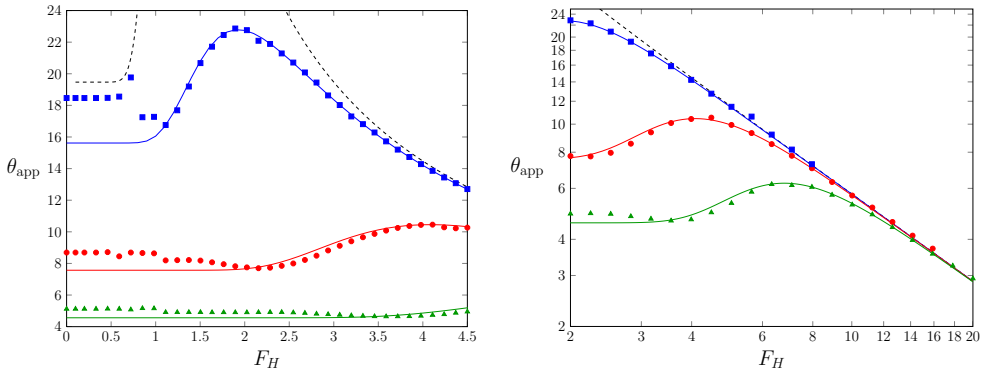

Figure 5.4: Measured apparent wake angles θ_{app} in degrees plotted against the depth-based Froude number F_H for the linear solution (5.2) for constant values of $F_L = 0.7$ (blue squares), 1.5 (red dots) and 2.5 (green triangles). Note that as F_H increases, δ increases such that $F_H/\sqrt{\delta} = F_L$. The solid lines represent (5.7), while the dashed line indicates the wedge angle θ_{wedge}.

depths (see Figure 5.4(b) for large F_H). It is interesting to compare these results with the phenomenological model (5.7); the agreement is not so good for deep channels, but improves as the depth decreases.

5.5 Discussion

In summary, we have considered the prototype problem of flow past an axisymmetric pressure distribution acting on the surface of a finite-depth channel. For the linearised solution, we have explored the dependence of the apparent wake angle θ_{app} (or angle of maximum peaks) on the dimensionless variables. This work extends previous studies for flow past an axisymmetric pressure distribution for the infinite depth case. It has been insightful to fix the depth of the channel and increase the speed of the flow (fixed δ, increasing F_H, see Figure 5.1) and also to fix the speed of the flow and decrease the depth (fixed F_L, increasing F_H, see Figure 5.4). It is remarkable that for much of the parameter space, the apparent wake angle θ_{app} varies smoothly as F_H is increased through critical value $F_H = 1$. On the other hand, for shallow water, we see the apparent wake angle θ_{app} tends to follow the wedge angle θ_{wedge} closely, which for near critical flows produces very large apparent angles, much higher than the Kelvin angle $\arcsin(1/3)$.

We close by noting that the we have deliberately used a very simple pressure distribution, which more easily facilitates a comparison with many recent studies, but may not accurately reflect the wave patterns produced by a real ship. An alternative simplified approach, for example, is to employ a pair of point pressures on the surface (Noblesse et al. 2014) (one positive and one negative), or a continuous distribution of sources (Zhang

et al. 2015). Indeed, the wave pattern generated by a finite-depth flow past a pair of point pressures was considered very recently by Zhu et al. (2015). This study found that for subcritical flows in very shallow channels, the wake angle was close to the wedge angle θ_{wedge}, which is very similar to our observations. On the other hand, their argument based on interference effects suggests that the wake angle scales like F_H^{-2} in the large Froude number limit, which is very different to (5.6). This difference in the large Froude number scaling is, at least in part, likely due to the difference in the flow configurations considered (see the relevant discussions in Moisy and Rabaud (2014b) and He et al. (2014) about the effect of non-axisymmetric pressure disturbances on the large Froude number scaling). Either way, a further advantage of our approach here is that we provide direct comparisons between analytical predictions and measured values.

6 Spectrograms of ship wakes: identifying linear and nonlinear wave signals

This chapter has been submitted for publication as

R. Pethiyagoda, S. W. McCue, and T. J. Moroney (2016). Spectrograms of ship wakes: identifying linear and nonlinear wave signals. Submitted to the *Journal of Fluid Mechanics* (arXiv:1604.05812)

Abstract

A spectrogram is a useful way of using short-time discrete Fourier transforms to visualise surface height measurements taken of ship wakes in real world conditions. For a steadily moving ship that leaves behind small-amplitude waves, the spectrogram is known to have two clear linear components, a sliding-frequency mode caused by the divergent waves and a constant-frequency mode for the transverse waves. However, recent observations of high speed ferry data have identified additional components of the spectrograms that are not yet explained. We use computer simulations of linear and nonlinear ship wave patterns and apply time-frequency analysis to generate spectrograms for an idealised ship. We clarify the role of the linear dispersion relation and ship speed on the two linear components. We use a simple weakly nonlinear theory to identify higher order effects in a spectrogram and, while the high speed ferry data is very noisy, we propose that certain additional features in the experimental data are caused by nonlinearity. Finally, we provide a possible explanation for a further discrepancy between the high speed ferry spectrograms and linear theory by accounting for ship acceleration.

6.1 Introduction

A useful method for observing and measuring ship wakes is to employ an echo sounder to record the water height over time as a ship passes nearby. The resulting output signal corresponds to the cross-section of the ship wake taken in the direction of travel (Torsvik et al. 2015b). The surface elevation at the echo sounder can be visualised as a spectrogram through the use of many short-time discrete Fourier transforms. In this paper, we aim to identify and explain features of spectrograms of ship wakes, concentrating on the differing effects that linearity and nonlinearity have on the wave time-frequency signal.

The study of ship waves has been of great academic interest for over a century (Darrigol 2003). From a mathematical perspective, a popular approach is to set up a potential flow model, with the effects of the ship approximated by a steadily moving pressure distribution acting on the surface of the water. By linearising the dynamic and kinematic boundary conditions on the free surface, one can write down exact solutions for the wave pattern using a Fourier transform. In this way, theoretical studies provide insight into how the speed of a ship affects the distinguishing features such as the divergent and transverse waves (Peters 1949; Ursell 1960; Chung and Lim 1991) and the wake angle (Rabaud and Moisy 2013; Darmon, Benzaquen, and Raphaël 2014; Noblesse et al. 2014; Pethiyagoda, McCue, and Moroney 2015, Ch. 5). Similarly, linear water wave theory has been used extensively to approximate the drag force associated with a ship wake (Michell 1898; Havelock 1932b; Noblesse 1981). For the fully nonlinear versions of these problems, direct analysis is much more difficult (Soomere 2007). Thus, studying the effects of nonlinearity on a ship wake is normally framed as a computational challenge (Forbes 1989; Părău and Vanden-Broeck 2002; Părău, Vanden-Broeck, and Cooker 2007a; Pethiyagoda et al. 2014, Ch. 3).

In the real world, analysis of ship wave data is limited due to the difficulty of accurately capturing the surface height outside of a towing tank. One method of observing ship wakes is with satellite photography (Munk, Scully-Power, and Zachariasen 1987; Rabaud and Moisy 2013) or radar (Milgram 1988; Reed and Milgram 2002). Unfortunately, satellite photography requires adequate lighting conditions to highlight the desired wake components (Munk, Scully-Power, and Zachariasen 1987). Even with sufficient clarity, a photograph can not provide quantitative data on the surface elevation, leaving only a few viable measurements to be performed on the ship wake, such as the wake angle (Rabaud and Moisy 2013). Radar can be hampered by backscattering that leads to a bright narrow V-pattern (Milgram 1988) caused by Bragg-resonant ship waves (Reed and Milgram 2002) and not related to the wake angles observed by Rabaud and Moisy (2013). Another method of observing ship wakes is to use an echo

sounder and to visualise the frequencies via a spectrogram, as mentioned above. We will focus on spectrograms in this paper.

Spectrograms are popular in many fields and, for example, have been used in signal processing for decades (Cohen 1989) to decompose signals into wave components of different frequency. Even though Tuck, Collins, and Wells (1971) determined the theoretical recovered wave frequencies for a sensor travelling over a far-field ship wake, spectrograms are a relatively new tool in the study of water waves, originally used by Wyatt and Hall (1988) to analyse ship wakes with a sensor moving perpendicular to the direction of the ship. The work of Wyatt and Hall (1988) was closely followed by Brown et al. (1989) who performed experiments with a stationary sensor and constructed low resolution spectrograms using experimental data. There has been a resurgence of interest in the use of spectrograms for analysing ship waves (Benassai, Piscopo, and Scamardella 2015; Didenkulova et al. 2013; Sheremet, Gravois, and Tian 2013; Torsvik et al. 2015a; Torsvik et al. 2015b), for which a stationary sensor is used to measure the wake of ships. For much of this recent work, the primary focus of the research has been on calculating the energy contained in a given wake and the effect that the propagating wake wash will have when it interacts with the coastal zone (Benassai, Piscopo, and Scamardella 2015; Didenkulova et al. 2013; Torsvik et al. 2015b). This work is important because regulators need to balance the protection of the coastal environment (both natural and built) against the need for efficient shipping systems.

By applying linear water wave theory, Torsvik et al. (2015b) showed that for small amplitude waves, the spectrogram of a steadily moving vessel has two linear components: a sliding-frequency mode (chirp) and a constant-frequency mode corresponding to divergent and transverse waves, respectively. The transverse and divergent components of the spectrogram were used to predict the ship's speed and the minimum distance from the echo sounder. However, by analysing high speed ferry data from the Gulf of Finland, Torsvik et al. (2015b) found and classified five wake components present in the spectrogram, the two linear components just mentioned plus three more; they referred to the additional three components as precursor solitary, leading and low frequency waves (Figure 6.1). Torsvik et al. (2015a) were able offer some evidence to the notion that two of the additional wake components (the so-called precursor and leading waves) were a result of wave shoaling and nonlinear effects caused by the ship waves approaching the shore.

Didenkulova et al. (2013) offered their own explanations for the features of the experimental spectrogram in Figure 6.1. Didenkulova et al. (2013) agree with Torsvik et al. (2015b) with respect to the cause of the precursor solitary wave and the leading wave being attributed to the nonlinear effects of the ship hull and wave shoaling. However, Didenkulova et al. (2013) attributed the two branches of colour intensity in the

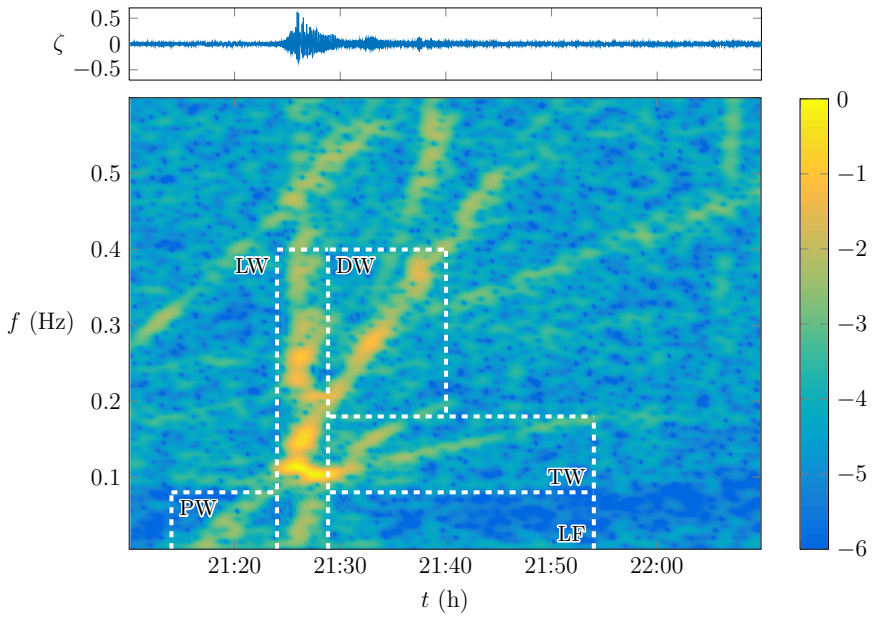

Figure 6.1: A spectrogram of the signal generated by a high speed ferry in the Gulf of Finland. This figure is identical to Figure 9(a) of Torsvik et al. (2015b), except a) we have re-computed the spectrogram using a different colour scheme, and b) we have used the colour intensity interval $(-6, 0)$ whereas they use $(-6, -1)$. The five wake components as identified by Torsvik et al. (2015b) are the precursor solitary (PW), leading (LW), divergent (DW), transverse (TW) and low frequency (LF) waves. The wave signal is presented above the spectrogram.

transverse wave component (in the boxed labelled TW in Figure 6.1) to the transverse and divergent waves, stating that the transverse wave component represents the entire Kelvin wake signal. Finally, Didenkulova et al. (2013) did not provide an explanation for the features in the divergent and low frequency wave components.

The motivation for the present study is to use theoretical and computational methods to identify linear and nonlinear features of idealised spectrograms and to better understand the origin of the wake components in experimental spectrograms such as those presented by Didenkulova et al. (2013), Torsvik et al. (2015b), and Torsvik et al. (2015a).

We begin by taking spectrograms of linear free-surface profiles to identify the two wake components that are present for linear flows past a pressure distribution (namely, the sliding-frequency mode and the constant-frequency mode). A geometric argument is provided to show that these components are present for all linear ship wave patterns. An advantage of using the idealised problem of flow past a pressure distribution (as opposed to flow past a single point pressure, as used by Torsvik et al. (2015b)), is that we are able to demonstrate how the high intensity signal in the spectrogram follows

the constant-frequency mode (sliding-frequency mode) for slower (faster) ships. We then modify the numerical method for computing nonlinear ship waves by Pethiyagoda et al. (2014) [Ch. 3] to significantly increase the domain size of the computed solution. We use the numerical solutions to generate accurate spectrograms of nonlinear ship waves; these spectrograms are free of wind waves that are present in experimental measurements, allowing us to more easily observe the effects of steep nonlinear waves. We identify features present in nonlinear spectrograms and use a weakly nonlinear theory to derive analytical results that match well with the numerical simulations. While it is very difficult to separate the direct influence of the high speed ferry in the spectrogram in Figure 6.1 from other effects or artefacts that may be unrelated to that particular vessel, we propose that nonlinear waves may be associated with the leading wave component recorded by Torsvik et al. (2015b). Finally, we see the transverse wave component in Figure 6.1 is not horizontal, as predicted by linear theory. We provide a possible explanation for this discrepancy by accounting for ship acceleration in the linear model.

6.2 Problem setup

In order to simulate a wake left behind a moving ship, we consider the idealised problem of calculating the free surface disturbance created by a steadily moving pressure distribution applied to the surface of an infinitely deep body of water. We suppose the pressure distribution is of a Gaussian type with strength P_0 and characteristic length L, and then formulate the mathematical problem in the reference frame of this moving pressure. We nondimensionalise the problem by scaling all velocities by the speed of the pressure distribution, U, and all lengths by U^2/g, where g is acceleration due to gravity. The governing equations are then

$$\nabla^2\phi = 0 \qquad \text{for } z < \zeta(x,y), \tag{6.1}$$

$$\frac{1}{2}|\nabla\phi|^2 + \zeta + \epsilon p = \frac{1}{2} \qquad \text{on } z = \zeta(x,y), \tag{6.2}$$

$$\phi_x\zeta_x + \phi_y\zeta_y = \phi_z \qquad \text{on } z = \zeta(x,y), \tag{6.3}$$

$$\phi \to x \qquad \text{as } x \to -\infty, \tag{6.4}$$

where $\phi(x,y,z)$ is the velocity potential, $\zeta(x,y)$ is the free-surface height, $\epsilon = P_0/(\rho U^2)$ is the dimensionless pressure strength, ρ is the fluid density and $\epsilon p(x,y)$ is the pressure distribution. For the present study we will use the pressure distribution

$$p(x,y) = \mathrm{e}^{-\pi^2 F_L^4 (x^2+y^2)}, \tag{6.5}$$

where $F_L = U/\sqrt{gL}$ is the Froude number. In this formulation, F_L is the parameter that measures the speed of the moving pressure, while the pressure strength ϵ provides

a measure of nonlinearity in the problem (the regime $\epsilon \ll 1$ is approximately linear). Note that in computing the Bernoulli constant on the right-hand side of (6.2), we have assumed the surface height $\zeta \to 0$ far upstream as $x \to -\infty$.

The use of (6.5) to represent a ship is obviously extremely simplistic. Other simple models include a pair of pressure distributions, one positive and one negative to represent the bow and stern waves of a ship (Noblesse et al. 2014), a thin-ship approximation for when the beam of the ship is much less than the length (Michell 1898) or a flat-ship approximation for when the draft is much less than the length (Maruo 1967; Tuck 1975). However, as a first step, we have found the use of (6.5) particularly insightful as the disturbance has a well defined centre point to aid our geometrical arguments. Additionally, Gaussian pressure distributions are still frequently used to approximate the ship when analysing properties of the wake (Darmon, Benzaquen, and Raphaël 2014; Ellingsen 2014; Pethiyagoda, McCue, and Moroney 2015, Ch. 5; Li and Ellingsen 2016).

6.3 Spectrograms of small amplitude ship waves

6.3.1 Exact solution to linear problem

For weak pressure distributions, $\epsilon \ll 1$, the problem (6.1)–(6.5) can be linearised. The linearised version has the exact solution (Wehausen and Laitone 1960)

$$\begin{aligned}\zeta(x,y) = &-\epsilon p(x,y) + \frac{\epsilon}{2\pi^2}\int_{-\pi/2}^{\pi/2}\int_{0}^{\infty}\frac{k^2\tilde{p}(k,\psi)\cos(k[|x|\cos\psi + y\sin\psi])}{k-k_0}\,\mathrm{d}k\,\mathrm{d}\psi \\ &-\frac{\epsilon H(x)}{\pi}\int_{-\pi/2}^{\pi/2} k_0^2\tilde{p}(k_0,\psi)\sin(k_0[x\cos\psi + y\sin\psi])\,\mathrm{d}\psi, \end{aligned} \tag{6.6}$$

where $\tilde{p}(k,\psi) = \exp(-k^2/(4\pi^2F_L^4))/(\pi F_L^4)$ is the Fourier transform of the pressure distribution (6.5), $H(x)$ is the Heaviside function and the path of integration over k is taken below the pole $k = k_0$, where $k_0 = \sec^2\psi$ (thus this integral can be interpreted as a Cauchy Principal Value integral plus half of the residue at $k = k_0$).

6.3.2 Linear spectrogram

A spectrogram of a ship wake is generated by first taking a cross-section of the wave surface at a constant value of y to create a wave signal, $s(t)$, where $t = x$ by changing the reference frame to move with the uniform flow (recall the dimensionless speed is unity). The spectrogram data is then given by the square magnitude of a short-time

Fourier transform:

$$S(t,\omega) = \left| \int_{-\infty}^{\infty} h(\tau - t) s(\tau) \mathrm{e}^{-i\omega\tau} \, \mathrm{d}\tau \right|^2 , \tag{6.7}$$

where the window function, $h(t)$, is an even function with compact support. In this paper we will use the Blackman-Harris 92dB window function (Harris 1978). The results are placed in a time-frequency heat map of angular frequency ω against scaled time t/y and colour intensity on a log scale, $\log_{10}(S(t,\omega))$.

Spectrograms computed from the linear solution (6.6) for the Froude numbers $F_L = 0.3$, 0.7, 1 and 1.5 are presented in Figure 6.2 together with a solid curve which we refer to as the linear dispersion curve. More details are provided in the following subsection, but for now we note the linear dispersion curve has two branches, the lower branch corresponding to the transverse wave component of the spectrogram and the upper branch corresponding to the divergent wave component. In this figure we have chosen to fix $y = 100$, but note that for sufficiently large y (say $y > 25$), the spectrograms appear the same on this scale. On the other hand, if y is chosen to be too small (that is, the sample is too close to the pressure disturbance), there will be some unwanted blurring between the two branches in the spectrogram.

There are two key features of the spectrograms in Figure 6.2. First, the high intensity portion of the spectrograms (the lighter coloured part) in parts (a)–(d) appears to be centred on the linear dispersion curve. Thus, for this problem of linearised flow past a pressure distribution, the linear dispersion curve provides an excellent prediction for the dominant wave signals propagating past a representative point in space. The second key feature is that the high intensity portion is confined to the lower branch of the dispersion curve for low Froude numbers (approximately $F_L < 0.4$), while for larger Froude numbers it follows the fold and the upper branch. This result is consistent with observations of ship wave patterns that suggest slowly moving ships give rise to wakes dominated by transverse waves, while fast vessels produce a wave train dominated by divergent waves. We note that this second feature is not evident if we treat the idealised problem of flow past a point pressure (as in Torsvik et al. (2015b)), since the solution to the point-pressure problem does not depend on any parameter values apart from the pressure strength ϵ (there is no length scale and so no Froude number).

6.3.3 Linear dispersion curve

The linear dispersion curve in Figure 6.2 is independent of the speed of the disturbance (that is, independent of F_L) and can be determined via the following geometric arguments. First we consider a ship moving along the path MO a distance of t_0 as shown in Figure 6.3. At the point M the ship will generate waves in all directions θ with phase

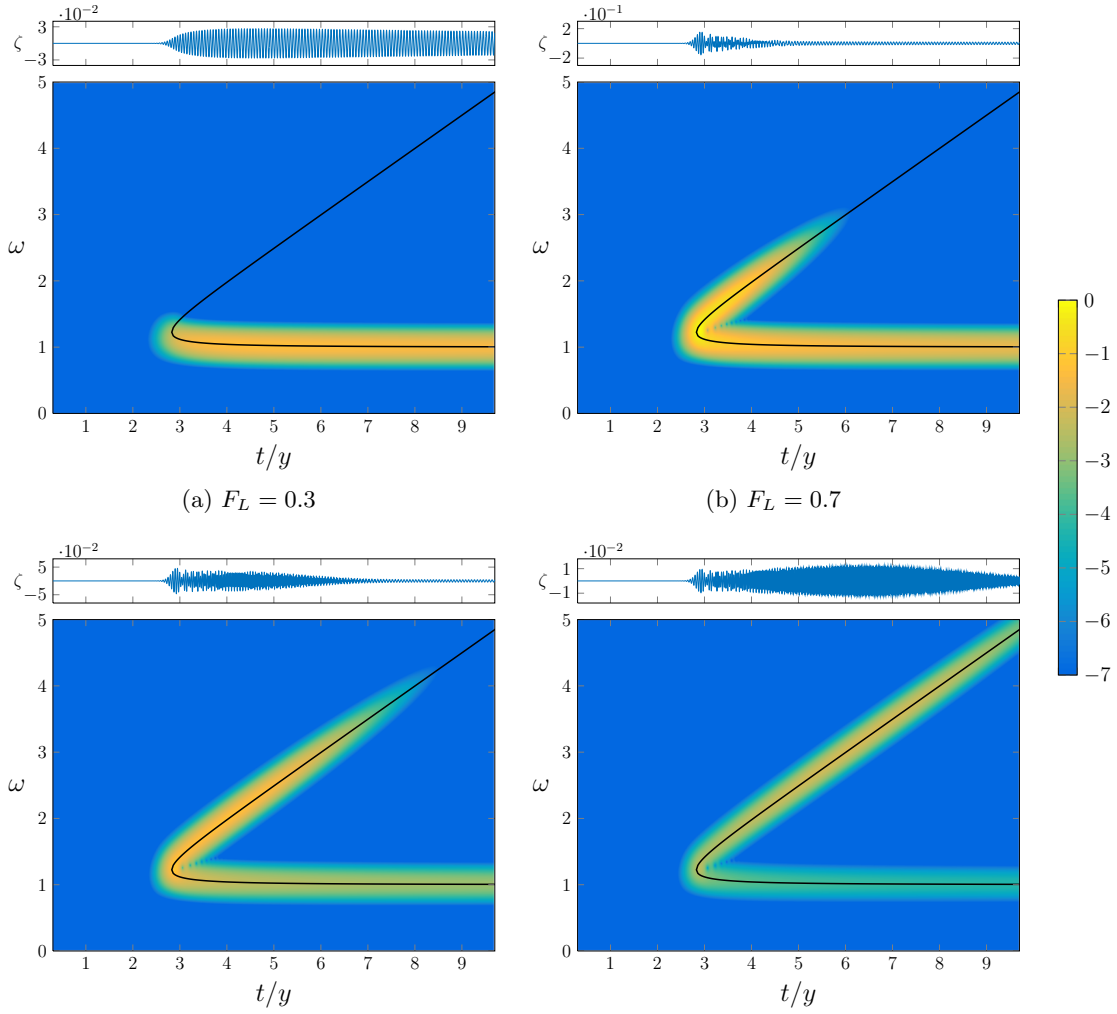

Figure 6.2: Spectrograms of linear ship waves for the Froude numbers $F_L = 0.3$, 0.7, 1 and 1.5. The solid curve is the dispersion curve given by equation (6.12). The colour intensity is given by $\log_{10}(S(t,\omega))$, where $S(t,\omega)$ is given by (6.7). In each case, the wave signal ζ, plotted against t/y, is shown above the related spectrogram.

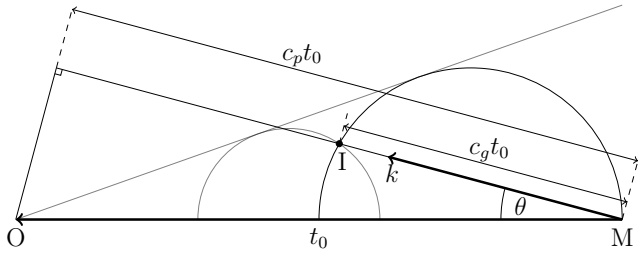

Figure 6.3: This schematic of ship wave dispersion illustrates a ship moving from the point M to the point O with a nondimensional speed 1 over the time period t_0. The waves generated by the ship at the point M propagate at all angles θ from the sailing line and wavenumbers k with phase velocity, c_p, and group velocity, c_g. The large black semicircle is traced out using the group velocity for all θ. The small grey semicircle follows the same rules but is generated at a different point. The grey line, tangent to the two semi circles, represents the geometric edge of the wake system. Finally, the point I is the location of the sensor.

velocity

$$c_p = \cos\theta \tag{6.8}$$

and group velocity, c_g. To obtain the frequency at a given point $\mathrm{I} = (t, y)$, we must determine the angle θ and the associated wavenumber k. We require the following properties: an implicit function $k(\theta)$

$$k(\theta)^2 \cos^2\theta - \Omega(k(\theta))^2 = 0, \tag{6.9}$$

where $\Omega(k) = \sqrt{k}$ is the dispersion function for waves on an infinite depth fluid; and a frequency relation given by projecting the wave vector $(-k\cos\theta, k\sin\theta)$ onto the direction the sensor is moving relative to the ship, $(1, 0)$, and then taking the absolute value,

$$\omega = k(\theta)\cos\theta. \tag{6.10}$$

Finally, we use geometry to determine θ, which can be found as a root of the equation

$$0 = \tan^2\theta - \frac{t}{y}\alpha(k(\theta))\tan\theta + 1 - \alpha(k(\theta)), \tag{6.11}$$

where $\alpha(k) = c_g/c_p = 1/2$ is the ratio of group velocity to phase velocity in a fluid of infinite depth. Solving (6.8)–(6.11) for ω gives

$$\omega_{1,2} = \frac{1}{2\sqrt{2}}\sqrt{\left(\frac{t}{y}\right)^2 \pm \frac{t}{y}\sqrt{\left(\frac{t}{y}\right)^2 - 8} + 4}. \tag{6.12}$$

The above argument is essentially equivalent to that provided by Wyatt and Hall (1988), although they do not provide the formula (6.12).

The linear dispersion curve (6.12) is the solid curve in Figure 6.2. As mention above, it has two branches, the upper branch ω_1 and lower branch ω_2, and a fold where the two branches meet at the point $(t/y,\, \omega)=(\sqrt{8},\sqrt{3/2})$. The upper branch corresponds to the divergent waves; it approaches the line $\omega = t/2y$ for large t/y and is represented by the smaller grey circle in Figure 6.3. The lower branch, represented by the large black circle in Figure 6.3, corresponds to the transverse waves and approaches $\omega = 1$ for large t/y. The fold represents the wedge boundary of the wave train in this geometric representation, providing the well-known Kelvin's ship wake angle, $\arctan(1/\sqrt{8})$ (Thomson 1887).

6.4 Nonlinear ship wakes

6.4.1 Numerical scheme

There are no known exact solutions to the fully nonlinear problem (6.1)–(6.5). To compute numerical solutions we reformulate the equations using a boundary integral method, and construct a system of nonlinear equations $\mathbf{F}(\mathbf{u}) = \mathbf{0}$ using collocation (Forbes 1989; Părău and Vanden-Broeck 2002; Părău, Vanden-Broeck, and Cooker 2007a). The key feature of this system is that the Jacobian is fully dense, which provides challenges in terms of accuracy and run-time. We have revisited this scheme recently with a preconditioned Jacobian-free Newton-Krylov (JFNK) method (Pethiyagoda et al. 2014, Ch. 3). The preconditioner used in the JFNK method was the block-banded linear preconditioner. The solution was computed over a mesh of N points in the x-direction and M points in the y-direction, hereafter written as $N \times M$, with mesh spacing in the x and y-directions given by Δx and Δy, respectively. Unfortunately, the largest computed domain provided by this method does not provide sufficient resolution in the frequency domain of the spectrogram to produce a reasonably accurate computed spectrogram. To overcome this limitation we have developed a sub-domain stitching method described here.

The sub-domain stitching method is an iterative procedure that computes sub-domains (hereafter referred to as panels) one at a time and connects them together, as shown in Figure 6.4. For clarity, subscripts are added to the parameters N, M, Δx and Δy denoting which panel they relate to. The first panel is computed on an $N_1 \times M_1$ mesh that begins upstream of the pressure distribution as in the unaltered method, shown as the first white rectangle in Figure 6.4. The first panel is then truncated from the downstream end onto a smaller $N_1' \times M_1$ mesh, where $N_1' < N_1$ is the number of points in the x-direction of the truncated domain. The truncation step is performed under the assumption that there exists domain truncation error near the downstream boundary. The next panel is chosen such that $\Delta y_1 = \Delta y_2$, $\Delta x_1 = \Delta x_2$, $M_1 \leq M_2$ and

is placed such that the upstream border of the second panel matches up with mesh points from the previous panel. The second panel is placed such that the upstream points coincide with the downstream points of the truncated first panel (first solid red rectangle in Figure 6.4). After the panel has been placed, the radiation conditions at the M_1 upstream points are changed from the algebraic decay of the original method (Pethiyagoda et al. 2014, Ch. 3) to make sure there is continuity between panels (ie. $\zeta^1_{N'_1,j} = \zeta^2_{1,j}$, $\phi^1_{N'_1,j} = \phi^2_{1,j}$, etc. for $j = 1 \dots M_1$ where $\zeta^i_{k,j}$ and $\phi^i_{k,j}$ are the surface height and velocity potential for the kth point in the x-direction and the jth point in the y-direction on the ith panel, respectively). The integral in the boundary integral equation can then be split into an integral over a known surface, the previously computed panel that does not overlap with the intended solution, and an integral over the unknown surface to be computed. This procedure is repeated with $\Delta y_1 = \Delta y_i$, $\Delta x_1 = \Delta x_i$ and $M_1 \leq M_2 \leq \cdots \leq M_i$ until a satisfactory domain size is reached. For example, Figure 6.4 shows a free-surface profile corresponding to a solution computed with six panels. The preconditioner used in the JFNK method only needs to be updated for panel i if $N_{i-2} = N_{i-1} = N_i$ and $M_{i-2} = M_{i-1} = M_i$ is not satisfied.

When computing highly nonlinear solutions it is prudent to use a bootstrapping method which takes the solution for a smaller value of ϵ as the initial guess to compute the solution for a larger value of ϵ. This presents two methods of calculating solutions: compute the solution over all panels for a constant value of ϵ before increasing ϵ (panels first); or compute the solution for all desired ϵ values one panel at a time (ϵ first). Computing panels first has the advantage that you receive the full solution to a given value of ϵ before continuing, as opposed to the ϵ first method which produces the full solutions for all ϵ only at the end of the procedure. The ϵ first method will fail to return a solution over the full domain if one of the values of ϵ chosen does not have a solution (or takes unreasonably long to converge to the solution); however, computing ϵ first is faster as the preconditioner only needs to be updated when the panel is changed. Therefore, the choice of method depends on whether or not a solution is known to exist for all chosen values of ϵ.

The main disadvantage of the stitching method described above is that spurious numerical waves are introduced at every boundary between panels. These numerical waves are roughly two-dimensional, small in amplitude, sinusoidal in nature, and more prominent for lower Froude numbers. Due to these numerical waves, a solution constructed via the stitching method will not be in complete numerical agreement with a single domain solution. Spectrograms, however, are robust against such numerical waves. In fact, due to the sinusoidal nature of the numerical waves, they appear as a band of colour intensity at the constant value $\omega = 1$ (that is, at the same frequency as the transverse waves along the centreline $y = 0$) and so are readily identifiable and can be

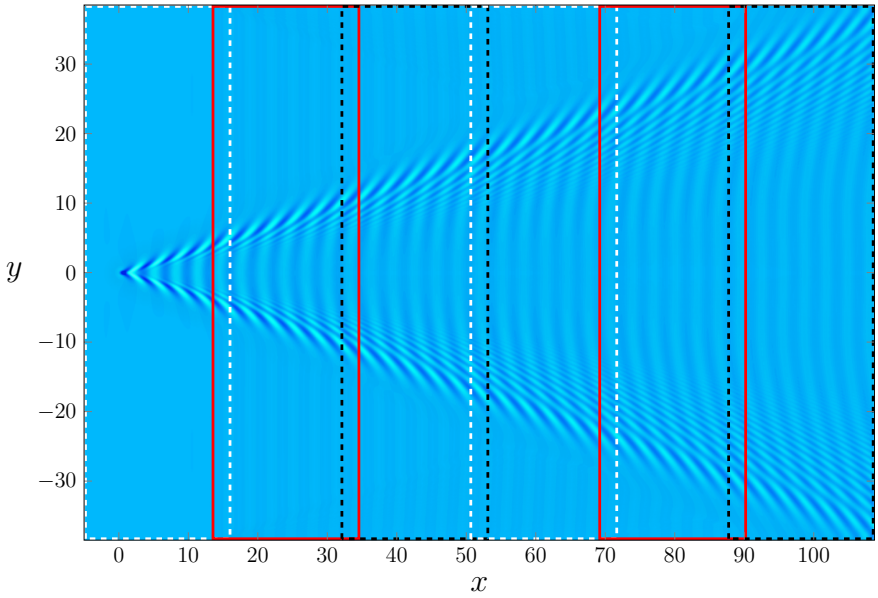

Figure 6.4: Plan view of a nonlinear free-surface solution computed with $F_L = 0.7$ and $\epsilon = 0.01$ using the sub-domain stitching method. The solution is on a 1625×551 mesh constructed from six 301×551 panels indicated by the dashed and solid rectangles.

easily ignored.

6.4.2 Second-order dispersion curves

At this stage we have discussed the linear dispersion curve (6.12) which does not account for nonlinear effects. In order to include nonlinearity, we now derive an expression for further dispersion curves using a weakly nonlinear analysis. We follow the approach of Hogben (1972), who proposed a second-order solution to a ship wave problem provided by a finite number of N monochromatic waves and their interaction terms,

$$\zeta(x,y) = \sum_{n=1}^{N} a_n \cos R_n + \sum_{r=1}^{N}\sum_{s=1}^{r} \{b_{rs+}\cos(R_r + R_s) + b_{rs-}\cos(R_r - R_s)\}\,, \qquad (6.13)$$

where the a_n (for $n = 1,\ldots,N$) are the primary monochromatic wave amplitudes, b_{rs+} and b_{rs-} are non-zero amplitudes of the interacting waves and $R_n = k_n(x\cos\theta_n + y\sin\theta_n)$ defines the primary wave number k_n and direction θ_n. By considering a solution which consists of only the two monochromatic waves ($N = 2$) from linear theory, the amplitudes $a_{1,2}$ can easily be identified by comparing with the stationary phase approximation to the linear solution (6.6) which depends on the nondimensional parameters ϵ and F_L (the details of this calculation are not included here). The wave number k_n and direction θ_n are given by solving (6.9) and (6.11) together to give

$$\theta_{1,2} = \tan^{-1}\left(\frac{(t/y) \pm \sqrt{(t/y)^2 - 8}}{4}\right), \qquad (6.14)$$

$$k_{1,2} = \sec^2\theta_{1,2} = \frac{1}{8}\left[\left(\frac{t}{y}\right)^2 \pm \frac{t}{y}\sqrt{\left(\frac{t}{y}\right)^2 - 8} + 4\right]. \tag{6.15}$$

The amplitudes of the interacting waves $b_{rs\pm}$ are proportional to $a_r a_s$. For further details, see Hogben (1972).

To determine the location of the additional dispersion curves that arise from the second-order solution (6.13), the actual wave amplitudes a_n and $b_{rs\pm}$ are not required (provided they are non-zero). Instead, by examining the phases of the interacting waves (that is, $R_r + R_s$ and $R_r - R_s$), we can easily calculate the additional dispersion curves by either doubling the linear frequencies, adding them together, or taking the difference between them:

$$\omega_{3,4} = 2\omega_{1,2} = \frac{1}{\sqrt{2}}\sqrt{\left(\frac{t}{y}\right)^2 \pm \frac{t}{y}\sqrt{\left(\frac{t}{y}\right)^2 - 8} + 4}, \tag{6.16}$$

$$\omega_{5,6} = \omega_1 \pm \omega_2 = \frac{1}{2}\sqrt{\left(\frac{t}{y}\right)^2 \pm 4\sqrt{\left(\frac{t}{y}\right)^2 - 1} + 4}. \tag{6.17}$$

We refer to the curves described by (6.16)–(6.17) as being the second-order dispersion curves as they come from analysing the second-order solution (6.13).

The linear and second-order dispersion curves are shown in Figure 6.5. We emphasise that, like their linear counterparts, these second-order dispersion curves do not depend on ϵ or F_L. Instead, they indicate which parts of the time-frequency domain could be highlighted in a spectrogram for a nonlinear wave pattern. Whether one or more of the branches are actually highlighted depends on the strength of the nonlinearity ϵ and the speed of the ship F_L, as we see in the following subsection.

6.4.3 Spectrograms computed using our nonlinear simulations

We now present in Figures 6.6–6.8 spectrograms computed using our fully nonlinear numerical simulations described in section 6.4.1 together with our linear and weakly nonlinear predictions (6.12) and (6.16)–(6.17). For all of the nonlinear spectrograms in these figures, we have fixed our y-coordinate to be $y = 35$, which we have found to be sufficiently large to prevent unwanted blurring between branches of the dispersion curves.

Figure 6.6 shows the spectrograms computed for Froude number $F = 0.2$, representative of a slow moving 'ship', and the four pressure strengths $\epsilon = 0.15$, 0.75, 1.65 and 2.25. Before proceeding to analyse these spectrograms, we note two features that are not of particular concern in this study. First, the low frequency intensity present in all spectrograms in Figure 6.6 (the horizontal band near $\omega = 0$) is caused by the local

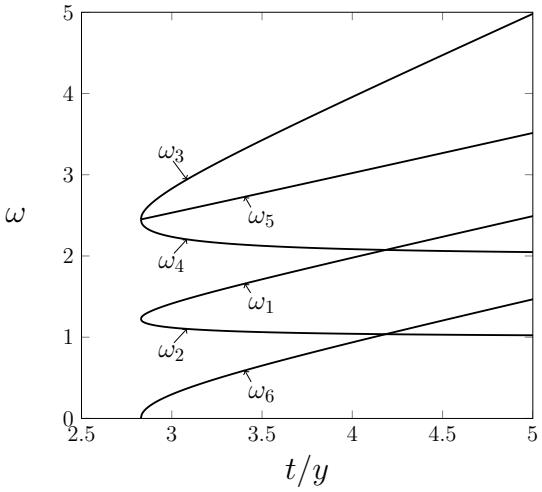

Figure 6.5: The linear and second order dispersion curves. The linear dispersion curve (with branches $\omega_{1,2}$) is given by (6.12). The second order dispersion curves (with branches $\omega_{3,4}$ and $\omega_{5,6}$) are given by (6.16) and (6.17), respectively.

change in surface height due to the presence of the pressure distribution, and is not part of the far field wave train. If we had the capacity to employ much larger computational domains for our numerical solution, then we could have fixed the y-coordinate to be larger than $y = 35$, which would begin to eliminate this effect. Either way, we ignore this low frequency band. Second, a signal is visible in the spectrogram as a band of intensity at $\omega = 1$ ahead of the dispersion curve (for $t/y < \sqrt{8}$). This effect is due to spurious numerical waves that are caused by numerical truncation and the stitching method, as discussed at the end of section 6.4.1.

Returning to the important trends in Figure 6.6, we see that for low nonlinearity ($\epsilon = 0.15$), the intensity in the spectrogram (Figure 6.6(a)) occurs on the lower branch of the linear dispersion curve, ω_2. As the nonlinearity increases, the spectrogram intensity moves up the lower branch towards the fold of the linear dispersion curve (Figure 6.6(b), $\epsilon = 0.75$). These observations are consistent with our linear spectrograms in Figure 6.2, which show the dominant part of the time-frequency signal for slowly moving ships lies on the transverse wave component (the lower branch of the linear dispersion curve, ω_2). For even higher nonlinearity ($\epsilon = 1.65$ in Figure 6.6(c) and $\epsilon = 2.25$ in Figure 6.6(d)), additional high intensity portions appear along the second-order mode ω_4, which comes from transverse waves interacting with themselves (recall $\omega_4 = 2\omega_2$). There is even a hint of a further signal at $\omega = 3\omega_2$, which would represent an even higher order mode. Finally, the extremely nonlinear solution in Figure 6.6(d) exhibits multiple modes appearing in a vertical section in line with the fold ($t/y = \sqrt{8}$). These multiple modes bare a striking resemblance to the so-called leading waves shown in Figure 6.1. Thus we can conclude that the leading wave component identified by

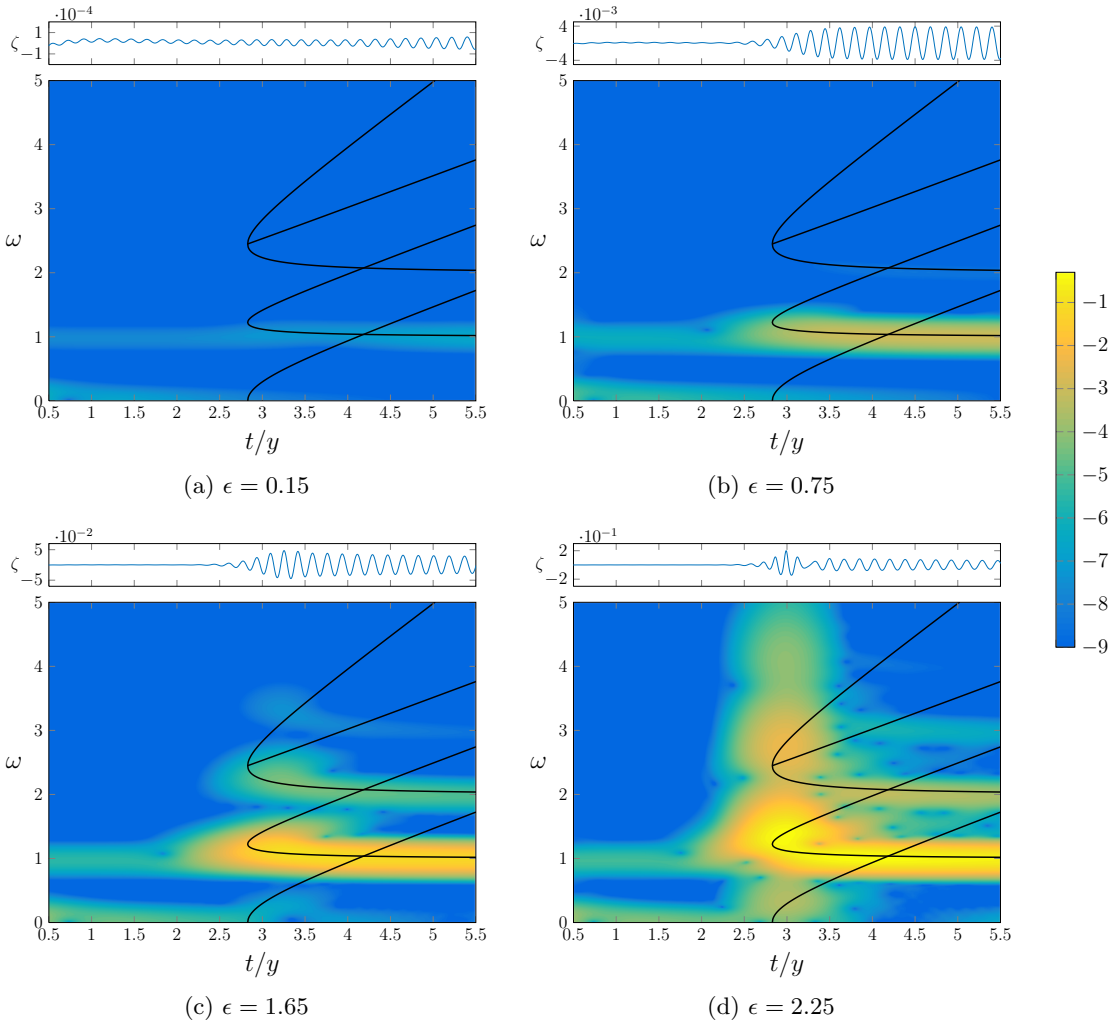

(a) $\epsilon = 0.15$ (b) $\epsilon = 0.75$

(c) $\epsilon = 1.65$ (d) $\epsilon = 2.25$

Figure 6.6: Spectrograms of nonlinear ship waves for nondimensional pressure strength number $\epsilon = 0.15, 0.75, 1.65, 2.25$ and Froude number $F_L = 0.2$. The solid curves are the linear and second-order dispersion curves given by equations (6.12), (6.16) and (6.17). The colour intensity is given by $\log_{10}(S(t,\omega))$ where $S(t,\omega)$ is given by (6.7). In each case, the wave signal ζ, plotted against t/y, is shown above the related spectrogram.

Torsvik et al. (2015b) is possibly due to nonlinearity (steep nonlinear waves).

For $F_L = 0.7$, representative of a faster moving 'ship', the maximum intensity of the spectrogram for the linear solution is around the fold of the linear dispersion curve (see Figure 6.2(b)). This behaviour is replicated in the nonlinear spectrograms in Figure 6.7(a), which is for the small value $\epsilon = 0.01$. For moderate nonlinearity, shown in Figure 6.7(b), an additional mode of intensity appears along ω_3 and ω_5. Further increasing nonlinearity allows for a clearer realisation of the additional modes and the appearance of colour intensity along ω_6 (Figure 6.7(c)). For a highly nonlinear solution, $\epsilon = 0.15$

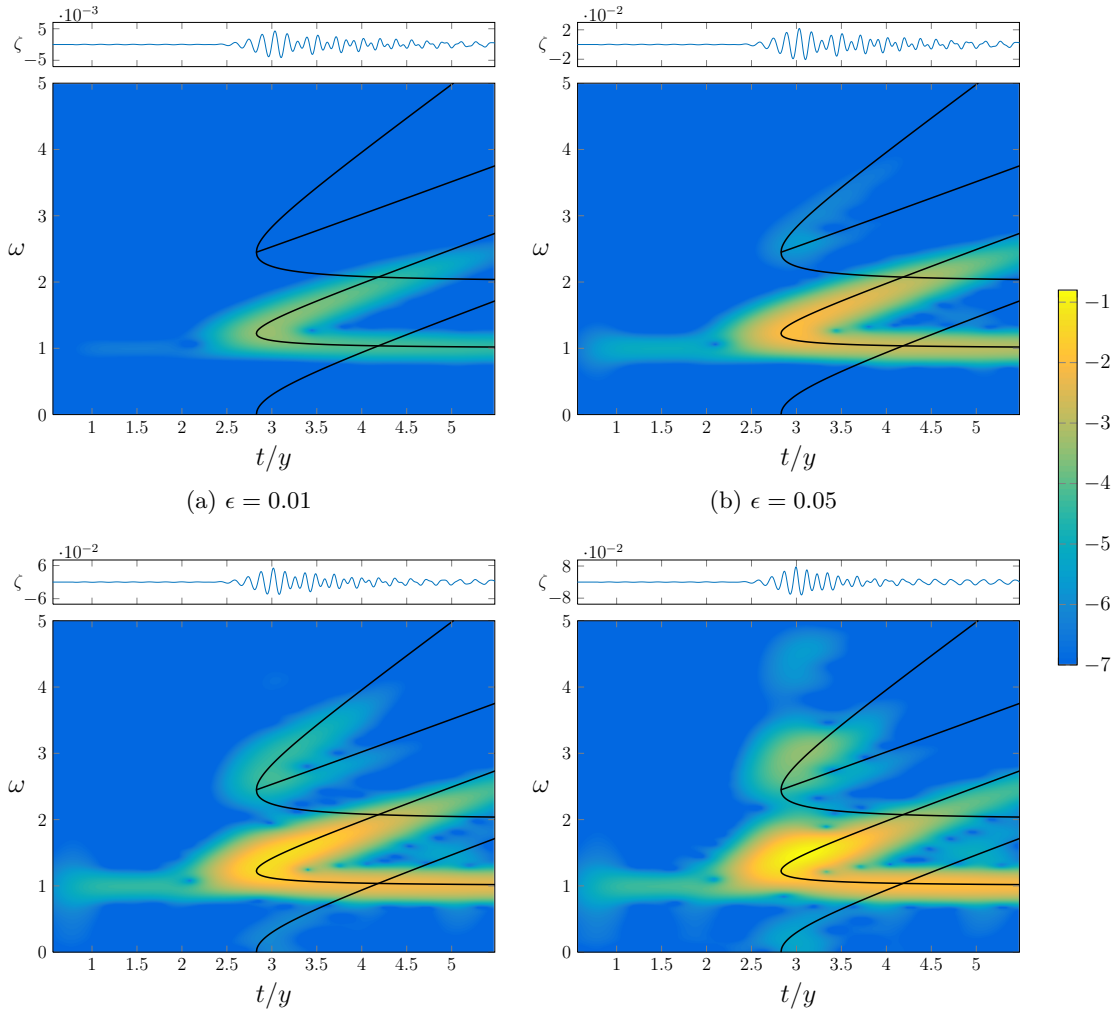

(a) $\epsilon = 0.01$ (b) $\epsilon = 0.05$

(c) $\epsilon = 0.11$ (d) $\epsilon = 0.15$

Figure 6.7: Spectrograms of nonlinear ship waves for nondimensional pressure strength number $\epsilon = 0.01, 0.05, 0.11, 0.15$ and Froude number $F_L = 0.7$. The solid curves and colour intensity are the same as in Figure 6.6.

(Figure 6.7(d)), the region of intensity distorts away from the linear dispersion curve, leading to high intensity regions of the time-frequency map appearing to the left of the fold (that is, for $t/y < \sqrt{8}$). Thus, for high nonlinear flows past a pressure distribution, there exists a visible part of the wave train that appears outside of Kelvin's wedge, as discussed by Pethiyagoda, McCue, and Moroney (2014) [Ch. 4] (that is, some highly nonlinear solutions have apparent wake angles that are greater than Kelvin's angle).

Figure 6.8 is for $F_L = 1$, representing an even faster 'ship'. Here the spectrogram follows the same trend as $F_L = 0.7$ with a clearer colour intensity along the second-order dispersion curves $\omega_{3,5}$ and an absence of colour intensity along ω_6. Thus, for highly

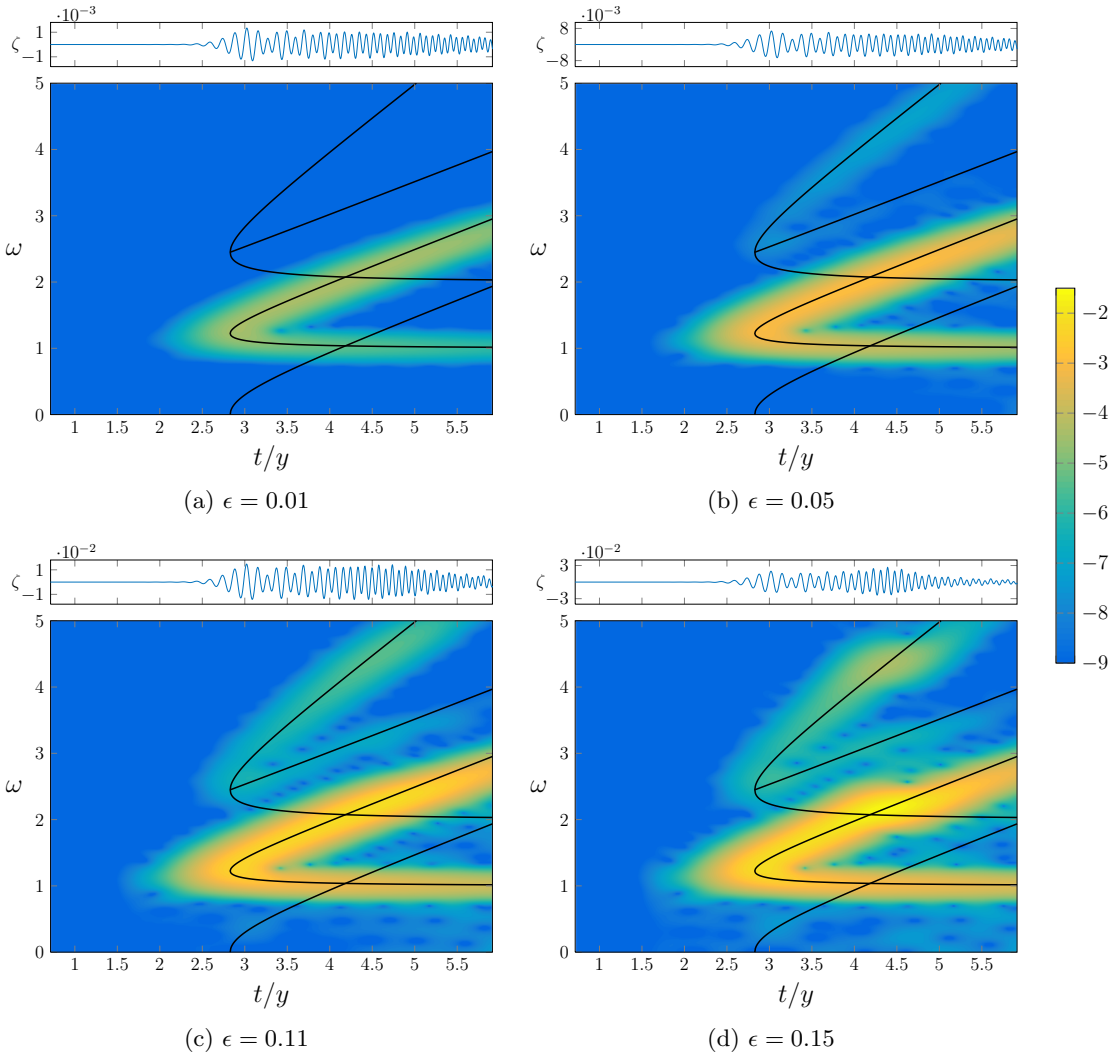

(a) $\epsilon = 0.01$ (b) $\epsilon = 0.05$

(c) $\epsilon = 0.11$ (d) $\epsilon = 0.15$

Figure 6.8: Spectrograms of nonlinear ship waves for nondimensional pressure strength number $\epsilon = 0.01, 0.05, 0.11, 0.15$ and Froude number $F_L = 1$. The solid curves and colour intensity are the same as in Figure 6.6.

nonlinear flows due to faster ships, we expect additional high intensity portions of the spectrogram along the second-order modes that come from divergent waves interacting with themselves ($\omega_3 = 2\omega_1$) and divergent waves interacting with transverse waves ($\omega_5 = \omega_1 + \omega_2$). Further, we see that the distortion observed in Figure 6.8(d) occurs later than that observed for $F_L = 0.7$ (Figure 6.7(d)). The different locations for the distortions is consistent with the location of the greatest intensity in the spectrograms for the exact linear solution.

6.4.4 Comparison with experimental data

We shall now make some comparisons with the experimental spectrogram shown in Figure 6.1. The high speed ferry that produced the wake in question is named the *Star*, which sails from Tallinn, Estonia to Helsinki, Finland. The reported operating speed of the *Star* at the time the data was measured was 14.2 ms^{-1} (Parnell et al. 2008). Its length and width are 186 m and 27.7 m, respectively. This corresponds to a half-length based Froude number of $F_L \approx 0.47$ and half-width based Froude number of $F_W \approx 1.21$. Obviously, the ferry has an aspect ratio which is much larger than unity. However, it is still instructive to compare with our mathematical model which assumes an axisymmetric disturbance.

Considering the spectrogram in Figure 6.1, we now overlay the linear and second-order dispersion curves in order to compare our theoretical results with experimental data. To do so we scale the axes based on the speed of the ship, U, and the minimum distance to the sensor, y, and align the time the ship is closest to the sensor with $t = 0$. As the exact speed, distance and passing time are not known, we match the divergent wave intensity and fold location to the upper branch of the linear dispersion curve, ω_1. The resulting scaled spectrogram is shown in Figure 6.9. Note that in this example we do not consider the transverse wave component ω_2 when matching between our theoretical and experimental results, because the lower branch of the linear mode in the experimental spectrogram in Figure 6.1 does not appear to be horizontal for large t/y, as the theory predicts. We return to this point in section 6.5.

By matching the experimental spectrogram as just described, we find the speed of the ship to be 15.75 ms^{-1}, the distance from the sensor to be 2.5 km and the time the ship is closest to the sensor to be at 21:18. Comparing the properties of the ship's voyage with the reported operating speed and the closest distance to the sensor given by Torsvik et al. (2015b), we see that our calculated speed is a slight over estimation of the reference value, 14.2 ms^{-1}. This could be due to a number of issues, for example the effects of a steady underlying current or finite depth effects that subtly change the shape of the dispersion curve. More encouragingly, having a clear divergent wave component means our estimated distance to the sensor falls in the reference bounds of 2.5–3 km, where 2.5 km corresponds to the outgoing shipping lane.

Visually, Figure 6.9 shows very good agreement between the dispersion curves and the experimental spectrogram in the time frame of the leading wave. In particular, for the region near $t/y = \sqrt{8}$ (roughly $2 < t/y < 4$), the high intensity part of the spectrogram follows the linear dispersion curve (made up of branches $\omega_{1,2}$) and the second-order curves (with branches ω_{3-6}). This exercise shows how important it is to understand the consequences of steep nonlinear waves when interpreting spectrograms.

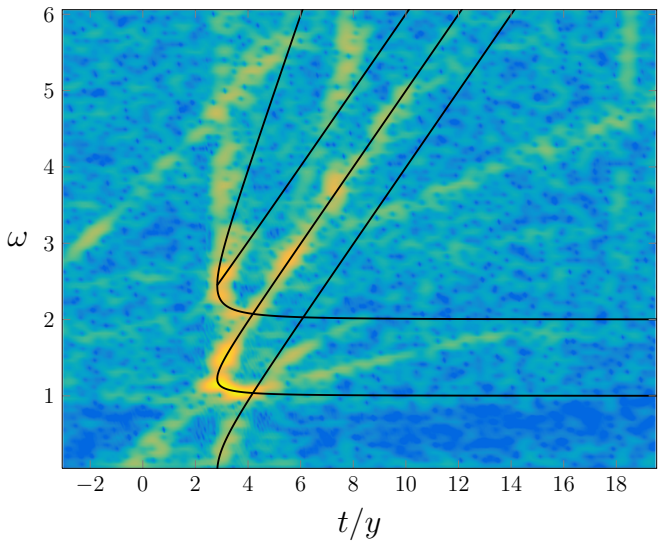

Figure 6.9: A scaled version of Figure 6.1, with the dispersion curves given by (6.12), (6.16) and (6.17) overlaid. The intensity of the spectrogram closely follows the linear and second order dispersion curves ω_{1-6} within the leading wave component of the spectrogram and follows the divergent wave portion of the linear dispersion curve ω_1 outside the leading wave. The transverse wave component of the spectrogram does not appear to follow the lower branch of the linear dispersion curve, ω_2, for large t/y.

It is worth noting that the experimental spectrograms presented by Wyatt and Hall (1988) (calculated from a tug boat named *Quapaw*) show very similar features, including the prominent high intensity regions in the leading wave component. Indeed, Wyatt and Hall (1988) comment that these properties are likely due to nonlinearity.

Finally, we note that to the right of the leading wave region of the spectrogram in Figure 6.9 (for roughly $t/y > 4$), there is an obvious disagreement between the experimental results and the lower (transverse) branch of the linear dispersion curve, ω_2. We consider this issue further now.

6.5 An accelerating ship

6.5.1 Linear dispersion curve with acceleration

One feature of the experimental spectrogram in Figure 6.9 that is not yet explained is the obvious difference between the transverse branch of the linear dispersion curve, ω_2, and the transverse component of the experimental spectrogram data. In an attempt to explain this discrepancy, we consider the case that the ship is accelerating from rest up to its cruising speed. We are motivated to explore this approach for two reasons: a ship travelling at a slower speed will generate transverse waves of higher frequency

(from the dispersion relation); and the transverse waves are caused by waves generated earlier than those that generate divergent waves.

We illustrate the second property by referring to Figure 6.10(a) and (b). In Figure 6.10(a), the solid curve represents a hypothetical ship speed versus time for a y value that is fixed to be the closest distance to the sensor. The actual curve is found by fitting to data, as explained below. The points A, B and C in the figure are associated with waves that are generated at a time $t_{\text{gen}} < 0$ (Figure 6.10(a)) and detected by the sensor at a later time $t_{\text{sen}} > 0$ (Figure 6.10(b)). With this particular velocity profile, the wave represented by the point A in Figure 6.10(a)–(b), generated at $t_{\text{gen}} \approx -6.05$ and detected by the sensor at $t_{\text{sen}} \approx 18.34$, falls on the transverse branch of the dispersion curve. The wave represented by the point B is generated later than A, at $t_{\text{gen}} \approx -4.4$, but still lies on the transverse branch of the dispersion curve. It is detected earlier by the sensor, at $t_{\text{sen}} \approx 5.61$. Waves generated at later times will eventually lie on the divergent wave branch, such as the wave represented by C. Thus, from this argument we see that if the ship is travelling at a slower speed when wave A is generated compared to when wave B is generated, the frequency of the wave A along the dispersion curve will be greater than the frequency of wave B if both waves fall on the transverse branch of the dispersion curve. Therefore, the transverse branch of the linear dispersion curve will grow in frequency as t/y increases if the ship is accelerating.

To determine the location of the linear dispersion curve for an accelerating ship, we first define the nondimensional displacement of the ship, $X(t)$, and its velocity, $U(t)$, with the following properties:

$$X(0) = 0, \quad U(t) = \frac{\mathrm{d}X}{\mathrm{d}t}, \quad 0 \leq U \leq 1, \quad U(t) = 1 \text{ for } t > 0$$

Here $t = 0$ corresponds to the time at which the ship is closest to the sensor. Thus, under these properties, the ship is accelerating during an interval of time before $t = 0$ but is moving with constant speed by the time $t = 0$. The dispersion curve can be defined parametrically in terms of θ by first determining where the ship generated the wave, $X_{\text{gen}} = -y \cot\theta$, and thus the time the wave was generated, $t_{\text{gen}} \leq 0$ such that $X(t_{\text{gen}}) - X_{\text{gen}} = 0$. The time taken for the wave to reach the sensor can then be calculated by $t_{\text{wave}} = y \operatorname{cosec}\theta / c_g$ where the group velocity $c_g = c_p/2 = U(t_{\text{gen}}) \cos\theta/2$. Finally, the variable speed version of equations (6.9) and (6.10) given by $k(\theta) = \sec^2\theta/U^2$ and $\omega = Uk(\theta)\cos\theta$, respectively, are used to derive the dispersion curve

$$\left(\frac{t}{y}, \omega\right) = \left(\frac{t_{\text{wave}} + t_{\text{gen}}}{y}, \frac{\sec\theta}{U(t_{\text{gen}})}\right). \tag{6.18}$$

6.5.2 Comparison with experimental data

The specific velocity function $U(t)$ will affect the shape of the new dispersion curve (6.18), thus in order to match with the experimental spectrogram (Figure 6.1) we require a rough approximation for the velocity of the ship observed in the experiment. We used the shipping traffic website run by the organisation MarineTraffic (MarineTraffic.com) to track the velocity of the *Star* on a particular day as it left port at Tallinn and travelled to the point closest to the sensor (the location of the sensor is given by Parnell et al. (2008)). The data we obtained is nondimensionalised by scaling the velocity by the cruising speed, U_{cruise}, and by scaling time by U_{cruise}/g. Time is shifted so that $t = 0$ corresponds to when the ship was closest to the sensor. An example of the data (for a day in February 2016) is given as the squares in Figure 6.10(a). It appears the ferry initially accelerates as it leaves port then slows down as it turns onto its sailing line before finally accelerating up to its cruising speed. For this specific dataset $U_{\text{cruise}} \approx 12.86\,\text{ms}^{-1}$. Considering only the final acceleration phase, the velocity data for this particular ship looks roughly like an error function, thus we represent it by

$$U(t) = \text{erf}\left(\frac{t/y - t_{\text{shift}}}{\beta}\right), \tag{6.19}$$

where $t_{\text{shift}} = -535/74$ and $\beta = 100/37$ are parameters that are determined by roughly fitting to the data. The velocity profile (6.19) with these parameters is the solid curve in Figure 6.10(a).

Figure 6.10(b) shows a comparison between the new linear dispersion curve (6.18) with $U(t)$ given by (6.19) for an accelerating ship (solid line) and the constant-speed linear dispersion curve ($\omega_{1,2}$, dashed). The transverse branch of the dispersion curve for the accelerating ship clearly increases in frequency as t/y increases; conversely, the divergent branch is very close to the constant-speed dispersion branch. The second-order dispersion curves for the accelerating ship have been derived using the method in section 6.4, and the full set of dispersion curves has been overlaid onto the experimental spectrogram in Figure 6.10(c), with the same axis-scaling as Figure 6.9. We see that the new linear dispersion curve does a much better job of predicting the transverse wave in the spectrogram. Of course the fitting process used here is very rough, but our goal is only to suggest a reasonable approximation of the velocity $U(t)$ on a given day (the data for the ferry observed in 2008 is no longer freely available). Given the clear improvement in the comparison between the measured spectrogram and the theoretical prediction, we are confident that the increase in frequency in the measured transverse wave is due to the observed ship accelerating before passing by the sensor (and not due to nonlinearity, say). We acknowledge that other explanations are possible, for example shoaling or other finite-depth effects such as wave refraction. Or perhaps

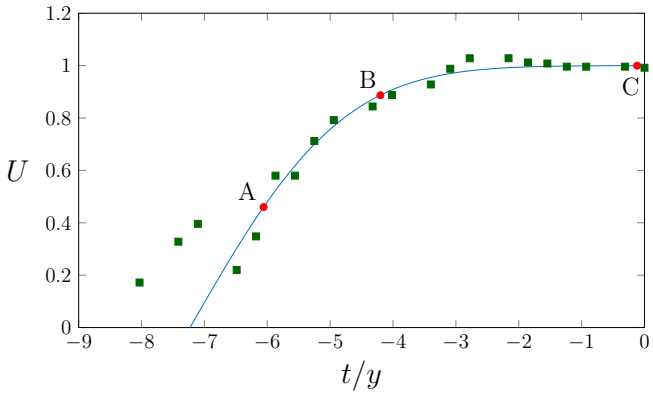

(a) Velocity function

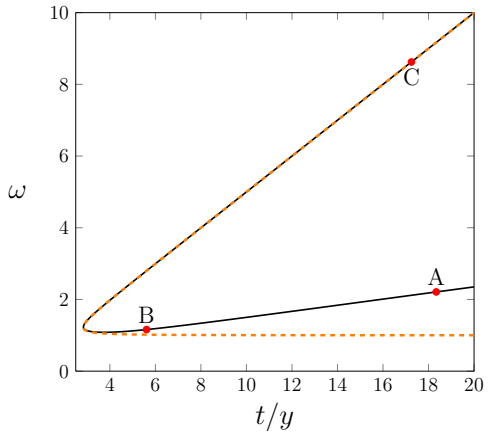

(b) Linear dispersion curves

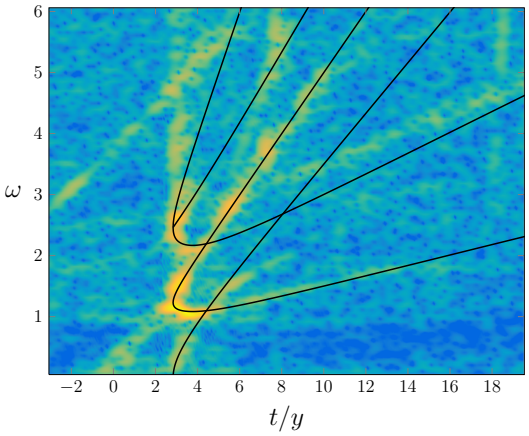

(c) Experimental spectrogram

Figure 6.10: (a) A plot of example data (squares) for nondimensional ship speed and the roughly fitted velocity function (6.19). (b) A plot of the comparison between the linear dispersion curve for an accelerating ship (6.18, solid) and constant-speed linear dispersion curve ($\omega_{1,2}$, dashed). (c) The dispersion curves computed for the accelerating ship overlaid on the scaled version of Figure 6.1. The labels A, B and C in (a) and (b) each identify a wave generated at the ship at a time in (a) and received by the sensor at the time in (b).

another explanation entirely.

6.6 Discussion

The use of spectrograms to analyse ship wakes has been explored recently in a number of studies (Benassai, Piscopo, and Scamardella 2015; Didenkulova et al. 2013; Sheremet, Gravois, and Tian 2013; Torsvik et al. 2015b; Torsvik et al. 2015a). A key observation is that real-world spectrograms appear to highlight components of the wave signal that are in addition to the linear components associated with the traditional transverse and

divergent wave systems. Determining the cause of these additional components has provided the motivation for the present study.

Through the use of classical linear water wave theory and numerical simulations of nonlinear free-surface flow past a pressure distribution, we have identified both linear and higher-order modes present in the spectrograms. As expected, the high intensity signal in the spectrogram for the linearised problem of flow past a pressure distribution follows the linear dispersion curve (6.12). By applying the analogy to flow past a ship, we have demonstrated that for slowly moving ships, the high intensity portion of the spectrogram lies on top of the transverse branch of the dispersion curve ω_2 (also referred to as the constant-frequency mode), while for faster ships, the dominant part of the spectrogram lies on top of the divergent branch ω_1 (the sliding-frequency mode). We have applied a weakly nonlinear theory to calculate the location of second-order modes ω_{3-6} (see (6.16)–(6.17)); these do an excellent job of predicting high intensity regions in the spectrogram for fully nonlinear numerical solutions. This approach has allowed us to derive a quantitative description of the modes in the so-called leading wave component identified by Torsvik et al. (2015b), including the parts that are due entirely to steep nonlinear waves, without the need to include finite-depth effects in our modelling. Finally, we showed that the frequency increase in the measured transverse waves component of an experimental spectrogram is possibly due to the ship accelerating before passing by the sensor (and not due to nonlinearity).

We are not in a position to provide an explanation for the cause of the precursor solitary wave in Figure 6.1, nor have we explained the existence of the two lines of intensity that appear to meet on ω_1 at $t \approx 21{:}32$ and $f \approx 0.3$ in the same figure. There are many effects that could potentially be the cause of these additional features. For example, the precursor solitary wave could be due to "precursor solitons" that are generated by vessels moving in shallow water (Soomere 2007). On the other hand, the two lines of intensity could be due to other slower vessels, either further away or closer to the sensor, or perhaps even a single accelerating vessel closer to the sensor.

The analytical results for the linear (6.12) and second-order dispersion curves (6.16)–(6.17) will hold for any problem in infinite depth for which the ship can be well approximated by a single disturbance. These results could be easily extended to flows of constant finite depth by changing the dispersion relation, phase velocity and group velocity used in equations (6.8)–(6.11). The approach can also be extended to 'ships' characterised by two disturbances (representing bow and stern waves) by including a second time shifted linear dispersion curve, and by considering up to four distinct waves (transverse and divergent waves from both disturbances) in the second order-approximation (6.13). Such an adjustment in the theory could be relevant for long thin ships (Noblesse et al. 2014; Zhu et al. 2015). We note, however, that if the time shift

between the two disturbances is sufficiently small, it will be difficult to differentiate between the two linear dispersion curves and, instead, the interference effects will be captured in the variation of the colour intensity.

Our work provides a deeper insight into the signature left behind in the wakes of ships. This work is important because spectrogram analysis in the real world is only useful if users understand how to identify the key features of a time-frequency heat map and relate them to physical properties of the moving vessel. As mentioned in the Introduction, an application of this work is to interpret data from an echo sounder placed in a shipping channel, with the goal of measuring the wave energy emitted by various vessels. This information is important for monitoring damage to the coast, docked vessels or man-made structures.

6.7 Computer code

The code used to generate Figure 6.2(b) is provided at:
`https://github.com/rPethiyagoda/Pethiyagoda-PhD-thesis-code`.

7 Conclusions

In this chapter we summarise the results and contributions of the thesis, and propose areas for further research.

7.1 Summary

The broad aims of this thesis were to develop new efficient numerical techniques for computing steady nonlinear ship wave patterns and to apply linear water wave theory and nonlinear simulations to study various properties of these ship wave patterns, such as the shape of the waves, the wake angle, and the frequency distribution at a fixed point in space. Specifically, the objectives as described in Chapter 1 were:

1. To apply Jacobian-free Newton-Krylov methods to develop a new framework for solving steady nonlinear free-surface flow problems in three dimensions with significantly less computational expense than existing methods; furthermore, to utilise graphics processing unit (GPU) technology to accelerate the computations. The focus here is on problems that involve classical Kelvin ship wave patterns but, more generally, the objective is to develop an approach that is versatile enough to apply to a wide range of nonlinear free-surface flow problems.

2. To use linear water wave theory and nonlinear simulations (from Objective 1) to explain recent observations presented by Rabaud and Moisy (2012, 2013) that suggest the wake half-angle θ_{app} that is observed for real vessels moving in the open sea is not the Kelvin angle $\arcsin(1/3)$, but in fact decreases with speed U like $O(U^{-1})$ for sufficiently large U. In order to determine the various effects on the apparent wake angle θ_{app}, the objective is to consider model problems with a number of different disturbances (that generate the waves) in both infinite and finite depth.

3. To use linear water wave theory, weakly nonlinear theory and nonlinear simula-

tions (from Objective 1) to identify features of ship wave patterns through the use of spectrograms and to isolate linear and nonlinear effects. The objective is to provide new theory and explanations for the patterns in spectrograms of ship waves that enable the end-user to infer characteristics of a ship, based on an experimental spectrogram.

The results for each objective are summarised below.

7.1.1 Numerical method for computing nonlinear ship wave patterns

In Chapter 3 we considered the fully nonlinear problem of free-surface flow past a submerged point source in a fluid of infinite depth. We used a boundary integral method to reformulate the problem into an integro-differential equation coupled with Bernoulli's equation. The integro-differential equation and Bernoulli's equation were discretised onto a mesh on a truncated domain, giving a system of nonlinear equations (Forbes 1989; Părău and Vanden-Broeck 2002). We utilised a preconditioned Jacobian-free Newton-Krylov (JFNK) method (Brown and Saad 1990) to solve the resulting nonlinear system of equations. To ensure the efficiency of the JFNK method, we developed a block-banded linear preconditioner, whose values are taken from the analogous linear problem. The preconditioner serves to approximate the true Jacobian. Because all elements are known explicitly, the linear preconditioner is fast to form. The block-banded structure allows for fast factorisation and efficient storage in system memory. An added feature of the linear preconditioner is its independence of the nondimensional parameter ϵ (a measure of nonlinearity). This requires that the preconditioner only needs to be formed once while computing multiple solutions on the same mesh and Froude number. With the application of the JFNK method, we computed solutions on meshes with a much larger number of collocation points than any contemporary mesh used at the time of publication.

Chapter 6 contains an extension to the JFNK method provided in Chapter 3. The proposed extension is to calculate a solution over a larger domain by dividing the domain into panels in the direction of flow. Starting from the farthest upstream panel, we compute each panel sequentially downstream using the previously computed solutions as input into the current panel. We refer to this as the sub-domain stitching method. This extension allows for solutions over a much larger domain than the original method discussed in Chapter 3, which is essential for our work on spectrograms (Chapter 6). An unfortunate consequence of the sub-domain stitching method is that it introduces spurious sinusoidal numerical waves emanating from the boundaries between panels. However, these numerical waves are easily identifiable in the spectrogram, and hence do no harm in the context in which the numerical solution has been used.

7.1.2 The apparent wake angle of a ship

The properties of the apparent wake angle θ_{app} were the subject of Chapters 4 and 5. In Chapter 4 we considered the effect "ship" speed and size has on the apparent wake angle, with the "ship" being represented by a submerged point source or doublet (analogous to a submarine). We chose this configuration to utilise the numerical scheme developed in Chapter 3 and to remove the possibility of bow and stern wave interaction, like those discussed in Noblesse et al. (2014).

We define the apparent wake angle θ_{app} as the angle between the centreline of the wake and a line of best fit going through the highest peaks in the wake. We used linear analysis to show that the apparent wake angle exhibited an $O(1/F_L)$ decrease for $F_L \gg 1$, where F_L is the Froude number (a nondimensional representation of speed), for both flows past a source and doublet. The linear results were consistent with the work by Darmon, Benzaquen, and Raphaël (2014) and Ellingsen (2014), who used a pressure distribution to represent the "ship". The apparent wake angle for nonlinear ship waves, computed using the method in Chapter 3, is plotted for a range ϵ (μ), a measure of source (doublet) strength and constant values of F_L. We show that, for flow past a point source, increasing ϵ (nonlinearity) increases the apparent wake angle to a value greater than Kelvin's angle (the maximum angle for linear flows). Similarly, for flow past a doublet, increasing nonlinearity increases the apparent wake angle. However, the apparent wake angle only increases above Kelvin's angle for low Froude numbers. The increasing of the apparent wake angle to a value greater than Kelvin's angle is an interesting result that deserves to be explored for different driving forces (ie. pressure distributions).

In Chapter 5 we consider the effect of ship speed on the apparent wake angle for linear finite depth flow past a pressure distribution. In contrast to the infinite depth linear flows, there are now two nondimensional parameters of interest, F_H, the depth-based Froude number and δ, the nondimensional pressure size. Finite depth ship waves can be categorised as subcritical, $F_H < 1$, exhibiting both transverse and divergent waves, and supercritical flows, $F_H > 1$, exhibiting only divergent waves. We discovered that for sufficiently deep flows, $\delta < 1$, the apparent wake angle was not greatly affected by the change of flow regimes. Similar to the infinite depth flows, the wake angle decreases like $\kappa/F_H = \kappa/(\sqrt{\delta}F_L)$ where κ is a constant that depends on δ and F_L is the length-based Froude number. The value of κ monotonically increases as δ increases (the fluid depth decreases), and asymptotically approaches 1 as $\delta \to \infty$.

7.1.3 Spectrograms on nonlinear ship waves

In Chapter 6 we consider free-surface flow past a pressure distribution in infinite depth and we examine spectrograms produced by taking multiple short-time discrete Fourier

transforms of a cross-section of the ship wake in the direction of flow. For linear flows we show that the colour intensity in the spectrograms follows the linear dispersion curve (6.12) that consists of two branches, a lower and upper branch representing the transverse and divergent waves, respectively. Additionally, the distribution of colour intensity depends on the Froude number, with the colour intensity appearing primarily on the lower branch for low Froude numbers and primarily on the upper branch for large Froude numbers. This is consistent with the well known behaviour of ship wakes being dominated by transverse waves for low Froude numbers and dominated by divergent waves for large Froude numbers.

Further, we examined the effect of nonlinearity on the measured spectrogram of a ship wake. Using weakly nonlinear theory by Hogben (1972), we derived four additional second-order dispersion curves by doubling the linear dispersion curve and adding/subtracting the two branches to/from each other, see equations (6.16) and (6.17). The additional dispersion curves well approximate the location of the colour intensity for the spectrograms of nonlinear ship waves. However, the colour intensity may only appear on select dispersion curves depending on the Froude number. The second-order dispersion curves were shown to match up with an experimental spectrogram by Didenkulova et al. (2013), with the exception of the transverse wave branch. To explain the discrepancy, we considered the effect of an accelerating ship. We found that, given a rough approximation of the ship's velocity, the dispersion curve for an accelerating ship accounts for the discrepancy.

7.2 Contributions to the literature

7.2.1 Objective 1

The numerical scheme we developed and implemented in Chapter 3 allows us to accurately compute the ship wake generated by an idealised disturbance (submerged singularity, surface pressure distribution, etc.) in an infinite depth fluid. The significance of this work is that solutions can now be calculated on meshes with a greater number of collocation points than any presented in contemporary literature for the boundary integral method. The added accuracy, afforded to us from our work in Chapter 3, allows us to compute highly nonlinear solutions like never before. One of the key features of the new computational framework is that it should be easily adapted to a range of configurations not considered here (and for two-dimensional free-surface flows, which is discussed in Appendix A). The highly nonlinear solutions can then be used for either, measuring the apparent wake angle (Chapter 4). The nonlinear properties of ship wakes presented in Chapters 4 could not have been confirmed without the work in Chapter 3.

The extension to the numerical scheme given in Chapter 6, referred to as the sub-domain stitching method, allows us to further extend the solution domain beyond what was possible in Chapter 3. The significance of the sub-domain stitching method is that it is now possible to apply spectrogram analysis to the solutions (Chapter 6), which was not previously possible.

7.2.2 Objective 2

In Chapter 4 we present the effect of nonlinearity on the apparent wake angle, a feature that has not been explored elsewhere at the time of writing. Additionally, we show that, for very high nonlinearity, the apparent wake angle can be greater than Kelvin's angle, a result alluded to by Hogben (1972). This work is significant because it shows that nonlinearity can be an important effect to consider if one was to attempt to use wake angle to predict ship speed, for example.

In Chapter 5 we look at the similar finite depth wake angle problem as Zhu et al. (2015), although our work was conducted before the paper by Zhu et al. was published. As we define the wake angle by the highest wave peaks (Chapter 4), instead of using the interference model of Noblesse et al. (2014), we draw different conclusions about the nature of the apparent wake angle for large Froude numbers. We identify the seemingly contradictory result that, as the depth-based Froude number approaches unity, the wedge angle increases but the observed wake angle remains constant or decreases. We then explain this contradiction by noting that, for sufficiently deep fluid, the peaks of the wake do not move away from the centreline, increasing the wake angle. This work explains why in the real world we do not observe large wake angles when the wedge angle is large.

We note that our work on studying the apparent wake angle was initially motivated by Rabaud and Moisy (2013) which was presented at the American Physical Society's Division of Fluid Dynamics meeting in San Diego in November 2012 (Rabaud and Moisy 2012)[1]. Rabaud and Moisy's work set off a new series of papers on this topic. Rabaud and Moisy's paper was published in May 2013, but left open a number of issues as explained in Section 2.3. We worked on this topic for the subsequent months, identifying the wave peak locations and their relation to ship speed as a possible explanation for the phenomena observed by Rabaud and Moisy (2013). However, Darmon, Benzaquen and Raphaël posted their preprint on the arXiv in September 2013, entitled "A solution to the Kelvin wake angle controversy" (arXiv:1309.6751v1). After the paper was published on arXiv, we expanded our work to include the effects of nonlinearity before submitting our first version on the arXiv (arXiv:1405.2500v1), initially entitled "What is the angle

[1]Principal Supervisor Prof Scott McCue attended this seminar.

of a nonlinear Kelvin ship wave pattern?".

As discussed in some detail in Section 2.3, there has been quite a deal of interest in this topic since the initial paper by Rabaud and Moisy (2013). For example, both groups Rabaud & Moisy and Darmon, Benzaquen & Raphaël have published a number of subsequent articles that cover extensions such as considering a non-axisymmetric pressure distribution (Benzaquen, Darmon, and Raphaël 2014) or including surface tension (Moisy and Rabaud 2014a). In addition, since 2014 a research group in China led by Professor Francis Noblesse has been working on closely related problems, having published nine papers that focus on the interference effects of waves generated by the bow and stern of a ship or the two bows of a catamaran and the consequences for the apparent wake angle. Thus, while the new results published in this thesis were generated in 2013-15, an extensive body of work in the area has been published, which explains why much of the literature review covers papers published after those associated with Chapters 4 and 5.

7.2.3 Objective 3

Finally, in Chapter 6 we make a vital contribution to the study of spectrograms of ship wakes, an under-represented area in fluid dynamics. We give simple equations for the nondimensional linear and second order dispersion curves represented in the spectrogram; a generalisation of the linear dispersion curve was previously given in Wyatt and Hall (1988). We verify the dispersion curves by comparing with an experimental spectrogram. This work is significant because it demonstrates how the key linear features can be described quantitatively (via the linear dispersion curve) and qualitatively (via regions of high and low intensity) without resorting to a CFD solution with an actual real ship hull.

Further, we have considered the effect of an accelerating ship on the dispersion curve. Considering an accelerating ship, together with the second order dispersion curve, has allowed us to provide possible explanations of features recently observed in experimental spectrograms by only considering an idealised disturbance. All of these properties of the dispersion curves can now be used to infer properties of a ship given only the measured spectrogram.

7.3 Future work

In this section we outline the potential future work inspired by the results in this thesis.

7.3.1 Numerical methods for nonlinear ship wave patterns

In Chapter 3 we applied a Jacobian-free Newton-Krylov (JFNK) method to compute solutions to the nonlinear problem of uniform flow past a submerged point source in a fluid of infinite depth. We modified the problem to flow past a submerged doublet in Chapter 4 and flow past a pressure distribution in Chapter 6. In all cases, the linear block-banded preconditioner developed in Chapter 3 was used. One potential future problem is to consider uniform flow of a fluid of constant or variable depth, a problem that has been extensively studied in two dimensions (Binder, Vanden-Broeck, and Dias 2005; Cokelet 1977; Havelock 1918; Lustri, McCue, and Binder 2012; Wade et al. 2014). The introduction of a variable finite depth will require additional equations, from evaluating the boundary integral equation along the bottom, be added to the system of nonlinear equations detailed in Chapter 3. With the additional nonlinear equations, the 2×2 submatrix structure of the Jacobian (Figure 3.1(a)) is replaced by a 3×3 structure, where at least 3 of the additional submatrices are fully dense. The increased submatrix dimension and the added dense submatrices greatly restrict the number of mesh collocation points due to system memory utilisation. Therefore, a new preconditioner matrix must be developed to ensure the effectiveness of the JFNK method.

An additional problem is to use the JFNK method to solve problems in two dimensions in much the same way as Chapter 3. Gardiner et al. (2015) has adapted this broad approach for Hele-Shaw flows which are formulated as integro-differential equations which, after collocation, lead to a dense Jacobian. Preliminary work on two-dimensional steady free-surface flow problems is the subject of Appendix A. For the two-dimensional problem, conformal mapping techniques are used to derive the boundary integral equation and Bernoulli's equation. Because the derivative of the resulting boundary integral equation and Bernoulli's equation with respect to the unknowns is simple (linear in the case of the boundary integral equation) and easy to evaluate exactly, the nonlinear entries of the Jacobian are used for the preconditioner matrix. Unlike the three-dimensional problem, the Schur compliment generated during the preconditioner factorisation step (see section 3.7.3) is only banded if both the top left and bottom right submatrices (A and D in section 3.7.3) have had elements removed. By intelligently removing elements from the full nonlinear Jacobian, we are able to generate a banded preconditioner matrix that can be used when implementing the JFNK method. Using the JFNK method, we can produce results on meshes with over 100,000 collocation points. Using the added resolution, we were able to compute results for a variety of flow configurations. For example, we were able to recreate the problem of uniform flow over a step presented by Chapman and Vanden-Broeck (2006) and produce solutions exhibiting waves much smaller than those presented in the paper (all

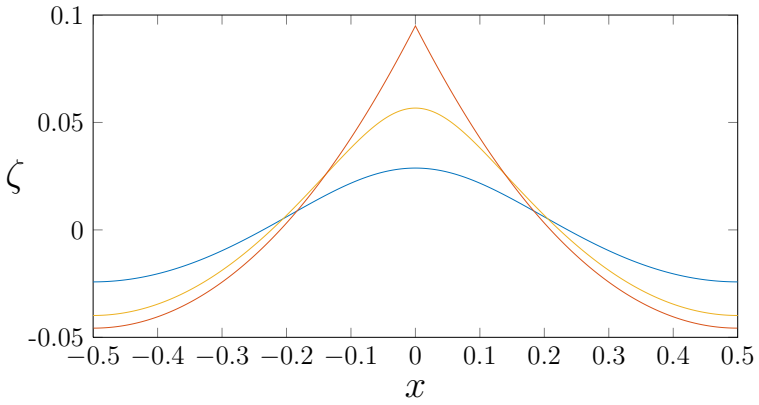

Figure 7.1: A plot of periodic two-dimensional ship waves for different measures of amplitude, ϵ, where $0 \leq \epsilon \leq 1$, $\epsilon = 0$ corresponds to the flat surface, $\zeta = 0$, and $\epsilon = 1$ corresponds to the highest possible wave. The waves for $\epsilon = 0.4, 0.7$ and 1 are given by the blue, orange and red curves, respectively. The curves were computed by the method of Vanden-Broeck and Miloh (1995).

this preliminary work is contained in Appendix A).

7.3.2 Highly nonlinear flows

With the application of the JFNK method in Chapters 3, 4 and 6 we are now able to compute highly nonlinear solutions to a variety of ship wave problems. This opens up the possibility of exploring the features of highly nonlinear waves. One of the more interesting features is the limiting configuration, the shape of the highest possible wave. The limiting configuration for a two-dimensional wave is well known to form a corner with an internal angle of 120° (Lamb 1916). The highest single two-dimensional wave is shown in Figure 7.1 as the red curve, $\epsilon = 1$ where ϵ is a measure of amplitude, along with two waves of smaller amplitude, $\epsilon = 0.4, 0.7$ given by the blue and orange curves, respectively. The curves were computed by the method of Vanden-Broeck and Miloh (1995).

Unfortunately, it is unknown what the shape of the highest wave in three dimensions is. It is possible that a corner could form on the crest of the highest wave. However, if a corner forms, what is its nature? Does the corner exist only in one direction (ie. the directional derivative is discontinuous in one direction at the crest) and if so, what direction is the corner and what is its internal angle? Alternatively, is the corner in the form of an apex (ie. the directional derivative is discontinuous in all directions at the crest) giving a stagnation point and, if so, what is the internal angle for every direction? In either case of limiting configuration, it is also possible that the properties of the highest wave change depending on the properties of the ship wave (eg. orientation of the wave crest with respect to the direction of flow). These questions are left for

further study.

Another feature to observe is the apparent wake angle discussed in Chapters 4 and 5. Even with all the recent work done on the apparent wake angle (Darmon, Benzaquen, and Raphaël 2014; Ellingsen 2014; Ma et al. 2016; Noblesse et al. 2014; Zhang et al. 2015; Zhu et al. 2015), Chapter 4 presents the only examination of the effect of nonlinearity with respect to the wake angle, and only for a submerged source/doublet. There are still many different driving forces (pressure distributions, distribution of sources, real ship hulls, etc.) yet to be analysed for nonlinear flows. The apparent wake angle will evolve differently as nonlinearity increases depending on the driving force (see Figure 4.7 for the differences between flow past a submerged source and a submerged doublet). Additionally, Figure 7.2 shows the evolution of the apparent wake angle with nonlinearity, for the problem of free-surface flow past a pressure distribution as defined in Section 6.2. The behaviour of the apparent wake angle for a pressure distribution (Figure 7.2) is closer to that of a submerged doublet (Figure 4.7(b)) than a submerged source (Figure 4.7(a)), but still does not exhibit the exact same properties. The difference between the behaviours of nonlinear wake angle for different driving forces stresses the importance of choosing the correct idealised disturbance for approximating the effect of a ship. Thus, the effect of nonlinearity on the apparent wake angle should be explored for many different driving forces.

7.3.3 Spectrograms of ship waves

In Chapter 6 we were able to theoretically predict the appearance of multiple spectrogram components of an experimental ship wave presented by Didenkulova et al. (2013). However, we were unable to determine the cause of the precursor wave component identified by Torsvik et al. (2015b). There are still many potential causes that have not been considered, for example finite depth effects, either constant depth or variable depth (for waves approaching the shore) or hull shape. The effects of these properties should be determined, either analytically or experimentally, to allow for spectrograms to be more widely used in ship wave analysis.

Our work has the potential to open up a whole new area of research. One aspect of this new area involves analysing the effects of different disturbances: idealised disturbances (eg. non-axisymmetric pressure distributions, thin-ship approximations, etc.), realistic hull/submarine shapes calculated using a CFD package or multi-hull ships (eg. catamarans, outriggers, etc.). Another aspect, is the effect of finite depth. Finite depth effects can be further subdivided as either constant or variable depth. Ship waves in constant depth can be classified as subcritical ($F_H < 1$), exhibiting both transverse and divergent waves, and supercritical ($F_H > 1$), exhibiting only divergent waves. The

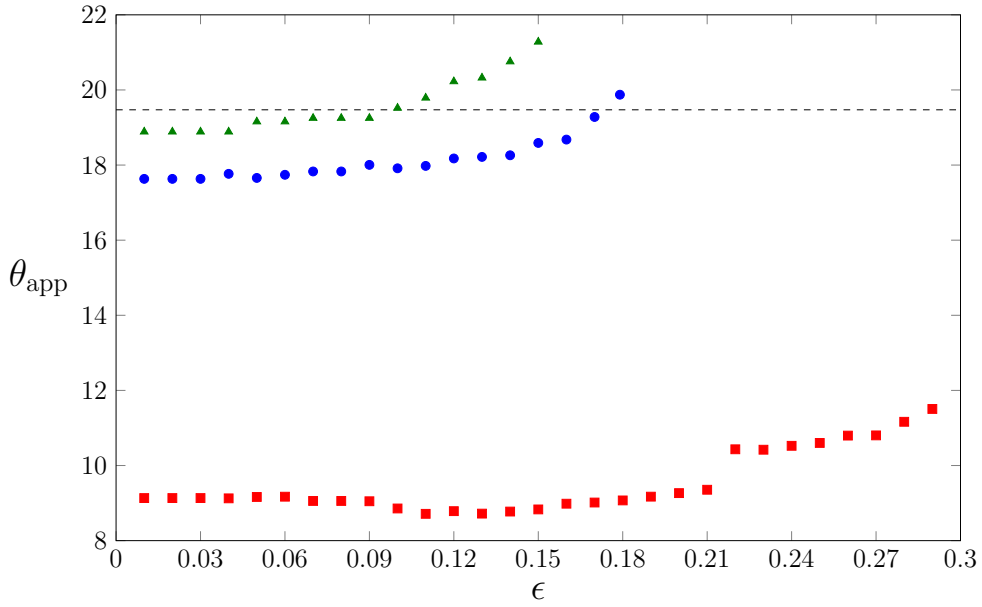

Figure 7.2: A plot of apparent wake angle θ_{app} (in degrees) against pressure strength, ϵ, for flow past a pressure distribution, as defined in Section 6.2 with $F_L = 0.5$ (green triangles), $F_L = 0.7$ (blue circles) and $F_L = 1.5$ (red squares). The dashed line is Kelvin's angle, $\arcsin(1/3) \approx 19.47°$. These results are the only known results for nonlinear flow past a pressure distribution, and generalise the results of Darmon, Benzaquen, and Raphaël (2014), which were for linear flows only.

spectrograms will differ for the different regimes (subcritical and supercritical) and special attention must be given to near critical ship waves (F_H near 1). Variable depth can be used to simulate ship waves approaching a river bank or shore line. The changing depth introduces the features of wave diffraction, refraction, reflection and wave shoaling, the effect of which must be understood to better interpret the information provided by ship waves measured close to shore (ie. the experiments by Didenkulova et al. (2013)).

Further research into the energy contained in various wave components, as in Torsvik et al. (2015b), should continue to be pursued in all aspects of spectrogram research. Additionally, the validity of using spectrograms to detect ship waves amongst the background noise of the ocean (ie. detecting the wake of a submerged submarine) is an interesting possible problem for future study.

Appendices

A Efficient computation of two-dimensional steady free-surface flows

Abstract

We consider a family of steady free-surface flow problems in two dimensions, concentrating on the effect of nonlinearity on the train of waves that appear downstream of a disturbance. By exploiting standard complex variable techniques, these problems are formulated in terms of a coupled system of Bernoulli's equation and an integral equation. When applying a numerical collocation scheme, the Jacobian for the system is dense, as the integral equation forces each of the algebraic equations to depend on each of the unknowns. We present here a strategy for overcoming this challenge, which leads to a numerical scheme that is much more efficient than what is normally employed for these types of problems, allowing for many more grid points over the free surface. In particular, we provide a simple recipe for constructing a sparse approximation to the Jacobian that is used as a preconditioner in a Jacobian-free Newton-Krylov method for solving the nonlinear system. This recipe is based on ideas proposed in our previous work (R. Pethiyagoda, S. W. McCue, T. J. Moroney, and J. M. Back. Jacobian-free Newton-Krylov methods with GPU acceleration for computing nonlinear ship wave patterns. J. Comput. Phys., 269:297–313, 2014.) for three-dimensional flows. We use this approach to compute numerical results for flows past pressure distributions, a surface-piercing object and bottom topographies.

A.1 Introduction

Steady nonlinear two-dimensional free-surface flow problems have been popular since the early 1980s, with computers allowing researchers to numerically solve the fully nonlinear problems using complex variable methods. One well-cited example is Forbes and Schwartz (1982), who considered the two-dimensional problem of flow of an ideal

fluid past a semi-circular bottom obstruction. Numerical solutions show how a train of waves develop on the free surface downstream from the disturbance, and how the waves themselves steepen as the size of the semi-circular disturbance increases. The crests of the waves become sharper, the troughs broader, and the wavelength decreases when compared to that predicted by linear theory. Since that time, this general approach has been adapted and extended in many studies for other bottom topographies with curved and straight boundaries (see, for example, Binder, Blyth, and McCue 2013; Binder, Dias, and Vanden-Broeck 2006, 2008; Dias and Vanden-Broeck 2002; Forbes 1982; King and Bloor 1987, 1990; Vanden-Broeck 1987; Zhang and Zhu 1996).

Other well-studied two-dimensional examples include flow past a pressure distribution that is applied to the surface of the stream (Schwartz 1981), flows with surface-piercing solid bodies (Farrow and Tuck 1995; Vanden-Broeck 1980) and flows past submerged obstacles or singularities (Forbes 1985; King and Bloor 1989). These configurations are interesting in their own right, but also provide simple models for flow due to a steadily moving two-dimensional ship or submarine. In each of these cases, a train of waves develops downstream from the disturbance. The complex variable formulation and subsequent numerical solution provides insight into how the size and steepness of the waves depends on the nature of the disturbance.

The overall approach taken for all of these examples is essentially the same. The Cauchy integral formula is used to enforce Laplace's equation, leaving an integral equation that holds on the free surface. This equation is coupled with Bernoulli's equation, also applied to the free surface. Discretising the equations and applying the integral equation at mesh points (or half-mesh points) leads to a system of algebraic equations, which can be solved using Newton's method. The nonlocal nature of the integral equation results in each of the unknowns at the mesh points appearing in all of the algebraic equations and, as such, the Jacobian of the system is either fully dense or has a fully dense block. For this reason, the number of mesh points used in practice is limited.

By considering a number of prototype problems, we illustrate shared properties of the Jacobians for each of these two-dimensional steady free-surface flows, such as the general block structure and the entries that depend on the integro-differential equation. Our core contribution is to demonstrate how the nonlinear systems of algebraic equations can be solved using a Jacobian-free Newton-Krylov method, which for a range of problems does not require the formation and factorisation of the dense Jacobian, and is much more efficient than standard schemes. An important component of the scheme is the formation of a sparse preconditioner that is a sufficiently good approximation to the full Jacobian. The scheme allows for solutions on much larger meshes and works equally well for all the problems treated.

The structure of the appendix is as follows. In section A.2 we formulate the problem of flow past a pressure distribution using the boundary integral approach mentioned above. This problem illustrates all of the key features we are concerned with. Section A.3 is devoted to outlining our new numerical scheme. In sections A.4 and A.5 we demonstrate our approach via examples. Finally, in section A.6 we discuss the significance of our study.

A.2 Governing equations

To begin, we consider a general two-dimensional free-surface flow problem for an ideal fluid of infinite depth with an unperturbed speed U in the positive x-direction. The fluid is subject to a prescribed surface pressure distribution $p(\phi)$, where the velocity potential of the fluid $\phi(x, y)$ satisfies Laplace's equation in the fluid domain

$$\nabla^2 \phi = 0, \tag{A.1}$$

and Bernoulli's equation on the surface $y = \eta(x)$

$$\frac{1}{2}|\nabla\phi|^2 + \frac{y}{F_L^2} + p(\phi) = \frac{1}{2}, \qquad \text{on } y = \eta(x), \tag{A.2}$$

where $F_L = U/\sqrt{gL}$ is the Froude number, g is acceleration due to gravity and L is some length scale relevant to the problem. The pressure distribution has the effect of disturbing the free-surface, causing a train of waves to develop downstream, as indicated in Figure A.1(a). From a practical perspective, this pressure can be interpreted as mimicking a two-dimensional air cushion vehicle such as a hovercraft. This nonlinear free-surface problem, which can be considered a prototype two-dimensional flow, has received a variety of attention since the work of Schwartz (1981).

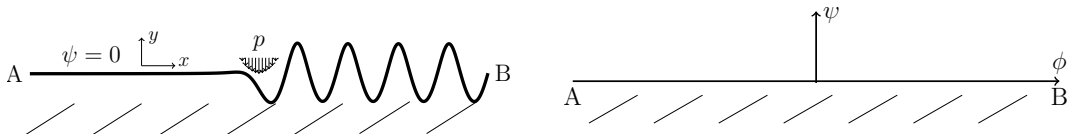

(a) z-plane (b) w-plane

Figure A.1: A schematic for flow past a pressure distribution, p, in infinite depth.

Considering the problem in the complex plane, we know that $w(z) = \phi + \mathrm{i}\psi$ is an analytic function of $z = x + \mathrm{i}y$, where ψ is the streamfunction. We set $\psi = 0$ on the free surface $y = \eta(x)$, thus mapping the fluid domain to the lower half-plane (Figure A.1). Differentiating $w(z)$ with respect to z gives

$$\frac{\mathrm{d}w}{\mathrm{d}z} = u - \mathrm{i}v = \mathrm{e}^{\tau - \mathrm{i}\theta}, \tag{A.3}$$

where u and v are the horizontal and vertical fluid velocities, respectively. Here e^{τ} is the fluid speed, while θ is the angle the streamline makes to the horizontal.

Because $\mathrm{d}w/\mathrm{d}z$ is an analytic function of w we can use Cauchy's integral formula to perform a contour integral of $\log(\mathrm{d}w/\mathrm{d}z)$ over the lower half-plane. Taking the imaginary part leads to the Halbert transform

$$\tau(\phi) = \frac{1}{\pi}\fint_{-\infty}^{\infty} \frac{\theta(\phi')}{\phi' - \phi}\,\mathrm{d}\phi', \qquad -\infty < \phi < \infty. \tag{A.4}$$

By enforcing (A.4), Laplace's equation (A.1) is identically satisfied. To satisfy Bernoulli's equation in terms of τ and θ, we differentiate equation (A.2) with respect to ϕ, using the relation $|\nabla\phi| = \mathrm{e}^{\tau}$, to give

$$F_L^2 \mathrm{e}^{3\tau}\frac{\mathrm{d}\tau}{\mathrm{d}\phi} + \sin\theta + F_L^2\mathrm{e}^{\tau}\frac{\mathrm{d}p}{\mathrm{d}\phi} = 0, \qquad -\infty < \phi < \infty. \tag{A.5}$$

Equations (A.4) and (A.5) are now our two governing equations for the two unknowns $\tau(\phi)$ and $\theta(\phi)$, that depend on the Froude number F_L and the prescribed pressure distribution $p(\phi)$.

A.3 Numerical scheme

A.3.1 Collocation

To solve the problem outlined in section A.2 computationally, we will construct a system of nonlinear equations to be solved with a Jacobian-free Newton-Krylov method. First, we need to truncate the domain from $-\infty < \phi < \infty$ to some finite domain. We then discretise the functions τ and θ along the truncated surface at the N equally spaced mesh points ϕ_i, for $i = 1, \ldots, N$, giving the values $\tau_i = \tau(\phi_i)$ and $\theta_i = \theta(\phi_i)$. The values τ_1 and θ_1 are given by the radiation condition far upstream. We are then left with $2(N-1)$ unknowns to be arranged in the vector $\mathbf{u}$,

$$\mathbf{u} = [\tau_2, \ldots, \tau_N, \theta_2, \ldots, \theta_N]^T. \tag{A.6}$$

We require $2(N-1)$ equations to close this system. Our first $N-1$ equations come from enforcing Bernoulli's equation (A.5) at the half-mesh points,

$$\tau_{i+1/2} = \frac{\tau_i + \tau_{i+1}}{2}, \quad \theta_{i+1/2} = \frac{\theta_i + \theta_{i+1}}{2}, \quad \frac{\mathrm{d}\tau_{i+1/2}}{\mathrm{d}\phi} = \frac{\tau_{i+1} - \tau_i}{\Delta\phi}, \tag{A.7}$$

for $i = 1, \ldots, N-1$ where $\Delta\phi$ is the mesh spacing. Our final $N-1$ equations come from the integral equation (A.4), but first we deal with the singularity by the addition and subtraction of the term

$$\frac{\theta(\phi)}{\pi}\fint \frac{1}{\phi' - \phi}\,\mathrm{d}\phi',$$

to give

$$\tau(\phi) = \frac{1}{\pi} \fint_{\phi_1}^{\phi_N} \frac{\theta(\phi') - \theta(\phi)}{\phi' - \phi} \, \mathrm{d}\phi' + \frac{\theta(\phi)}{\pi} \ln \left| \frac{\phi_N - \phi}{\phi_1 - \phi} \right|, \qquad -\infty < \phi < \infty. \tag{A.8}$$

Now we can enforce equation (A.8) at the half-mesh points (A.7) by moving all terms to the left hand side and computing the integral by the trapezoidal rule to form our final $N-1$ equations. We have then a system of $2(N-1)$ equations, $\mathbf{F}(\mathbf{u}) = \mathbf{0}$, for the $2(N-1)$ unknowns $\mathbf{u}$. We solve this system using a preconditioned Jacobian-free Newton-Krylov (JFNK) method.

A.3.2 The Jacobian-free Newton-Krylov method

The JFNK method is a Newton-like scheme where the preconditioned Generalised Minimum Residual (GMRES) algorithm is used for the typical Newton solve step (Brown and Saad 1990; Saad and Schultz 1986). For clarity, the Newton solve step determines the search direction $\delta\mathbf{u}_k$ by solving the system

$$\mathbf{J}(\mathbf{u}_k)\delta\mathbf{u}_k = -\mathbf{F}(\mathbf{u}_k), \tag{A.9}$$

where $\mathbf{J}(\mathbf{u}_k)$ is the Jacobian evaluated at the kth iterate $\mathbf{u}_k$. The GMRES algorithm solves equation (A.9) by first solving for $\mathbf{z}$ in

$$\mathbf{J}(\mathbf{u}_k)\mathbf{P}^{-1}\mathbf{z} = -\mathbf{F}(\mathbf{u}_k), \tag{A.10}$$

where

$$\mathbf{z} = \mathbf{P}\delta\mathbf{u}_k, \tag{A.11}$$

and $\mathbf{P}$ is a preconditioner matrix. Equation (A.10) is solved by projecting obliquely onto the preconditioned Krylov subspace of dimension m

$$\mathcal{K}_m(\mathbf{J}_k\mathbf{P}^{-1}, \mathbf{F}_k) = \mathrm{span}\{\mathbf{F}_k, \mathbf{J}_k\mathbf{P}^{-1}\mathbf{F}_k, \ldots, (\mathbf{J}_k\mathbf{P}^{-1})^{m-1}\mathbf{F}_k\},$$

where for simplicity we write $\mathbf{J}_k = \mathbf{J}(\mathbf{u}_k)$, $\mathbf{F}_k = \mathbf{F}(\mathbf{u}_k)$. The preconditioner matrix $\mathbf{P}$, chosen such that $\mathbf{P} \approx \mathbf{J}_k$, is needed to keep the Krylov subspace dimension m small. Finally, we solve for $\delta\mathbf{u}_k$ using (A.11). The JFNK method is advantageous in that the full Jacobian does not need to be computed at every Newton iteration. The preconditioner matrix, however, must be chosen to be easily computed and inverted to make effective use of the method.

A.3.3 Preconditioning

By differentiating (A.5) and (A.8) with respect to the unknowns τ_i and θ_i for $i = 2, \ldots, N$, we can easily compute the exact Jacobian $\mathbf{J}_k$ by hand: details are provided

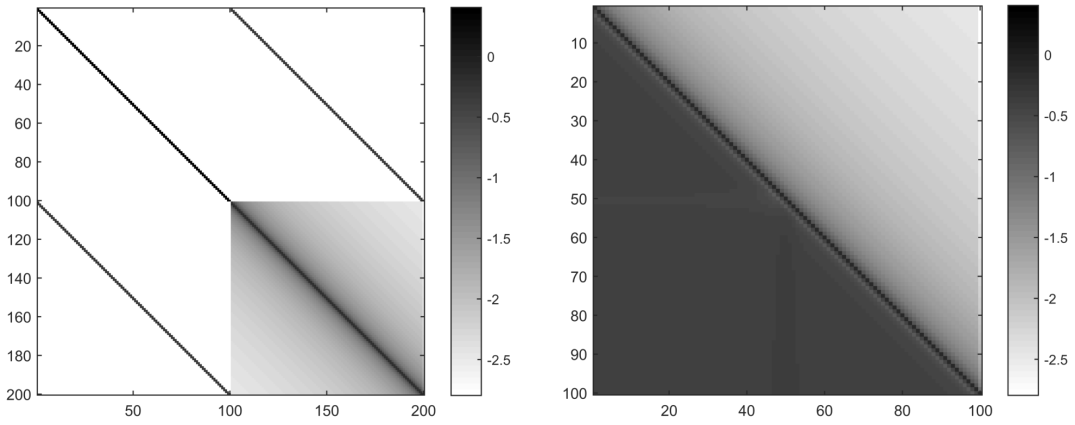

(a) Full Jacobian (b) Schur complement

Figure A.2: A visualisation of the magnitude of the (a) Jacobian and (b) Schur complement entries for the problem of flow past a pressure distribution given by (A.13) where $\mathbf{u}_k = \mathbf{0}$, $N = 101$, $\phi_1 = -20$, $\Delta\phi = 0.4$, $\epsilon = 0.1$ and $F_L = 1$. The entries are on a log scale: $\log_{10}|J_{i,j}|$ for all i, j. Each element is assigned a shade based on its value: the larger the value, the darker the shade.

in section A.7.1. A first thought might be to use the full Jacobian at the initial Newton iterate as a preconditioner, updated only as often as required to keep the Krylov subspace dimension from growing too large. Unfortunately, this would require storing and factorising a $2(N-1) \times 2(N-1)$ matrix, which would restrict the maximum number of mesh points allowable on a given machine due to available system memory.

A better approach exploits the structure of the Jacobian (Figure A.2(a)), noticing that it can be partitioned into four submatrices:

$$\mathbf{J} = \begin{bmatrix} A & B \\ C & D \end{bmatrix}, \tag{A.12}$$

where A, B and C are lower bidiagonal and D is fully dense. Block LU factorisation of this matrix requires only the storage of A, a sparse matrix, and the Schur complement $D - CA^{-1}B$ (Figure A.2(b)), while B and C need only be actioned as matrix products. This approach greatly reduces the storage requirements and factorisation time when using the Jacobian as the preconditioner matrix.

We can further reduce the storage and factorisation time by dropping selected matrix entries in order to force the Schur complement to be banded, thereby permitting banded storage and factorisation schemes to be used. This approach is motivated by the observation in Figure A.2(b) that the largest magnitude entries of the Schur complement occur within a small bandwidth of the main diagonal. To retain values only within a bandwidth $2b+1$, we first set entries $A_{i+1,i} = 0$ for $i = b + n(b-1)$ where $n = 0, 1, 2, \ldots$, thereby forcing A^{-1} to have lower bandwidth $b-1$. Then we set all

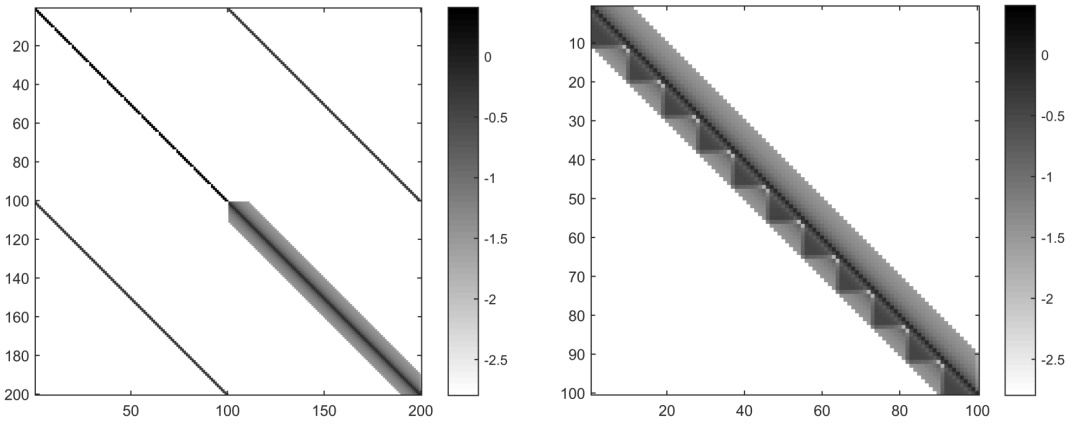

(a) Banded preconditioner (b) Banded Schur complement

Figure A.3: A visualisation of the magnitude of the (a) banded preconditioner and (b) banded Schur complement entries with upper and lower bandwidth $b = 10$ for the problem of flow past a pressure distribution given by (A.13) where $\mathbf{u}_k = \mathbf{0}$, $N = 101$, $\phi_1 = -20$, $\Delta\phi = 0.4$, $\epsilon = 0.1$ and $F_L = 1$. The entries are on a log scale: $\log_{10}|J_{i,j}|$ for all i, j. Each element is assigned a shade based on its value: the larger the value, the darker the shade.

entries of D outside bandwidth $2b + 1$ to be zero. The computed Schur complement $D - CA^{-1}B$ then inherits the bandwidth $2b + 1$. A banded preconditioner and Schur complement with upper and lower bandwidths $b = 10$ are shown in Figure A.3. Choosing an appropriate value of the bandwidth requires some experimentation, to find a suitable trade off between the efficiency of forming and factorising the preconditioner against its effectiveness at reducing the Krylov subspace dimension.

A.3.4 Implementation

To implement the JFNK method we used the Sundials KINSol package (Collier et al. 2011) with a MATLAB interface. The code to evaluate the nonlinear function $\mathbf{F(u)}$ was written in CUDA (Compute Unified Device Architecture) to run on a Graphics Processing Unit (GPU), which greatly reduced the evaluation time for this function. Factorising the preconditioner was performed using Intel's Math Kernel Library (MKL) to take advantage of a banded storage scheme. All remaining code, including forming the preconditioner as described in sections A.3.3 and A.7.1, was written in MATLAB. The high performance workstation used to produce the solutions in this appendix included 2× Intel Xeon E5-2670 CPUs with 2.66 GHz processors, K40 Nvidia Tesla GPU and 124 GB of system memory.

To compute highly nonlinear solutions a bootstrapping process was used, whereby a previously computed solution was used as the initial guess for the current solution.

Typically this was the solution from a similar, but more linear version of the problem (eg. for flow past a pressure distribution a previous solution with the same Froude number and a smaller value of ϵ was used).

A.4 Infinite depth flow examples

A.4.1 Flow past a pressure distribution

Flow past a pressure distribution has been well studied in both infinite depth (Schwartz 1981; Vanden-Broeck and Tuck 1984) and finite depth (Grimshaw and Maleewong 2013; Maki et al. 2012; Vanden-Broeck and Miloh 1996). The change in the wave train produced due to many different factors, such as surface tension (Grimshaw and Maleewong 2013) or a layer of mud under the water (Vanden-Broeck and Miloh 1996), among others, has also been considered. For simplicity, we will only consider infinite depth flows with no surface tension.

For simplicity, we consider flow past a pressure distribution given in dimensionless variables by

$$p(\phi) = \epsilon \mathrm{e}^{-\phi^2}, \tag{A.13}$$

where ϵ is the dimensionless pressure strength. The governing equations are given by equations (A.5) and (A.8) with $p(\phi)$ given by (A.13). The radiation conditions for this problem are $\tau_1 = \theta_1 = 0$.

Using our numerical scheme, we are able to generate solutions on meshes with $N = 120,001$ collocation nodes in under one hour on a high performance workstation. A preconditioner matrix with a submatrix bandwidth of 48,001, occupying roughly 65GB of system memory, was used to compute the solution. Figure A.4 shows the solution for flow past the pressure distribution (A.13) with $\epsilon = 0.08$ and $F_L = 0.7$. The total time required to bootstrap up to the $\epsilon = 0.1$ solution was approximately 35 hours. This solution represents a substantial increase in the number of collocation points used for two-dimensional free-surface flow problems in recent times. For example, the number of mesh points typically used is roughly $1000 \leq N \leq 2000$ (Lustri, McCue, and Binder 2012; Trinh, Chapman, and Vanden-Broeck 2011; Vanden-Broeck and Chapman 2002; Wade et al. 2014). The increased number of points can allow for a solution with much higher resolution or over a much larger domain.

A.4.2 Flow under a semi-infinite plate

The problem of flow past a semi-infinite plate is a common prototype for approximating bow and stern waves of a two-dimensional ship in infinite depth (Farrow and Tuck 1995; Vanden-Broeck 1980; Vanden-Broeck, Schwartz, and Tuck 1978; Vanden-Broeck and

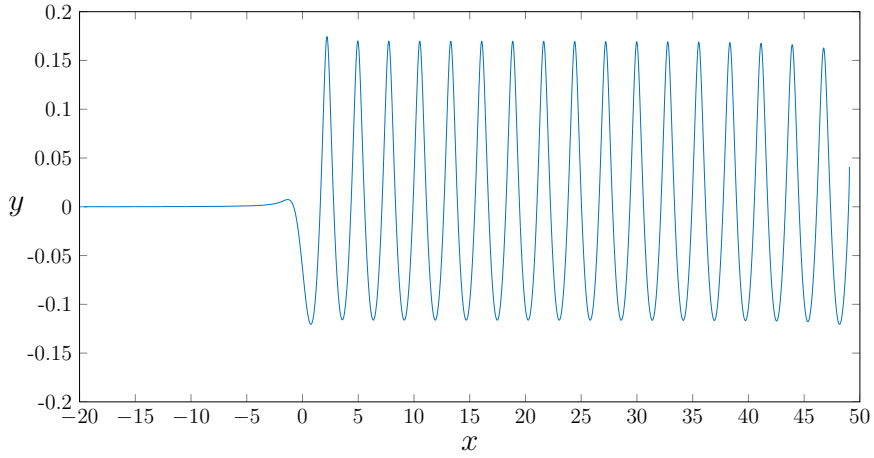

Figure A.4: A free-surface profile for flow past a pressure distribution for $F_L = 0.7$ and $\epsilon = 0.1$ where $N = 120,001$.

Tuck 1977; Trinh, Chapman, and Vanden-Broeck 2011) or finite depth (McCue and Forbes 1999, 2002; McCue and Stump 2000). The plate considered can either be horizontal for mathematical simplicity (Ogilat et al. 2011; Vanden-Broeck, Schwartz, and Tuck 1978; Vanden-Broeck and Tuck 1977) or curved for a better representation of a ship's hull (Farrow and Tuck 1995; Trinh, Chapman, and Vanden-Broeck 2011). For the following work, we only consider a horizontal plate with infinite depth fluid for simplicity.

We can take the numerical scheme from section A.3 and apply it to the specific case of flow under a semi-infinite plate displaced a distance L from the x-axis ($y = 0$). The complex governing equations (A.5) and (A.8) hold with $p(\phi) = 0$ for $\phi > 0$. The integral in equation (A.8) can be updated with the knowledge that the fluid surface is flat under the plate:

$$\tau(\phi) = \frac{1}{\pi}\int_0^{\phi_N} \frac{\theta(\phi') - \theta(\phi)}{\phi' - \phi}\mathrm{d}\phi' + \frac{\theta(\phi)}{\pi}\ln\left|\frac{\phi_N - \phi}{\phi_1 - \phi}\right|, \qquad 0 < \phi < \infty. \tag{A.14}$$

And finally the boundary conditions at the edge of the plate can be given as

$$\tau_1 = \frac{1}{2}\ln\left(1 \pm \frac{2}{F_{L,}^2}\right), \qquad \theta_1 = 0,$$

where the $\pm$ in τ_1 is taken as '$+$' for lowering the plate below the x-axis or '$-$' for raising the plate above the x-axis. The rest of the numerical method remains unchanged.

As with flow past a pressure distribution, we use $N = 120,001$ nodes and compute the solution using a preconditioner matrix with a submatrix bandwidth of 48,001. We have computed solutions for different Froude numbers and have plotted the steepness (ie. the amplitude of the wave over its wavelength) of the wave train of these solutions

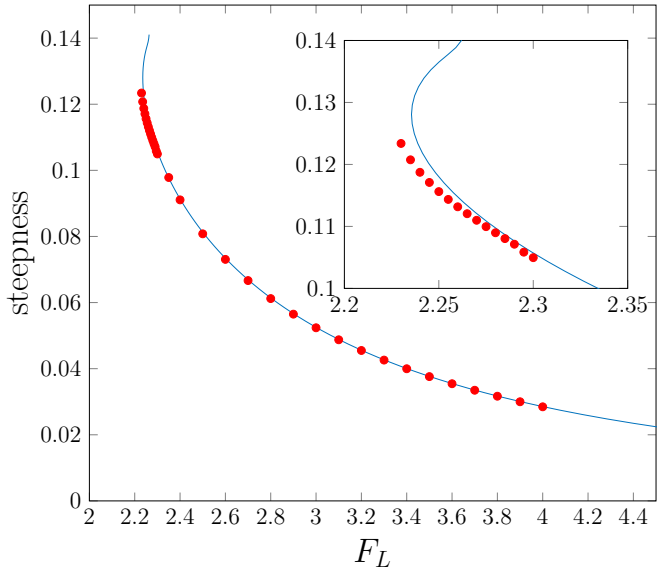

Figure A.5: A plot of the maximum steepness of a a wave train for flow under a semi-infinite plate against the Froude number (red dots). The solid line is the theoretical relationship given be equation (2.2) in Vanden-Broeck (1980). An inset focusing on the results for $2.2 < F_L < 2.35$ is also provided.

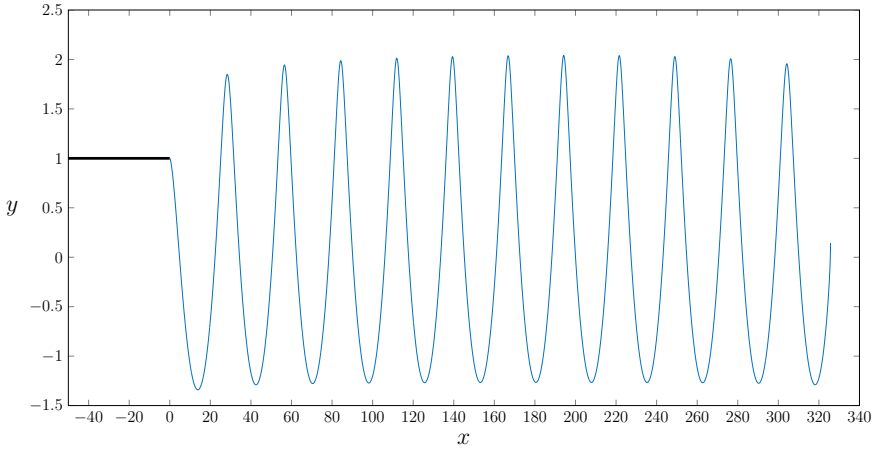

Figure A.6: A free-surface profile for flow under a raised semi-infinite plate for $F_L = 2.235$ where $N = 120,001$. The thick line represents the plate. The maximum steepness of the wave train is 0.12.

in Figure A.5. Due to the large number of collocation nodes, we are able to compute solutions with large steepness, while still maintaining high definition around the crest. For example, see the free-surface profile in Figure A.6 which was computed for $F_L = 2.235$ and a steepness of 0.12.

A.5 Finite depth flow examples

A variant of the presented numerical scheme can be used to compute finite-depth flows over a bottom topography. For finite-depth flows with an upstream dimensionless depth of α, dimensionless speed 1 and some bottom topography, we follow a similar procedure to the infinite depth case by mapping the physical z-plane to an infinite strip in the potential w-plane. We then map the infinite strip to the half-ζ-plane via $\zeta = \mathrm{e}^{\beta\pi w/\alpha}$ where $\zeta = \xi + i\eta$ and $\beta = \pm 1$. If $\beta = 1$ the infinite strip is mapped to the lower half-plane with the upstream limit mapped to $\zeta = 0$; otherwise, when $\beta = -1$ the infinite strip is mapped to the upper half-plane with the downstream limit mapped to $\zeta = 0$. The choice of β depends on the type of solutions computed. For subcritical flows, $F_H < 1$ where $F_H = U/\sqrt{gH}$ is the depth-based Froude number, choosing $\beta = -1$ greatly reduces upstream numerical waves. Conversely, for supercritical flows, $F_H > 1$, β must be set to 1, to eliminate downstream waves. An example is shown for flow over a step with $\beta = -1$ in Figure A.7.

We can now formulate a new integral equation for finite depth

$$\tau(\xi) = \frac{1}{\beta\pi} \int_{-\infty}^{\infty} \frac{\theta(\xi')}{\xi' - \xi} \, \mathrm{d}\xi', \qquad -\infty < \xi < \infty. \tag{A.15}$$

Additionally, we know the value of $\theta(\xi)$ for $\xi \in (-\infty, 0)$ and can therefore break up the integral

$$\tau(\xi) = f(\xi) + \frac{1}{\beta\pi} \int_{0}^{\infty} \frac{\theta(\xi')}{\xi' - \xi} \, \mathrm{d}\xi', \qquad 0 < \xi < \infty,$$

where $f(\zeta)$ is the integral evaluated over the known bottom. Finally, to implement the numerical scheme, we perform the integral with respect to ϕ and dampen the singularity, to form the finite depth equivalent of equation (A.8):

$$\tau(\phi) = f\left(\mathrm{e}^{\frac{\beta\pi\phi}{\alpha}}\right) + \frac{\beta}{\alpha} \int_{\phi_1}^{\phi_N} \frac{\theta(\phi') - \theta(\phi)}{1 - \mathrm{e}^{\frac{\beta\pi}{\alpha}(\phi - \phi')}} \, \mathrm{d}\phi' + \frac{\theta(\phi)}{\pi} \ln \left| \frac{\mathrm{e}^{\frac{\beta\pi\phi_N}{\alpha}} - \mathrm{e}^{\frac{\beta\pi\phi}{\alpha}}}{\mathrm{e}^{\frac{\beta\pi\phi_1}{\alpha}} - \mathrm{e}^{\frac{\beta\pi\phi}{\alpha}}} \right|. \tag{A.16}$$

The numerical scheme described in Section A.3 can now be applied to equations (A.5) and (A.16). Here, F_L is replaced by F_H where the reference length is the depth of the fluid H.

The elements in the dense lower-right submatrix of the Jacobian no longer decrease to zero both above and below the diagonal. Instead the elements approach $-\beta/\alpha$ away from the diagonal either above for $\beta = 1$ or below for $\beta = -1$. Regardless, we implement the numerical scheme as before.

A.5.1 Flow over a step

The problem of free-surface flow over a step has been thoroughly explored in the literature (Binder, Dias, and Vanden-Broeck 2006, 2008; Chapman and Vanden-Broeck 2006;

King and Bloor 1987; Lustri, McCue, and Binder 2012; Toison and Hureau 2000), due to the simplicity of defining a step in terms of the direction of flow, θ. A step bottom is defined as horizontal, $\theta = 0$, upstream and downstream of the step, and some constant gradient segment connecting the two depths (see Figure A.7(a) for a raised 90° step). There are two different Froude numbers (upstream or downstream) that can be defined depending on which depth (before or after the step) is used. There are different flow regimes for flow over a step, depending on the properties of the flow. Subcritical flows, where both upstream and downstream Froude numbers are less than one, produce a wave train downstream of the step (King and Bloor 1987). Supercritical flows, where both upstream and downstream Froude numbers are greater than one, do not produce any waves and the water height moves in the direction of the step (increases/decreases for a raised/lowered step) (King and Bloor 1987). However, when one Froude number is less than one and the other is greater than one, we produce hydraulic fall flows (Binder, Dias, and Vanden-Broeck 2006, 2008). Hydraulic falls exhibit no waves, but unlike supercritical flows, the water height moves in the opposite direction to the step (decreases/increases for a raised/lowered step). In addition to the well studied 90° step, steps of different gradients have been studied by Lustri, McCue, and Binder (2012).

We first consider flow over a 90° step as shown in Figure A.7 where we choose the w-plane such that the downstream edge of the step maps to $\zeta = -1$ and the upstream edge maps to $\zeta = -b$ where $\log(b)/\beta < 0$. Thus the integral evaluated over the bottom, $f(\zeta)$, is

$$f(\zeta) = \frac{1}{2} \ln \left| \frac{\zeta + b}{\zeta + 1} \right| \tag{A.17}$$

and the radiation conditions are $\tau_1 = \theta_1 = 0$. For the following results we choose $\alpha = \pi$ and $\beta = -1$.

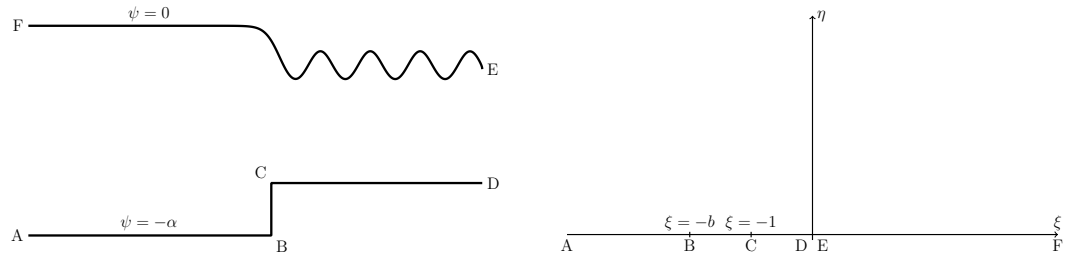

(a) z-plane (b) ζ-plane

Figure A.7: A schematic for flow over a step.

To determine the height of the step, h, we integrate the identity $\mathrm{d}z/\mathrm{d}w = \mathrm{e}^{-\tau + i\theta}$ with respect to ϕ to give

$$h = \beta \int_0^{\frac{\alpha \log b}{\beta \pi}} \exp\left(-\tau\left(\phi - i\alpha\right)\right) \mathrm{d}\phi. \tag{A.18}$$

The height of the step can be specified as an input to the problem by adding the equation (A.18) to the system of equations and the parameter b to the vector of unknowns. The 2×2 submatrix structure of the preconditioner (A.12) has now been augmented with an additional row and column related to the equation (A.18) and the unknown b, respectively. The preconditioner can now be considered to have a 3×3 submatrix structure. The additional 5 blocks, given by the additional row and column, are small in size and are kept in their entirety. Block LU factorisation is applied the 3×3 submatrix structure.

We reproduce the results of Chapman and Vanden-Broeck (2006) by looking at exponentially small waves generated by flow over a step for varying b with constant Froude number (Figure A.8) and varying Froude number with constant b (Figure A.9). In both cases, we demonstrate the ability to compute solutions with exponentially small waves which is quite a computational challenge. Additionally, we were able to resolve solutions with smaller waves than those presented by Chapman and Vanden-Broeck (2006).

A.5.2 Flow over a triangular obstruction

Another finite depth flow that has been extensively studied is flow over an obstruction (Binder, Blyth, and McCue 2013; Binder, Vanden-Broeck, and Dias 2005; Cole 1983; Dias and Vanden-Broeck 1989; Forbes and Schwartz 1982; Forbes 1988; Lee and Whang 2015; Lustri, McCue, and Binder 2012; Toison and Hureau 2000; Vanden-Broeck 1987; Zhang and Zhu 1996). The bottom for flow past an obstruction is defined as horizontal both upstream and downstream of the obstruction with the same depth, and the obstacle can be any deviation from the horizontal. Many different obstructions have been explored: triangles (Binder, Vanden-Broeck, and Dias 2005; Dias and Vanden-Broeck 1989), semicircles (Forbes 1988; Forbes and Schwartz 1982; Vanden-Broeck 1987), or an arbitrary curved surface (Toison and Hureau 2000). Like flow over a step, flow over a obstruction can be classified as subcritical, exhibiting downstream waves, or supercritical, exhibiting no waves.

We will consider flow over an isosceles triangular obstruction, because it can be simply defined by two flat surfaces with an internal angle to the horizontal and a height. The function, $f(\zeta)$, can be evaluated, giving

$$f(\zeta) = \frac{\Theta_I}{\pi} \ln \left| \frac{(\zeta + b)(\zeta + a)}{(\zeta + 1)^2} \right|, \tag{A.19}$$

where Θ_I is the interior base angles of an isosceles triangle, $\log(a)/\beta > 0$ is the downstream edge of the triangle in the ζ-plane and b is the same as with the step. In the presented results we choose $\Theta_I = \pi/4$, $\alpha = 1$ and $\beta = 1$. We will only be presenting

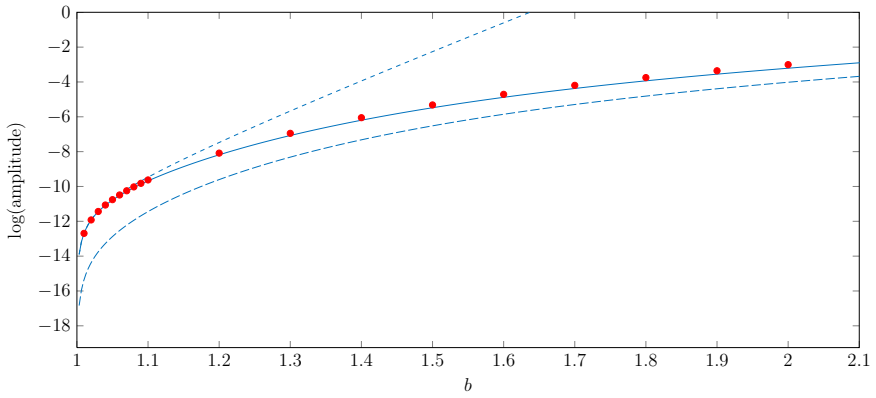

(a) $F_H = \sqrt{0.1}$

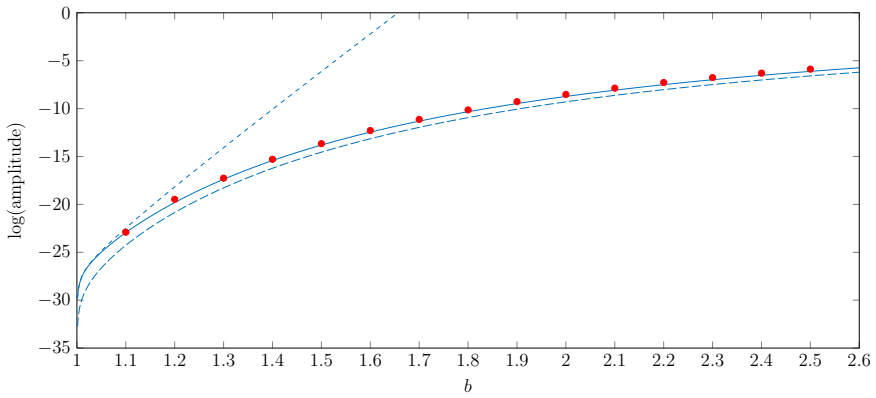

(b) $F_H = 0.2$

Figure A.8: A plot of the log of the downstream wave amplitude against the parameter b for flow over a step with (a) $F_H = \sqrt{0.1}$ and (b) $F_H = 0.2$. The long dashed, dashed, and solid curves are given in Chapman and Vanden-Broeck (2006) as equations (5.12), (B 16) and a uniform approximation generated from the previous two, respectively.

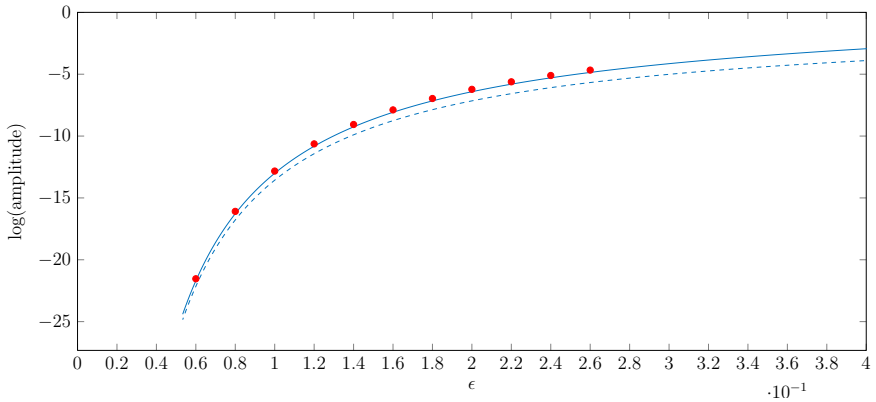

Figure A.9: A plot of the log of the downstream wave amplitude against the parameter $\epsilon = F_H^2$ for flow over a step with $b = 1.8$. The long dashed, and solid curves are given in Chapman and Vanden-Broeck (2006) as equations (5.12) and a uniform approximation generated from the equations (5.12) and (B 16), respectively.

results for supercritical flows, echoing some of the forced solitary wave results of Wade et al. (2014).

We can see in Figure A.10 that for a given triangle height h, there exists a Froude number, F_H^*, for which solutions only exist for $F_H > F_H^*$. If $y^* = y_{\max}(F_H^*)$, where $y_{\max}$ is the maximum height of the wave, then it is known that the solutions where $y_{\max} < y^*$ are perturbations of the flat surface $y = 0$ and solutions where $y_{\max} > y^*$ are perturbations of the solitary wave solution (Wade et al. 2014). However, it is possible to have 3 or possibly more solutions for a single value of triangle height, h, and Froude number, and an example is given in Figure A.11. This is due to the fact that the maximum solitary wave height is a multivalued function of the Froude number (Longuet-Higgins and Fox 1996; Wade et al. 2014) and thus multiple solutions can be found for a given Froude number by perturbing solitary wave solutions for above and below the fold. An example of multiple (three) solutions for a given triangle height, $h = 0.437$, and Froude number, $F_H = \sqrt{2}$, is given in Figure A.11.

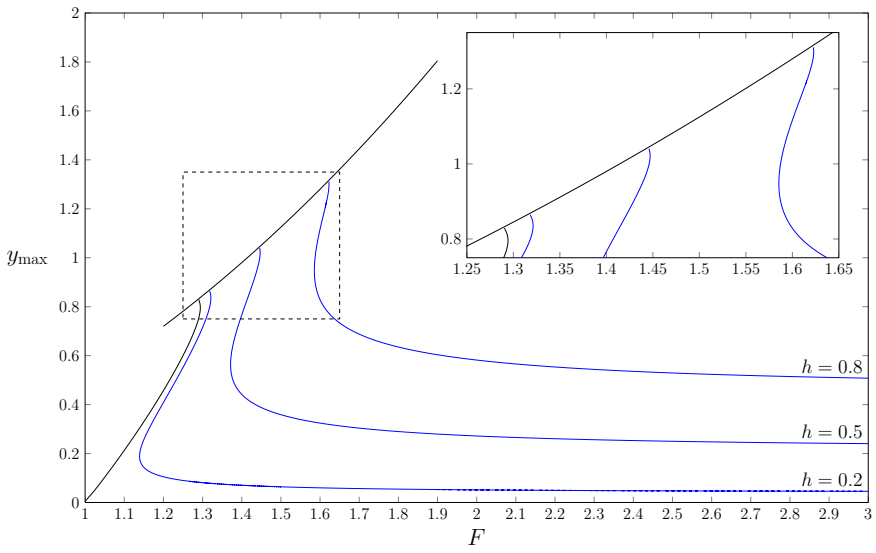

Figure A.10: A plot of the maximum wave height against the Froude number for constant values of triangle height, h. The black curves are the limiting configurations for supercritical flow over an obstacle. An inset is given to more clearly show the second fold.

A.6 Discussion

A.6.1 Options for implementing JFNK scheme

We have developed the framework for using a preconditioned Jacobian-free Newton-Krylov (JFNK) method to solve two-dimensional free-surface flow problems. However,

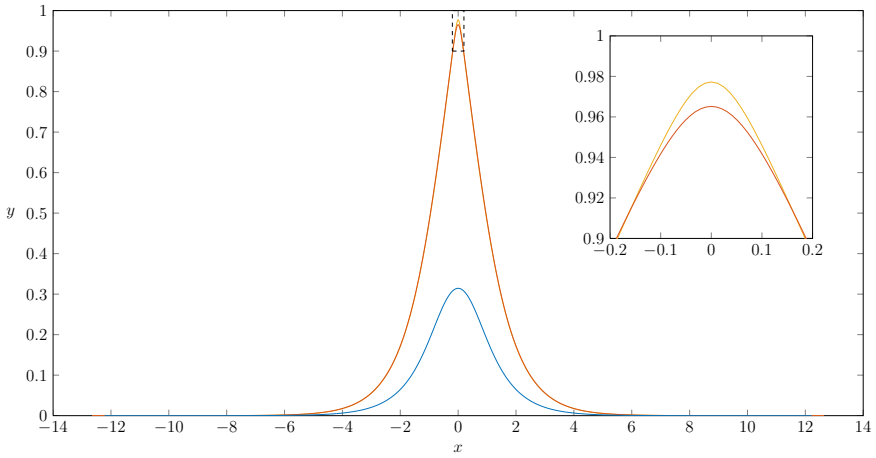

Figure A.11: The three possible free-surface profiles for supercritical flow over a triangular obstacle of height $h = 0.437$ and $F_H = \sqrt{2}$.

it is not necessary to perform the full implementation (section A.3.4) to compute a solution. There are three levels of sophistication that can be used:

1. Implement the JFNK method using KINSol (or equivalent) with a preconditioner matrix given by the full Jacobian calculated as in section A.7.1 (or by finite-difference if the entries of the Jacobian cannot be determined exactly). The KINSol package is simple to install and use, and its JFNK implementation is much more efficient than using the full Newton's method.

2. Perform implementation 1 while exploiting the structure of the Jacobian as in section A.3.3 to construct a preconditioner that makes more efficient use of system memory. Additionally, the use of Intel MKL (or equivalent) to performed banded factorisation of the Jacobian is recommended. This level of implementation is the most efficient for a standard desktop computer.

3. If a Graphics Processing Unit (GPU) is available, the evaluation of the nonlinear function $\mathbf{F}(\mathbf{u})$ can be coded in CUDA (or equivalent) to run in parallel on a GPU. Utilising a GPU will greatly decrease the runtime of either implementation 1 or 2.

The implementation used depends on the available hardware and the familiarity of the user with different programming languages and architectures.

A.6.2 Versatility of our JFNK scheme

Our approach was motivated by our previous work for three-dimensional free-surface flows (Pethiyagoda et al. 2014, Ch. 3) due to its versatility in computing solutions for

different disturbances. Many of the ideas carry over from our previous work such as the use of the JFNK method, the general structure of the Jacobian (comprising four submatrices) and the advantage of GPU computing.

We were also motivated by Gardiner et al. (2015), who used a numerical scheme similar to implementation 2 for the problem of Hele-Shaw flows with kinetic undercooling. Gardiner et al. use a conformal mapping approach to form the boundary integral equation by mapping the fluid domain to the infinite strip and then to the half-plane, similar to our finite depth examples. However, Gardiner et al. perform multiple coordinate transforms to the integral to achieve mesh refinement near the boundaries. These transformations slightly change the structure of the Jacobian. Due to the different structure of the Jacobian Gardiner et al. chose to keep a few of the rightmost columns along with a chosen bandwidth about the main diagonal when forming a sparse preconditioner. The coordinate transformations performed were specific to the Hele-Shaw problem considered by Gardiner et al. and thus diminished the generality of their numerical scheme.

Conversely, we have considered two-dimensional free-surface flow problems in either finite or infinite depth. All of the problems presented involve conformally mapping the fluid domain to the half plane or to the infinite strip, which is then mapped to the half plane, with no additional transformations. In both cases the associated Jacobian is primarily comprised of three sparse submatrices and one dense submatrix, and in the case of finite depth flows five additional submatrices with one dimension (row or column) being small. Additionally, the magnitude of the elements of the dense submatrix are greatest close to the diagonal and decrease away from the diagonal, approaching zero above and below the diagonal for infinite depth flows. For finite depth flows the magnitude of the elements approaches zero above the diagonal and a constant below the diagonal or visa versa. The difference between the dense submatrices is not significant enough to require altering our numerical scheme.

If, instead of conformal mapping techniques, Green's second identity was used to form the boundary integral equation (as in Pethiyagoda et al. (2014), Ch. 3) the elements of the dense submatrix of the Jacobian would not diminish away from the diagonal. Thus, complex variable methods must be used to form the boundary integral equation.

We have shown examples for applying the JFNK method with a suitably chosen preconditioner to compute solutions to different two-dimensional free-surface flow problems. As we have multiple working examples for the two conformal maps considered we are confident that this numerical scheme can be applied to similar problems involving these two mappings. If additional transformations are required as in Gardiner et al. (2015) or a different mapping is used (mapping the infinite strip to the semi-unit-circle (Dias

and Vanden-Broeck 1989)), the approach for forming a sparse preconditioner should be altered.

A.6.3 Significance of new results

We have proposed a general banded preconditioner that can be used with the JFNK method to generate solutions with a much greater number of collocation points than recent solutions presented in the literature (Lustri, McCue, and Binder 2012; Trinh, Chapman, and Vanden-Broeck 2011). The greater number of collocation points achieves more accurate solutions using a scheme that is notorious for not being accurate. We have computed solutions for flow under a semi-infinite plate or past a pressure distribution in infinite depth (Section A.4), along with solutions for flow past a bottom topography (step or triangle obstruction) in finite depth to show the adaptability of our numerical scheme to a variety of different two-dimensional free-surface flow problems.

For the infinite depth problems, the increased number of collocation points has allowed for greater definition around the crest. This added definition has allowed us to compute steep nonlinear solutions with sharp crests and wide troughs for both flow under a semi-infinite plate and flow past a pressure distribution.

The increased number of collocation points in the solutions has also allowed us to not only reproduce the work of Chapman and Vanden-Broeck (2006), but to generate solutions exhibiting waves with much smaller amplitude and wavelength than those presented in their paper. Further, we have examined the forced solitary wave problem considered by Wade et al. (2014), though we use a triangle obstruction instead of a pressure distribution to force the wave. We were able to find three distinct solutions for a given triangle height and Froude number, without assuming symmetry of the solution or adding mesh refinement at the crest of the wave. Therefore, there was less analytic work and knowledge of the expected solution required to successfully utilise our numerical scheme. The generality of the numerical scheme, and the ability to implement the scheme without knowledge of the final solution, means this scheme is a great first choice when considering which numerical scheme to use when solving a two-dimensional free-surface flow problem.

A.7 Appendix

A.7.1 Forming the Jacobian

To construct the Jacobian to be used as a preconditioner matrix (section A.3) we first consider the ordering of unknowns (A.6) and the equations in

$$\mathbf{F}(\mathbf{u}) = \begin{bmatrix} \mathbf{F}_1 \\ \mathbf{F}_2 \end{bmatrix}, \tag{A.20}$$

where $\mathbf{F}_1$ and $\mathbf{F}_2$ are the discretised forms of Bernoulli's equation (A.5) and the boundary integral equation (A.8), respectively. The elements of $\mathbf{F}_1$ and $\mathbf{F}_2$ are given by

$$\mathbf{F}_{1_k} = F_L^2 \mathrm{e}^{3\tau_{k+1/2}} \frac{\mathrm{d}\tau_{k+1/2}}{\mathrm{d}\phi} + \sin\theta_{k+1/2} + F_L^2 \mathrm{e}^{\tau_{k+1/2}} \left.\frac{\mathrm{d}p}{\mathrm{d}\phi}\right|_{\phi=\phi_{k+1/2}}, \tag{A.21}$$

$$\mathbf{F}_{2_k} = \tau_{k+1/2} - \frac{1}{\pi}\sum_{i=1}^{N} \frac{\theta_i - \theta_{k+1/2}}{\phi_i - \phi_{k+1/2}} - \frac{\theta_{k+1/2}}{\pi} \ln\left|\frac{\phi_N - \phi_{k+1/2}}{\phi_1 - \phi_{k+1/2}}\right|, \tag{A.22}$$

for $k = 1, \ldots, N-1$.

The derivatives of (A.21) and (A.22) can now be found with respect to the unknowns τ_n and θ_n for $n = 2, \ldots, N$, giving

$$\frac{\partial \mathbf{F}_{1_k}}{\partial \tau_n} = \begin{cases} F_L^2 \mathrm{e}^{3\tau_{k+1/2}} \left(\frac{3}{2}\frac{\mathrm{d}\tau_{k+1/2}}{\mathrm{d}\phi} + \frac{1}{\Delta\phi}\right) & \\ \quad + F_L^2 \mathrm{e}^{\tau_{k+1/2}} \left.\frac{\mathrm{d}p}{\mathrm{d}\phi}\right|_{\phi=\phi_{k+1/2}}, & n = k+1 \\ F_L^2 \mathrm{e}^{3\tau_{k+1/2}} \left(\frac{3}{2}\frac{\mathrm{d}\tau_{k+1/2}}{\mathrm{d}\phi} - \frac{1}{\Delta\phi}\right) & \\ \quad + F_L^2 \mathrm{e}^{\tau_{k+1/2}} \left.\frac{\mathrm{d}p}{\mathrm{d}\phi}\right|_{\phi=\phi_{k+1/2}}, & n = k \\ 0 & \text{otherwise} \end{cases} \tag{A.23}$$

$$\frac{\partial \mathbf{F}_{1_k}}{\partial \theta_n} = \begin{cases} \frac{1}{2}\cos\theta_{k+1/2}, & n = k, k+1 \\ 0, & \text{otherwise} \end{cases} \tag{A.24}$$

$$\frac{\partial \mathbf{F}_{2_k}}{\partial \tau_n} = \begin{cases} \frac{1}{2}, & n = k-1, k \\ 0, & \text{otherwise} \end{cases} \tag{A.25}$$

$$\frac{\partial \mathbf{F}_{2_k}}{\partial \theta_n} = \begin{cases} -\frac{1}{\pi}\frac{1}{\phi_n - \phi_{k+1/2}} & \\ \quad + \frac{1}{2\pi}\sum_{i=1}^{N} \frac{1}{\phi_i - \phi_{k+1/2}} & n = k, k+1 \\ \quad - \frac{1}{2\pi}\ln\left|\frac{\phi_N - \phi_{k+1/2}}{\phi_1 - \phi_{k+1/2}}\right|, & \\ -\frac{1}{\pi}\frac{1}{\phi_n - \phi_{k+1/2}}, & \text{otherwise} \end{cases} \tag{A.26}$$

for $k = 1 \ldots N-1$ and $n = 2 \ldots N$. The derivatives (A.23)–(A.26) can be arranged in a matrix according to the ordering of unknowns (A.6) and equations (A.20).

B Contribution statements

This appendix outlines the contributions of the authors to each paper. The presentation of these papers in this thesis has been approved by all co-authors.

B.1 Chapter 3: Jacobian-free Newton-Krylov methods with GPU acceleration for computing nonlinear ship wave patterns

This chapter was first published as

R. Pethiyagoda, S. W. McCue, T. J. Moroney, and J. M. Back (2014). Jacobian-free Newton-Krylov methods with GPU acceleration for computing nonlinear ship wave patterns. *Journal of Computational Physics* **269**, 297–313.

Abstract: The nonlinear problem of steady free-surface flow past a submerged source is considered as a case study for three-dimensional ship wave problems. Of particular interest is the distinctive wedge-shaped wave pattern that forms on the surface of the fluid. By reformulating the governing equations with a standard boundary integral method, we derive a system of nonlinear algebraic equations that enforce a singular integro-differential equation at each midpoint on a two-dimensional mesh. Our contribution is to solve the system of equations with a Jacobian-free Newton-Krylov method together with a banded preconditioner that is carefully constructed with entries taken from the Jacobian of the linearised problem. Further, we are able to utilise graphics processing unit acceleration to significantly increase the grid refinement and decrease the run-time of our solutions in comparison to schemes that are presently employed in the literature. Our approach provides opportunities to explore the nonlinear features of three-dimensional ship wave patterns, such as the shape of steep waves close to their limiting configuration, in a manner that has been possible in the two-dimensional analogue for some time.

Statement of joint authorship:

- **Ravindra Pethiyagoda** performed all the coding required to generate solutions using the Jacobian-free Newton-Krylov (JFNK) method, developed the banded preconditioner used in the JFNK method and drafted most of the manuscript.
- Scott McCue directed the research, acted as the corresponding author and helped draft the manuscript.
- Timothy Moroney directed the research, suggested the use of the JFNK method, the use of a graphics processing unit (GPU) and helped draft the manuscript.
- Julian Back helped guide the initial implementation of the nonlinear system of equations.

B.2 Chapter 4: What is the apparent angle of a Kelvin ship wave pattern?

This chapter was first published as

R. Pethiyagoda, S. W. McCue, and T. J. Moroney (2014). What is the apparent angle of a Kelvin ship wave pattern? *Journal of Fluid Mechanics* **758**, 468–485.

Abstract: While the half-angle which encloses a Kelvin ship wave pattern is commonly accepted to be 19.47°, recent observations and calculations for sufficiently fast-moving ships suggest that the apparent wake angle decreases with ship speed. One explanation for this decrease in angle relies on the assumption that a ship cannot generate wavelengths much greater than its hull length. An alternative interpretation is that the wave pattern that is observed in practice is defined by the location of the highest peaks; for wakes created by sufficiently fast-moving objects, these highest peaks no longer lie on the outermost divergent waves, resulting in a smaller apparent angle. In this paper, we focus on the problems of free surface flow past a single submerged point source and past a submerged source doublet. In the linear version of these problems, we measure the apparent wake angle formed by the highest peaks, and observe the following three regimes: a small Froude number pattern, in which the divergent waves are not visible; standard wave patterns for which the maximum peaks occur on the outermost divergent waves; and a third regime in which the highest peaks form a V-shape with an angle much less than the Kelvin angle. For nonlinear flows, we demonstrate that nonlinearity has the effect of increasing the apparent wake angle so that some highly nonlinear solutions have apparent wake angles that are greater than Kelvin's angle. For large Froude numbers, the effect on apparent wake angle can be

more dramatic, with the possibility of strong nonlinearity shifting the wave pattern from the third regime to the second. We expect our nonlinear results will translate to other more complicated flow configurations, such as flow due to a steadily moving closed body such as a submarine.

Statement of joint authorship:

- **Ravindra Pethiyagoda** proposed the method used to measure the apparent wake angle of computed nonlinear solutions, derived the equations and performed the numerical computation in this paper and drafted most of the manuscript.
- Scott McCue directed the research, acted as the corresponding author and helped draft the manuscript.
- Timothy Moroney guided the research, offered guidance on computational techniques and helped draft the manuscript.

B.3 Chapter 5: Wake angle for surface gravity waves on a finite depth fluid

This chapter was first published as

R. Pethiyagoda, S. W. McCue, and T. J. Moroney (2015). Wake angle for surface gravity waves on a finite depth fluid. *Physics of Fluids* **27**, 061701.

Abstract: Linear water wave theory suggests that wave patterns caused by a steadily moving disturbance are contained within a wedge whose half-angle depends on the depth-based Froude number F_H. For the problem of flow past an axisymmetric pressure distribution in a finite-depth channel, we report on the apparent angle of the wake, which is the angle of maximum peaks. For moderately deep channels, the dependence of the apparent wake angle on the Froude number is very different to the wedge angle, and varies smoothly as F_H passes through the critical value $F_H = 1$. For shallow water, the two angles tend to follow each other more closely, which leads to very large apparent wake angles for certain regimes.

Statement of joint authorship:

- **Ravindra Pethiyagoda** derived the equations and performed the numerical computation in this paper and drafted most of the manuscript.
- Scott McCue directed the research, acted as the corresponding author and helped draft the manuscript.

- Timothy Moroney guided the research and helped draft the manuscript.

B.4 Chapter 6: Spectrograms of ship wakes: identifying linear and nonlinear wave signals

This chapter has been submitted for publication as

R. Pethiyagoda, S. W. McCue, and T. J. Moroney (2016). Spectrograms of ship wakes: identifying linear and nonlinear wave signals. Submitted to the *Journal of Fluid Mechanics* (arXiv:1604.05812)

Abstract: A spectrogram is a useful way of using short-time discrete Fourier transforms to visualise surface height measurements taken of ship wakes in real world conditions. For a steadily moving ship that leaves behind small-amplitude waves, the spectrogram is known to have two clear linear components, a sliding-frequency mode caused by the divergent waves and a constant-frequency mode for the transverse waves. However, recent observations of high speed ferry data have identified additional components of the spectrograms that are not yet explained. We use computer simulations of linear and nonlinear ship wave patterns and apply time-frequency analysis to generate spectrograms for an idealised ship. We clarify the role of the linear dispersion relation and ship speed on the two linear components. We use a simple weakly nonlinear theory to identify higher order effects in a spectrogram and, while the high speed ferry data is very noisy, we propose that certain additional features in the experimental data are caused by nonlinearity. Finally, we provide a possible explanation for a further discrepancy between the high speed ferry spectrograms and linear theory by accounting for ship acceleration.

Statement of joint authorship:

- **Ravindra Pethiyagoda** proposed examining the effect of nonlinearity and ship acceleration has on the spectrogram, derived the equations and performed the numerical computation in this paper and drafted most of the manuscript.
- Scott McCue guided the research, acted as the corresponding author and helped draft the manuscript.
- Timothy Moroney offered guidance on computational techniques and helped draft the manuscript.

Bibliography

Bal, S. (2008). Prediction of wave pattern and wave resistance of surface piercing bodies by a boundary element method. *International Journal for Numerical Methods in Fluids* 56, 305–329.

Bal, S. (2011). The effect of finite depth on 2D and 3D cavitating hydrofoils. *Journal of Marine Science and Technology* 16, 129–142.

Bal, S. and S. A. Kinnas (2002). A BEM for the prediction of free surface effects on cavitating hydrofoils. *Computational Mechanics* 28, 260–274.

Bal, S., S. A. Kinnas, and H. Lee (2001). Numerical analysis of 2-D and 3-D cavitating hydrofoils under a free surface. *Journal of Ship Research* 45, 34–49.

Barnell, A. and F. Noblesse (1986). Far-field features of the Kelvin wake. In: *Proceedings of the 16th Suymposium Naval Hydrodynamics*. National Academy Press, 18–36.

Barratt, M. J. (1965). The wave drag of a Hovercraft. *Journal of Fluid Mechanics* 22, 39–47.

Batchelor, G. K. (2000). *An introduction to fluid dynamics*. Cambridge university press.

Beatson, R. and L. Greengard (1997). A short course on fast multipole methods. *Wavelets, multilevel methods and elliptic PDEs* 1, 1–37.

Benassai, G., V. Piscopo, and A. Scamardella (2015). Spectral analysis of waves produced by HSC for coastal management. *Journal of Marine Science and Technology* 20, 1–12.

Bensabat, J., Q. Zhou, and J. Bear (2000). An adaptive pathline-based particle tracking algorithm for the Eulerian-Lagrangian method. *Advances in Water Resources* 23, 383–397.

Benzaquen, M., A. Darmon, and E. Raphaël (2014). Wake pattern and wave resistance for anisotropic moving disturbances. *Physics of Fluids* 26, 092106.

Bettess, P. and J. A. Bettess (1983). Analysis of free surface flows using isoparametric finite elements. *International Journal for Numerical Methods in Engineering* 19, 1675–1689.

Binder, B. J., M. G. Blyth, and S. W. McCue (2013). Free-surface flow past arbitrary topography and an inverse approach for wave-free solutions. *IMA Journal of Applied Mathematics* 78, 685–696.

Binder, B. J., F. Dias, and J.-M. Vanden-Broeck (2006). Steady free-surface flow past an uneven channel bottom. *Theoretical and Computational Fluid Dynamics* 20, 125–144.

Binder, B. J., F. Dias, and J.-M. Vanden-Broeck (2008). Influence of rapid changes in a channel bottom on free-surface flows. *IMA Journal of Applied Mathematics* 73, 254–273.

Binder, B. J., J.-M. Vanden-Broeck, and F Dias (2005). Forced solitary waves and fronts past submerged obstacles. *Chaos* 15, 037106.

Brown, E. D., S. B. Buchsbaum, R. E. Hall, J. P. Penhune, K. F. Schmitt, K. M. Watson, and D. C. Wyatt (1989). Observations of a nonlinear solitary wave packet in the Kelvin wake of a ship. *Journal of Fluid Mechanics* 204, 263–293.

Brown, P. N. and Y. Saad (1990). Hybrid Krylov methods for nonlinear systems of equations. *SIAM Journal on Scientific and Statistical Computing* 11, 450–481.

Carusotto, I. and G. Rousseaux (2013). The Čerenkov Effect Revisited: From Swimming Ducks to Zero Modes in Gravitational Analogues. In: *Lecture Notes in Physics*. Springer Berlin, 109–144.

Chacón, L., D. C. Barnes, D. A. Knoll, and G. H. Miley (2000). An implicit energy-conservative 2D Fokker-Planck algorithm: II. Jacobian-free Newton-Krylov solver. *Journal of Computational Physics* 157, 654–682.

Chang, C.-H. and K.-H. Wang (2011). Generation of three-dimensional fully nonlinear water waves by a submerged moving object. *Journal of Engineering Mechanics* 137, 101–112.

Chapman, S. J. and J.-M. Vanden-Broeck (2006). Exponential asymptotics and gravity waves. *Journal of Fluid Mechanics* 567, 299–326.

Chatellier, L., S. Jarny, F. Gibouin, and L. David (2013). A parametric PIV/DIC method for the measurement of free surface flows. *Experiments in Fluids* 54, 1–15.

Cho, A. (2013). Lord Kelvin Wipes Out on Speed Boat Wakes? *Science Now* 9, 2013–05–09.

Chung, Y. K. and J. S. Lim (1991). A Review of the Kelvin Ship Wave Pattern. *Journal of Ship Research* 35, 191–197.

Cohen, L. (1989). Time-frequency distributions-a review. *Proceedings of the IEEE* 77, 941–981.

Cokelet, E. D. (1977). Steep gravity waves in water of arbitrary uniform depth. *Philosophical Transactions of the Royal Society of London A: Mathematical, Physical and Engineering Sciences* 286, 183–230.

Cole, S. L. (1983). Near critical free surface flow past an obstacle. *Q. Appl. Math.* 41, 301–309.

Collier, A. M., A. C. Hindmarsh, R. Serban, and C. S. Woodward (2011). *User Documentation for kinsol v2.7.0*. Tech. rep. UCRL-SM-208116, LLNL.

Craik, A. D. D. (2004). The origins of water wave theory. *Annual Review of Fluid Mechanics* 36, 1–28.

Crapper, G. D. (1964). Surface waves generated by a travelling pressure point. *Proceedings of the Royal Society of London A: Mathematical, Physical and Engineering Sciences* 282, 547–558.

Crawford, F. S. (1984). Elementary derivation of the wake pattern of a boat. *American Journal of Physics* 52, 782–785.

Dallaston, M. C. and S. W. McCue (2010). Accurate series solutions for gravity-driven Stokes waves. *Physics of Fluids* 22, 082104.

Darmon, A., M. Benzaquen, and E. Raphaël (2014). Kelvin wake pattern at large Froude numbers. *Journal of Fluid Mechanics* 738, R3.

Darrigol, O. (2003). The spirited horse, the engineer, and the mathematician: water waves in nineteenth-century hydrodynamics. *Archive for History of Exact Sciences* 58, 21–95.

Dias, F. (2014). Ship waves and Kelvin. *Journal of Fluid Mechanics, Focus on Fluids* 746, 1–4.

Dias, F. and T. J. Bridges (2006). The numerical computation of freely propagating time-dependent irrotational water waves. *Fluid Dynamics Research* 38, 803–830.

Dias, F. and J.-M. Vanden-Broeck (1989). Open channel flows with submerged obstructions. *Journal of Fluid Mechanics* 206, 155–170.

Dias, F. and J.-M. Vanden-Broeck (2002). Generalised critical free-surface flows. *Journal of Engineering Mathematics* 42, 291–301.

Didenkulova, I., A. Sheremet, T. Torsvik, and T. Soomere (2013). Characteristic properties of different vessel wake signals. *Journal of Coastal Research* SI 65, 213–218.

Doyle, T. B. and J. F. McKenzie (2013). Stationary wave patterns in deep water. *Quaestiones Mathematicae* 36, 487–500.

Ellingsen, S. Å. (2014). Ship waves in the presence of uniform vorticity. *Journal of Fluid Mechanics* 742, R2.

Farrow, D. E. and E. O. Tuck (1995). Further studies of stern wavemaking. *The Journal of the Australian Mathematical Society. Series B. Applied Mathematics* 36, 424–437.

Fochesato, C. and F. Dias (2006). A fast method for nonlinear three-dimensional free-surface waves. *Proceedings of the Royal Society of London A: Mathematical, Physical and Engineering Sciences* 462, 2715–2735.

Forbes, L. K. (1982). Non-linear, drag-free flow over a submerged semi-elliptical body. *Journal of Engineering Mathematics* 16, 171–180.

Forbes, L. K. (1985). A numerical method for non-linear flow about a submerged hydrofoil. *Journal of Engineering Mathematics* 19, 329–339.

Forbes, L. K. (1988). Critical free-surface flow over a semi-circular obstruction. *Journal of Engineering Mathematics* 22, 3–13.

Forbes, L. K. (1989). An Algorithm for 3-Dimensional Free-Surface Problems in Hydrodynamics. *Journal of Computational Physics* 82, 330–347.

Forbes, L. K. and G. C. Hocking (2005). Flow due to a sink near a vertical wall, in infinitely deep fluid. *Computers & Fluids* 34.

Forbes, L. K. and L. W. Schwartz (1982). Free-surface flow over a semicircular obstruction. *Journal of Fluid Mechanics* 114, 299–314.

Gardiner, B. P. J., S. W. McCue, M. C. Dallaston, and T. J. Moroney (2015). Saffman-Taylor fingers with kinetic undercooling. *Physical Review E* 91, 023016.

Gomit, G., L. Chatellier, D. Calluaud, and L. David (2013). Free surface measurement by stereo-refraction. *Experiments in Fluids* 54, 1–11.

Gomit, G., G. Rousseaux, L. Chatellier, D. Calluaud, and L. David (2014). Spectral analysis of ship waves in deep water from accurate measurements of the free surface elevation by optical methods. *Physics of Fluids* 26, 122101.

Gomit, G., L. Chatellier, D. Calluaud, L. David, D. Frchou, R. Boucheron, O. Perelman, and C. Hubert (2015). Large-scale free surface measurement for the analysis of ship waves in a towing tank. *Experiments in Fluids* 56, 1–13.

Grandison, S. and J.-M. Vanden-Broeck (2006). Truncation approximations for gravity-capillary free-surface flows. *Journal of Engineering Mathematics* 54, 89–97.

Greengard, L. and V. Rokhlin (1987). A fast algorithm for particle simulations. *Journal of Computational Physics* 73, 325–348.

Grilli, S. T., P. Guyenne, and F. Dias (2000). Modeling of overturning waves over arbitrary bottom in a 3D numerical wave tank. In: *Proceedings of the 10th Offshore and Polar Engineering Conference*, 221–228.

Grilli, S. T., P. Guyenne, and F. Dias (2001). A fully non-linear model for three-dimensional overturning waves over an arbitrary bottom. *International Journal for Numerical Methods in Fluids* 35, 829–867.

Grilli, S. T., J. Skourup, and I. A. Svendsen (1989). An efficient boundary element method for nonlinear water waves. *Engineering Analysis with Boundary Elements* 6, 97–107.

Grilli, S. T. and R. Subramanya (1996). Numerical modeling of wave breaking induced by fixed or moving boundaries. *Computational Mechanics* 17, 374–391.

Grimshaw, R. and M. Maleewong (2013). Stability of steady gravity waves generated by a moving localised pressure disturbance in water of finite depth. *Physics of Fluids* 25, 076605.

Harris, F. J. (1978). On the use of windows for harmonic analysis with the discrete Fourier transform. *Proceedings of the IEEE* 66, 51–83.

Havelock, T. H. (1908). The propagation of groups of waves in dispersive media, with application to waves on water produced by a travelling disturbance. *Proceedings of the Royal Society of London A: Mathematical, Physical and Engineering Sciences* 81, 398–430.

Havelock, T. H. (1918). Periodic irrotational waves of finite height. *Proceedings of the Royal Society of London A: Mathematical, Physical and Engineering Sciences* 95, 38–51.

Havelock, T. H. (1919). Wave resistance: Some cases of three-dimensional fluid motion. *Proceedings of the Royal Society of London A: Mathematical, Physical and Engineering Sciences* 95, 354–365.

Havelock, T. H. (1928). Wave resistance. *Proceedings of the Royal Society of London A: Mathematical, Physical and Engineering Sciences* 118, 24–33.

Havelock, T. H. (1931). The wave resistance of a spheroid. *Proceedings of the Royal Society of London A: Mathematical, Physical and Engineering Sciences* 131.817, 275–285.

Havelock, T. H. (1932a). Ship waves: the calculation of wave profiles. *Proceedings of the Royal Society of London A: Mathematical, Physical and Engineering Sciences* 135, 1–13.

Havelock, T. H. (1932b). The theory of wave resistance. *Proceedings of the Royal Society of London A: Mathematical, Physical and Engineering Sciences* 138, 339–348.

He, J., C. Zhang, Y. Zhu, H. Wu, C.-J. Yang, F. Noblesse, X. Gu, and W. Li (2014). Comparison of three simple models of Kelvins ship wake. *European Journal of Mechanics-B/Fluids* 49, 12–19.

He, J., C. Zhang, Y. Zhu, L. Zou, W. Li, and F. Noblesse (2016). Interference effects on the Kelvin wake of a catamaran represented via a hull-surface distribution of sources. *European Journal of Mechanics-B/Fluids* 56, 1–12.

Hennings, I., R. Romeiser, W. Alpers, and A. Viola (1999). Radar imaging of Kelvin arms of ship wakes. *International Journal of Remote Sensing* 20, 2519–2543.

Higgins, P. J., W. W. Read, and S. R. Belward (2012). Analytical series solutions for three-dimensional supercritical flow over topography. *Journal of Engineering Mathematics* 77, 39–49.

Hindmarsh, A. C., P. N. Brown, K. E. Grant, S. L. Lee, R. Serban, D. E. Shumaker, and C. S. Woodward (2005). SUNDIALS: Suite of nonlinear and differential/algebraic equation solvers. *ACM Transactions on Mathematical Software (TOMS)* 31, 363–396.

Hogben, N. (1972). Nonlinear distortion of the Kelvin ship-wave pattern. *Journal of Fluid Mechanics* 55, 513–528.

Hughes, B. A., H. L. Grant, and R. W. Chappell (1977). A fast response surface-wave slope meter and measured wind-wave moments. *Deep Sea Research* 24, 1211–1223.

Hughes, S. A. (1993). Laboratory Measurement and Analysis. In: *Physical models and laboratory techniques in coastal engineering*. Vol. 7. World Scientific.

Janson, C.-E., M. Leer-Andersen, and L. Larsson (2003). Calculation of deep-water wash waves using a combined Rankine/Kelvin source method. *Journal of Ship Research* 47, 313–326.

Keller, J. B. (1979). Ray Theory of Ship Waves and the Class of Streamlined Ships. *Journal of Fluid Mechanics* 91, 465–488.

Khatiwala, S. (2008). Fast spin up of ocean biogeochemical models using matrix-free Newton-Krylov. *Ocean Modelling* 23, 121–129.

King, A. C. and M. I. G. Bloor (1987). Free-surface flow over a step. *Journal of Fluid Mechanics* 182, 193–208.

King, A. C. and M. I. G. Bloor (1989). A semi-inverse method for free-surface flow over a submerged body. *The Quarterly Journal of Mechanics and Applied Mathematics* 42, 183–202.

King, A. C. and M. I. G. Bloor (1990). Free-surface flow of a stream obstructed by an arbitrary bed topography. *The Quarterly Journal of Mechanics and Applied Mathematics* 43, 87–106.

Knoll, D. A. and D. E. Keyes (2004). Jacobian-free Newton-Krylov methods: a survey of approaches and applications. *Journal of Computational Physics* 193, 357–397.

Kurennoy, D., K. E. Parnell, and T. Soomere (2011). Fast-ferry generated waves in south-west Tallinn Bay. *Journal of Coastal Research* SI 64, 165–169.

Lamb, H. (1916). *Hydrodynamics*. 4th ed. Cambridge University Press.

Lee, S. and S. Whang (2015). Trapped supercritical waves for the forced KdV equation with two bumps. *Applied Mathematical Modelling* 39, 2649–2660.

Li, Y. and S. Å. Ellingsen (2016). Ship waves on uniform shear current at finite depth: wave resistance and critical velocity. *Journal of Fluid Mechanics* 791, 539–567.

Lighthill, J. (1978). *Waves in Fluids*. Cambridge University Press.

Longuet-Higgins, M. S. and M. J. H. Fox (1996). Asymptotic theory for the almost-highest solitary wave. *Journal of Fluid Mechanics* 317, 1–19.

Lukomsky, V., I. Gandzha, and D. Lukomsky (2002). Steep sharp-crested gravity waves in deep water. *Physical Review Letters* 89, 164502.

Lustri, C. J. and S. J. Chapman (2013). Steady gravity waves due to a submerged source. *Journal of Fluid Mechanics* 732, 660–686.

Lustri, C. J., S. W. McCue, and B. J. Binder (2012). Free surface flow past topography: A beyond-all-orders approach. *European Journal of Applied Mathematics* 23, 441–467.

Ma, C., Y. Zhu, H. Wu, J. He, C. Zhang, W. Li, and F. Noblesse (2016). Wavelengths of the highest waves created by fast monohull ships or catamarans. *Ocean Engineering* 113, 208–214.

Maki, K. J., R. Broglia, L. J. Doctors, and A. Di Mascio (2012). Nonlinear wave resistance of a two-dimensional pressure patch moving on a free surface. *Ocean Engineering* 39, 62–71.

MarineTraffic. AIS Vessel Tracking - AIS Positions Maps. Retrieved 26 February 2016, from http://www.marinetraffic.com/en/ais/home/shipid:352956/zoom:10.

Markle, D. G. and H. C. Greer (1992). *Crescent City Instrumented Model Dolos Study: Coastal Model Investigation.* Tech. rep. DTIC Document.

Maruo, H. (1967). High-and low-aspect ratio approximation of planing surfaces. *Schiffstechnik* 14, 57–64.

McCue, S. W. and L. K. Forbes (1999). Bow and stern flows with constant vorticity. *Journal of Fluid Mechanics* 399, 277–300.

McCue, S. W. and L. K. Forbes (2002). Free-surface flows emerging from beneath a semi-infinite plate with constant vorticity. *Journal of Fluid Mechanics* 461, 387–407.

McCue, S. W. and D. M. Stump (2000). Linear stern waves in finite depth channels. *The Quarterly Journal of Mechanics and Applied Mathematics* 53, 629–643.

Mekias, H. and J.-M. Vanden-Broeck (1991). Subcritical flow with a stagnation point due to a source beneath a free surface. *Physics of Fluids A: Fluid Dynamics* 3, 2652–2658.

Michell, J. H. (1898). The wave resistance of a ship. *The London, Edinburgh, and Dublin Philosophical Magazine and Journal of Science* 45, 106–123.

Milgram, J. H. (1988). Theory of radar backscatter from short waves generated by ships, with application to radar (SAR) imagery. *Journal of Ship Research* 32, 54–69.

Moisy, F. and M. Rabaud (2014a). Mach-like capillary-gravity wakes. *Physical Review E* 90, 023009.

Moisy, F. and M. Rabaud (2014b). The scaling of far-field wake angle of non-axisymmetric pressure disturbance. *Physical Review E* 89, 063004.

Moroney, T. J. and Q. Yang (2013). A banded preconditioner for the two-sided, nonlinear space-fractional diffusion equation. *Computers & Mathematics with Applications* 66, 659–667.

Munk, W. H., P. Scully-Power, and F. Zachariasen (1987). The Bakerian lecture, 1986. Ships from space. *Proceedings of the Royal Society of London A: Mathematical, Physical and Engineering Sciences* 412, 231–254.

Noblesse, F. (1978). The steady wave potential of a unit source, at the centerplane. *Journal of Ship Research* 22, 80–88.

Noblesse, F. (1981). Alternative integral representations for the Green function of the theory of ship wave resistance. *Journal of Engineering Mathematics* 15, 241–265.

Noblesse, F., G. Delhommeau, and C. Yang (2009). Practical evaluation of steady flow resulting from a free-surface pressure patch. *Journal of Ship Research* 53, 137–150.

Noblesse, F., F. Huang, and C. Yang (2013). The Neumann-Michell theory of ship waves. *Journal of Engineering Mathematics* 79, 51–71.

Noblesse, F. and C. Yang (1995). Fourier-Kochin formulation of wave diffraction-radiation by ships or offshore structures. *Ship Technology Research* 42, 167–185.

Noblesse, F., G. Delhommeau, H. Y. Kim, and C. Yang (2009). Thin-ship theory and influence of rake and flare. *Journal of Engineering Mathematics* 64, 49–80.

Noblesse, F., J. He, Y. Zhu, L. Hong, C. Zhang, R. Zhu, and C. Yang (2014). Why can ship wakes appear narrower than Kelvins angle? *European Journal of Mechanics-B/Fluids* 46, 164–171.

Noblesse, F., C. Zhang, J. He, Y. Zhu, C. Yang, and W. Li (2016). Observations and computations of narrow Kelvin ship wakes. *Journal of Ocean Engineering and Science*, doi:10.1016/j.joes.2015.12.005.

Ogilat, O., S. W. McCue, I. W. Turner, J. A. Belward, and B. J. Binder (2011). Minimising wave drag for free surface flow past a two-dimensional stern. *Physics of Fluids* 23, 072101.

Ohring, S. and J. Telste (1977). Numerical solutions of transient three-dimensional ship-wave problems. In: *Proceedings of the Second International Conference on Numerical Ship Hydrodynamics*.

Parnell, K., N. Delpeche, I. Didenkulova, T. Dolphin, A. Erm, A. Kask, L. Kelpšaite, D. Kurennoy, E. Quak, and A. Räämet (2008). Far-field vessel wakes in Tallinn Bay. *Estonian Journal of Engineering* 14, 273–302.

Peters, A. S. (1949). A new treatment of the ship wave problem. *Communications on Pure and Applied Mathematics* 2, 123–148.

Pethiyagoda, R., S. W. McCue, and T. J. Moroney (2014). What is the apparent angle of a Kelvin ship wave pattern? *Journal of Fluid Mechanics* 758, 468–485.

Pethiyagoda, R., S. W. McCue, and T. J. Moroney (2015). Wake angle for surface gravity waves on a finite depth fluid. *Physics of Fluids* 27, 061701.

Pethiyagoda, R., S. W. McCue, and T. J. Moroney (2016). Spectrograms of ship wakes: identifying linear and nonlinear wave signals. *arXiv preprint*, arXiv:1604.05812.

Pethiyagoda, R., S. W. McCue, T. J. Moroney, and J. M. Back (2014). Jacobian-free Newton-Krylov methods with GPU acceleration for computing nonlinear ship wave patterns. *Journal of Computational Physics* 269, 297–313.

Părău, E. and J.-M. Vanden-Broeck (2002). Nonlinear two- and three-dimensional free surface flows due to moving disturbances. *European Journal of Mechanics-B/Fluids* 21, 643–656.

Părău, E. and J.-M. Vanden-Broeck (2011). Three-dimensional waves beneath an ice sheet due to a steadily moving pressure. *Philosophical Transactions of the Royal Society of London A: Mathematical, Physical and Engineering Sciences* 369, 2973–2988.

Părău, E., J.-M. Vanden-Broeck, and M. J. Cooker (2005a). Nonlinear three-dimensional gravity-capillary solitary waves. *Journal of Fluid Mechanics* 536, 99–105.

Părău, E., J.-M. Vanden-Broeck, and M. J. Cooker (2005b). Three-dimensional gravity-capillary solitary waves in water of finite depth and related problems. *Physics of Fluids* 17, 122101.

Părău, E., J.-M. Vanden-Broeck, and M. J. Cooker (2007a). Nonlinear three-dimensional interfacial flows with a free surface. *Journal of Fluid Mechanics* 591, 481–494.

Părău, E., J.-M. Vanden-Broeck, and M. J. Cooker (2007b). Three-dimensional capillary-gravity waves generated by a moving disturbance. *Physics of Fluids* 19, 082102.

Părău, E., J.-M. Vanden-Broeck, and M. J. Cooker (2007c). Three-dimensional gravity and gravity-capillary interfacial flows. *Mathematics of Computation Sim.* 74, 105–112.

Părău, E., J.-M. Vanden-Broeck, and M. J. Cooker (2010). Time evolution of three-dimensional nonlinear gravity-capillary free-surface flows. *Journal of Engineering Mathematics* 68, 291–300.

Rabaud, M. and F. Moisy (2012). Are the wake angles of a duck and a ship really the same? In: *American Physical Society's Division of Fluid Dynamics meeting*. 1, R30.001.

Rabaud, M. and F. Moisy (2013). Ship Wakes: Kelvin or Mach Angle? *Physical Review Letters* 110, 214503.

Rabaud, M. and F. Moisy (2014). Narrow ship wakes and wave drag for planing hulls. *Ocean Engineering* 90, 34–38.

Rayleigh, Lord (1883). The form of standing waves on the surface of running water. *Proceedings London Mathematical Society* 1, 69–78.

Reed, A. M. and J. H. Milgram (2002). Ship wakes and their radar images. *Annual Review of Fluid Mechanics* 34, 469–502.

Saad, Y. and M. H. Schultz (1986). GMRES: A generalised minimum residual algorithm for solving nonsymmetric linear systems. *SIAM Journal on Scientific and Statistical Computing* 7, 856–869.

Schwartz, L. W. (1974). Computer extension and analytic continuation of Stokes expansion for gravity waves. *Journal of Fluid Mechanics* 62, 553–578.

Schwartz, L. W. (1981). Nonlinear solution for an applied overpressure on a moving stream. *Journal of Engineering Mathematics* 15, 147–156.

Scullen, D. C. (1998). *Accurate computation of steady nonlinear free-surface flows*. PhD thesis.

Scullen, D. C. and E. O. Tuck (2011). Free-surface elevation due to moving pressure distributions in three dimensions. *Journal of Engineering Mathematics* 70, 29–42.

Sheremet, A., U. Gravois, and M. Tian (2013). Boat-wake statistics at Jensen Beach, Florida. *Journal of Waterway, Port, Coastal, and Ocean Engineering* 139, 286–294.

Soomere, T. (2007). Nonlinear components of ship wake waves. *Applied Mechanics Reviews* 60, 120–138.

Sung, H. G. and S. T. Grilli (2006). Combined Eulerian-Lagrangian or pseudo-Lagrangian descriptions of waves caused by an advancing free surface disturbance. In: *The Sixteenth International Offshore and Polar Engineering Conference*, 487–494.

Sung, H. G. and S. T. Grilli (2008). BEM computations of 3-D fully nonlinear free-surface flows caused by advancing surface disturbances. *International Journal of Offshore and Polar Engineering* 18, 292–301.

Thomson, W. (1887). On ship waves. *Proceedings of the Institution of Mechanical Engineers* 38, 409–434.

Toison, F. and J. Hureau (2000). Open-channel flows and waterfalls. *European Journal of Mechanics-B/Fluids* 19, 269–283.

Torsvik, T., H. Herrmann, I. Didenkulova, and A. Rodin (2015a). Analysis of ship wake transformation in the coastal zone using time-frequency methods. *Proceedings of the Estonian Academy of Sciences* 64, 379–388.

Torsvik, T., T. Soomere, I. Didenkulova, and A. Sheremet (2015b). Identification of ship wake structures by a time-frequency method. *Journal of Fluid Mechanics* 765, 229–251.

Trinh, P. H. and S. J. Chapman (2014). The wake of a two-dimensional ship in the low-speed limit: results for multi-cornered hulls. *Journal of Fluid Mechanics* 741, 492–513.

Trinh, P. H., S. J. Chapman, and J.-M. Vanden-Broeck (2011). Do waveless ships exist? Results for single-cornered hulls. *Journal of Fluid Mechanics* 685, 413–439.

Tuck, E. O. (1965). The effect of non-linearity at the free surface on flow past a submerged cylinder. *Journal of Fluid Mechanics* 22, 401–414.

Tuck, E. O. (1975). Low-aspect-ratio flat-ship theory. *Journal of Hydronautics* 9, 3–12.

Tuck, E. O. (2004). Computation and Minimisation of Ship Waves. In: *Applied Mathematics Entering the 21st Century: Invited Talks from the ICIAM 2003 Congress*. 116. SIAM, 353–369.

Tuck, E. O., J. I. Collins, and W. H. Wells (1971). On ship wave patterns and their spectra. *Journal of Ship Research* 15, 11–21.

Tuck, E. O. and D. C. Scullen (2002). A comparison of linear and nonlinear computations of waves made by slender submerged bodies. *Journal of Engineering Mathematics* 42, 255–264.

Tuck, E. O., D. C. Scullen, and L. Lazauskas (2001). Ship-wave patterns in the spirit of Michell. In: *IUTAM Symposium on Free Surface Flows*. Springer, 311–318.

Ursell, F. (1960). On Kelvin's ship-wave pattern. *Journal of Fluid Mechanics* 8, 418–431.

Vanden-Broeck, J.-M. (1980). Nonlinear stern waves. *Journal of Fluid Mechanics* 96, 603–611.

Vanden-Broeck, J.-M. (1987). Free-surface flow over an obstruction in a channel. *Physics of Fluids* 30.8, 2315–2317.

Vanden-Broeck, J.-M ., L. W. Schwartz, and E. O. Tuck (1978). Divergent low-Froude-number series expansion of nonlinear free-surface flow problems. *Proceedings of the Royal Society of London A: Mathematical, Physical and Engineering Sciences* 361, 207–224.

Vanden-Broeck, J.-M. and S. J. Chapman (2002). Exponential asymptotics and capillary waves. *SIAM Journal on Applied Mathematics* 62, 1872–1898.

Vanden-Broeck, J.-M. and T. Miloh (1995). Computations of steep gravity waves by a refinement of Davies-Tulin's approximation. *SIAM Journal on Applied Mathematics* 55, 892–903.

Vanden-Broeck, J.-M. and T. Miloh (1996). The influence of a layer of mud on the train of waves generated by a moving pressure distribution. *Journal of Engineering Mathematics* 30, 387–400.

Vanden-Broeck, J.-M. and E. O. Tuck (1977). Computation of near-bow or stern flows, using series expansion in the Froude number. In: *Proceedings of the 2nd International Conference of Numerical Ship Hydrodynamics*, 371–381.

Vanden-Broeck, J.-M. and E. O. Tuck (1984). *Wave-Less Free-Surface Pressure Distributions*. Tech. rep. DTIC Document.

Verberck, B. (2013). Hydrodynamics: Wake up. *Nature* 9, 390.

Von Kerczek, C. and N. Salvesen (1977). Nonlinear free-surface effects-the dependence on Froude number. In: *Proceedings of the Second International Conference on Numerical Ship Hydrodynamics*, 292–300.

Wade, S. L., B. J. Binder, T. W. Mattner, and J. P. Denier (2014). On the free-surface flow of very steep forced solitary waves. *Journal of Fluid Mechanics* 739, 1–21.

Wanek, J. M. and C. H. Wu (2006). Automated trinocular stereo imaging system for three-dimensional surface wave measurements. *Ocean Engineering* 33, 723–747.

Wehausen, J. V. and E. V. Laitone (1960). *Surface waves*. Springer.

Williams, J. M. (1981). Limiting gravity waves in water of finite depth. *Philosophical Transactions of the Royal Society of London A: Mathematical, Physical and Engineering Sciences* 302, 139–188.

Wyatt, D. C. and R. E. Hall (1988). Analysis of ship-generated surface waves using a method based upon the local Fourier transform. *Journal of Geophysical Research: Oceans* 93, 14133–14164.

Zhang, C., J. He, Y. Zhu, C.-J. Yang, W. Li, Y. Zhu, M. Lin, and F. Noblesse (2015). Interference effects on the Kelvin wake of a monohull ship represented via a continuous distribution of sources. *European Journal of Mechanics-B/Fluids* 51, 27–36.

Zhang, Y. and S. Zhu (1996). Open channel flow past a bottom obstruction. *Journal of Engineering Mathematics* 30, 487–499.

Zhu, Y., J. He, C. Zhang, H. Wu, D. Wan, R. Zhu, and F. Noblesse (2015). Farfield waves created by a monohull ship in shallow water. *European Journal of Mechanics-B/Fluids* 49, 226–234.

Zhu, Y., C. Ma, H. Wu, J. He, C. Zhang, W. Li, and F. Noblesse (2016). Farfield waves created by a catamaran in shallow water. *European Journal of Mechanics-B/Fluids* 59, 197–204.